ABSTRACT

Title of dissertation: STRUCTURAL PERFORMANCE EVALUATION AND OPTIMIZATION THROUGH CYBER-PHYSICAL SYSTEMS USING SUBSTRUCTURE REAL-TIME HYBRID SIMULATION

Ruiyang Zhang, Doctor of Philosophy, 2017

Dissertation directed by: Assistant Professor, Brian M. Phillips
Department of Civil and Environmental Engineering

Natural hazards continue to demonstrate the vulnerability of civil infrastructure worldwide. Engineers are dedicated to improving structural performance against natural hazards with improved design codes and computational tools. These improvements are often driven by experiments. Experimental testing not only enables the prediction of structural responses under those dynamic loads but also provide a reliable way to investigate new solutions for hazard mitigation. Common experimental techniques in structural engineering include quasi-static testing, shake table testing, and hybrid simulation. In recent years, real-time hybrid simulation (RTHS) has emerged as a powerful alternative to drive improvements in civil infrastructure as the entire structure's dynamic performance is captured with reduced experimental requirements. In addition, RTHS provides an attractive opportunity to investigate the optimal performance of complex structures or components against multi-hazards by embedding it in an optimization framework. RTHS stands to accelerate advancements in civil engineering, in particular for designing new structural systems or devices in a performance-based design environment.

This dissertation focuses on the use of cyber-physical systems (CPS) to evaluate structural performance and achieve optimal designs for seismic protection. This dissertation presents systematic studies on the development and validation of the dynamic substructuring RTHS technique using shake tables, novel techniques in increasing RTHS stability by introducing artificial damping to an under-actuated physical specimen, and the optimal design of the structure or supplemental control devices for seismic protection through a cyber-physical substructure optimization (CPSO) framework using substructure RTHS.

STRUCTURAL PERFORMANCE EVALUATION AND OPTIMIZATION THROUGH CYBER-PHYSICAL SYSTEMS USING SUBSTRUCTURE REAL-TIME HYBRID SIMULATION

by

Ruiyang Zhang

Dissertation submitted to the Faculty of the Graduate School of the
University of Maryland, College Park in partial fulfillment
of the requirements for the degree of
Doctor of Philosophy
2017

Advisory Committee:

Professor Brian M. Phillips, Chair
Professor Sherif M. Aggour
Professor Inderjit Chopra
Dr. Chung C. Fu
Professor Yunfeng Zhang

To my family.

ACKNOWLEDGEMENTS

I would like first to express my thanks to my advisor, Professor Brian M. Phillips, for his advice, encouragement, and support throughout my graduate studies at the University of Maryland, College Park. It has been an honor to pursue my Ph.D. degree under his supervision. His academic insight and passion have greatly inspired me in many ways. I sincerely appreciate all his support to make my Ph.D. experience productive and memorable.

I would also like to thank the efforts of my committee members, Professor Sherif M. Aggour, Professor Inderjit Chopra, Professor Chung C. Fu, and Professor Yunfeng Zhang. All their support and comments are greatly appreciated.

I gratefully acknowledge the support of Professor Yunfeng Zhang for the experimental studies at the University of Maryland Structural Engineering Laboratory. I also very much appreciate the support and contribution of Professor Ikago and Professor Ikenaga on the large-scale testing at Tohuku University in Japan.

The research in this dissertation is based upon work supported by the National Science Foundation under Grant No. 1444160 and by the Japan Society for the Promotion of Science (JSPS) under Grant-in-Aid for Scientific Research (B) No. 15H04070. These supports are gratefully appreciated. Any opinions, findings, and conclusions or recommendations expressed in this material are those of the author and do not necessarily reflect the views of these agencies.

I would like to thank all my fellow graduate students, Jingzhe Wu, Ashkan Keivan, Sami Khan, Michael Whiteman, and Katie Russell. Their support, friendship, and collaboration have been most valuable to me.

I also appreciate the help of my best friend Meng Wang at the University of California San Diego for his support and encouragement all the time. His academic excellence and research vision directly influenced and motivated me.

Most importantly, I would like to thank my parents for their continuous support and understanding as I pursued my goals so far away from home. Without their love and support, I would never be the person that I am today. I love you both.

TABLE OF CONTENTS

LIST OF FIGURES

LIST OF TABLES

CHAPTER 1 INTRODUCTION

1.1 Motivation

Natural hazards continue to demonstrate the vulnerability of civil infrastructure worldwide. Earthquakes, as one of the most destructive hazards, have resulted in tremendous economic and societal devastation. Recent significant examples include the 2011 Tohoku earthquake with a magnitude of 9.0 in Japan, the 2015 Nepal earthquake with a magnitude of 7.9, and the 2016 Ecuador earthquake with a magnitude of 7.8. Over the years, engineers gain a better understanding of structural behavior through these unfortunate events, and create improvements to structural performance through more detailed design codes and computational tools. Experimental testing supplements post-disaster evaluations, allowing engineers to study structural behavior under simulated loads in a controlled environment. Experimental testing not only enables the prediction of structural responses under these dynamic loads, but also provides a reliable way to investigate new solutions for hazard mitigation. This is particularly true when the structure behaves inelastically and/or includes components whose behavior is strongly rate-dependent, such as dampers or other nonlinear energy dissipation devices. In addition, experimental testing provides important validation of numerical simulation and structural optimization. Furthermore, when the response of a structure or system is not well understood or difficult to model numerically, experimental testing provides the only accurate way to assess the structural responses. This dissertation proposes new experimental techniques that expand the range of structural systems that can be evaluated in laboratories worldwide. These techniques are based on the dynamic substructuring of a

system, leveraging the accuracy of experimental testing and efficiency of numerical simulation.

With pushes toward performance-based design, optimization provides an efficient tool to cost-effectively address competing performance objectives such as minimizing displacements and accelerations. Currently, structural optimization uses numerical simulation to evaluate candidate designs. However, when dealing with complex structures that are difficult to model numerically, large errors could exist between the numerical model and the physical system. This is particularly true when exploring a large solution space that may take the numerical model outside of the range for which it was calibrated. In such cases, optimization is less reliable because the best results are optimal for the numerical models instead of the as-built structure. Experiments can be included in the optimization algorithm to represent complex structures or components. However, there are significant time and cost limitations when constructing each candidate design for experimental evaluation. A more efficient framework is needed that combines the accuracy of experimental testing and efficiency of numerical simulation to evaluate candidate designs. In this dissertation, an optimization framework with substructured experimental testing is proposed. The proof-of-concept studies show great potential and broad applicability.

1.2 Proposed Work

Cyber-physical systems (CPS) link the real world with the cyber world, leveraging the capabilities of digital computers to monitor and control physical attributes in real time. Example applications of CPS to experimental testing in civil engineering include

substructuring and optimization. In substructuring, a structure's response is obtained from the experimental evaluation of components of interest, coupled with the numerical simulation of the remainder of the structure. Sensing and actuation link these substructures together in a loop of action and reaction. In optimization, experimental responses are numerically analyzed to determine and then create physical changes that iteratively achieve better designs. This dissertation proposes advances in both substructuring and optimization to improve protective systems for civil infrastructure.

This dissertation begins with the development of a simple and versatile substructure RTHS framework using shake tables. A model-based shake table control approach is successfully implemented for online acceleration tracking of substructure interface degrees-of-freedom. In the model-based controller, the feedforward controller compensates for the linearized shake table dynamics while the feedback controller accounts for any uncertainties or nonlinearities in the shake table performance. A Kalman filter is introduced to reduce measurement noise in the RTHS loop without introducing phase lag. The performance of the proposed RTHS technique is demonstrated using a simple uni-axial shake table and shear building specimen. A challenging substructuring scenario with low system damping is selected to demonstrate the robustness of the proposed RTHS framework. Even for shake tables with large control-structure interaction and structures with low damping, the proposed framework is robust, reliable, and uses readily available equipment, providing a new experimental tool to laboratories worldwide for assessing the responses of structures with realistic dynamic properties through RTHS.

In addition, a novel technique is proposed to introduce artificial damping to an under-actuated dynamic specimen through shake table control. The performance of the

proposed artificial damping by feedforward control (AD-FF) is investigated for both traditional shake table testing and shake table RTHS. Artificial damping can be introduced to lower modes to increase the specimen's apparent damping or to higher modes to improved RTHS stability, a feature that cannot be realized by using physical damping devices. In RTHS, proposed AD-FF represents a significant contribution toward increasing stability without changing the dominant structural response by adding damping to higher modes (even if they manifest in the specimen).

The proposed RTHS approach is then applied to investigate the seismic performance of a 14-story high-rise building with inter-story isolation, a practical application study enabled by the cost-effective approach. The effectiveness of RTHS in reproducing the total structural behavior was verified through comparisons with numerical simulations. This confidence will enable studies of more complex inter-story isolation systems which may not be as easily modeled numerically, necessitating experimental studies through RTHS. The benefits of implementing inter-story isolation such as on retrofit application were confirmed through RTHS.

Finally, a cyber-physical substructure optimization (CPSO) framework is proposed for structural optimization through substructure RTHS against natural hazards. The framework incorporates substructure experimental testing to for accurate and cost-effective evaluation of candidate designs. The proposed technique is explored through a proof-of-concept study on a two-story base-isolated structure. Furthermore, the proposed technique is implemented to improve the seismic performance of a highly nonlinear system. In the nonlinear optimization, the control algorithm of a physical MR damper is iteratively improved to deliver optimal seismic protection for a 5-story base-isolated

structure against a suite of design earthquakes. To improve the efficiency of the CPSO framework, an improved particle swarm optimization (PSO) algorithm is proposed.

Chapter 2 provides a detailed review of previous studies on RTHS and shake table control strategies. A review on structural optimization is also presented.

Chapter 3 develops the proposed RTHS framework through a simple uni-axial shake table and shear building specimen. A challenging substructuring scenario is selected to demonstrate the favorable performance of the proposed RTHS technique.

Chapter 4 presents a novel technique to provide artificial damping to an experimental specimen in traditional shake table testing and shake table RTHS. The benefits of the proposed technique g are illustrated.

In Chapter 5, the proposed substructure RTHS framework is applied to evaluate the performance of a 14-story high-rise building with inter-story isolation with a supplemental damping in the isolation layer. The favorable stability and suitability of RTHS for inter-story isolation is illustrated.

Chapter 6 develops and validates a cyber-physical substructure optimization framework for structural optimization against natural hazards. The approach incorporates RTHS for the efficient evaluation of candidate designs. The optimal design of isolation for base-isolated structure is conducted using the proposed technique under a single earthquake, several earthquakes, and a suite of designed earthquakes. The robustness and favorable performance of the proposed CPSO framework is demonstrated.

In Chapter 7, the CPSO framework proposed in Chapter 6 is applied to the seismic protection of a nonlinear system. The control of a physical MR damper is optimized to mitigate seismic responses of a 5-story base-isolated structure. To improve

the efficiency of the proposed CPSO for structural optimization against multiple dynamic excitations, a multi-interval PSO (MI-PSO) technique is proposed. The efficiency of CPSO is greatly improved, especially for complex systems with multiple control variables under a large number of design excitations. This study further demonstrates the favorable performance of the proposed CPSO and the significant potential for studying nonlinear systems or devices that are difficult to model numerically.

Chapter 8 summarizes the research detailed in this dissertation. Additionally, recommendations and a number of research areas for future studies are proposed.

CHAPTER 2 LITERATURE REVIEW

2.1 Experimental Techniques

Current experimental testing techniques commonly used by structural engineers include quasi-static testing, shake table testing, and hybrid simulation (also referred to as pseudo-dynamic testing and hybrid testing). Quasi-static testing is the most straightforward experimental testing technique in which a structure or structural component is loaded in a predefined force or displacement on an extended time scale (i.e., slow rate). Typically quasi-static testing is used to investigate the strength, stress distribution, or hysteretic behavior of a material or structural component. Therefore, it is essential in developing and improving design code provisions by providing capacity information. However, quasi-static testing is limited by its predefined loading protocol, resulting in no interaction between structural behavior and future load steps.

Shake table testing is a dynamic testing method where the entire structure is modeled and subjected to a ground motion applied by a shake table. Because the test is dynamic, the dynamic responses and rate-dependent behavior are completely captured, making this experimental technique attractive for seismic studies. Although some large-scale shake tables exist that are capable of testing full-scale building structures (e.g., the E-Defense table in Japan), reduced-scale structural models are generally required due to limitations on the size and payload capacity of the shake table, as well as economic concerns. Similitude laws should be followed for scaled models to assure the accurate representation of the target full-scale buildings. However, many behaviors especially local effects, such as fatigue, local buckling in steel, crack propagation, and welds, limit

the accuracy of the scaled models. Shake table testing is also not applicable to other types of dynamic loads such as wind due to base excitation. It is also challenging to capture soil-structure interaction unless the foundation is modeled physically on the table.

Hybrid testing provides an attractive alternative for dynamic testing of structural systems by combining experimental testing and numerical simulation (Hakuno et al., 1969; Takanashi et al., 1975; Mahin and Shing, 1985; Takanashi and Nakashima, 1987; Mahin et al., 1989; Shing et al., 1996). First, the structure is idealized as a discrete system with limited number of degree-of-freedom (DOF). The structural responses are solved by means of a direct time-stepping integration scheme, with the mass and viscous damping properties of the structure modeled numerically. The computed displacements are imposed on the specimen using actuators in a quasi-static manner. The response of the experimental component is measured and used to update the numerical integration. Essentially, it is similar in concept to dynamic structural analysis, except that the stiffness of some structural components are directly measured from the specimen during a test. In conventional hybrid testing, the specimen is loaded on an extended time-scale allowing for the use of larger actuators without high hydraulic flow requirements and increasing flexibility during testing. This makes hybrid testing inapplicable to rate-dependent specimens.

In hybrid simulation, the structural components for which the response is well understood are modeled numerically, greatly reducing the required laboratory space and equipment. Because only the less understood, critical structural components are physically tested, they can be large or full-scale representations of the actual components,

reducing size effects. In this way, even small laboratories can conduct accurate experiments of complex structures.

2.2 Real-time Hybrid Simulation

Real-time hybrid simulation (RTHS; also known as model-in-the-loop and hardware-in-the-loop testing) is increasingly recognized as a powerful experiment technique to evaluate the performance of structural components subjected to earthquake loads. Essentially, it is a variation of hybrid simulation in which the experiment is executed in real time, thus offering the capability to test rate-dependent components, such as dampers and other structural control devices (Carrion et al., 2009; Christenson et al., 2008; Zapateiro et al., 2010). The numerical simulation, which runs in parallel to the experimental testing, is executed with a small enough time step to ensure continuous real-time motion of the specimen. Figure 2.1 shows a simple diagram of the communication between the numerical and experimental components in RTHS loop. RTHS provides an attractive alternative to traditional shake table testing for earthquake engineering studies (Nakashima et al., 1992) by combining experimental testing and numerical simulation in an efficient and cost-effective framework. The loop of action and reaction between experimental and numerical components is executed in real-time, ensuring accurate representation of both the local and global dynamic behavior of the structure.

Although the concept is very attractive, challenges do exist in its implementation. The major features and challenges in RTHS are summarized in the following subsections.

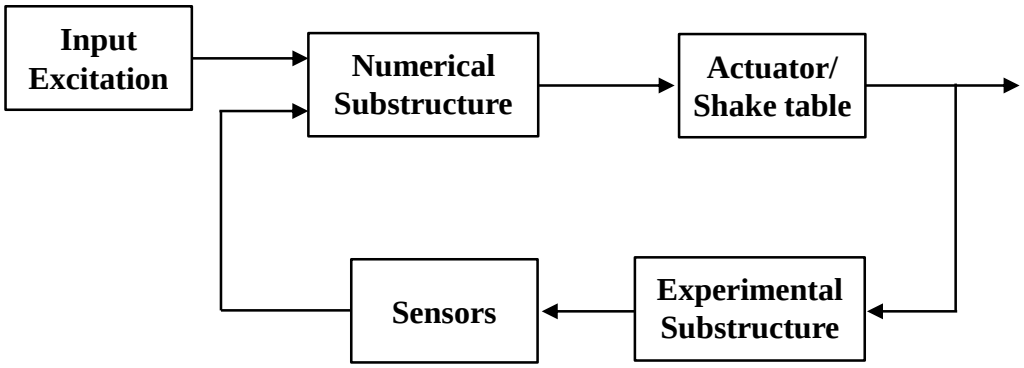

Figure 2.1 Basic diagram for real-time hybrid simulation

2.2.1 Integration time step

One of the major challenges for RTHS is that it requires a fixed, small sampling time in the execution of each testing cycle. Because the test is conducted in real time, it is necessary to perform all calculations, apply the interface reactions, and measure and feedback the forces within a single time step. This time constraint is problematic for complex or nonlinear numerical models. However, the numerical substructure is often taken as the portion of the structure that is easy to model, making it possible to use small, fixed integration time steps.

2.2.2 Time delays and time lags

In RTHS, there is a continuous exchange of information between all of the components (e.g., numerical and experimental) within a closed-loop. Thus, RTHS is very sensitive to time delays and time lags. Time delays generally are caused by the communication of data, analog to digital (A/D) and digital to analog (D/A) conversion, and the computation time. These delays are not a function of frequency, and can be reduced by using faster hardware and smaller numerical integration time steps. Time lags are caused by the given command and the realization of this command by the actuator, as a result of the physical

dynamics and limitation of the servo-hydraulic actuators. In contrast to time delays, time lags vary with both the frequency of excitation and specimen conditions (Dyke et al., 1995). The effect of time delays and time lags is that the measured displacement lags behind desired displacement, leading to experimental errors that accumulate over time. Figure 2.2(a) illustrates a desired and measured signal with an assumed fixed delay T_d. Figure 2.2(b) shows the response of a linear spring subject to a fixed time delay T_d between the desired and the measured response. If the desired displacement is associated with the measured force delayed by T_d, the observed specimen behavior is a counter-clockwise hysteretic loop (i.e., negative damping), instead of the straight line corresponding to the desired linear behavior. Unless properly compensated, time delays and time lags introduced by the experimental equipment may lead to stability and accuracy problems (Horiuchi et al., 1996). Undershooting the displacement or a lag in the displacement will decrease the apparent damping (adding energy) of the system (Shing and Mahin, 1983; Shing and Mahin, 1987). Therefore, mitigation of the effects of time delays and time lags is essential part of RTHS.

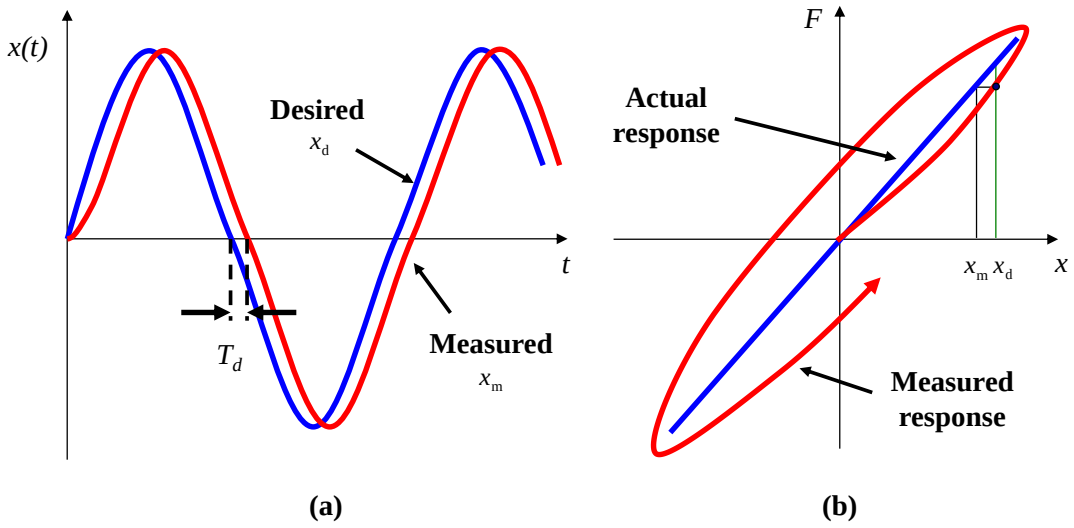

Figure 2.2 (a) Time delay; (b) Effect of time delay on hysteresis

Lin et al. (2015) systematically studied the influence of time delays on RHTS stability. This study provided an example single-degree-of-freedom system with a ratio of numerical to experimental stiffness of 0.69 and critical damping ratio of 1.4% which exhibited unstable behavior when the time delay exceeded 15 msec. One of the most effective approaches to mitigate the effect of time delays and time lags is through actuator control strategies designed to compensate for the modeled dynamics of the servo-hydraulic system (Carrion and Spencer, 2007; Phillips and Spencer, 2012).

2.2.3 System damping

All building structures exhibit some degree of energy loss during vibrations through inherent damping. The most significant source of inherent damping is internal friction in the structural materials, connections, and nonstructural components (Charney, 2008). Damping plays an important role in structural dynamics due to its effect of reducing, restricting, or preventing large and sustained structural oscillations.

In experimental studies of civil structures, reduced scale models are designed and constructed according to similitude theory (geometry, boundary conditions, and dynamic properties, etc.) to achieve comparable dynamic responses between the model (specimen) and prototype (structure of interest). Damping is an important structural parameter that requires particular attention in scaled testing as it is influenced by the material.

Damping not only plays a significant role due to its effects of absorbing energy and reducing structural responses, but also in the stability of experimental testing techniques. As described in the previous subsection, time delays and time lags can lead system to be unstable in form of introducing additional energy into the system. Horiuchi et al. (1996) demonstrated that for a linear-elastic, single-degree-of-freedom (SDOF)

system, the effect of the energy introduced by a time delay is equivalent to negative damping. The negative damping was shown to be not only related to the time delay T_d, but also related to the stiffness of the specimen k^E. The equivalent damping added by the delay and stiffness is given as $-k^E T_d$. Therefore, negative damping can be especially problematic for steel frames and shear walls, which exhibit high stiffness and low structural damping. When negative damping exceeds the inherent structural damping of the system, the RTHS loop can become unstable. For multi-degree-of-freedom (MDOF) systems, higher modes are normally less dominant in structural responses; however, higher modes are more sensitive to time delays and time lags, are more difficult to control using actuators, and are more easily contaminated by sensor noise. If energy is added to these higher modes and time delays and lags are not adequately mitigated, the system can become unstable.

Researchers have developed many artificial damping techniques to achieve the target damping and damp out the responses at higher modes for numerical studies. However, these techniques do not work when there is an experimental dynamic substructure. The inherent damping in the specimen, especially for bare steel frame specimens, may be less than the target level of damping and furthermore small enough to cause stability issues in the RTHS loop. In the experimental tests, extra damping could be added through physical damping devices (e.g., oil dampers) which are expensive and require additional specimen design and installation considerations. Furthermore, there is no direct way to introduce damping to specific modes. The need to accurately represent or even increase structural damping in a cost-effective way is an important need for RTHS and is addressed by this dissertation.

2.2.4 Substructuring

In RTHS, substructuring divides the total structure or system into a numerical substructure and an experimental substructure. The experimental substructure, including the physical components of interest (e.g., where damage is expected, or difficult to model numerically), is tested experimentally, while the rest of the structure is analyzed numerically. Substructuring directly influences the model of interaction between numerical and experimental components. It is challenging to synchronize the boundary conditions between the numerical and experimental substructure interfaces. Servo-hydraulic actuators or shake tables are capable of providing interface boundary conditions. An example RTHS loop with implementation of actuators is shown in Figure 2.3. In addition, the substructuring partitioning (ratio of experimental and numerical portions) will influence the stability and accuracy of the RTHS (Lin et al., 2015). With similar levels of damping, a RTHS framework with larger experimental substructure partitioning has less tolerance for time delay, requiring larger control efforts to maintain the system stability.

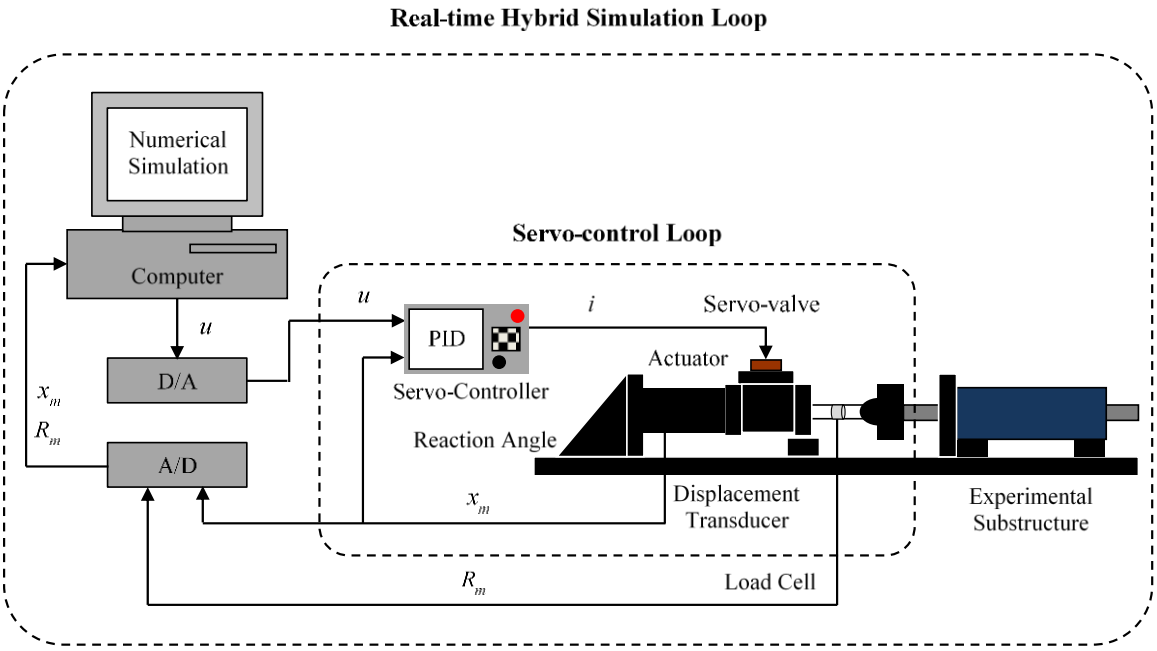

Figure 2.3 Schematic of real-time hybrid simulation loop with substructuring

2.2.5 Control-structure interaction

When shake tables or actuators are used to excite a specimen, a strong dynamic coupling is often present between the loading device and specimen, identified as control-structure interaction (CSI) (Dyke et al., 1995). It is acceptable to neglect CSI in conventional hybrid testing due to the slow loading rate while unacceptable in RTHS due to the dynamic loading rate. When specimens change in behaviors through damage or nonlinearity, the actuator dynamics will change due to CSI, making actuator control more challenging. The interaction between specimen and actuator must be considered in the actuator control for accurate time delay and time lag compensation.

2.2.6 Shake table control

Shake tables are inherently nonlinear devices due to nonlinearities in actuator behavior, friction in the table (Rea et al., 1977), and control-structure interaction (CSI) (Blondet et

al., 1988; Rinawi and Clough, 1991). Therefore, it is challenging to reproduce a desired acceleration over a wide range of frequencies. In addition to the challenges due to the physical shake table system, challenges are also induced by the desired tracking signal. Shake table testing is unique in that the desired trajectory is an acceleration signal, however, for stability, servo-hydraulic actuators still operate in displacement feedback through an inner-loop PID controller. Many shake table controllers are developed as outer-loop controllers built around inner-loop displacement feedback controller. With this understanding, the most basic approach to achieve the desired acceleration record is to first integrate twice to determine a compatible displacement record. Simova and Mamucevski (1980) present this offline method, whereby the resulting displacement record is tracked by the shake table using displacement feedback. With this approach, shake table dynamics lead to difficulties matching the desired accelerations, especially at higher frequencies and around frequencies influenced by CSI.

Fletcher (1990) presents a transfer function iteration method used by many commercial shake tables, later applied to a small-scale shake table in Spencer and Yang (1998). This approach is based on a linearized model of the shake table commands to measured acceleration. An inverse of this model is used to generate a command signal history from the acceleration record, taking into account the modeled table behavior. However, nonlinearities lead to error between desired and measured accelerations. In transfer function iteration, these errors are used to iteratively modify the input shake table command signal to reduce errors in subsequent tests.

Nakata (2010) proposed an acceleration tracking control in which a linearized model of the shake table is used to develop the feedfoward controller, joined by a

displacement feedback controller to provide stability to the shake table and avoid excessive drift. In this approach, commands are sent directly to the servo-valve (no inner-loop controller is used). Phillips et al. (2014) developed a feedforward-feedback approach based on a linearized model of the shake table dynamics and included both acceleration and displacement feedback though the use of LQG control. This method was demonstrated to be effective for evaluating nonlinear specimens in traditional shake table testing.

2.2.7 Shake tables for substructure RTHS

Shake tables present an opportunity in the area of RTHS because the equipment is widely available and the creation of substructure boundary conditions is straightforward. The shake table base plate can serve as the interface between numerical and experimental substructures, a convenient convention for certain structural systems. This configuration is particularly useful when the lower portion of the structure can be represented numerically (as shown in Figure 2.4). In dynamic substructuring (Shing, 2008), where there is significant vibrating mass in the experimental substructure, the shake table must track absolute accelerations at the interface boundary to ensure that the inertial forces of the specimen are accurately represented. Acceleration tracking strategies have been developed for decades, allowing shake tables to track desired ground motions for earthquake studies. Acceleration-based shake table control strategies can be repurposed for shake table RTHS if the strategy accepts an acceleration generated in real time.

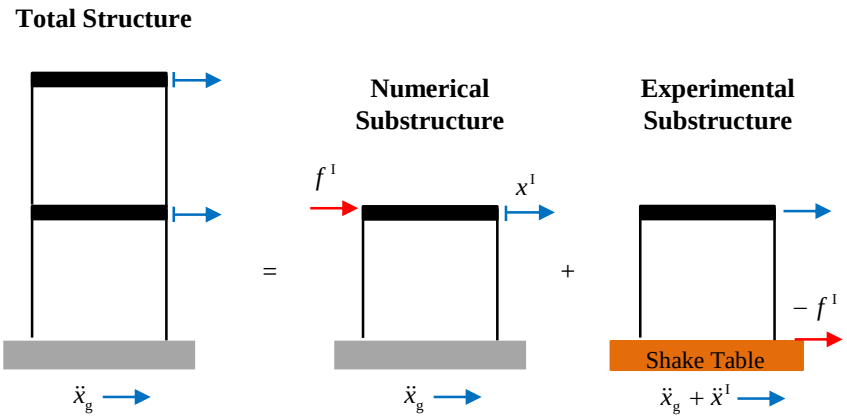

Figure 2.4 Substructuring using shake table

Unlike traditional shake table testing, in RTHS the acceleration trajectory is not known prior to testing (i.e., the acceleration is calculated online). Therefore, shake table control strategies in the literature requiring offline calculations and configuration (Simova and Mamucevski, 1980; Fletcher, 1990; Spencer and Yang, 1998) cannot be used for real-time testing. In contrast, some recently developed acceleration-tracking shake table control strategies (Kuehn et al., 1999; Nakata, 2010; Phillips et al., 2014) do not require the desired acceleration to be predefined and can potentially be employed in RTHS.

There are a few examples in the literature of successful RTHS using a shake table to enforce substructure boundary conditions. Nakata and Stehman (2014) presented a model-based actuator delay compensation and a force correction technique to achieve desired interface acceleration tracking. Shao et al. (2010) investigated a more complex RTHS configuration with the experimental substructure taken as the middle floor of a building by using both a shake table and actuators. In these examples, the structures investigated are highly damped, resulting in a system that is less representative of a realistic structure but easier to control and achieve stability in RTHS. The damping ratios

of the total structure in Nakata and Stehman (2014) are 8%, 11%, and 19% for the first three modes and 11%, 19%, and 7% for the first three modes in Shao et al. (2010). In addition, the numerical substructures are large relative to the experimental substructure, another favorable condition for RTHS stability and accuracy. In this dissertation, a lightly damped structure with relatively large experimental substructure is investigated to demonstrate the stability of the proposed framework as well as develop techniques to introduce damping into substructured experimental systems.

2.3 Structural Optimization

In the past three decades, a great attention has been paid to structural optimization, especially in design and construction fields. Many algorithms have been developed to optimize structural design for strength and serviceability while minimizing costs. In general, structural optimization can be divided into size optimization, shape optimization, and topology optimization (Rozvany, 2009). Size optimization is focused on optimizing the cross-section of the discrete structural members such as beams and columns, or the thickness of continuous materials such as panels and slabs. In shape optimization, positioning of nodes and connections are varying. Topology optimization concentrates on the distribution of material and structural connectivity, aiming to find the optimal layout of the structure.

Optimization empowers engineers to discover more efficient structures in an automated, algorithmic framework. In structural engineering, systems are often nonlinear and subject to physical or design code constraints, narrowing the field of optimization to nonlinear constrained problems. In this type of optimization, engineers seek the

parameter values that minimize an objective function while subject to constraints. The optimization problem must first be expressed in this basic mathematical form and then solved using an optimization algorithm of choice.

Two major categories of optimization algorithms include gradient-based and heuristic algorithms. In gradient-based algorithms, the gradient of the objective function is used to determine which design variables have the greatest influence on the objective function. The gradient may be explicitly calculated or estimated by perturbing the variables around their current value, e.g., using finite differences. The gradient is used to create a subsequent design iteration that most effectively decreases (or increases, depending on the type of problem) the objective function.

The major benefit of gradient-based algorithms is that they adapt at each iteration, selecting the most efficient path toward the global minimum (or maximum). In gradient-based algorithms, the gradient estimation is essential to the reliability and efficiency of the optimization. A large error in gradient estimation may result in a movement in an entirely wrong direction. Furthermore, for some complicated engineering problems without a "direct path" from the starting point (e.g., no exact solution), gradient information may not be available for solving the problem. Researchers have developed a suite of gradient estimation techniques, including finite differences (Azadivar, 1992), likelihood ratios (Glynn, 1987; Rubenstein, 1989), Newton's method, conjugate gradient method, gradient descent, subgradient method, andperturbation analysis.

In contrast to gradient-based methods, Heuristic algorithms do not require gradient information to converge to an optimal solution. These techniques provide faster convergent for complicated structural systems. Heuristic methods make few or no

assumptions about the nature of the problem being optimized. Heuristic algorithms start with an arbitrary initial condition, iteratively generate and evaluate candidate solutions, and guide the exploration of the design space toward the optimal solution. At each iteration, a set of designs are generated with some degree of randomness applied to the design variables, depending on the algorithm. The development of candidate solutions is based on probabilistic rules rather than deterministic rules. Designs that are valid as defined by the constraints are then evaluated using an analysis tool such as finite element method (FEM). Analysis results that satisfy any remaining constraints are then evaluated using the objective function. The results are synthesized and designs which performed best help inform the next generation of solutions.

Heuristic methods approximate the optimal solution rather than guarantee that the optimal solution will be found. Moreover, the solution is by definition sub-optimal in that the solution is not rigorously demonstrated to be the optimal solution. For brevity, the converged sub-optimal solution results from heuristic algorithms will be referred to as the optimal solution in this dissertation. Limitations aside, heuristic algorithms can be applied to very complicated problems with multiple design variables and when a gradient is unknown or unavailable. Additional benefits stem from the broad exploration of the design space and randomization, which can lead to non-intuitive solutions.

Recently developed heuristic algorithms include simulated annealing (SA) (Juan et al., 2003; Wang et al., 2005), genetic algorithms (GAs) (Li and Li, 2000), particle swarm optimization (PSO) (Tandon et al., 2002; Kurdi et al., 2004; Baskar et al., 2005; Kurdi, 2005), and ant colony optimization (ACO) (Baskar et al., 2005). The inspiration behind these intelligent search techniques is to simulate natural phenomena and they are

named according to the phenomenon that is used in the construction of the method. Genetic algorithms make use of the idea of survival of the fittest. Simulated annealing utilizes energy minimization that happens in the cooling process of molten metals. Ant colony optimization imitates the way that ant colonies find the shortest route between the food and their nest. Genetic algorithms are based on the concepts of natural selection and natural genetics; they rely on the principles of Darwinian theory of survival of the fittest (Holland 1975; Goldberg 1989). Genetic algorithms are popular because they efficiently incorporate information from previous iterations to create new search points in the design space, resulting in an improved performance. Simulated mutations incorporate randomness into the exploration of the design space. Genetic algorithms are related to simulated annealing. The connections between simulated annealing and genetic algorithms are explored by Davis (1987).

2.3.1 Particle swarm optimization

PSO is inspired by the social behavior of animals such as fish schooling, insects swarming, and birds flocking (Kennedy et al., 2001). It involves a number of particles, which are initialized randomly in the search space of an objective function. The group of particles is referred to as a swarm. Each particle of the swarm represents a potential solution of the optimization problem. The particles explore the search space; their positions are updated based on their current path, their own best known design, and the swarm's best known design. In each iteration, the swarm is updated using the following equations:

$$V_i^{k+1} = \omega V_i^k + c_1 r_1 (P_i^k - X_i^k) + c_2 r_2 (P_g^k - X_i^k) \tag{2.1}$$

$$X_i^{k+1} = X_i^k + V_i^{k+1} \tag{2.2}$$

where X_i and V_i represent the current position and the velocity of the *i-th* particle, respectively; P_i is the best previous position of the *i-th* particle (called pbest) and P_g is the best global position among all the particles in the swarm (called gbest); r_1 and r_2 are two uniform random sequences generated from U(0, 1); and ω is the inertia weight used to preserve a portion of the previous velocity of the particle (Shi and Eberhart, 1998).

The flowchart of the algorithm is given in Figure 2.5. First, the swarm of particles is initialized with sequence numbers and initial velocities that are randomly distributed throughout the design space. Second, the objective function values are evaluated using the design space positions. Next, the optimum particle position at the current iteration and the global optimum particle position are updated. Then, the velocity vector of each particle is updated considering the current position of the particle, the current velocity of the particle, the best position of the particle, and the best position of the swarm. The sequence number for the position of each particle is updated. Finally, the previous steps are repeated until the pre-determined number of iterations or a stopping criteria is reached.

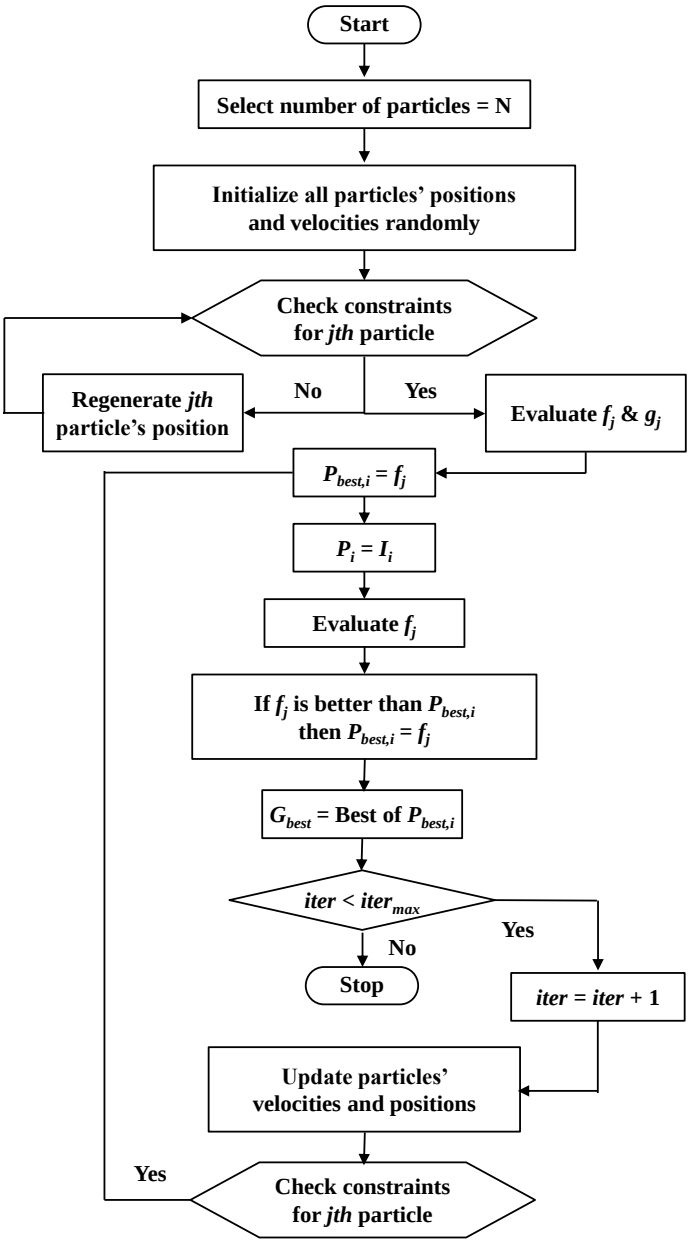

Figure 2.5 Flowchart of particle swarm optimization

The PSO can be enhanced incorporating additional social behaviors such as bird flocking, fish schooling and insects swarming, which are considered as congregation. Passive congregation is an attraction of an individual to other group members but not a display of social behavior (He et al., 2004). Fish schooling is one of the representative

types of passive congregation. He et al. proposed a hybrid PSO with passive congregation (PSOPC) as follows (He et al., 2004):

$$V_i^{k+1} = \omega V_i^k + c_1 r_1 (P_i^k - X_i^k) + c_2 r_2 (P_g^k - X_i^k) + c_3 r_3 (R_i^k - X_i^k) \tag{2.1}$$

$$X_i^{k+1} = X_i^k + V_i^{k+1} \tag{2.2}$$

where R_i is a particle selected randomly from the swarm, c_3 is the passive congregation coefficient, and r_3 is a uniform random sequence in the range (0, 1): r_3–U(0,1). Several benchmark functions have been tested in (He et al., 2004). The results show that the PSOPC has a better convergence rate and a higher accuracy than the PSO for the problems studied.

The difficulties encountered in optimization include high computational costs where thousands of iterations are necessary. The efficiency not only depends on the optimization techniques but also on the system being optimized. Currently, most optimization algorithms are developed to achieve the optimum objectives (e.g., sectional areas, construction costs) based on numerical models. Benefits are obvious including saving computing time and costs. However, when dealing with complex structures which are difficult to model numerically, large errors could exist between the numerical model and the physical structure. In that case, the optimization is less meaningful because the best results achieved are optimal for the numerical models instead of the physical structure in reality. Experiments can be included in the optimization scheme for those complex structures or components. However, time and costs stay as obstacles in this study. RTHS provides an alternative to investigate the optimal performance of those complex structures or components.

This dissertation proposes the novel use of RTHS in an optimization framework. To successfully, achieve this new approach to structural optimization, several challenges are identified and addresses. The challenges of RTHS described in previous section intrinsically present, and made more complicated in combination with optimization because the candidate solutions of optimization are not known prior to testing. Therefore, the constraints of variables should be properly defined avoiding instability in RTHS. Additionally, a combined hardware-software platform for optimization through RTHS with automatic updates on variables and testing results must be developed from scratch.

CHAPTER 3 SUBSTRUCTURE RTHS FRAMEWORK DEVELOPMENT

In this chapter, a versatile substructure RTHS framework using shake tables is developed for evaluating structural performance. A challenging substructuring scenario with low damping is selected to investigate the stability and accuracy of the proposed RTHS techniques. Results are compared to numerical simulation to demonstrate the accurate RTHS performance. The proposed RTHS framework is validated to be accurate, efficient, and reliable in evaluating seismic responses of the structural system. The study in this chapter increases the confidence for applying the proposed technique to more complex structures, as well as incorporating into an optimization framework.

3.1 Substructure Shake Table RTHS

For a simple illustration of the use of a shake table in RTHS, a linear 3DOF shear building is considered (see Figure 3.1(a)). The equations of motion governing the dynamic response of the structure subjected to an input ground motion are represented as follows:

$$\begin{bmatrix} m_1 & 0 & 0 \\ 0 & m_2 & 0 \\ 0 & 0 & m_3 \end{bmatrix} \begin{Bmatrix} \ddot{x}_1 \\ \ddot{x}_2 \\ \ddot{x}_3 \end{Bmatrix} + \begin{bmatrix} c_1 + c_2 & -c_2 & 0 \\ -c_2 & c_2 + c_3 & -c_3 \\ 0 & -c_3 & c_3 \end{bmatrix} \begin{Bmatrix} \dot{x}_1 \\ \dot{x}_2 \\ \dot{x}_3 \end{Bmatrix} + \begin{bmatrix} k_1 + k_2 & -k_2 & 0 \\ -k_2 & k_2 + k_3 & -k_3 \\ 0 & -k_3 & k_3 \end{bmatrix} \begin{Bmatrix} x_1 \\ x_2 \\ x_3 \end{Bmatrix} = -\begin{bmatrix} m_1 & 0 & 0 \\ 0 & m_2 & 0 \\ 0 & 0 & m_3 \end{bmatrix} \begin{Bmatrix} 1 \\ 1 \\ 1 \end{Bmatrix} \ddot{x}_g \quad (3.1)$$

where m_i, c_i, and k_i are the mass, damping, and stiffness of the *i*-th story, x_i is displacement relative to the ground of the *i*-th story, $\ddot{x}_g$ is the ground acceleration, and dots represent differentiation with respect to time. For RTHS, the equations of motion in Eq. 3.1 are separated into numerical and experimental components as in Eq. 3.2 and Figure 3.1(b). Structural parameters as well as DOF associated with the experimental substructure are indicated by the superscript “E”. Structural parameters as well as DOF

associated with the numerical substructure are indicated by the superscript "N". The DOF at the interface between components are indicated by the superscript "I".

$$\begin{bmatrix} m_1^{\mathrm{N}}+m_1^{\mathrm{E}} & 0 & 0 \\ 0 & m_2^{\mathrm{E}} & 0 \\ 0 & 0 & m_3^{\mathrm{E}} \end{bmatrix}\begin{Bmatrix} \ddot{x}_1^{\mathrm{I}} \\ \ddot{x}_2^{\mathrm{E}} \\ \ddot{x}_3^{\mathrm{E}} \end{Bmatrix}+\begin{bmatrix} c_1^{\mathrm{N}}+c_2^{\mathrm{E}} & -c_2^{\mathrm{E}} & 0 \\ -c_2^{\mathrm{E}} & c_2^{\mathrm{E}}+c_3^{\mathrm{E}} & -c_3^{\mathrm{E}} \\ 0 & -c_3^{\mathrm{E}} & c_3^{\mathrm{E}} \end{bmatrix}\begin{Bmatrix} \dot{x}_1^{\mathrm{I}} \\ \dot{x}_2^{\mathrm{E}} \\ \dot{x}_3^{\mathrm{E}} \end{Bmatrix}+\begin{bmatrix} k_1^{\mathrm{N}}+k_2^{\mathrm{E}} & -k_2^{\mathrm{E}} & 0 \\ -k_2^{\mathrm{E}} & k_2^{\mathrm{E}}+k_3^{\mathrm{E}} & -k_3^{\mathrm{E}} \\ 0 & -k_3^{\mathrm{E}} & k_3^{\mathrm{E}} \end{bmatrix}\begin{Bmatrix} x_1^{\mathrm{I}} \\ x_2^{\mathrm{E}} \\ x_3^{\mathrm{E}} \end{Bmatrix}=-\begin{bmatrix} m_1^{\mathrm{N}}+m_1^{\mathrm{E}} & 0 & 0 \\ 0 & m_2^{\mathrm{E}} & 0 \\ 0 & 0 & m_3^{\mathrm{E}} \end{bmatrix}\begin{Bmatrix} 1 \\ 1 \\ 1 \end{Bmatrix}\ddot{x}_{\mathrm{g}} \tag{3.2}$$

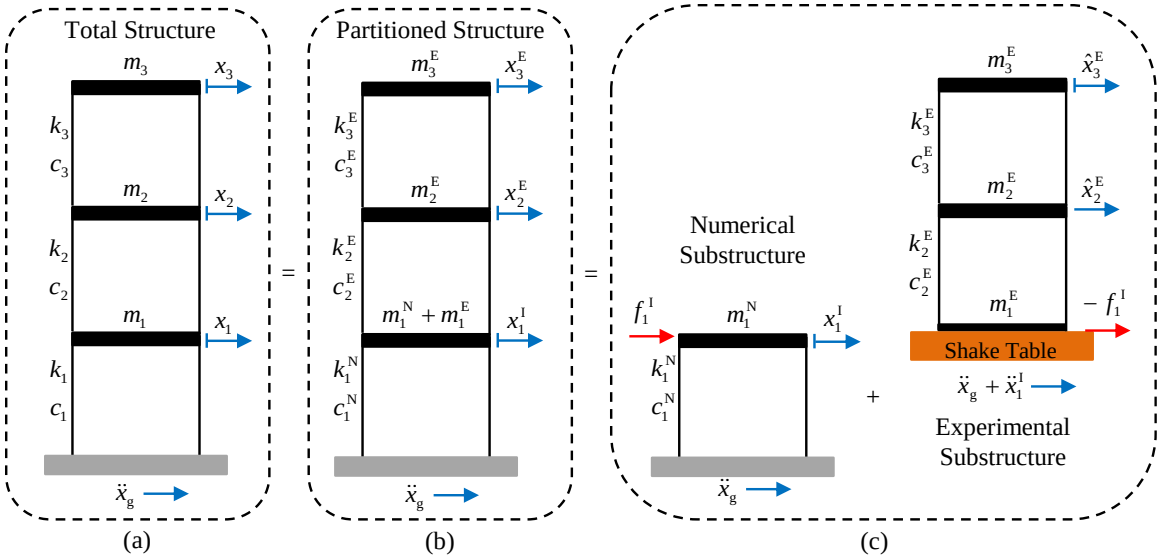

Figure 3.1 Example 3DOF structure for RTHS using a shake table

Numerical integration is performed solely on the numerical substructure, containing both numerical and interface DOF. This approach is consistent with the dynamic substructuring approach of Shing (2008). The numerical substructure is described by the following equations of motion:

$$m_1^{\mathrm{N}}\ddot{x}_1^{\mathrm{I}}+c_1^{\mathrm{N}}\dot{x}_1^{\mathrm{I}}+k_1^{\mathrm{N}}x_1^{\mathrm{I}}=-m_1^{\mathrm{N}}\ddot{x}_g+f_1^{\mathrm{I}} \tag{3.3}$$

The contribution from the experimental substructure is included as an external force f_1^{I}. The experimental substructure follows the equations of motion:

$$\begin{bmatrix} m_1^{\mathrm{E}} & 0 & 0 \\ 0 & m_2^{\mathrm{E}} & 0 \\ 0 & 0 & m_3^{\mathrm{E}} \end{bmatrix}\begin{Bmatrix} \ddot{x}_1^{\mathrm{I}} \\ \ddot{x}_2^{\mathrm{E}} \\ \ddot{x}_3^{\mathrm{E}} \end{Bmatrix}+\begin{bmatrix} c_2^{\mathrm{E}} & -c_2^{\mathrm{E}} & 0 \\ -c_2^{\mathrm{E}} & c_2^{\mathrm{E}}+c_3^{\mathrm{E}} & -c_3^{\mathrm{E}} \\ 0 & -c_3^{\mathrm{E}} & c_3^{\mathrm{E}} \end{bmatrix}\begin{Bmatrix} \dot{x}_1^{\mathrm{I}} \\ \dot{x}_2^{\mathrm{E}} \\ \dot{x}_3^{\mathrm{E}} \end{Bmatrix}+\begin{bmatrix} k_2^{\mathrm{E}} & -k_2^{\mathrm{E}} & 0 \\ -k_2^{\mathrm{E}} & k_2^{\mathrm{E}}+k_3^{\mathrm{E}} & -k_3^{\mathrm{E}} \\ 0 & -k_3^{\mathrm{E}} & k_3^{\mathrm{E}} \end{bmatrix}\begin{Bmatrix} x_1^{\mathrm{I}} \\ x_2^{\mathrm{E}} \\ x_3^{\mathrm{E}} \end{Bmatrix}=-\begin{bmatrix} m_1^{\mathrm{E}} & 0 & 0 \\ 0 & m_2^{\mathrm{E}} & 0 \\ 0 & 0 & m_3^{\mathrm{E}} \end{bmatrix}\begin{Bmatrix} 1 \\ 1 \\ 1 \end{Bmatrix}\ddot{x}_{\mathrm{g}}-\begin{Bmatrix} f_1^{\mathrm{I}} \\ 0 \\ 0 \end{Bmatrix} \tag{3.4}$$

To create an experimental substructure appropriate for shake table testing, the DOF in Eq. 3.4 are redefined relative to the interface DOF. Taking $\hat{x}_2^{\mathrm{E}} = x_2^{\mathrm{E}} - x_1^{\mathrm{I}}$ and $\hat{x}_3^{\mathrm{E}} = x_3^{\mathrm{E}} - x_1^{\mathrm{I}}$, Eq. 3.4 can be separated into equations of motion for the experimental substructure relative to the base of the shake table, subject to a base acceleration:

$$\begin{bmatrix} m_2^{\mathrm{E}} & 0 \\ 0 & m_3^{\mathrm{E}} \end{bmatrix} \begin{Bmatrix} \ddot{\hat{x}}_2^{\mathrm{E}} \\ \ddot{\hat{x}}_3^{\mathrm{E}} \end{Bmatrix} + \begin{bmatrix} c_2^{\mathrm{E}} + c_3^{\mathrm{E}} & -c_3^{\mathrm{E}} \\ -c_3^{\mathrm{E}} & c_3^{\mathrm{E}} \end{bmatrix} \begin{Bmatrix} \dot{\hat{x}}_2^{\mathrm{E}} \\ \dot{\hat{x}}_3^{\mathrm{E}} \end{Bmatrix} + \begin{bmatrix} k_3^{\mathrm{E}} & -k_3^{\mathrm{E}} \\ -k_3^{\mathrm{E}} & k_3^{\mathrm{E}} \end{bmatrix} \begin{Bmatrix} \hat{x}_2^{\mathrm{E}} \\ \hat{x}_3^{\mathrm{E}} \end{Bmatrix} = -\begin{bmatrix} m_2^{\mathrm{E}} & 0 \\ 0 & m_3^{\mathrm{E}} \end{bmatrix} \begin{Bmatrix} 1 \\ 1 \end{Bmatrix} \ddot{x}_{1,\mathrm{abs}}^{\mathrm{I}} \tag{3.5}$$

and the base shear, or external force to return to the numerical substructure:

$$f_1^{\mathrm{I}} = -m_1^{\mathrm{E}} \ddot{x}_{1,\mathrm{abs}}^{\mathrm{I}} - m_2^{\mathrm{E}} \ddot{\hat{x}}_{2,\mathrm{abs}}^{\mathrm{E}} - m_3^{\mathrm{E}} \ddot{\hat{x}}_{3,\mathrm{abs}}^{\mathrm{E}} \tag{3.6}$$

where $\ddot{x}_{1,abs}^{\mathrm{I}} = \ddot{x}_1^{\mathrm{I}} + \ddot{x}_g$, $\ddot{\hat{x}}_{2,\mathrm{abs}}^{\mathrm{E}} = \ddot{\hat{x}}_2^{\mathrm{E}} + \ddot{x}_{1,abs}^{\mathrm{I}}$, and $\ddot{\hat{x}}_{3,\mathrm{abs}}^{\mathrm{E}} = \ddot{\hat{x}}_3^{\mathrm{E}} + \ddot{x}_{1,abs}^{\mathrm{I}}$. Note that this representation of the base shear is only appropriate for lumped mass structures. In the general case, the base shear could be measured directly using load cells between the specimen and shake table or using the shake table actuator's load cell (if present) after subtracting table inertial and frictional forces.

The resulting numerical and experimental substructures are illustrated in Figure 3.1(c). The procedure for RTHS using a shake table in this configuration can be extracted from Eq. 3.3, Eq. 3.5, and Eq. 3.6. To summarize, the numerical substructure is excited by ground acceleration and the numerical and interface DOF values are determined through numerical integration. The absolute acceleration of the interface DOF is taken as the desired acceleration for the shake table. This acceleration is not known prior to testing, requiring a special class of shake table control strategies that can track accelerations determined online. The base shear due to the mass, damping, and stiffness of the specimen must be measured and returned to the numerical substructure. Here, it is important to include only the dynamics of the structure and not that of the shake table

(e.g., the shake table mass). This loop of action and reaction is carried out in real time until the entire response history has been conducted.

3.2 Framework for RTHS

To capture the inertial effects of the experimental substructure, the shake table must be able to track the desired accelerations accurately (e.g., absolute acceleration at the interface between numerical and experimental substructures, as in Eq. 3.5). Without compensation, the dynamics of the shake table will appear within the RTHS loop, added to the dynamics of the substructured system. Phase lags from command to response of the shake table as well as the dynamic coupling between the shake table and the specimen have a direct impact on the accuracy and stability of the RTHS loop, in some cases leading to inaccurate or unstable RTHS. The model-based shake table control strategy proposed by Phillips et al. (2014) is adopted to provide real time online tracking predefined acceleration. The goal of this strategy is to cancel out the modeled dynamics of the shake table through feedforward control and provide robustness to changes in specimen dynamics (e.g., damage) and to shake table nonlinearities and uncertainties (e.g., friction and modeling errors) through feedback control.

The feedforward controller is created as an inverse of the identified shake table model designed to compensate for the modeled dynamics of the shake table. When the desired acceleration is input to the controller, a voltage command is generated such that the shake table will nominally track the desired acceleration. The feedback controller is added to enhance the performance of the feedforward controller by providing robustness in the presence of changing specimen conditions, modeling errors, and disturbances. The

feedback controller is designed to reduce the error between the desired and measured accelerations online. The feedback controller was found to be essential for the accurate control of the nonlinear shake table in the presence of strong CSI (Phillips et al., 2014).

During RTHS, measurement noise from sensors can enter into the numerical substructure (e.g., via Eq. 3.3 and Eq. 3.6), excite the numerical substructure, and result in high-frequency commands to the experimental substructure (e.g, Eq. 3.5). High-frequency content in the RTHS loop could lead to problems for numerical integration stability or damage to the experimental equipment. To eliminate this phenomenon, a Kalman filter is added to the measurement signals used in the feedback loop. The Kalman filter takes inputs of measured acceleration from the experimental DOF and uses the identified model of the experimental specimen to estimate an uncontaminated signal.

The block diagram of the complete RTHS loop is shown in Figure 3.2. During the experiment, the ground acceleration is sent to the numerical substructure, from which the desired interface absolute acceleration is determined. This acceleration is passed through the feedforward-feedback controller to determine the command voltage to the shake table. The shake table then excites the experimental substructure with the dynamics of the two coupled through CSI. The measured shake table acceleration is used by the feedback controller while the measured structural accelerations are filtered by a Kalman filter and converted to a base shear using a lumped mass assumption. The base shear is returned to the numerical substructure to complete the RTHS loop. The individual components of Figure 3.2 are described herein. The procedure is then illustrated in the proceeding section for a uni-axial shake table with a shear building.

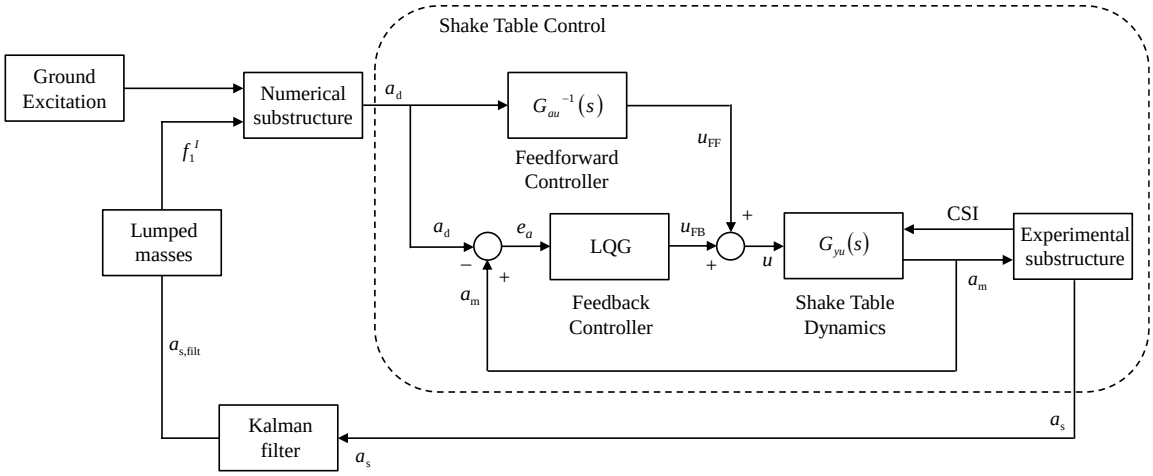

Figure 3.2 Block diagram of shake table RTHS including model-based controller

3.3 Experimental Setup

The substructure RTHS procedure is developed and verified using a small-scale experimental setup. The setup consists of a uni-axial shake table, a two-story steel shear building model as the experimental specimen, and a control and data acquisition system. The dynamic properties of both the experimental substructure and the total structure are presented in this section. The specimen and equipment are located at the University of Maryland and is part of the Structural Engineering Laboratory.

3.3.1 Uni-axial shake table and sensors

The shake table used in this study is a model APS 400 ELECTRO-SEIS manufactured by SPEKTRA. It has a 35.6 cm × 35.6 cm top plate driven by an electrodynamic vibration generator with a stroke of ± 15.8 cm. The shake table has a dynamic load capacity of 445 N and it can support a payload up to 23 kg.

The control hardware for the shake table consists of a dSPACE DS1103 Controller Board and a windows-based host PC. The dSPACE board, working as a real-time controller, is fully programmable from the MATLAB Simulink block diagram

environment. The dSPACE board performs numerical integration, provides shake table control through the proposed algorithms, and records all data. The board has 8 16-bit D/A channels and 20 16-bit A/D channels to interface with the experimental setup. Additional equipment includes a 4-channel PCB Piezotronics signal conditioner (Model 4821C) and four PCB Piezotronics accelerometers (Model 393B04). The accelerometers have a measurement range of ± 5 g, a frequency range of 0.05 to 750 Hz, and a sensitivity of 1000 mV/g. The accelerometers are attached on the shake table and each story of the specimen.

3.3.2 Experimental substructure

A two-story steel shear building model is used as the experimental specimen as shown in Figure 3.3 mounted on the shake table. The floor size is 20.3 cm × 20.3 cm and the height of each story is 14.0 cm. At each floor, seven steel blocks are attached as additional masses. The total mass of the first and second floors are 6.91 kg and 6.95 kg, respectively. Two spring-steel columns with a thickness of 0.5 mm connect the floor plates. The spring steel allows the building to undergo large deformations without yielding, a useful feature for RTHS algorithm development. The test setup with linear specimen behavior enabled many scenarios to be explored quickly and cost effectively. Furthermore, a linear specimen enabled an easier comparison with the numerical simulations in the following section, avoiding issues with numerically modeling nonlinear behavior which would likely have to be calibrated to the experimental results. The lumped mass assumption is considered appropriate for the structure because there is significant mass at each floor and the structure behaves nominally as a shear building. Furthermore, the shake table

maintains horizontal motion, so the uni-directional accelerometers are nominally detecting horizontal motions.

Foam is added to the connections between the columns and floor plates to increase the structural damping beyond the inherent damping. In this case, the bare steel structure exhibited very small damping, approximately 0.5% for the first mode. With the foam, damping ratios of 4.3% and 3.9% in the first and second mode, respectively, were identified using free vibration tests. The specimen was then subject to a 0 to 10 Hz band-limited white noise base excitation to determine the natural frequencies and extract the stiffness. The experimental transfer functions from input ground motion to measured story accelerations are presented in Figure 3.4. The identified mass, damping, and stiffness were combined into a 2DOF shear building model. Both magnitude and phase between the measured transfer function and identified model match well as shown in Figure 3.4. The first and second natural frequencies of the structure are 3.2 Hz and 8.4 Hz, respectively.

Figure 3.3 Shear building specimen mounted on shake table

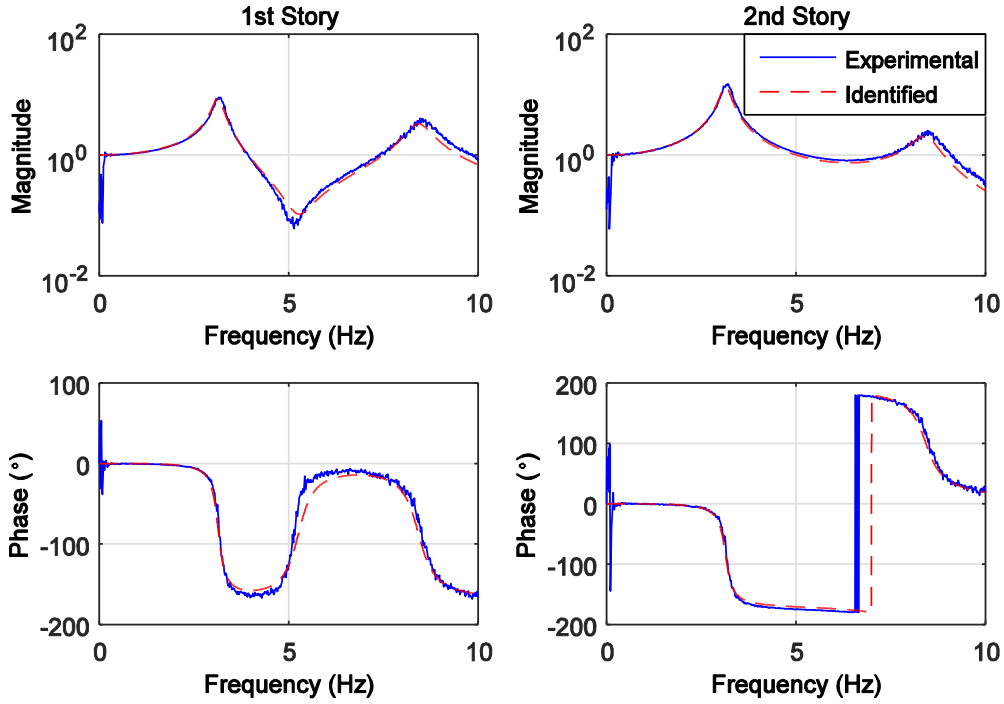

Figure 3.4 System identification of the two-story specimen

3.3.3 Total structure

The total three-story shear structure consists of a numerically simulated lower story and experimentally represented upper stories. Natural frequencies and damping ratios of the total structure are designed to be similar to those of typical midrise steel structure (ASCE, 2010). The mass and stiffness of the lower (numerical) story are chosen as the average of the mass and stiffness of the upper two (experimental) stories, resulting in total system natural frequencies of 2.3 Hz, 6.5 Hz, and 9.2 Hz. Table 3.1 summarizes the mass and the stiffness of the total structure, which is the combined result of the mass and stiffness of the substructures. Selection of the damping ratio for the numerical substructure is significant in that it has a direct influence on the stability of the RTHS loop. Artificially high damping could be chosen, which could mask potential instability or accuracy issues. In this study, low and realistic damping ratios for a steel frame building are created for

the numerical substructure and intrinsically present in the experimental substructure. To analyze the influence of damping on RTHS stability and accuracy, two values of damping are chosen for the numerical substructure, resulting in total structure damping ratios for the three modes of either 2.6%, 3.5%, and 9.4% or 3.6%, 5.6%, and 10.2%. By investigating the RTHS performance of the low damping structures, the proposed shake table RTHS framework stands to push the limit of what has been accomplished in the literature.

Table 3.1 Parameters of the total structure

Floor	Mass (kg)	Stiffness (kN/m)
1	6.93	7.25
2	6.91	6.90
3	6.95	7.60

3.3.4 Shake table identification

The input-output model of the shake table is determined using a 0 to 10 Hz band-limited white noise voltage command to the shake table (input) and measured acceleration of the base (output). The two-story specimen is mounted on the table during identification to include the effects of CSI. Figure 3.5 shows the experimentally identified transfer function of the shake table along with the identified model. Two features can clearly be seen from this figure. First, since the command to the shake table is approximately proportional to the displacement, the output acceleration approaches zero at zero frequency. Second, there are valleys around the two natural frequencies of the experimental specimen, clearly illustrating the interaction between shake table and specimen (i.e., CSI). In all, 8 zeros and 8 poles are used to create a model that matches

the experimentally identified transfer function, shown in Eq. 3.7. The model was fit using a nonparametric linear system identification technique MFDID (Kim et al., 2005).

$$G_{au}(s) = \frac{2.8373s^2(s+463)(s+0.5991)(s^2+1.454s+397.9)(s^2+3.926s+2902)}{(s+11.35)(s+1.131)(s^2+36.68s+483.7)(s^2+19.7s+1024)(s^2+5.875s+3272)} \quad (3.7)$$

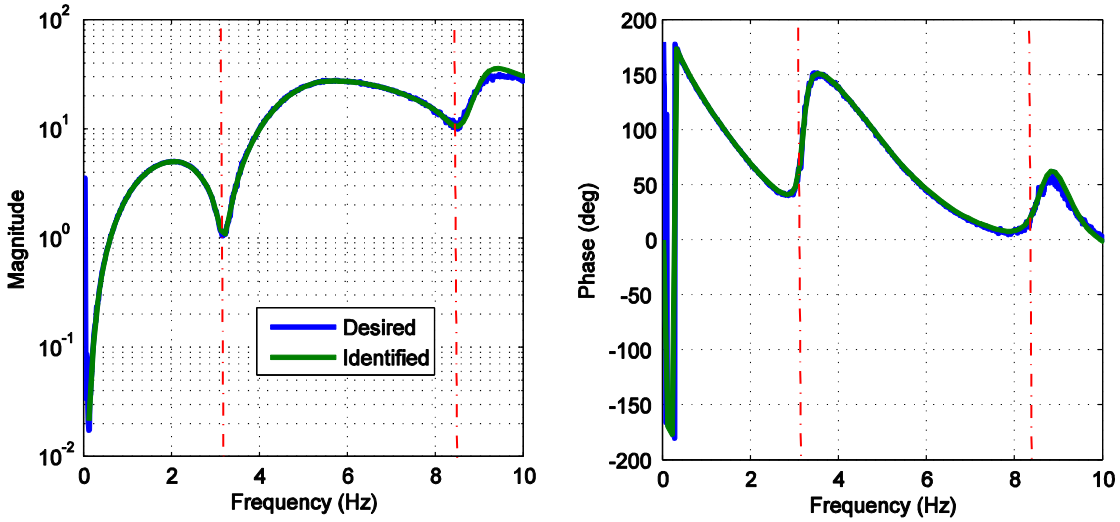

Figure 3.5 Identified and modeled shake table transfer functions

3.3.5 Controller development

The feedforward controller is created as an inverse of the identified model to compensate for the modeled dynamics of the shake table, as shown in Eq. 3.8.

$$G_{FF} = G_{au}^{-1}(s) = \frac{0.3525(s+11.35)(s+1.131)(s^2+36.68s+483.7)(s^2+19.7s+1024)(s^2+5.875s+3272)}{s^2(s+463)(s+0.5991)(s^2+1.454s+397.9)(s^2+3.926s+2902)} \quad (3.8)$$

Both the feedforward controller and the inverse of the experimental transfer function are shown in Figure 3.6. The peaks and valleys of the feedforward controller (Figure 3.6) inversely match the peaks and valleys of the shake table (Figure 3.5), resulting in unity magnitude and zero phase when placed in series.

For this particular feedforward controller, the magnitude increases appreciably beyond the expected range of control (e.g., the natural frequencies of the total structure

and the specimen itself). For traditional shake table testing where the input ground motion would not have any high frequency content, this amplification would not be problematic. However, in RTHS, high frequency measurement noise will enter into the RTHS loop. A feedforward controller with a large magnitude at high frequencies may turn the measurement noise into high-frequency commands to the table. To avoid potential spurious excitation, a second order Butterworth low-pass filter with a cutoff frequency of 50 Hz is added in series with the feedforward controller. The filter is designed to reduce the magnitude at higher frequencies without altering the performance over the range of interest (0 to 10 Hz). The feedforward controller plus filter is shown in Eq. 3.9. Figure 3.6 includes the feedforward controller plus filter, which is used for all subsequent testing.

$$G_{FF,filt} = \frac{34785.109(s+11.35)(s+1.131)(s^2+36.68s+483.7)(s^2+19.7s+1024)(s^2+5.875s+3272)}{s^2(s+463)(s+0.5991)(s^2+1.454s+397.9)(s^2+3.926s+2902)(s^2+444.3s+98700)} \quad (3.9)$$

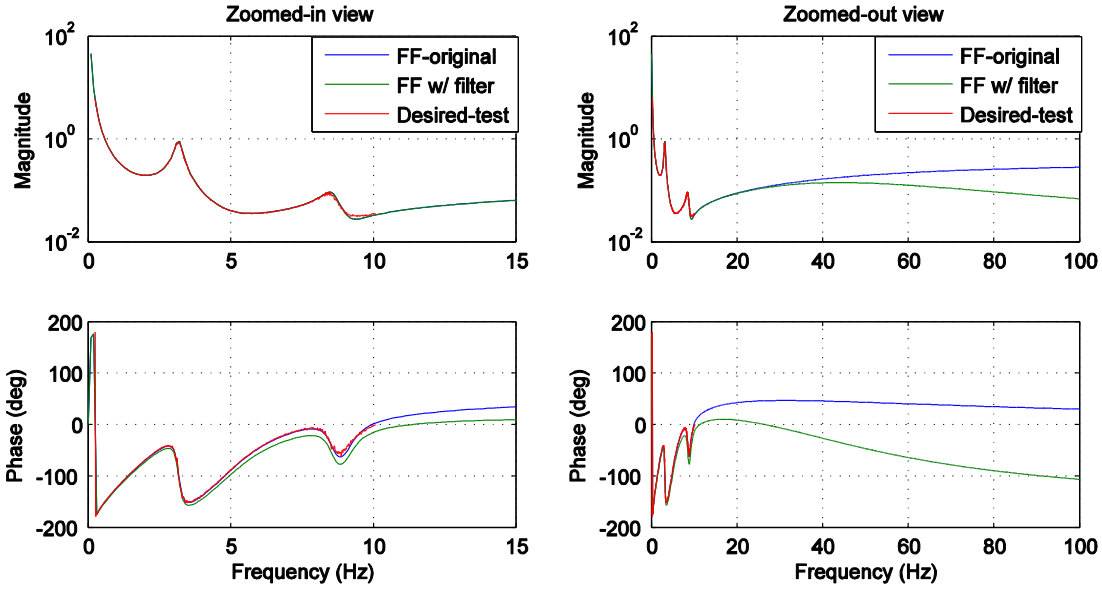

Figure 3.6 Feedforward controller transfer function with and without a low-pass filter

3.3.6 Filtering of measured accelerations

To prevent measurement noise from entering the numerical structure, a Kalman filter is added in line with the measured accelerations as shown in Figure 3.2. With process noise assumed to enter the structure in the same way as the input ground motion and with two accelerometers, the Kalman filter will have a scalar weighting parameter for the process noise and a 2×2 weighting matrix for the measurement noise. The Kalman filter parameters were determined offline using previously recorded data to be $Q=1\times10^{3}$, $\mathbf{R}=\mathbf{I}_{2\times2}$. Incorporating the selected parameters, the filtered results of Figure 3.2 demonstrate excellent noise reduction while matching the amplitude and phase of the original signal. Figure 3.7 presents the performance of a RTHS using the filtered measurements in the feedback loop. Accelerations of the top floor are shown before and after filtering when the total structure is subjected to 30% El Centro. From the zoomed-in view, it is observed that the noise contained in the measured accelerations is eliminated by the Kalman filter without altering the dominant structural responses. Most importantly, the Kalman filter does not introduce phase lag which would lead to stability problems in the RTHS loop. Without the Kalman filter, stable yet spurious high-frequency commands and responses could be observed in the shake table. To avoid damage to equipment, a complete RTHS using unfiltered accelerations was not conducted.

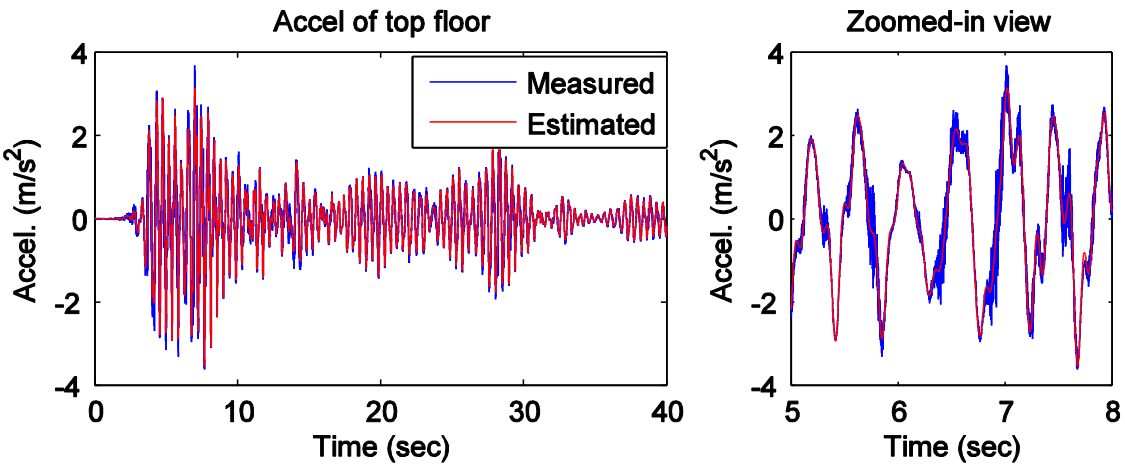

Figure 3.7 Effect of Kalman filter on acceleration measurements

For systems with higher damping or different substructuring, filtering of the measurement noise may not be necessary and the Kalman filter could be removed from Figure 3.2. The Kalman filter is added to push the limits of RTHS, enabling the evaluation of structures with lower damping and challenging substructuring. Additionally, in the case that the specimen behavior is nonlinear or difficult to model, the Kalman filter could be removed, replaced by another filter (e.g., non-model-based), or tuned to be less sensitive to the plant (i.e., place more weight on the sensor measurements for prediction of the model states). Additionally, the linear Kalman filter can be replaced by a nonlinear (extended or unscented) Kalman filter in the case of nonlinear structures. For example, real-time nonlinear model updating using an unscented Kalman filter was demonstrated successful in (Song and Dyke, 2013), and approach that could be extended for the filtering of measurement noise.

3.3.7 Earthquake ground motions

Two earthquake ground motion records with different magnitudes and frequency content are selected as the input to the structure, taken from a study on structural control (Ohtori

et al., 2004): (1) El Centro: The N-S component recorded at the Imperial Valley Irrigation District substation in El Centro, California, during the Imperial Valley, California earthquake of May 18, 1940, and (2) Hachinohe: The N-S component recorded at Hachinohe City during the Tokachi-oki earthquake of May 16, 1968. The reference earthquakes are passed through a 2-pole Butterworth high-pass filter with a cutoff frequency of 0.25 Hz to remove the low-frequency behavior without altering the desired frequency content. All earthquake records, as shown in Figure 3.8, are scaled to 30% of the original amplitude due to the limitations of the shake table.

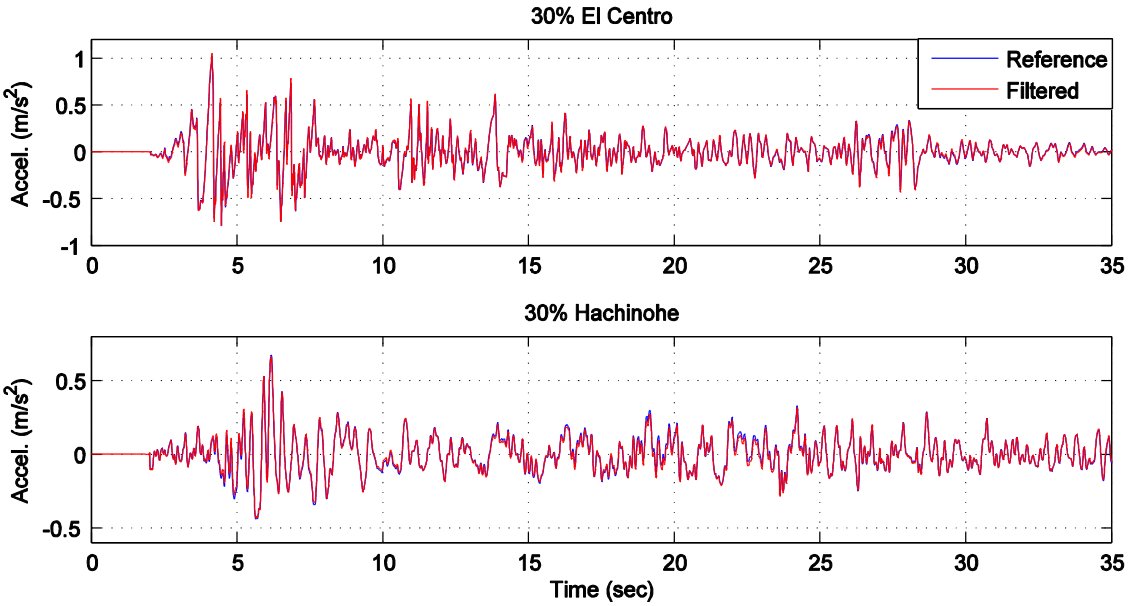

Figure 3.8 Historic ground motions

3.4 Performance of Shake Table Control and RTHS Results

This section investigates the performance of the proposed RTHS approach with a focus on tracking the desired acceleration signal and achieving overall accurate RTHS when compared to numerical simulations. First, acceleration tracking performance of

feedforward control (FF) and combined feedforward-feedback (FF + FB) control are presented for both predefined accelerations (i.e., traditional shake table testing of the two-story shear building) and accelerations determined online during RTHS. Second, RTHS results are compared to numerical simulations to verify the overall performance of the proposed RTHS approach. All accelerations are passed through a low-pass filter with a cutoff frequency of 20 Hz in post-processing to remove high frequency noise. The evaluation criteria are all calculated using the filtered accelerations. The results and conclusions are based on the total structure with lower damping (2.6% in the first mode) and using the FF + FB controller unless otherwise explicitly stated.

3.4.1 Acceleration tracking

Before advancing to a shake table RTHS, the ability of the shake table controller to track a predefined acceleration is assessed. Figure 3.9 shows the shake table acceleration tracking performance for both the FF and FF + FB controller to track the 30% El Centro record with the two-story specimen attached. Both time domain and frequency domain analysis demonstrate excellent reproduction of the desired ground motion. During RTHS, the shake table will instead track the absolute acceleration of the interface DOF. Figure 3.10 shows the online acceleration tracking performance for RTHS at the interface DOF when the total structure is subjected to the 30% El Centro and 30% Hachinohe earthquakes. Excellent tracking performance is observed for desired accelerations determined both offline (traditional shake table testing; Figure 3.9) and online (RTHS; Figure 3.10). In addition, it can be observed that the PSD of the interface DOF acceleration contains significant energy at the natural frequencies of the total structure (e.g., 2.3 Hz, 6.5 Hz, and 9.2 Hz), reflecting that the numerical and experimental

substructures behave like the total structure. In Figure 3.10, only FF + FB results are presented because the RTHS loop will lead to slightly different desired accelerations, thus the tracking performance must be evaluated independently. Peak and RMS errors are used to evaluate the performance achieved by the proposed techniques, as shown in Eq. 3.10 through Eq. 3.13 where $\ddot{x}_d$ is selected as the reference acceleration, and $\ddot{x}_m$ is selected as the measured acceleration. Quantitative tracking results are summarized in Table 3.2 and Table 3.3 for traditional shake table testing and shake table RTHS, respectively. Because the shake table performance is accurately described by the linearized model, feedforward control alone provides excellent tracking. The tracking performance is augmented by feedback control, improving the ability of the shake table to match the acceleration peaks as well as reducing RMS error in the presence of modeling errors or nonlinearities.

$$Max\ \ error = \max|\ddot{x}_d - \ddot{x}_m| \tag{3.10}$$

$$RMS\ \ error = \sqrt{\frac{1}{N}\sum_{i=1}^{N}(\ddot{x}_{d,i} - \ddot{x}_{m,i})^2} \tag{3.11}$$

$$Normalized\ \ max\ \ error = \frac{\max|\ddot{x}_d - \ddot{x}_m|}{\max|\ddot{x}_d|} \times 100\% \tag{3.12}$$

$$Normalized\ \ RMS\ \ error = \sqrt{\frac{\frac{1}{N}\sum_{i=1}^{N}(\ddot{x}_{d,i} - \ddot{x}_{m,i})^2}{\frac{1}{N}\sum_{i=1}^{N}(\ddot{x}_{d,i})^2}} \times 100\% \tag{3.13}$$

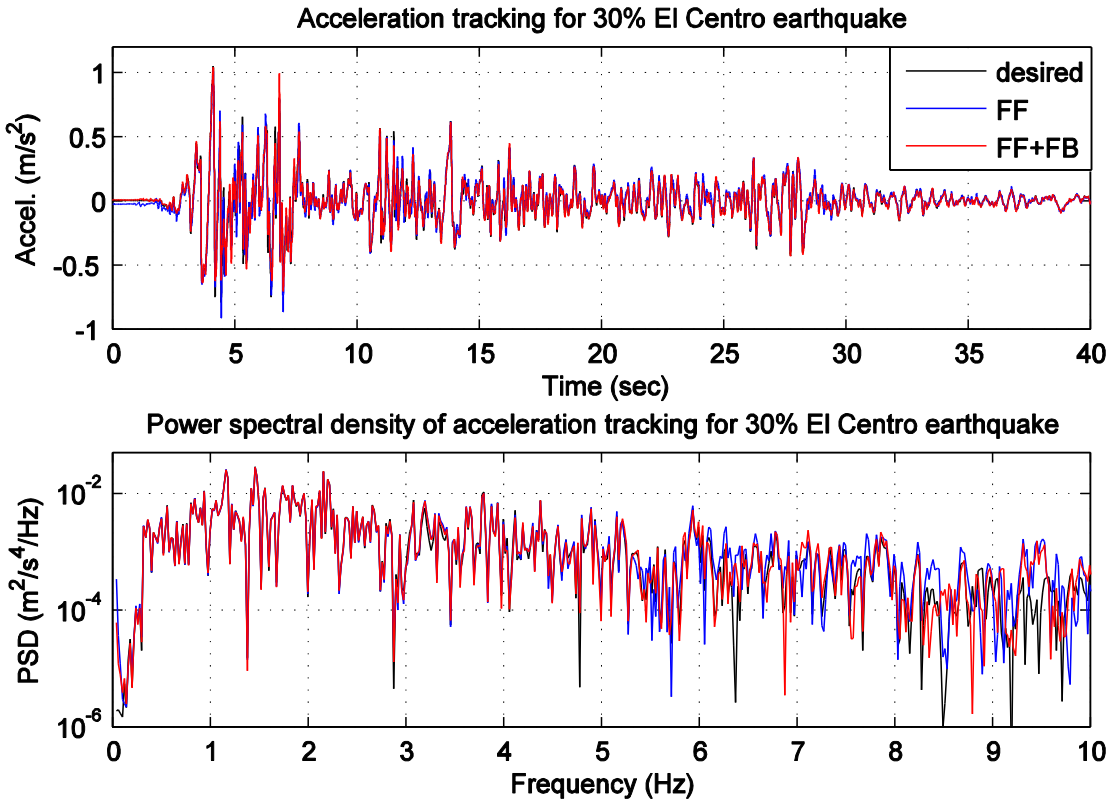

Figure 3.9 Acceleration tracking performance for traditional shake table testing

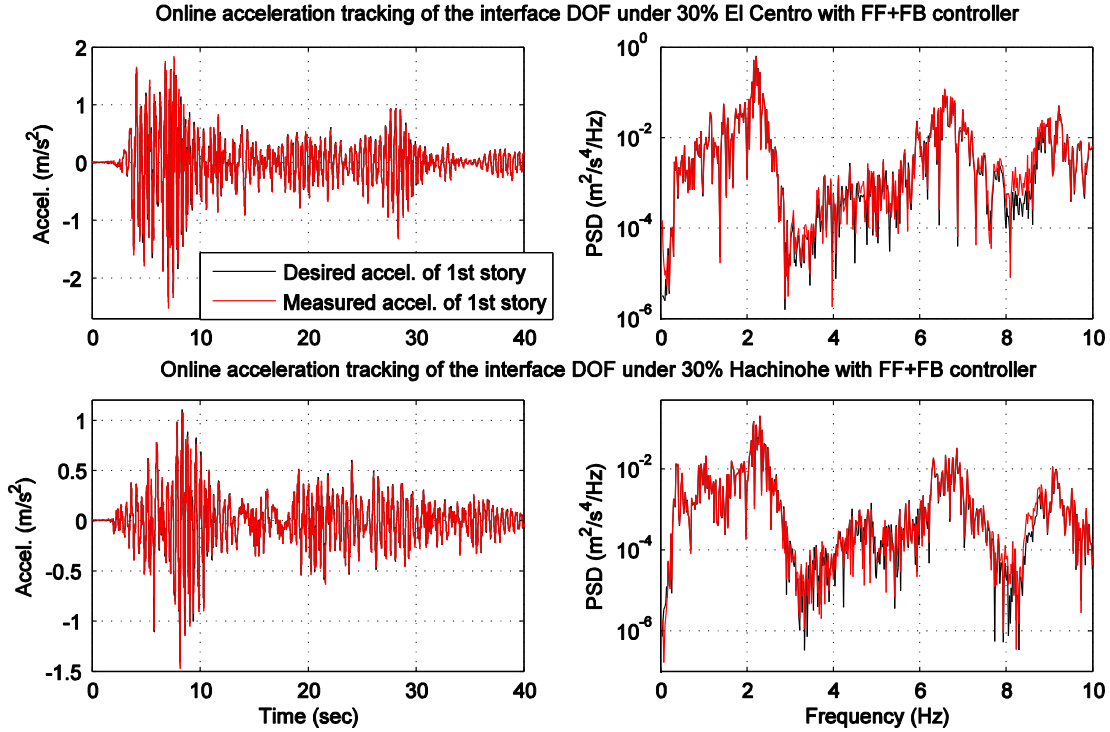

Figure 3.10 Online acceleration tracking performance for RTHS

Table 3.2 Acceleration tracking performance of the shake table during traditional shake table testing for the 30% El Centro record

Controller	(1) Time history analysis		(2) PSD analysis	
	Max tracking error [m/s^2; (%)]	RMS tracking error [m/s^2; (%)]	Max tracking error [$m^2/s^4/Hz$; (%)]	RMS tracking error [$m^2/s^4/Hz$; (%)]
FF	0.3012 (28.69)	0.0358 (25.24)	0.01 (34.94)	0.0005 (15.53)
FF + FB	0.2477 (23.59)	0.0272 (19.20)	0.0018 (6.17)	0.0003 (7.76)

Table 3.3 Online acceleration tracking performance at the interface DOF during RTHS

Ground motion	Controller	(1) Time history analysis		(2) PSD analysis	
		Max tracking error [m/s^2; (%)]	RMS tracking error [m/s^2; (%)]	Max tracking error [$m^2/s^4/Hz$; (%)]	RMS tracking error [$m^2/s^4/Hz$; (%)]
30% El Centro	FF	0.4443 (19.91)	0.0539 (15.33)	0.0299 (4.82)	0.0030 (6.32)
	FF + FB	0.2691 (12.02)	0.0311 (9.10)	0.0250 (3.95)	0.0016 (3.47)
30% Hachinohe	FF	0.2349 (18.23)	0.0247 (13.63)	0.0074 (3.42)	0.0011 (7.82)
	FF + FB	0.1459 (11.18)	0.0160 (7.74)	0.0057 (2.80)	0.0006 (4.13)

3.4.2 Performance of RTHS

In this section, first the influence of delay on the RTHS loop is explored through numerical simulation. Second, the accuracy of the RTHS framework is assessed as

compared to numerical simulation results. Because the specimen remains linear and is well-approximated by a lumped mass assumption, strong agreement is expected to validate the approach. The two cases for comparison are listed below:

1. Numerical simulation of the total three-story structure (SIM);
2. Numerical simulation of the three-story structure, substructured for RTHS with simulated interface delay (SIM-Delay); and
3. RTHS of the three-story structure, substructured into a numerical SDOF system for the first story and experimental specimen representing the upper two stories (EXP-RTHS).

Analyses are conducted for structures with both levels of damping (selecting either 2.6% or 3.6% for damping in the first mode by changing the damping of the numerical substructure). All structures are subjected to the 30% El Centro and 30% Hachinohe records.

3.4.2.1 Numerically simulated RTHS with delay

The scenarios considered in this study are very challenging due to the low damping and the substructuring (larger experimental/numerical component ratio). To better illustrate the challenge, the influence of time delay on RTHS performance is calculated based on pure numerical simulation with added time delay (SIM-Delay). Using simulated substructuring, the delay is added to the shear force before it is returned to the numerical substructure. Table 3.4 shows the absolute and normalized RMS acceleration errors of the first floor calculated from Eq. 3.11 and Eq. 3.13 for 30% El Centro earthquake. For this comparison using Eq. 3.11 and Eq. 3.13, $\ddot{x}_d$ is selected as the simulated acceleration in

SIM and $\ddot{x}_m$ is selected as the simulated acceleration in SIM-Delay. It can be clearly seen that stability and accuracy is greatly affected by the time delay. The tolerance for time delay can be increased by increasing the damping ratio (as seen in Table 3.4) or by more conservative substructuring (larger numerical/experimental component ratio; as discussed in (Lin et al., 2015)).

Table 3.4 RTHS performance compared to numerical simulation

Time delay (ms)	RMS acceleration error of SIM-Delay relative to SIM	
	Structure with lower damping [m/s^2; (%)]	Structure with higher damping [m/s^2; (%)]
0.0	0 (0)	0 (0)
2.5	0.0658 (18.61)	0.0412 (13.39)
5.0	0.1334 (37.71)	0.0733 (23.86)
7.5	0.4541 (128.41)	0.1088 (35.40)
10	**unstable**	0.1663 (54.11)
15	**unstable**	**unstable**

3.4.2.2 RTHS performance compared to numerical simulations

Table 3.5 summarizes the overall RTHS performance of absolute accelerations for the two structure systems with different damping ratios subjected to 30% El Centro and 30% Hachinohe records. The RMS errors of EXP-RTHS are calculated by comparing the results to the respective results in the numerical simulation case SIM. Comparisons are made using Eq. 3.11 and Eq. 3.13 where $\ddot{x}_d$ is selected as the simulated acceleration in SIM and $\ddot{x}_m$ is selected as the measured acceleration in EXP-RTHS. As expected, better RTHS performance is demonstrated for the structure with larger damping. The relatively large normalized RMS errors in acceleration are the result of accelerometer measurement

noise as well as accelerations being more sensitive to higher frequency vibrations. A clearer visualization of the match between RTHS and numerical simulation is shown in Figure 3.11 and Figure 3.12.

Table 3.5 RTHS performance compared to numerical simulation

Earthquake excitation	Story	RMS acceleration error of EXP-RTHS relative to SIM	
		Structure with lower damping [m/s^2; (%)]	Structure with higher damping [m/s^2; (%)]
30% El Centro	1st	0.1797 (45.54)	0.1329 (38.74)
	2nd	0.2022 (31.58)	0.1330 (24.12)
	3rd	0.2302 (29.47)	0.1507 (22.44)
30% Hachinohe	1st	0.0905 (38.01)	0.0587 (28.03)
	2nd	0.0827 (20.69)	0.0602 (17.25)
	3rd	0.0943 (19.16)	0.0769 (17.90)

Figure 3.11 and Figure 3.12 show the time histories of the absolute accelerations for the low damping structure subjected to 30% El Centro and 30% Hachinohe, respectively. The RTHS techniques perform well not only on the peak responses but also throughout the entire time history. Some high-frequency responses are present in the accelerations of the first floor. Accelerations are more sensitive to higher frequencies than displacements or velocities, and therefore high frequency behavior will manifest most clearly in acceleration readings. From Figure 3.6, it is clear that there is a slight phase lag introduced by the filtered FF controller. The lag is larger at higher frequencies and consequently introduces energy at the second mode of the experimental structure (i.e., adds slight negative damping around 8.4 Hz). This lag coupled with the lightly damped specimen leads to small oscillations that do not significantly affect the overall

performance of the RTHS in this case. The oscillations could be eliminated by a closer FF match with the inverse model or through a more aggressive FB controller. Moreover, this observation highlights that accurate control of the shake table is important across all significant natural frequencies of the experimental specimen.

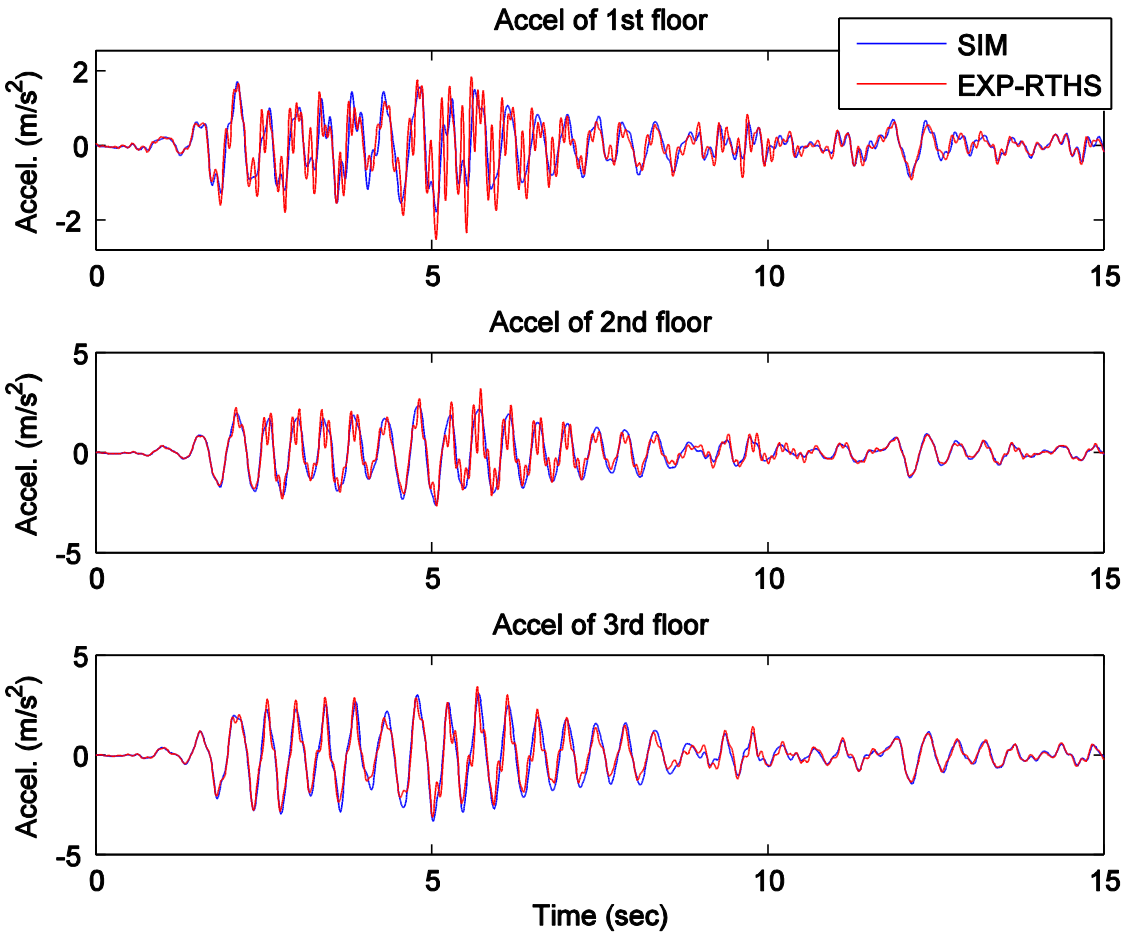

Figure 3.11 Performance of RTHS compared to numerical simulations for 30% El Centro

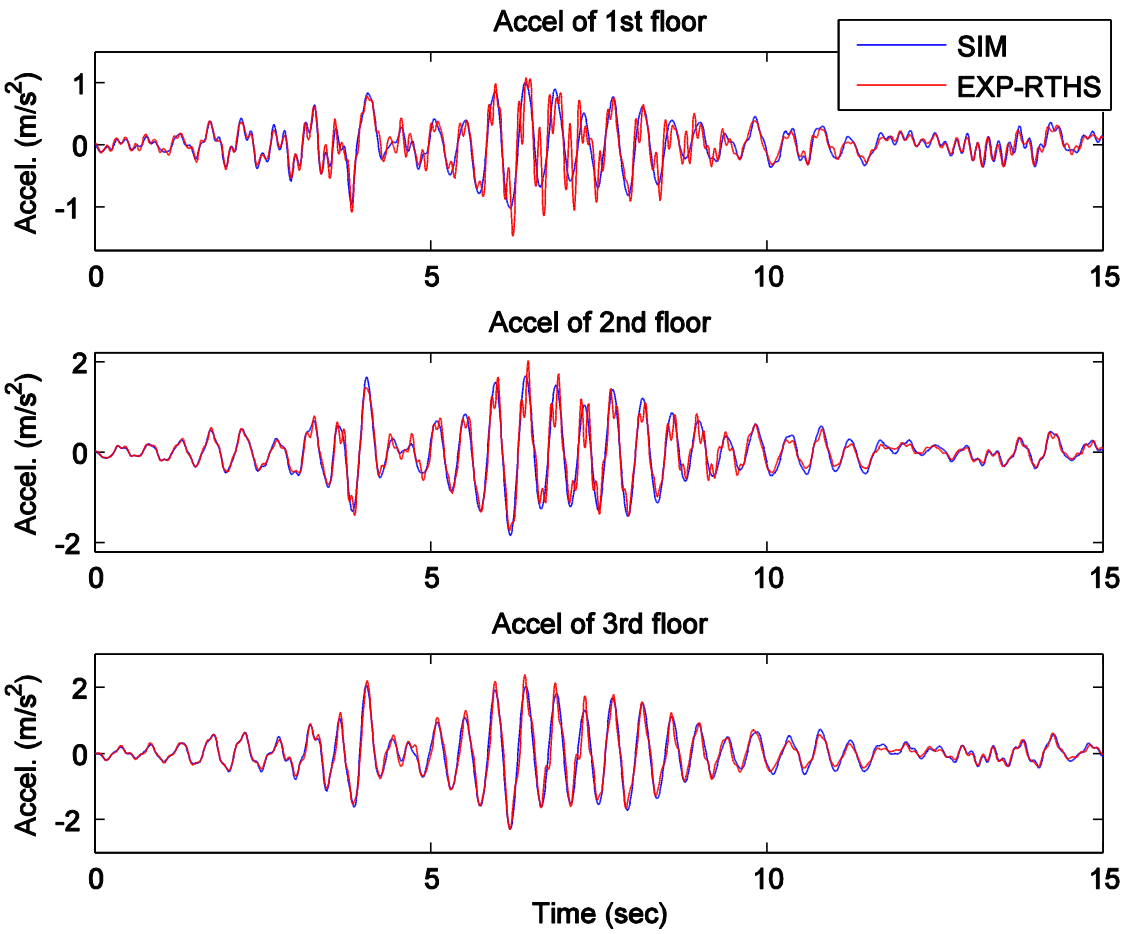

Figure 3.12 Performance of RTHS compared to numerical simulations for 30% Hachinohe

Table 3.6 RTHS performance compared to numerical simulation (1st mode)

Earthquake excitation	**RMS acceleration error of EXP-RTHS relative to SIM**	
	Structure with lower damping [m/s^2; (%)]	Structure with higher damping [m/s^2; (%)]
30% El Centro	0.5030 (17.88)	0.3670 (15.15)
30% Hachinohe	0.2405 (13.66)	0.1933 (12.57)

For a clearer comparison over the significant frequencies of vibration, the accelerations of the first mode are calculated through modal analysis and summarized in

Table 3.6. From Table 3.6, it is observed that the RMS errors of EXP-RTHS are small which indicates good reproduction of the numerical simulation. The excellent agreement can also be seen from Figure 3.13 which shows the structural acceleration of the first mode under 30% Elcentro earthquake.

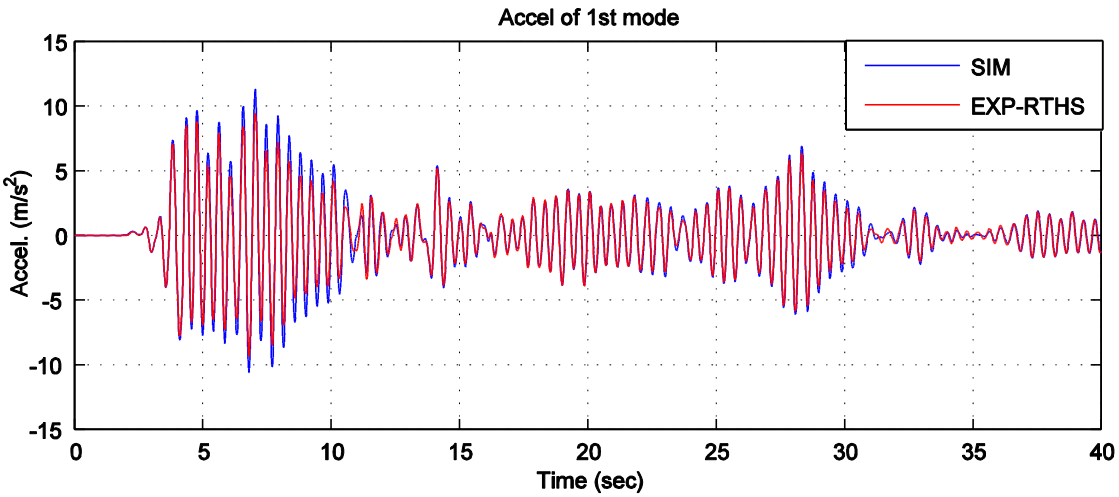

Figure 3.13 Acceleration of the first mode; RTHS compared to numerical simulations for 30% El Centro

3.5 Summary

This study proposes a simple and versatile shake table RTHS framework for assessing dynamic structural responses. The proposed RTHS framework is demonstrated to be effective and reliable for structures with low damping, a necessary development for shake table RTHS of realistic structures. The proposed framework includes a model-based feedforward-feedback controller for acceleration tracking. Modeled dynamics of the shake table, including the substantial coupling with the specimen (CSI), are included in the development of the feedforward and feedback controllers. In this application, the strong CSI, low damping, and large experimental substructure relative to the total

structure led to considerable control challenges. An accurately designed feedforward controller across all significant frequencies was found to provide excellent performance which can be supplemented by a feedback controller for robustness in the presence of specimen or shake table nonlinearities.

The Kalman filter added to the RTHS loop prevented high-frequency sensor noise from being introduced to the numerical substructure and leading to high-frequency commands to the shake table. The Kalman filter also avoided introducing phase lag associated with many filters that could lead to RTHS instability. In addition, a low-pass filter was added to the feedforward controller such that the controller was not sensitive to high frequency noise. The filter was designed such that it did not impact the performance of the controller over the frequency range of interest.

The proposed framework was validated using a uni-axial shake table and two-story shear building specimen with low damping at the University of Maryland. The strategy for shake table control in the context of RTHS was verified to offer a good offline and online acceleration tracking performance. The effectiveness of proposed techniques on overall RTHS accuracy were verified through comparisons with numerical simulations. The results from RTHS and numerical simulations exhibit a good agreement for the linear structure, offering confidence toward broader application studies of shake table RTHS.

The proposed RTHS framework uses readily available equipment, providing a new experimental tool to laboratories worldwide. Researchers can develop similar substructuring equations as Eq. 3.1 to Eq. 3.6 and the shake table would be used track the interface DOF. The dynamics of shake table should be identified with the specimen

attached to accurately capture CSI. Additionally, specimen system identification should be carried out to implement any model-based filter such as the Kalman filter. Note that the Kalman filter and the Butterworth filter are not necessary and can be introduced as needed. These filtering techniques enabled a framework that pushed the limits on RTHS capabilities.

There are a few limitations to the proposed method which warrant further study. These include the need for system identification in the creation of the model-based control and limitation to uni-axial shake table motion. These limitations can be overcome through improved shake table control algorithms including multi-axial control algorithms. Furthermore, for convenience the specimen used was linear (allowing for cost effective and repeatable studies) and used a lumped-mass assumption (allowing for approximate base shear measurements in the absence of a load cell). These restrictions could be relaxed with different specimens and equipment. In its current form, the proposed approach offers a versatile framework for shake table RTHS studies that can be adapted for individual testing needs.

CHAPTER 4 ARTIFICIAL SPECIMEN DAMPING FOR SUBSTRUCTURE RTHS

Damping plays an important role in RTHS accuracy and stability. In Chapter 3, foam was added to the specimen to both achieve a reasonable level of damping and for RTHS stability. This chapter presents a novel technique in artificially introducing damping to dynamic specimens. With the proposed technique, artificial damping can be added to all modes of the specimen in both traditional shake table testing and RTHS. More importantly, extra damping can be introduced only to the specific modes of the specimen (e.g., higher modes), which cannot be realized through other techniques. The control of damping in higher models is a significant contribution toward increasing RTHS stability without altering dominant structural responses.

4.1 Role of Damping in Structural Testing

In addition to the importance of accurately representing the target level of damping in a specimen, damping plays a significant role in the stability of some newer experimental testing techniques. The stability and accuracy of RTHS is related to the ability of the actuator system to track the desired trajectory. Time delays and time lags can introduce negative damping (Horiuchi et al., 1996) which can supersede the inherent structural damping and lead to instability.

For purely numerical simulations, there are many methods to achieve the desired level of damping (Jeary, 1997; Chaney 2008). Examples include Rayleigh damping (Rayleigh 1896) which can achieve target levels of damping for lower vibrational modes

and the Hilber-Hughes-Taylor method (HHT-α method) (Hilber et al., 1977) which can damp out the responses at higher vibrational modes. These approaches do not work when there is an experimental specimen with degrees-of-freedom not directly controlled by an actuator (i.e., free to vibrate).

In experimental studies, the inherent damping in the specimen, especially for steel frame specimens, may be less than the target level of damping and furthermore small enough to cause stability issues in the RTHS loop. For experimental studies, the most widely used methods to provide extra damping are by using external physical damping devices (e.g., oil dampers) which can be expensive, labor intensive to install, and require specimen-specific design to meet the target level of damping. Alternatively, foam and other dissipative materials can be added to increase the specimen damping. However, added materials may introduce undesired nonlinear behavior or increase the stiffness. In addition to the cost and limited effectiveness of currently available experimental damping techniques, there is no direct way to introduce damping to specific modes.

There is strong promise for dynamic substructuring through shake table RTHS, however additional techniques are needed to (1) easily achieve a target level of damping in an experimental specimen and (2) mitigate RTHS stability issues by introducing damping to higher modes, even those that appear in the specimen. This chapter presents a novel technique to provide artificial damping to the structure through shake table control. The desired structural damping is provided by first designing a feedforward controller (FF) to compensate for the shake table dynamics. The FF controller is then modified using dynamics of the original specimen and target specimen to create the proposed artificial damping FF controller (AD-FF). The performance of the proposed technique is

investigated for both traditional shake table testing and RTHS through a uni-axial shake table and a two-story shear building specimen with very low damping. In traditional shake table testing, extra damping is artificially added to all modes of the specimen through the proposed techniques, demonstrating the potential of the proposed techniques. The structural responses are compared to the target structure in both time domain and frequency domain. As a broader application, the performance of the proposed techniques is also investigated in RTHS. The damping of the experimental specimen can be easily achieved based on the damping of the target structure by using the proposed techniques, greatly reducing labors and costs. In addition, the proposed techniques make it possible to introduce damping only on the specific modes of a structure, which cannot be realized by using discrete damping devices. In this way, the RTHS stability can be increased especially for high-rise structures without changing the target structural responses which are dominated by the fundamental modes. The performance of the proposed techniques in achieving the target total structure in RTHS is verified for further demonstration of the potentials and favorable performance of the proposed techniques, as well as the performance in adding damping on the specific modes.

4.2 Methodology for Adding Specimen Damping through Shake Table Control

To better illustrate the methodology of the proposed AD-FF, the FF controller and shake table including control-structure interaction (CSI) shown in Figure 3.2 are extracted and shown in Figure 4.1(a). The blocks enclosed in the dash line can be viewed as a continuous time dynamic system as shown in Eq. 4.1. To achieve the desired acceleration (i.e., $a_m = a_d$), the feedforward controller (FF) is typically designed as an inverse of the

identified shake table model to cancel out the dynamics of the shake table. In an ideal case of with the transfer function $G_{\mathrm{FF}} = G_{\mathrm{ST}}^{-1}$, the continuous system G_{SYS} will exhibit the dynamic properties of the experimental specimen. Accordingly, if the FF were designed differently, G_{SYS} could behave with dynamic properties different from that of the specimen, as shown in Eq. 4.2. In an ideal setting, target specimen performance would be achieved by simply testing the target specimen on a shake table with a traditional inverse FF controller as shown in Eq. 4.3. When it is not possible to test the target specimen, it may be possible to achieve similar behavior through modification of the FF controller. By intelligently designing the FF, the original specimen can represent the dynamic properties of the target system as shown in Eq. 4.4 and Eq. 4.5. In Eq. 4.5, $G_{\mathrm{FF\_new}}(s)$ is the only unknown dynamic component. The dimensions of $G_{\mathrm{ST}}(s)$, $G_{\mathrm{FF}}(s)$, and $G_{\mathrm{FF\_new}}(s)$ are 1 × 1 (i.e., all single-input-single-output (SISO) systems), while the dimensions of $G_{\mathrm{ES}}(s)$ and $G_{\mathrm{ES\_target}}(s)$ are n × 1 (i.e., single-input-multiple-output (SIMO) systems) where n is the number of specimen outputs.

$$G_{\mathrm{SYS}}(s) = G_{\mathrm{ES}}(s) \cdot G_{\mathrm{ST}}(s) \cdot G_{\mathrm{FF}}(s) \tag{4.1}$$

$$G_{\mathrm{SYS\_new}}(s) = G_{\mathrm{ES}}(s) \cdot G_{\mathrm{ST}}(s) \cdot G_{\mathrm{FF\_new}}(s) \tag{4.2}$$

$$G_{\mathrm{SYS\_target}}(s) = G_{\mathrm{ES\_target}}(s) \cdot G_{\mathrm{ST}}(s) \cdot G_{\mathrm{FF}}(s) \tag{4.3}$$

$$G_{\mathrm{SYS\_new}}(s) = G_{\mathrm{SYS\_target}}(s) \tag{4.4}$$

$$G_{\mathrm{ES}}(s) \cdot G_{\mathrm{ST}}(s) \cdot G_{\mathrm{FF\_new}}(s) = G_{\mathrm{ES\_target}}(s) \cdot G_{\mathrm{ST}}(s) \cdot G_{\mathrm{FF}}(s) = G_{\mathrm{SYS\_target}}(s) \tag{4.5}$$

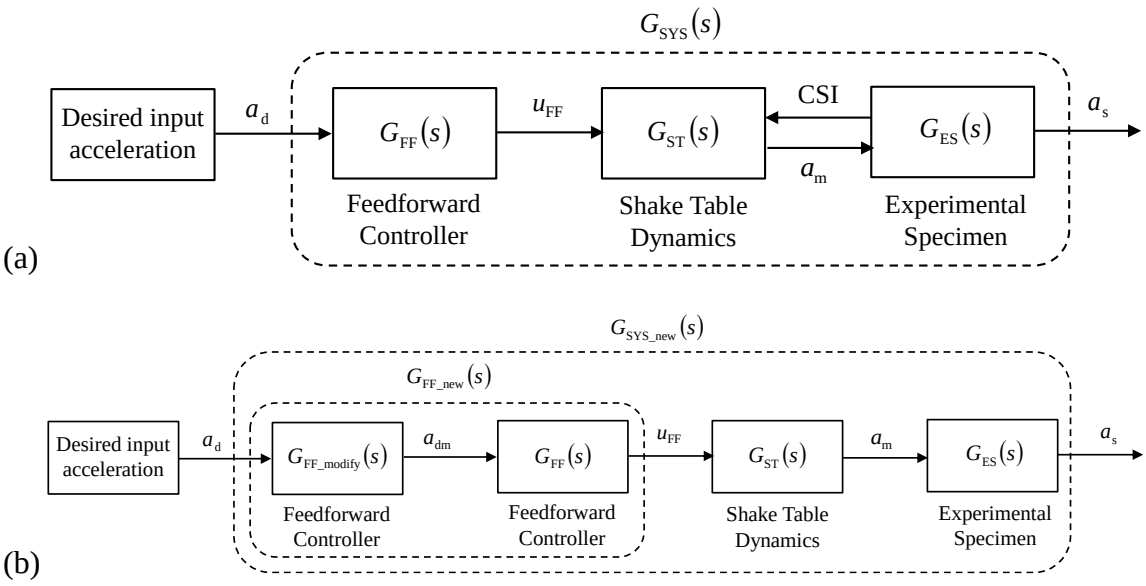

Figure 4.1 Block diagram of the model-based controller: (a) original FF controller; (b) modified FF controller

Since $G_{ES}(s)$ and $G_{ES\_target}(s)$ may have multiple outputs, there is no unique solution to their inverse. Therefore, a pseudo inverse is created by using a weighted sum of system outputs to create SISO representations of $G_{ES}(s)$ and $G_{ES\_target}(s)$, denoted as $\overline{G}_{ES}(s)$ and $\overline{G}_{ES\_target}(s)$ respectively. The modified FF controller, $G_{FF\_new}(s)$, can be obtained as shown in Eq. 4.6 and Eq. 4.7. $\overline{G}_{ES}(s)$ and $\overline{G}_{ES\_target}(s)$ are shown in Eq. 4.8 and Eq. 4.9 in terms of the gains, poles and zeros.

$$G_{FF\_new}(s) = G_{ST}^{-1}(s) \cdot \overline{G}_{ES}^{-1}(s) \cdot \overline{G}_{ES\_target}(s) \cdot G_{ST}(s) \cdot G_{FF}(s) \tag{4.6}$$

$$G_{FF\_new}(s) = \overline{G}_{ES}^{-1}(s) \cdot \overline{G}_{ES\_target}(s) \cdot G_{FF}(s) \tag{4.7}$$

$$\overline{G}_{ES}(s) = \frac{\Pi(s - z_s)}{\Pi(s - p_s)} \cdot k_s \tag{4.8}$$

$$\overline{G}_{ES\_target}(s) = \frac{\Pi(s - z_{s\_target})}{\Pi(s - p_{s\_target})} \cdot k_{s\_target} \tag{4.9}$$

By substituting Eq. 4.8 and Eq. 4.9 into Eq. 4.7, the modified FF for achieving the target system can be obtained as Eq. 4.10, where $G_{\mathrm{FF\_modify}}(s)$ represents the modification on the original FF controller. Figure 4.1(b) shows the block diagram with the modified FF controller. Note that the shaker tracks the desired modified acceleration a_{dm} instead of the input acceleration.

$$G_{\mathrm{FF\_new}}(s) = \left(\frac{\Pi(s - z_{\mathrm{s\_target}})(s - p_{\mathrm{s}})}{\Pi(s - p_{\mathrm{s\_target}})(s - z_{\mathrm{s}})} \cdot \frac{k_{\mathrm{s\_target}}}{k_{\mathrm{s}}} \right) \cdot G_{\mathrm{FF}}(s) = G_{\mathrm{FF\_modify}}(s) \cdot G_{\mathrm{FF}}(s) \quad (4.10)$$

In this study, acceleration measurements are readily available for each vibrating mass of the specimen. In this situation, SISO systems $\overline{G}_{\mathrm{ES}}(s)$ and $\overline{G}_{\mathrm{ES\_target}}(s)$ can be created from weighted averages of the output accelerations. Example weights include using full weight on one DOF where a good match of the target system is desired, using full weight on one mode where a good match of the target system is desired, or a weighted combination of DOF or modes.

4.3 Numerical Illustration of the Proposed Feedforward Controller

To investigate the feasibility of the proposed techniques, a simple simulation was conducted. The responses in both frequency domain and time domain are presented for the numerical model of a two-story steel shear building with very low damping (0.95% and 0.23% in the 1st and 2nd modes), selected as the original structure (i.e., specimen). The two-story building is assumed to be mounted on a uni-axial shake table. The model from desired to measured base acceleration is represented by a model with 8 poles and 8 zeros in this numerical study. Higher levels of damping as defined by the target structure will be achieved through the proposed AD-FF techniques. The natural frequencies of the

specimen are 2.2 Hz and 6.3 Hz. The other mechanical and geometrical properties of the specimen are introduced in detail in the following section. The damping ratios of the target structure are set as 5% for both modes. Figure 4.2 shows the frequency responses of the 1st and 2nd floor of the structure using AD-FF controllers. Six different weights on the acceleration outputs are considered, resulting in six different AD-FF controllers and thus six different achieved systems. Weights considered include: acceleration of 1st floor; 2nd floor; 1st mode; 2nd mode; equal combination of 1st and 2nd floor; and equal combination of 1st and 2nd mode. In an ideal situation, the achieved system will match the target system. The best agreement in both magnitude and phase is achieved from either output weighting on the 2nd floor or output weightings combining the 1st and 2nd mode. The response of the 2nd floor contains significant from both the 1st and 2nd mode, resulting in similar levels of performance for these two options. For other cases, target damping can only be achieved for the specific DOF or mode which is selected for the output weighting. For example, placing weight on the 1st mode achieves a good match in the 1st mode but not the 2nd mode.

In the remainder of this study, the modified FF will be designed based on the equal output weighting of the 1st and 2nd mode to achieving the target structure with artificially added damping. Figures 4.3, 4.4, 4.5, and 4.6 are created using this output weighting to further demonstrate the technique. The modified FF through AD-FF is shown in Figure 4.3 compared to the FF for the original structure. Figure 4.4 shows the frequency responses of $G_{\mathrm{ST}}(s)\cdot G_{\mathrm{FF\_new}}(s)$. Since the dynamics of the original FF controller and the shake table cancel out, this figure reflects the modification on the input

acceleration (i.e., the additional zeros, poles, and gain in Eq. 4.10). It can be seen clearly that supplemental damping is added in the 1st and 2nd mode of the specimen.

The combined system $G_{ST}(s) \cdot G_{FF\_new}(s)$ looks similar to a notch filter. Notch filters are band-stop filters which attenuates the magnitude of a signal over a specific range of frequencies. Notch filters have been used in shake table tests to attenuate unwanted vibrations which may lead to resonance of something other than the specimen (Tagawa et al., 2007; Seki et al., 2009). While worth noting the similarity in appearance, in this study $G_{ST}(s) \cdot G_{FF\_new}(s)$ is specifically created to achieve a target level of damping in a specimen rather than ad-hoc attenuation of undesired vibrations or resonance.

The FF created through the proposed techniques could have high frequency dynamics which could cause problems if they are large relative to the sampling frequency of the digital signal processor implementing the FF controller. The issue of high frequency dynamics in the controller can be solved by modal truncation techniques or by using a higher sampling frequency. In this study, the modal truncation techniques are used to eliminate the high frequency states without altering the desired dynamic properties. The MATLAB function 'modred' is selected for model truncation. The effect of modal truncation is shown in Figure 4.5 in a bode plot. It can be seen that the modified FF before and after model truncation behaves nearly identically from 0-100 Hz, adequate for most civil structures. Time histories of the accelerations of the structure with artificially added damping subjected to 30% El Centro are presented in Figure 4.6 for further demonstration of the potential of the proposed techniques. Good agreement can be seen from Figure 4.6 between target structure and the structure with added damping achieved by the proposed techniques.

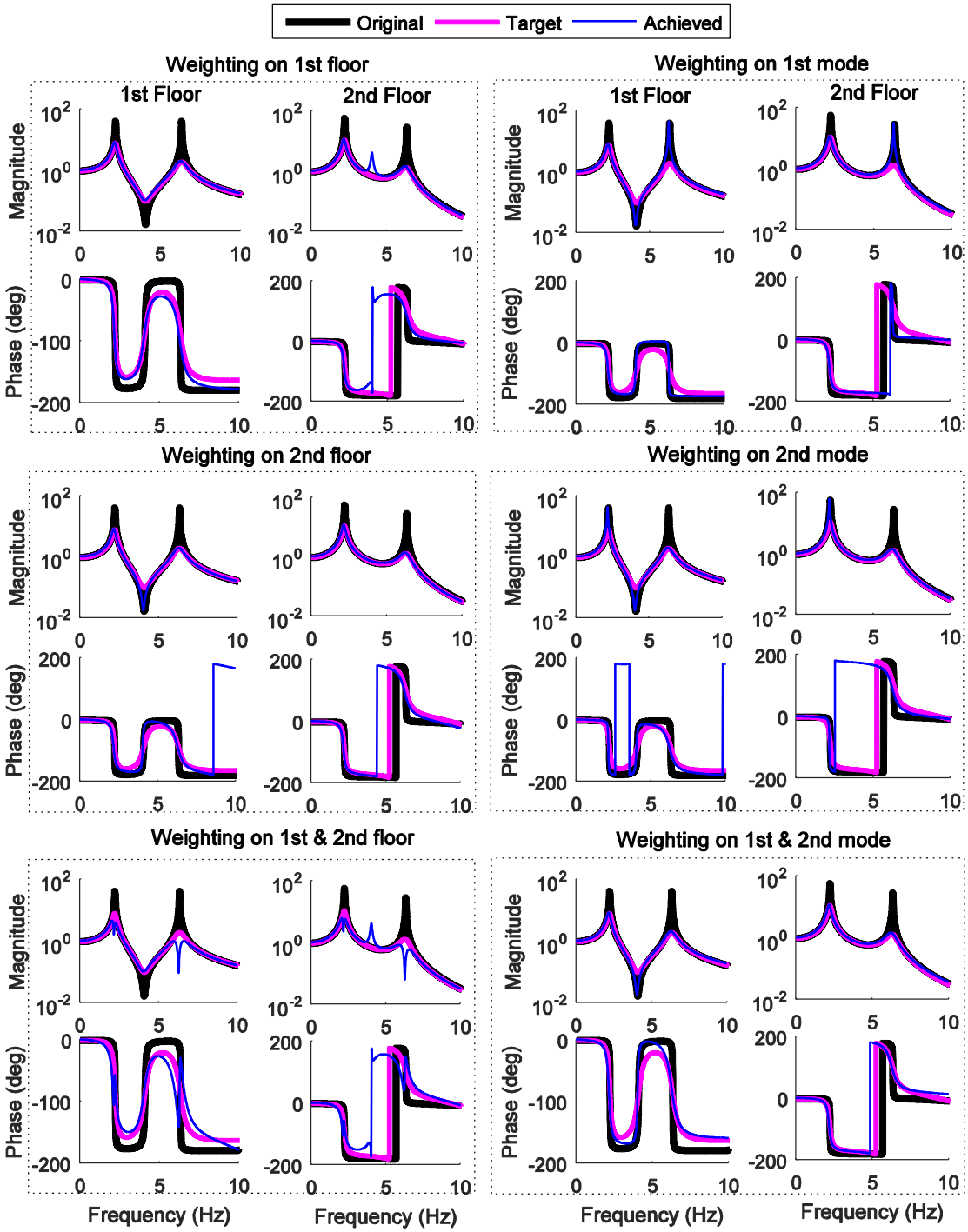

Figure 4.2 Frequency responses of the target structure and original structure with artificially added damping; investigation of output weighting

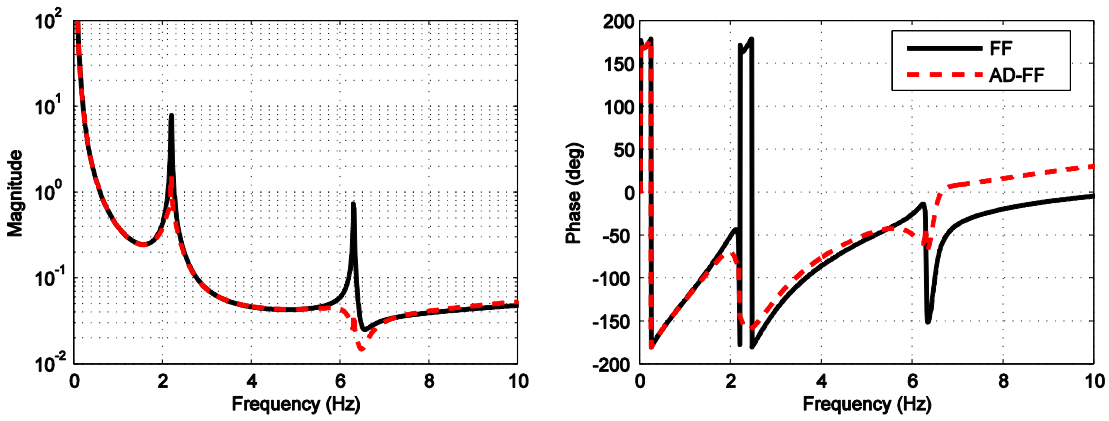

Figure 4.3 Transfer function of the modified FF for achieving the target structure

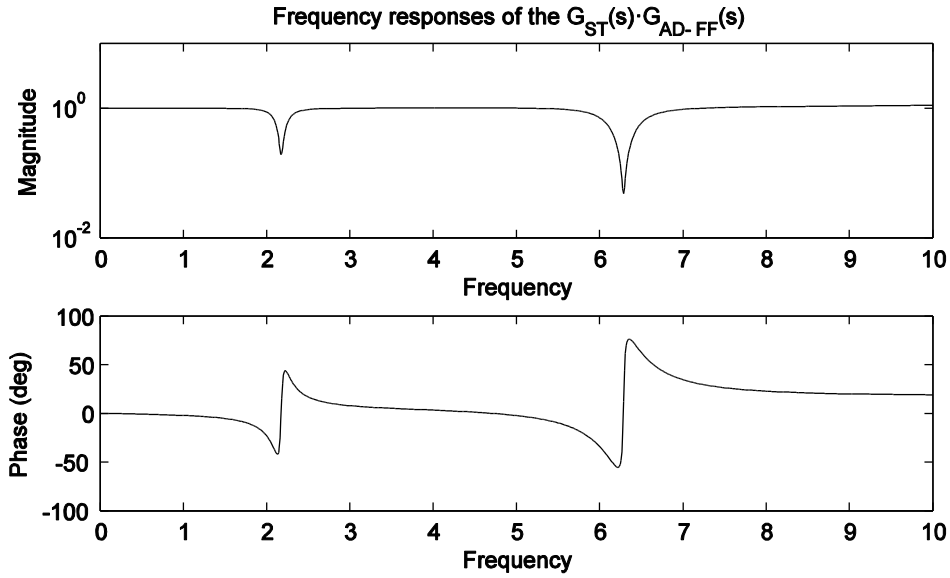

Figure 4.4 Frequency responses of $G_{ST}(s) \cdot G_{FF\_new}(s)$

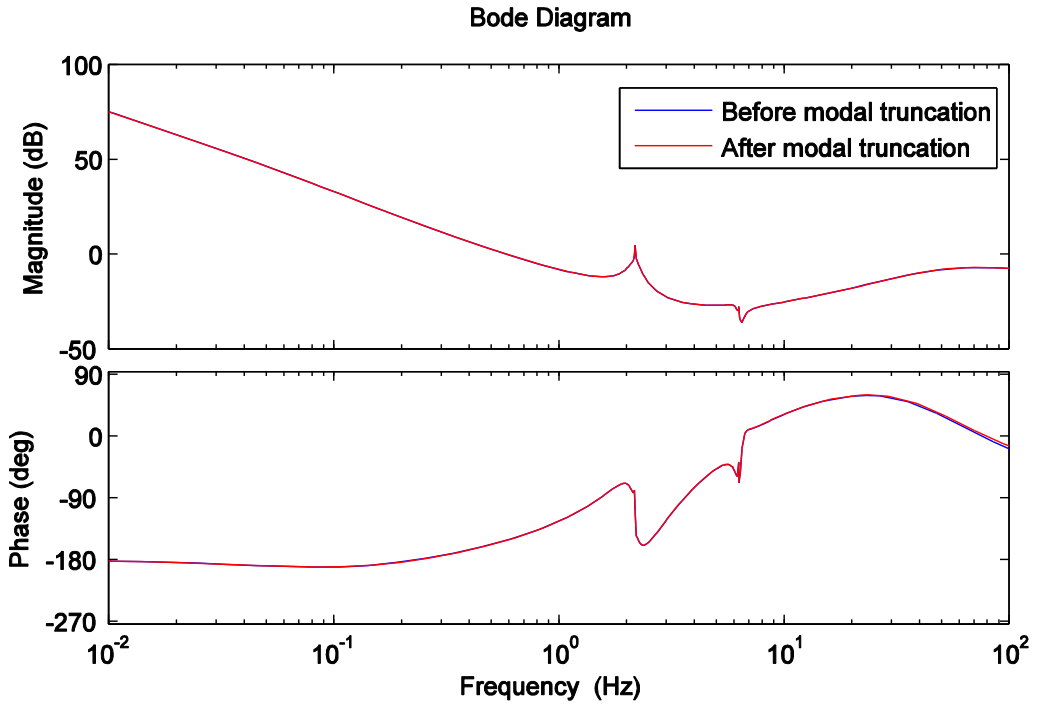

Figure 4.5 Transfer function of the modified FF for achieving the target structure

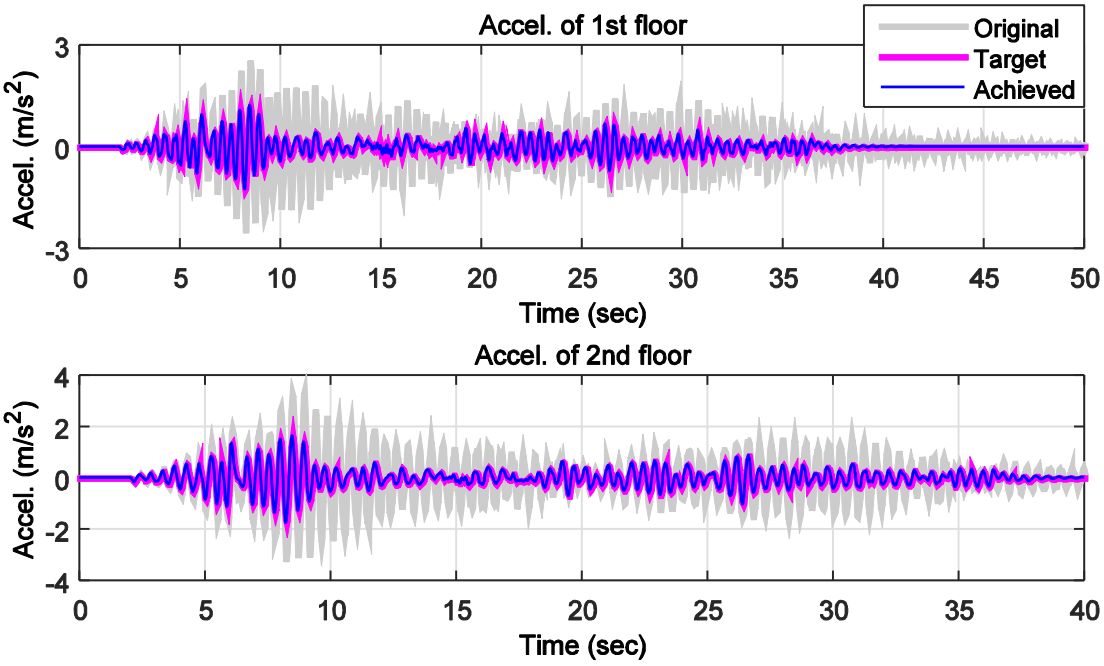

Figure 4.6 Time histories of accelerations of the structure with artificial damping

4.4 Experimental Setup

The proposed techniques of adding artificial damping to the specimen are developed and verified using a small-scale experimental setup. The setup consists of a uni-axial shake table, a two-story steel shear building model as the experimental specimen, and a control and data acquisition system. The dynamic properties of both the experimental substructure and the total structure are presented in this section. The specimen and equipment are located at the University of Maryland and is part of the Structural Engineering Laboratory.

4.4.1 Uni-axial shake table and sensors

The setup of facilities are same as the previous study, including the shake table, control hardware and software, and data acquisition system. Detailed information can be found in Chapter 3 (Section 3.3.1).

4.4.2 Experimental substructure and total structure

A two-story steel shear building model is used as the experimental specimen in this study as shown in Figure 4.7 mounted on the shake table. The floor size is 20.3 cm × 20.3 cm and the height of each story is 14.0 cm. At each floor, six steel blocks are attached as additional masses. The total mass of the first and second floors are 6.36 kg and 6.40 kg, respectively. Two spring-steel columns with a thickness of 0.5 mm connect the floor plates. The spring steel ensures that the building can undergo large deformations without yielding, appropriate for the development of new experimental techniques.

The raw specimen was subjected to a 0 to 10 Hz band-limited white noise base excitation to determine the natural frequencies and extract the stiffness. The experimental transfer function from input ground motion to measured story accelerations is presented

in Figure 4.8. Free vibration tests were conducted to determine the structural damping. The identified mass, damping, and stiffness were combined into a 2DOF shear building model. Both magnitude and phase between the measured transfer function and identified model match well as shown in Figure 4.8. The first and second natural frequencies of the structure are 2.2 Hz and 6.3 Hz, respectively.

The total three-story shear structure consists of a numerically simulated lower story and experimentally represented upper stories. The mass and stiffness of the lower story are chosen as the average of the mass and stiffness of the upper two stories, resulting in undamped natural frequencies of 1.6 Hz, 4.8 Hz, and 6.6 Hz. The damping ratios are given in the following section for different total structure used for different studies. Table 4.1 summarizes the mass and the stiffness of the total structure which is the combined result of the mass and stiffness of the substructures.

The bare steel structure exhibited very low inherent damping, approximately 0.95% and 0.23% for the 1^{st} and 2^{nd} modes, which are insufficient for stability during RTHS. The foams were attached to add extra damping to increase stability in RTHS in the previous study (Zhang et al., 2016). In this chapter, a novel technique instead is proposed and applied to artificially add damping to the structure.

Table 4.1 Parameters of the total structure

Floor	Mass (kg)	Stiffness (kN/m)
1	6.38	3.50
2	6.36	2.87
3	6.40	4.13

Figure 4.7 Shear building specimen mounted on shake table

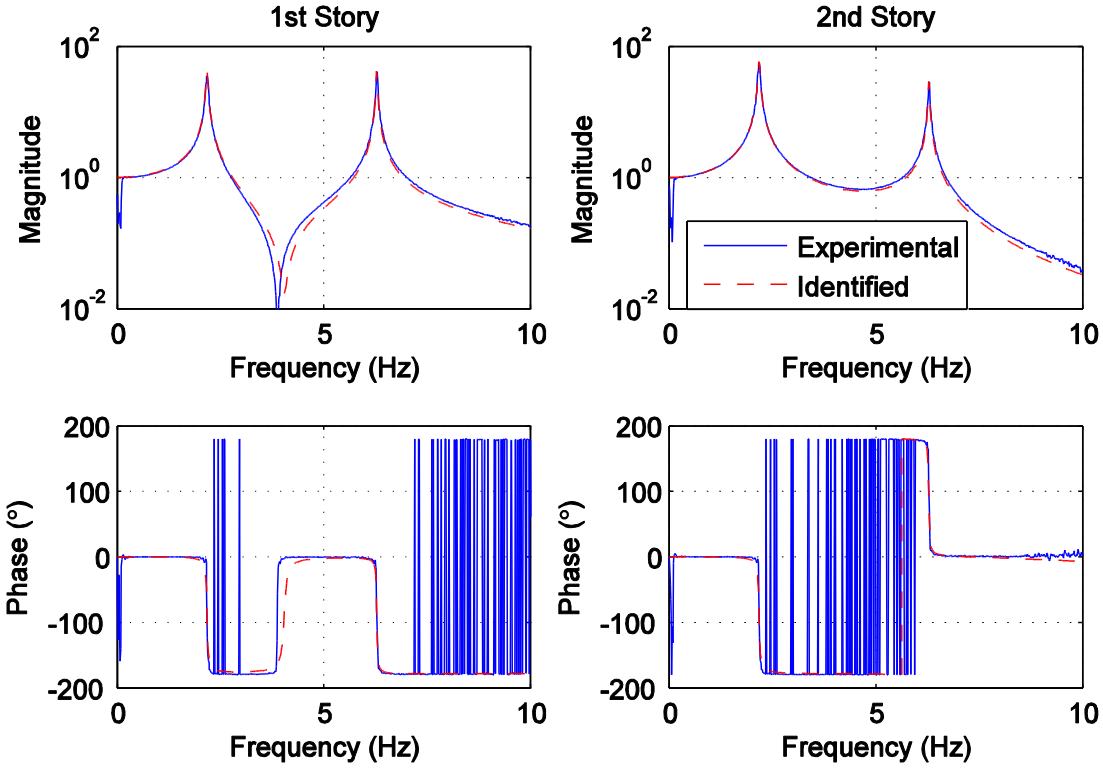

Figure 4.8 System identification of the two-story specimen

4.4.3 Shake table identification and controller development

The input-output model of the shake table is determined using a 0 to 10 Hz band-limited white noise voltage command to the shake table and measured acceleration of the base.

The two-story specimen is mounted on the table during identification to include the effects of CSI. Figure 4.9 shows the experimentally identified transfer function of the shake table along with the identified model. Two features can clearly be seen from this figure. First, since the command to the shake table is approximately proportional to the displacement, the output acceleration approaches zero at zero frequency. Second, there are valleys around the two natural frequencies of the experimental specimen, clearly illustrating the interaction between shake table and specimen (i.e., CSI). In all, 8 zeros and 8 poles are used to create a model that matches the experimentally identified transfer function. The model was fit using a nonparametric linear system identification technique MFDID (Kim et al., 2005).

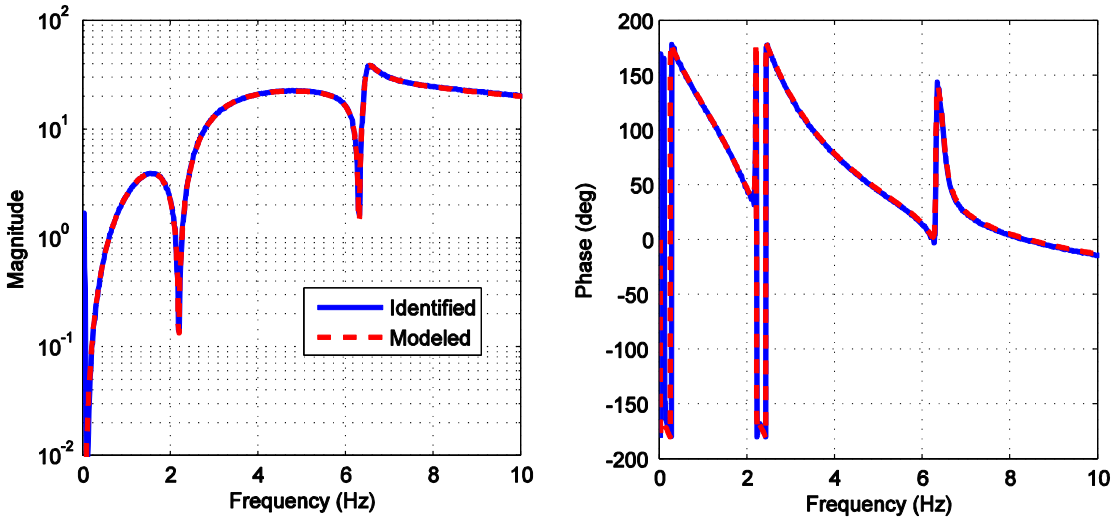

Figure 4.9 Identified and modeled shake table transfer functions

The feedforward controller is created as an inverse of the identified model to compensate for the modeled dynamics of the shake table. The FF controller is modified to achieve different target structures discussed in the following section through the proposed techniques. In RTHS, high frequency measurement noise will enter into the RTHS loop. A feedforward controller with a large magnitude at high frequencies may

turn the measurement noise into high-frequency commands to the table. To avoid potential spurious excitation, a second order Butterworth low-pass filter with a cutoff frequency of 50 Hz is added in series with the feedforward controller. The filter is designed to reduce the magnitude at higher frequencies without altering the performance over the range of interest (0 to 10 Hz). All experimental results in next section are based on the low-pass filtered FF controller, while the responses from numerical simulation are generated from the modified FF without low-pass filtering.

4.4.4 Earthquake ground motions

Two earthquake ground motion records with different magnitudes and frequency content are selected as the input to the structure, taken from a study on structural control (Ohtori et al., 2004): (1) Hachinohe: The N-S component recorded at Hachinohe City during the Tokachi-oki earthquake of May 16, 1968, and (2) Kobe: the N-S component of the Japanese Meteorological Agency station during the Kobe earthquake of January 17, 1995. The reference earthquakes are passed through a 2-pole Butterworth high-pass filter with a cutoff frequency of 0.25 Hz to remove the low-frequency behavior without altering the desired frequency content. The earthquake records are scaled down as shown in Figure 4.10 during traditional shake table testing and RTHS due to the limitations of the shake table.

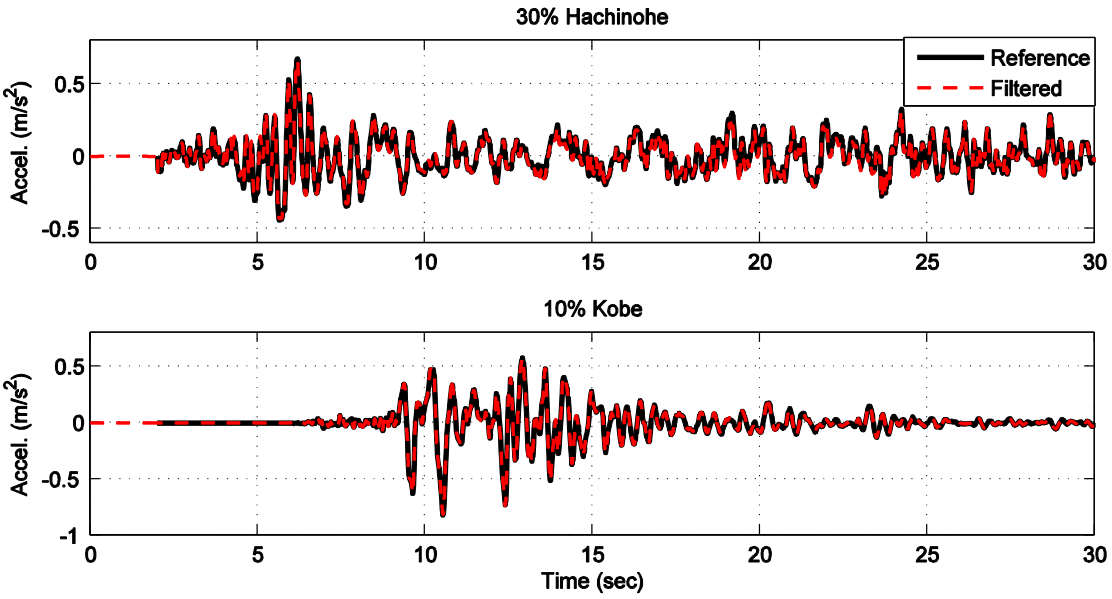

Figure 4.10 Historic ground motions

4.5 Experimental Evaluation of the Proposed Technique

This section investigates the performance of the proposed techniques to artificially add structural damping for both traditional shake table testing and RTHS. Traditional shake table testing is used to demonstrate the performance of the proposed techniques in a straightforward way by comparing the target structure with the achieved responses of the specimen. The original and target structures are analyzed in numerical simulation (SIM), while the achieved responses are obtained from experimental testing (ST). RTHS is used to demonstrate as a broader application of the proposed techniques. In RTHS, system damping is an important factor for stability and accuracy. Time delays and time lags introduce negative damping into the RTHS loop. Negative damping introduced through time delays and time lags increases with the natural frequency of the specimen. For multi-degrees-of-freedom (MDOF) specimens, the higher natural frequencies are more likely to cause stability problems. When higher modes are problematic to RTHS stability,

the proposed AD-FF can be used to introduce damping to the specimen higher modes. In this way, a larger tolerance of time delay can be created without significantly changing specimen behavior since most structures are dominated by lower modes. Selective added modal damping is the most important contribution of the proposed techniques, especially for the models of MDOF structures.

By using the proposed techniques, researchers can assign extra damping to the existed specimen in traditional shake table testing and RTHS without installing extra damping devices, saving labors and costs and increasing the flexibility. All accelerations from tests are passed through a low-pass filter with a cutoff frequency of 20 Hz in post-processing to remove high frequency noise. To better illustrate the performance of the proposed techniques in add damping through modified FF controller, no feedback (FB) controller was used for acceleration tracking through shake table. Tracking performance can be further enhanced with the implementation of the FB controller.

4.5.1 Traditional shake table testing

In traditional shake table testing, typically the shake table should track the input ground acceleration. However, in this study, since the FF is designed based on the specimen and the target structure as shown in Eq. 4.10, the tracking acceleration will be different from the ground acceleration. The reason is that the dynamics of the specimen and the target structure are included in the AD-FF, thus generating the acceleration subjected to which the specimen would behave as the target structure. Figure 4.11 shows the tracking acceleration of the 30% Hachinohe earthquake and 10% Northridge earthquake using the designed FF. The damping of the target structure is set as 5% for both modes. The responses of the specimen with the added damping and the target structure are shown in

Figure 4.12 and Figure 4.13 for the excitation of 30% Hachinohe earthquake and 10% Kobe earthquake, respectively. Good agreement is observed between the target structure and the achieved responses, demonstrating the favorable performance of the proposed techniques in achieving target damping. The behavior of the specimen without using the proposed AD-FF approach is shown to illustrate the significant change in dynamic behavior achieved.

In traditional shake table testing, typically the shake table should track the input ground acceleration. However, in this study, since the FF is designed based on the specimen and the target structure as shown in Eq. 4.10, the tracking acceleration will be different from the ground acceleration. The reason is that the dynamics of the specimen and the target structure are included in the AD-FF, thus generating the acceleration which will cause the specimen to behave as the target structure. Figure 4.11 shows the tracking acceleration of the 30% Hachinohe earthquake and 10% Kobe earthquake using the designed FF. The damping of the target structure is set as 5% for both modes. The transfer function of the system with added damping using AD-FF technique can be found in Fig. 4 with output weightings on equal combination of 1^{st} and 2^{nd} mode. The responses of the specimen with the added damping and the target structure are shown in Figure 4.12 and Figure 4.13 for the excitation of 30% Hachinohe earthquake and 10% Kobe earthquake, respectively. Good agreement is observed between the target structure and the achieved responses, demonstrating the favorable performance of the proposed techniques in achieving target damping. The behavior of the specimen without using the proposed AD-FF approach is shown to illustrate the significant change in dynamic behavior achieved.

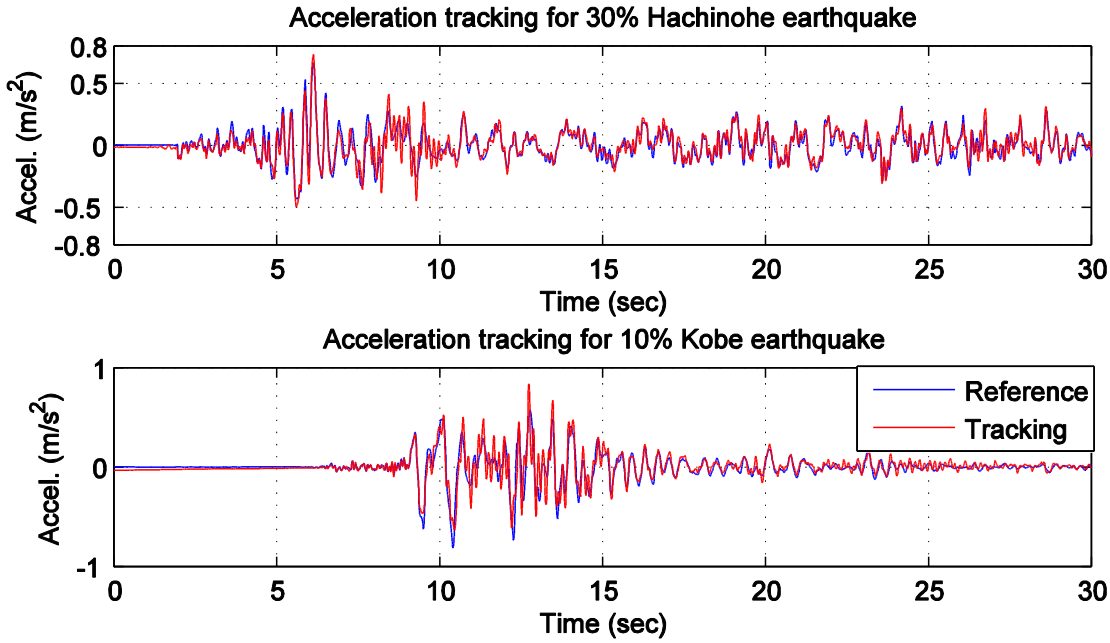

Figure 4.11 Acceleration tracking performance for traditional shake table testing

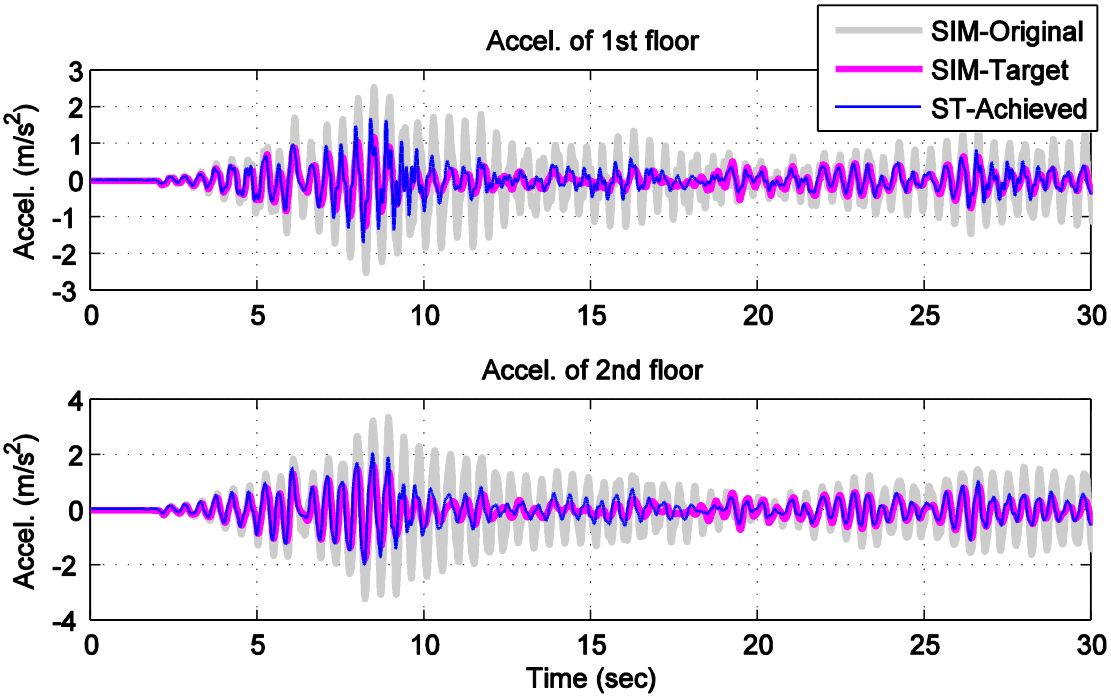

Figure 4.12 Structural accelerations under 30% Hachinohe compared to the original and target structure

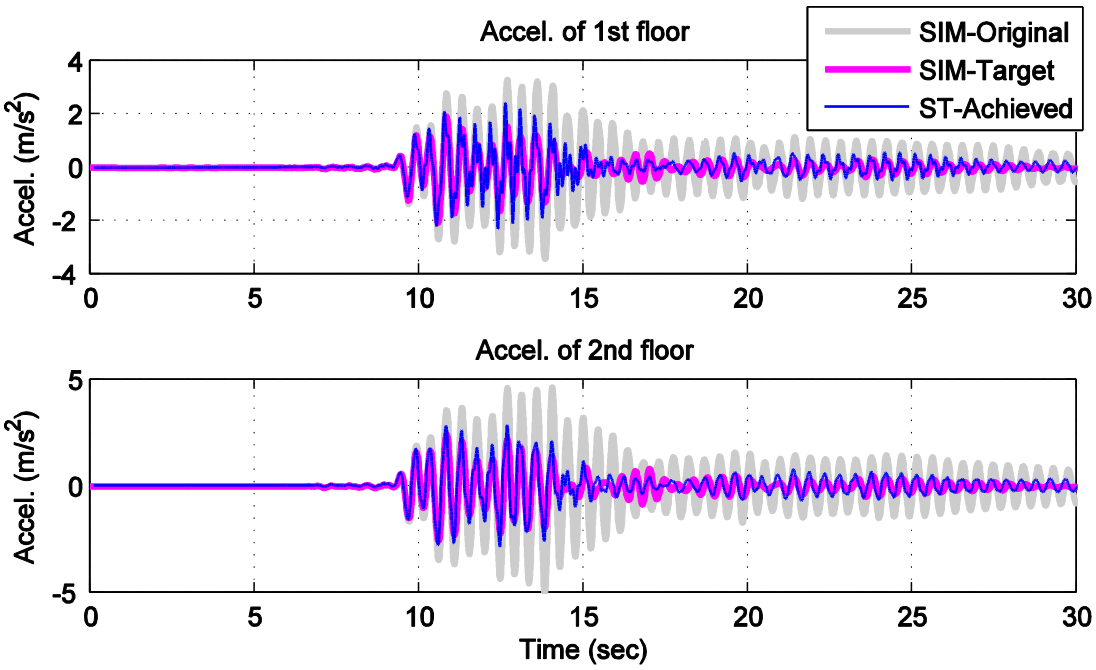

Figure 4.13 Structural accelerations under 10% Kobe compared to the original and target structure

4.5.2 RTHS performance

In this section, the performance of the proposed techniques as applied to RTHS is investigated. First, stability problems in RTHS of MDOF specimens are often caused by the higher modes, including the example multi-story building model. The proposed techniques make it possible to introduce damping only on the specific modes which cannot be realized by using actual devices. In this way, the stability of RTHS can be increased without changing the structural responses which are dominated by the lower modes. Second, the structure with a target level of damping can be easily achieved with the raw specimen by using the proposed AD-FF technique. In addition, the implementation of the proposed techniques in RTHS offers an easy-accessible alternative to study the effect of damping on RTHS stability and accuracy, without installing and updating the external damping devices. The proposed techniques make it very easy to

explore multiple levels of damping on specimens in RTHS. The following discuss is divided into two subsections to demonstrate the performance of the proposed techniques in RTHS.

4.5.2.1 Damp out higher specimen modes

The total three-story shear structure consists of a numerically simulated lower story and experimentally represented upper stories. Two total structures are analyzed with quite different damping ratios on the 2nd and 3rd mode, controlled by increasing the damping in the 2nd mode of the experimental specimen to 10% through the proposed techniques. Since the modes of the substructures influence all modes of the total structure, the numerical substructure is selected in order to get similar damping in the 1st mode of the total structures. The damping ratios are 3.3%, 7.8% and 2.6% for the three modes of the original structure, and 3.3%, 10.8%, and 8.9% for the target structure. The natural frequencies are 1.6 Hz, 4.8 Hz, and 6.6 Hz for the original structure, and 1.6 Hz, 4.8 Hz, and 6.7 Hz for the target structure. The frequency responses of the experimental specimen without and with extra damping are shown in Figure 4.14. It is clear that the damping is increased only at the second mode. Figure 4.15 shows the frequency responses of the structure with added damping in higher modes compared to the original structure and the target structure. It is clear that the damping is identical for the 1st mode and is much increased for the 2nd and 3rd mode. It can be seen that the achieved transfer function of the 1st floor is exactly identical to the target. For the 2nd and 3rd floor, the amplification is observed at the 2nd mode. Generally, the achieved structure through the proposed techniques performs very well in RTHS. Time histories of the structures are further investigated and shown in Figure 4.16 and Figure 4.17 for the structures under

30% Hachinohe earthquake and 10% Kobe earthquake respectively. Three conclusions can be obtained as following. First, the responses of the original structure and the target structure are closed as expected because the total structure is dominated by the 1st mode. Second, although the original structure is stable in simulation without adding time delay, the RTHS framework of the original structure is unstable in real tests due to the low damping in the higher modes. Last, good agreement is observed between the target responses and the achieved responses from tests, representing that the proposed techniques work effectively in providing the system with the extra artificial damping in RTHS.

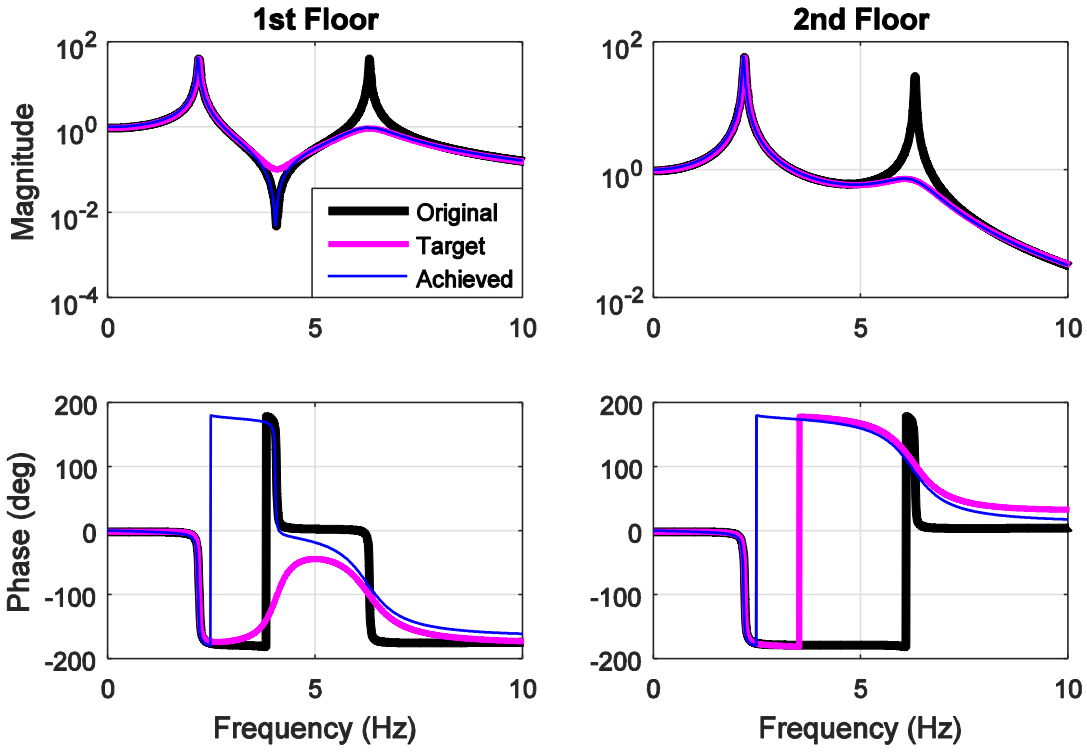

Figure 4.14 Frequency responses of the experimental specimen with added damping

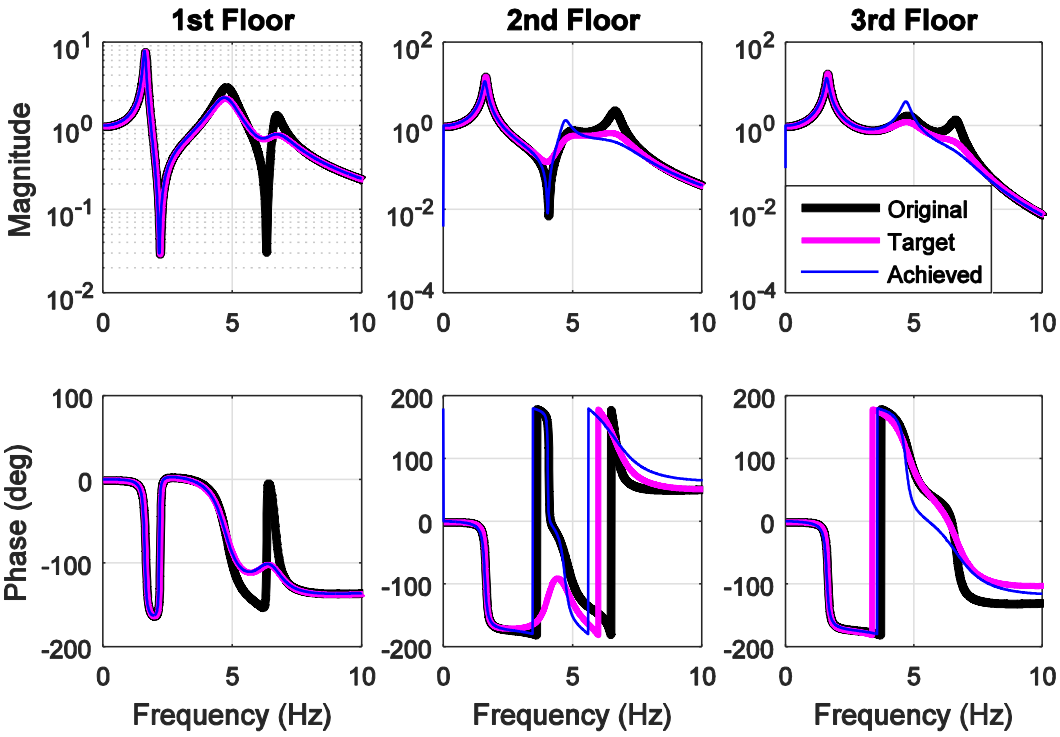

Figure 4.15 Frequency responses of the total structures with added damping

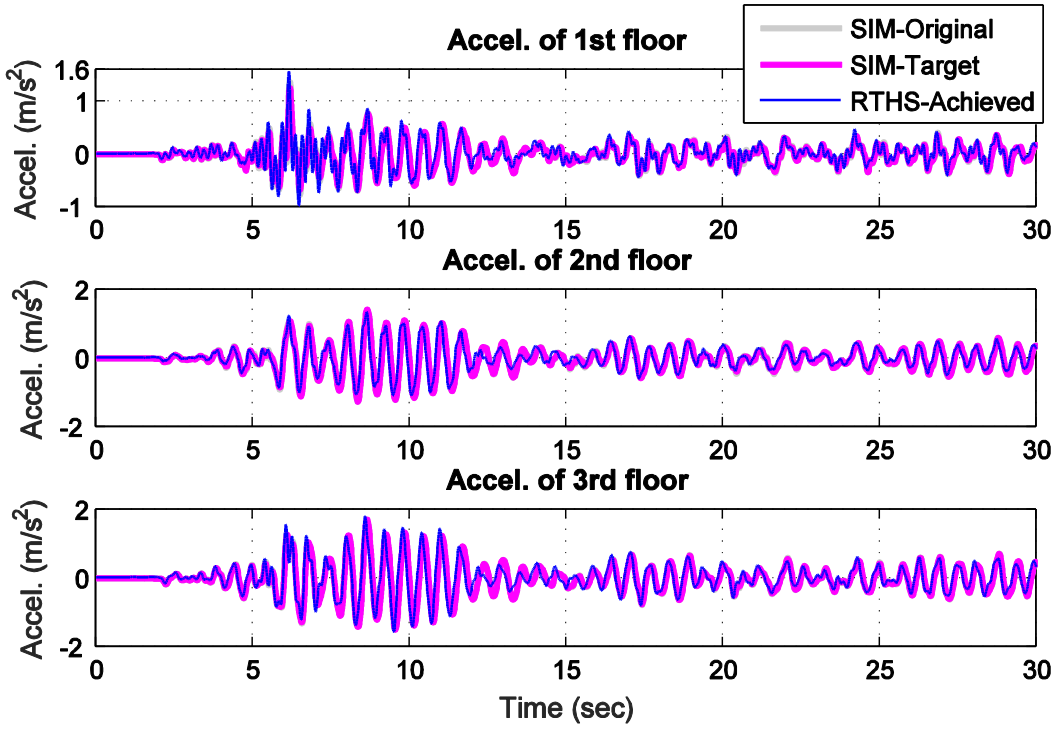

Figure 4.16 Structural accelerations in RTHS under 30% Hachinohe compared to the original and target structure

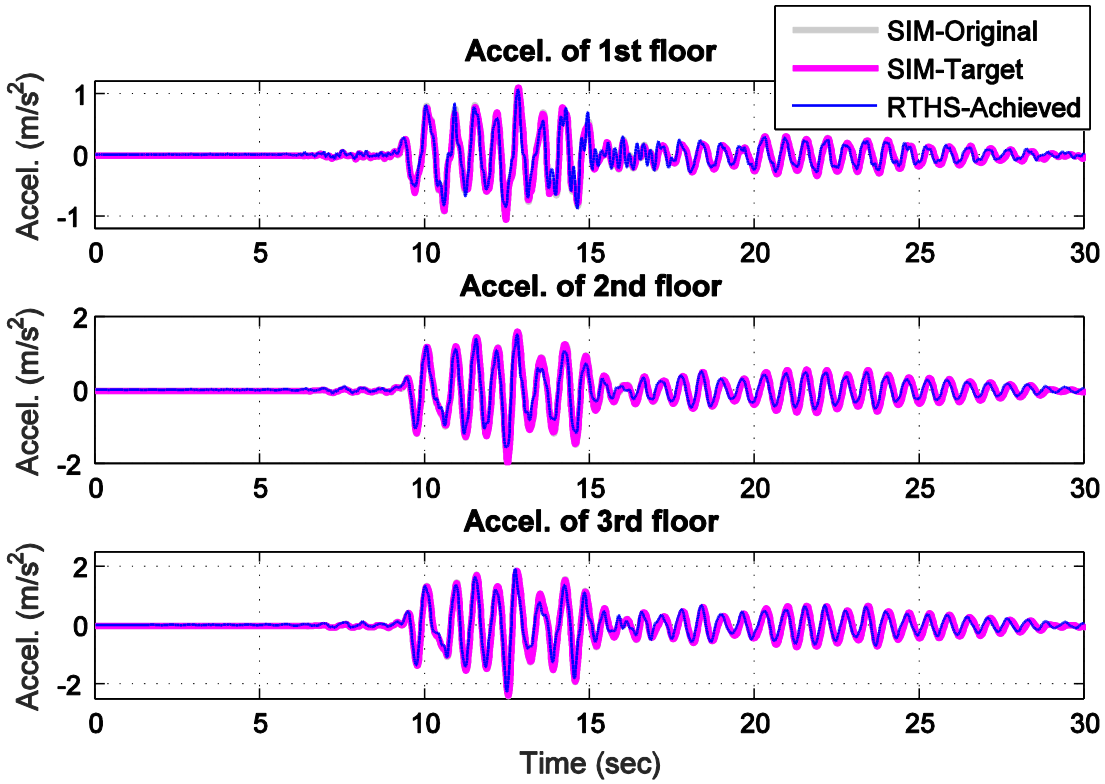

Figure 4.17 Structural accelerations in RTHS under 10% Kobe compared to the original and target structure

The total three-story shear structure consists of a numerically simulated lower story and experimentally represented upper stories. Two total structures are analyzed in this section, one created by combining the numerical substructure with specimen (i.e., original structure) and another created by combining the numerical substructure with the specimen where damping in the 2nd specimen mode is increased to 10% (i.e., target structure). Both structures can be evaluated in simulation, but only the target structure (realized using the proposed AD-FF) was stable in RTHS. Since the modes of the substructures influence all modes of the total structure, the numerical substructure damping is selected to get similar damping in the 1st mode of both total structures. The damping ratios are 3.3%, 7.8% and 2.6% for the three modes of the original structure, and

3.3%, 10.8%, and 8.9% for the target structure. The natural frequencies are 1.6 Hz, 4.8 Hz, and 6.6 Hz for the original structure, and 1.6 Hz, 4.8 Hz, and 6.7 Hz for the target structure. The frequency responses of the specimen, the target behavior of the experimental specimen (10% damping in the 2nd mode), and the achieved behavior of the experimental specimen (through AD-FF) are shown in Figure 4.14. It is clear that the damping is increased only at the second mode. Figure 4.15 shows the frequency responses of the the original total structure, the target total structure, and the achieved total structure (through AD-FF). It is clear that the damping is identical for the 1st mode and is much increased for the 2nd and 3rd mode. It can be seen that the achieved transfer function of the 1st floor is exactly identical to the target. For the 2nd and 3rd floor, the amplification is observed at the 2nd mode. Generally, the achieved structure through the proposed techniques performs very well in RTHS. Time histories of the structures are shown in Figure 4.16 and Figure 4.17 for the structures under 30% Hachinohe earthquake and 10% Kobe earthquake respectively. Numerical simulation was used to determine the original and target responses while RTHS was used to determine the achieved responses. Three conclusions can be obtained as following. First, the responses of the original structure and the target structure are closed as expected because the total structure is dominated by the 1st mode. Second, it was not possible to perform a RTHS of the original total structure due to the low damping in the specimen. Only when damping is added to the 2nd mode of the specimen could RTHS be performed. Last, good agreement is observed between the target responses and the achieved responses from tests, representing that the proposed techniques work effectively in providing the system with the extra artificial damping in RTHS.

The performance of the proposed techniques for transient loadings is numerically investigated through the impulse function (e.g., the response to an impulsive load modeled as a Dirac delta function $\delta(t)$). Figure 4.18 shows the impulse response of the experimental specimen (1st and 2nd floor) before and after adding extra artificial damping through the proposed techniques. It can be seen that the added damping effectively suppresses the structural responses for transient loadings, meaning that the technique does not require continuous external input produce the added damping.

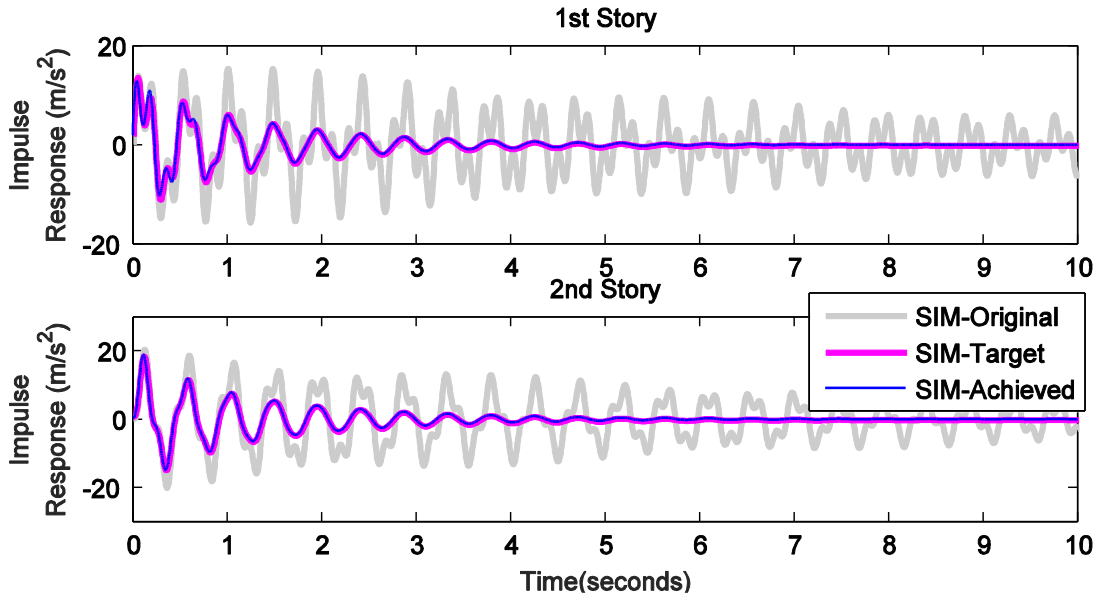

Figure 4.18 Simulated impulse response of the experimental substructure

4.5.2.2 Achieve desired damping across all modes

Another benefit of the proposed techniques in RTHS is that it offers great flexibility to the experimental specimen for achieving the total structure with the target damping properties. An example is given in this section to demonstrate the performance of the proposed techniques in RTHS. The target structure is determined as a three-story structure with the natural frequencies of 1.6 Hz, 4.8 Hz, and 6.6 Hz. The desired damping ratios are 3%, 7%, and 10% for the three modes. With the predefined numerical

substructure and the available raw steel specimen, the target damping of the experimental specimen can be obtained as 4.62% and 7.21%. By using the proposed techniques, the damping of the specimen can be easily increased from 0.95% and 0.23% to 4.62% and 7.21%. Figure 4.19 shows the frequency responses of the specimen before and after increasing the damping. More damping is observed at both 1st and 2nd mode. Figure 4.20 shows the frequency responses of the 3-story target structure and the structure achieved through the proposed techniques. It can be seen that the achieved transfer function of the 1st floor is exactly identical to the target. Amplifications are observed at the 2nd mode of the 2nd and 3rd floor. Figure 4.21 and Figure 4.22 show the structural accelerations of the structure with extra damping through the proposed techniques compared with the target structure subjected to 30% Hachinohe earthquake and 10% Kobe earthquake. Good agreement observed in Figure 4.21 and Figure 4.22 demonstrate the performance of the proposed techniques in providing extra structural damping in RTHS.

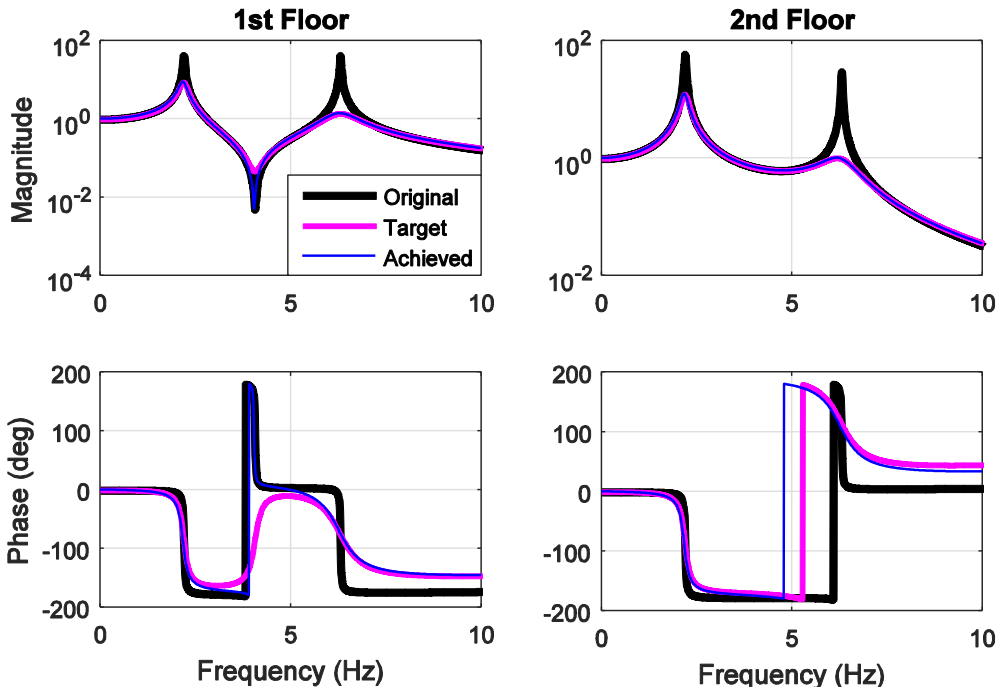

Figure 4.19 Frequency responses of the experimental specimen with added damping

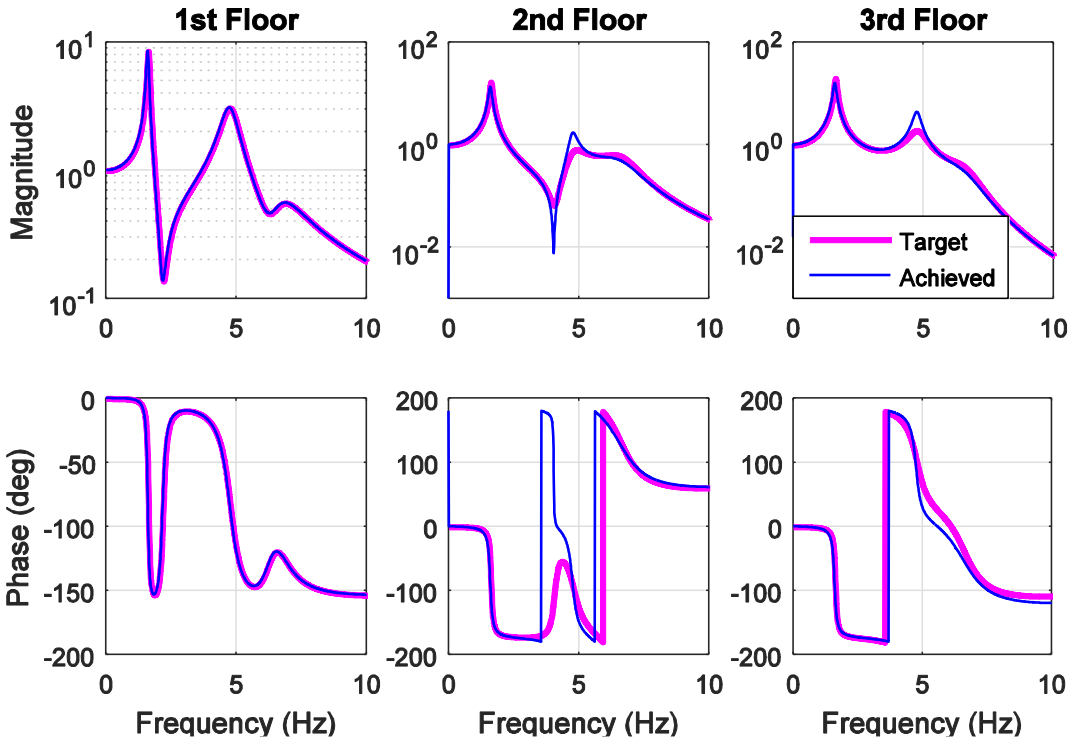

Figure 4.20 Frequency responses of the total structures with added damping

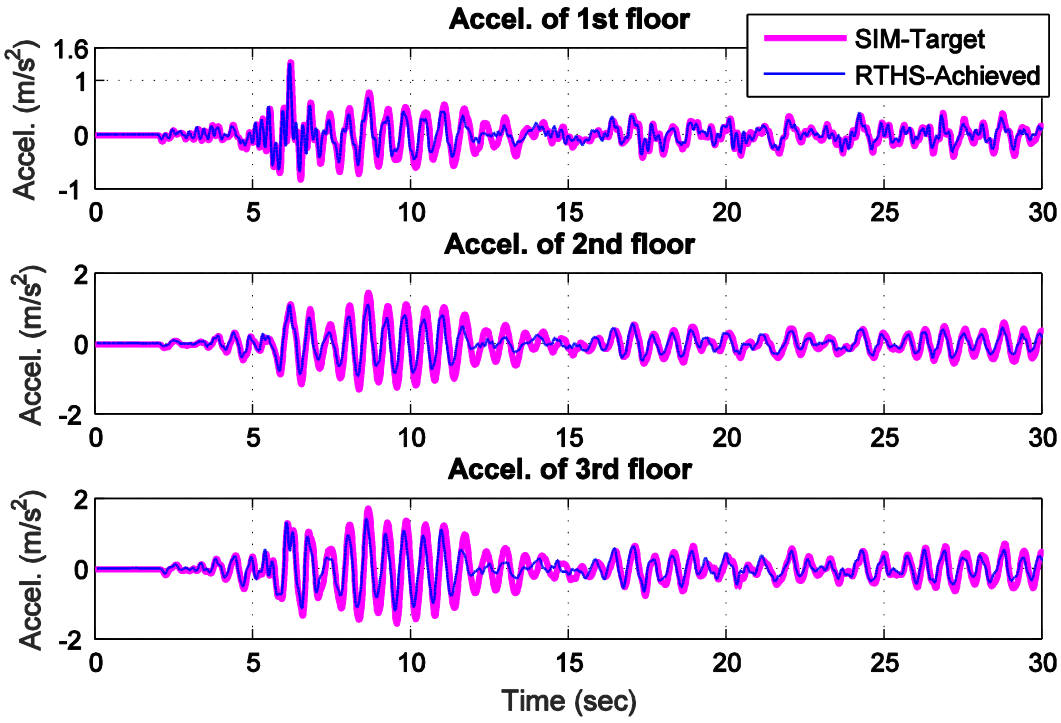

Figure 4.21 Performance of the proposed techniques in RTHS in achieving the target structure for 30% Hachinohe

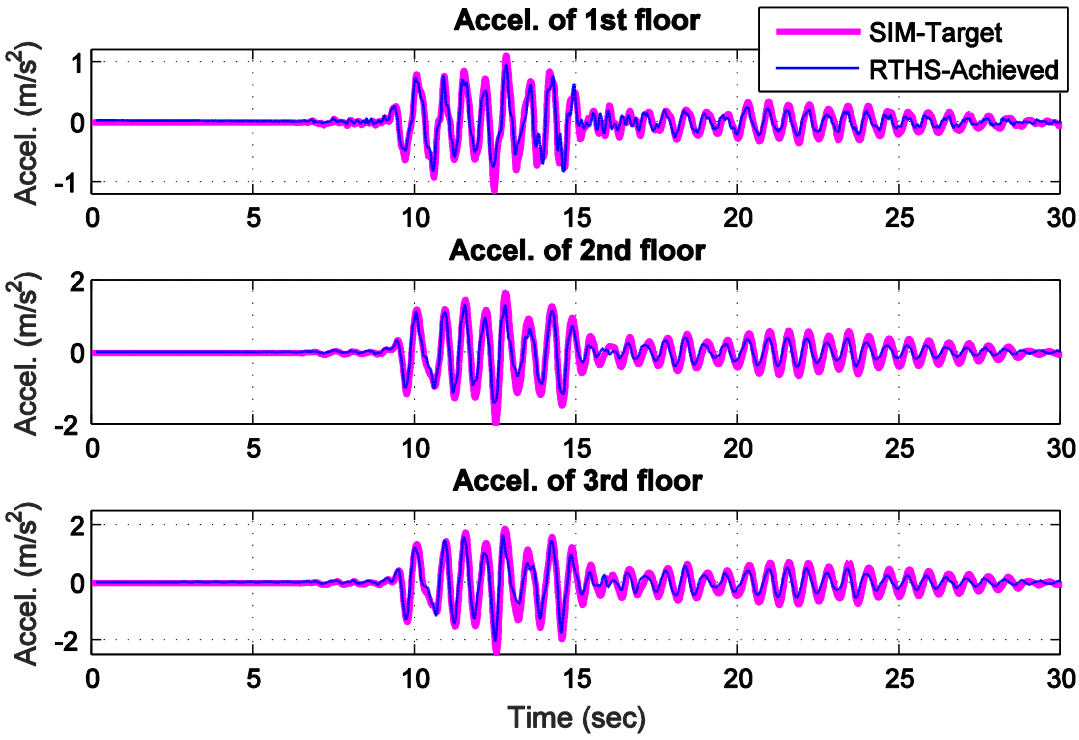

Figure 4.22 Performance of the proposed techniques in RTHS in achieving the target structure for 10% Kobe

Another benefit of the proposed techniques in RTHS is that it offers great flexibility to the experimental specimen for achieving the total structure with the target damping properties. An example is given in this section to demonstrate the performance of the proposed techniques in RTHS. The target structure is determined as a three-story structure with the natural frequencies of 1.6 Hz, 4.8 Hz, and 6.6 Hz. The desired damping ratios are 3%, 7%, and 10% for the three modes. With the predefined numerical substructure (discussed in previous section) and the available raw steel specimen, the damping of the 3-story structure is only 1.81%, 3.59%, and 1.64% for the three modes, denoted as original structure. To achieve the target structure, the damping of the specimen is increased from 0.95% and 0.23% in the two modes to 4.62% and 7.21% in the two modes by using the proposed techniques. Figure 4.19 shows the frequency

responses of the specimen before and after increasing the damping. Figure 4.20 shows the frequency responses of the 3-story target structure and the structure achieved through the proposed techniques. It can be seen that the achieved transfer function of the 1st floor (numerical substructure) is exactly identical to the target. Additionally, for all floors, the first mode response matches the target very well. Small amplifications are observed at the 2nd mode of the 2nd and 3rd floor. Figure 4.21 and Figure 4.22 show the accelerations of the structure with extra damping through the proposed techniques compared with the target structure subjected to 30% Hachinohe earthquake and 10% Kobe earthquake. Good agreement observed in Figure 4.21 and Figure 4.22 demonstrate the performance of the proposed techniques in providing extra structural damping in RTHS, even to lower modes.

The performance of the proposed techniques for transient loads in RTHS is also investigated. Figure 4.23 shows the impulse response of the total structure in RTHS before and after adding extra artificial damping through the proposed techniques. It further validates the stability contributed from the added artificial damping through the proposed techniques.

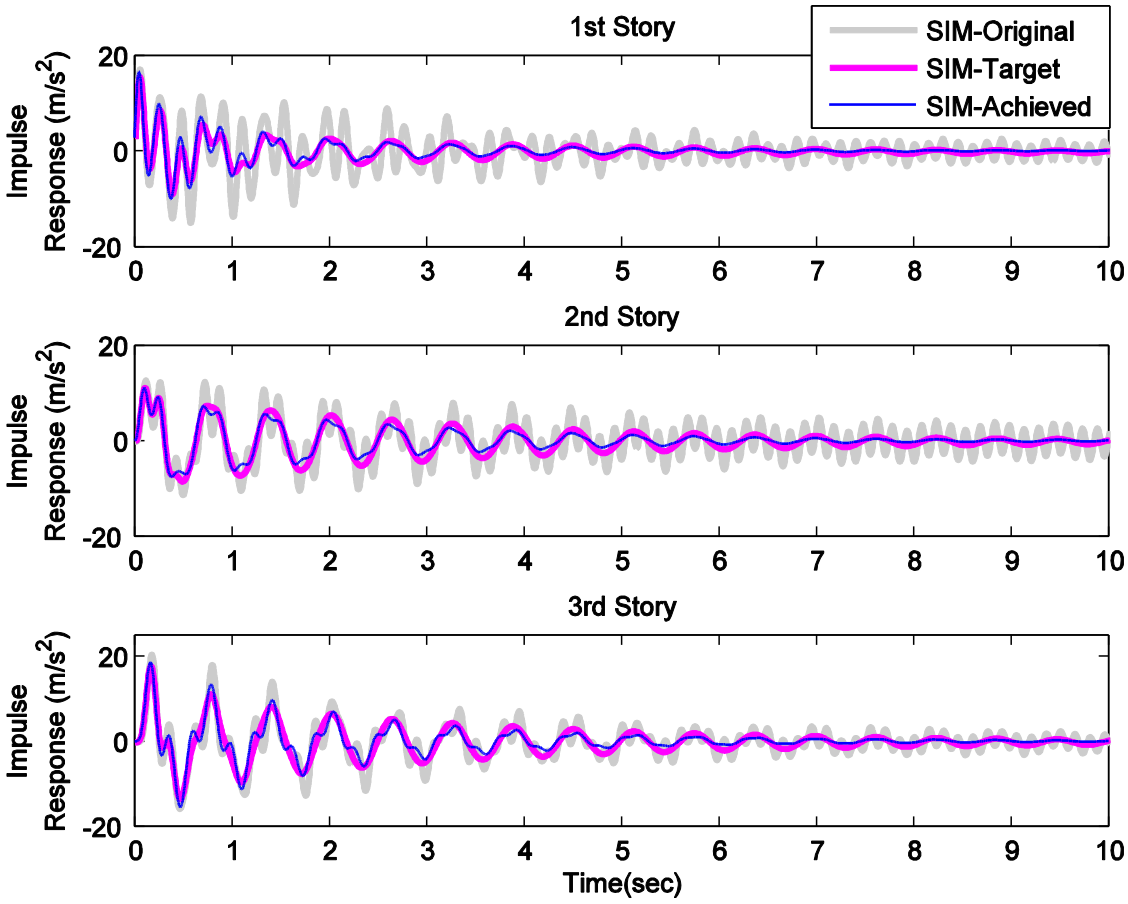

Figure 4.23 Impulse response of the total structure in RTHS

4.6 Summary

This chapter proposes the novel technique of introducing artificial damping to the experimental specimen in traditional shake table testing and RTHS. The artificial damping can be introduced either in all modes or to specific higher modes. A model-based shake table control strategy is used for acceleration tracking. Instead of tracking the input acceleration, the FF controller is designed to generate the acceleration subjected to which the specimen would behave as the target structure with larger damping. The modified FF is developed based on the poles and zeros tuned from the original specimen and the target structure with output weightings on average modal acceleration.

The performance of the proposed techniques is investigated in both traditional shake table testing and RTHS through a uni-axial shake table and a two-story shear building specimen with very low damping. In traditional shake table testing, extra damping was artificially added to all modes of the specimen through the proposed techniques, demonstrating the potential of the proposed techniques. The performance of the proposed techniques was also investigated in RTHS. The damping of the experimental specimen can be easily achieved based on the damping of the target structure by using the proposed techniques, greatly reducing labors and costs. Most importantly, the proposed techniques are powerful in assigning extra damping to specific modes of the structure. This benefit is a significant contribution of the proposed techniques in increasing RTHS stability by stabilizing higher modes with extra damping without changing the dominant modal responses.

CHAPTER 5 PERFORMANCE EVALUATION OF HIGH-RISE BUILDINGS WITH INTER-STORY ISOLATION THROUGH SUBSTRUCTURE RTHS

This chapter presents the structural performance evaluation of a 14-story high-rise building with inter-story isolation by using the substructure RTHS framework proposed in Chapter 3. Through this application of the work in Chapter 3, the performance of the proposed RTHS technique is further demonstrated. Inter-story isolation is well-suited for evaluation through shake table RTHS and enables new development and validation for this unique structural system.

5.1 Inter-Story Isolation

While traditional base isolation remains one of the most widely employed systems for mitigating seismic response, inter-story isolation has recently gained popularity, especially in densely populated areas, due to architectural concerns, performance benefits, and construction feasibility. In inter-story isolation, the isolation system is incorporated between stories instead of at the base of the structure. Moving the isolation system to upper floors reduces the need for a seismic gap or moat wall at the base, which is desirable for aesthetic and economic reasons and for preventing any possibility of accidental collisions with an outer stop or moat wall. Researchers have shown that outer wall collision is an ineffective safeguard against unexpected exceedance of the design deformation of the isolation systems (Hall et al., 1995; Ryan and Hall, 1998).

In addition, installing base isolation is straightforward for new buildings, but complicated and costly for retrofit applications, requiring excavation and temporary supports. Installing an isolation system at the roof level is relatively simple and

frequently inexpensive and disruption free (if the existing foundations are vertically sufficiently strong). By using inter-story isolation, accelerations of the added floors are reduced, allowing additional floors to be constructed on an existing structure without increasing the base shear demand. Obviously, the vertical capacity of the existing structural system including the foundation must be able to support the additional stories, otherwise retrofit of the existing structural system is required, negatively impacting the cost-benefit of this retrofit approach.

An example application is the 185 Berry St. building located in San Francisco (Dutta et al., 2008), which was built in 1989 as a 3-story concrete moment frame, and had been retrofitted with two extra floors on top of an isolation system. Another example of early practical retrofit application, appearing in China, is a four-story office building built in the 1950's, which was retrofit with four extra floors through inter-story isolation (Zhou, 2001). Additional practical applications of inter-story isolation appeared in high-rise buildings in Japan, including the Iidabashi First Building (IFB) (Murakami et al., 1999), the Shidome Sumitomo Building (SSB) (Sueoka et al., 2004; Tasaka et al., 2008), and the Umeda DT Tower (Yamane et al., 2003).

Because inter-story isolation nominally separates the building system into two independent structural parts, the upper and lower structures can be designed with different form and function. For example, the IFB is a 14-story multi-functional building with inter-story isolation located at the 9^{th} floor, and the SSB is a 25-story complex building with inter-story isolation located at the 12^{th} floor. In both buildings, the upper and lower floors are designed for different purposes and with different structural forms. Another example of application to tall buildings, more recent than that previously

mentioned, is an 11-story building in Beijing, China. An isolation layer was installed at the top of 2nd floor, separating the substructure of 2-story platform covering a railway area and the superstructure of 9-story residence building (Zhou, 2004). Inter-story isolation has a large potential to improve the design flexibility in high-rise buildings, especially for multi-purpose buildings, to achieve unique architectural features, and in retrofit applications.

5.2 Structural Models

This section illustrates the structural models used in this study, including the target total structure, scaled structure, experimental substructure, and the numerical substructure. The target structure is a constructed inter-story isolated building, idealized as a 15-DOF model. A 10-DOF scaled structure is created to match the dynamic properties (i.e., natural frequencies and mode shapes) as the target structure, with mass and stiffness scaled down to match the experimental specimen. The 6 stories above the isolation layer are modeled as a SDOF system to match the nominally SDOF experimental specimen, resulting in a 10-DOF structure. The scaled structure is partitioned into an experimental substructure containing the upper DOF and isolation layer and a numerical substructure containing the remaining 9-DOF.

5.2.1 Target structure

The target structure investigated in this study is the Iidabashi First Building (IFB) located in Tokyo, taken as a realistic representation of high-rise buildings with inter-story isolation. The IFB is a 14-story high-rise building with a inter-story seismic isolation on the 9th floor. The building was designed to blend well with the surroundings and to

provide better housing and commercial facilities in the central urban area. Figure 5.1 shows the structural system and its simplified shear model. In the IFB, offices are located on the 2nd to 9th floor with large column-free spaces up to about 5,000 m^2, while apartments are located on the 10th to 14th floor. A roof garden is located on the 10th floor, enabled by the change in floor plan. The lower structure is a combination of shear wall and moment-resisting frame of steel framed reinforced concrete while the upper structure is a shear wall system of reinforced concrete. On the isolation level, both seismic isolations and dampers are installed. The parameters of the structural model (with isolation and without dampers) are provided in Table 5.1, adopted from (Murakami et al., 1999).

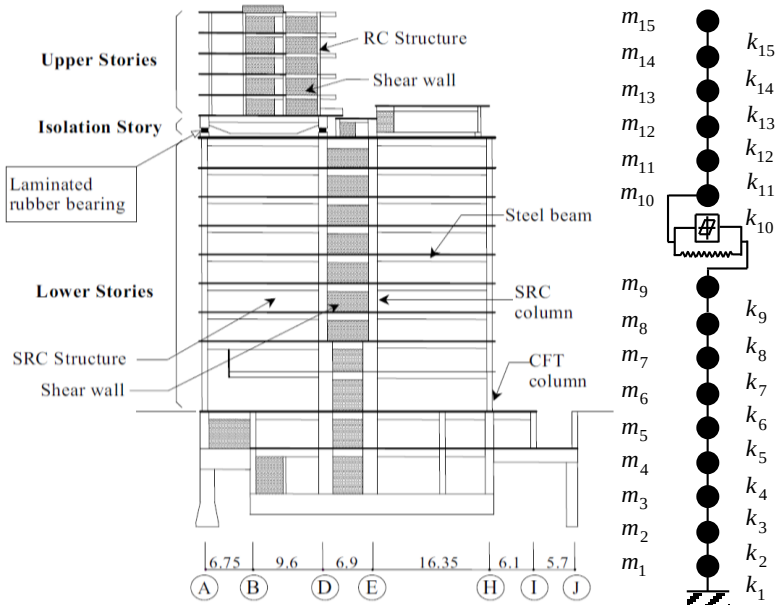

Figure 5.1 Structural system of the IFB (Murakami et al., 1999)

5.2.2 Experimental substructure

Due to the isolation layer on the 9th floor of the IFB, the upper stories will nominally respond in their first mode. By replacing the upper stories with a SDOF model, a simpler

physical specimen can represent their dynamics, instead placing emphasis on the isolation layer performance including supplemental damping devices. In this study, the upper stories including inter-story isolation are represented by a base-isolated specimen. Figure 5.2 shows the base isolated single-story specimen with a length of 2.5 m and a height of 2 m. With the braces, the frame behaves as a rigid body. The total mass of the specimen is 5 metric tons.

Table 5.1 Parameters of the simplified structural model of the IFB

Floor/Story	**Floor Mass ($kg \times 10^3$)**	**Story Stiffness ($kN/m \times 10^5$)**
1	5,435	123.0
2	5,533	128.1
3	5,209	109.6
4	5,189	98.21
5	5,180	91.24
6	5,091	85.48
7	4,915	79.61
8	4,915	74.60
9	12,704	71.67
10	4,022	0.530
11	2,315	344.3
12	2,315	228.8
13	2,305	201.1
14	2,305	165.9
15	1,658	94.31

The specimen is mounted on two linear guide rails with very low friction coupled with four steel coil springs at the base. The stiffness of the isolation system was identified as 12.3 kN/m. The natural frequency of the base-isolated specimen with braces locked is 0.25 Hz, which is similar to the natural frequency of 0.3 Hz for the upper stories of IFB with isolation. In addition, the friction force in the isolation system was identified through free vibration tests as 0.062 kN, estimated to provide an equivalent linear damping ratio of 2.4%. To achieve a level of damping comparable with the IFB isolation

system, a long-stroke magnetorheological damper (MR damper) was installed in the isolation layer of the specimen.

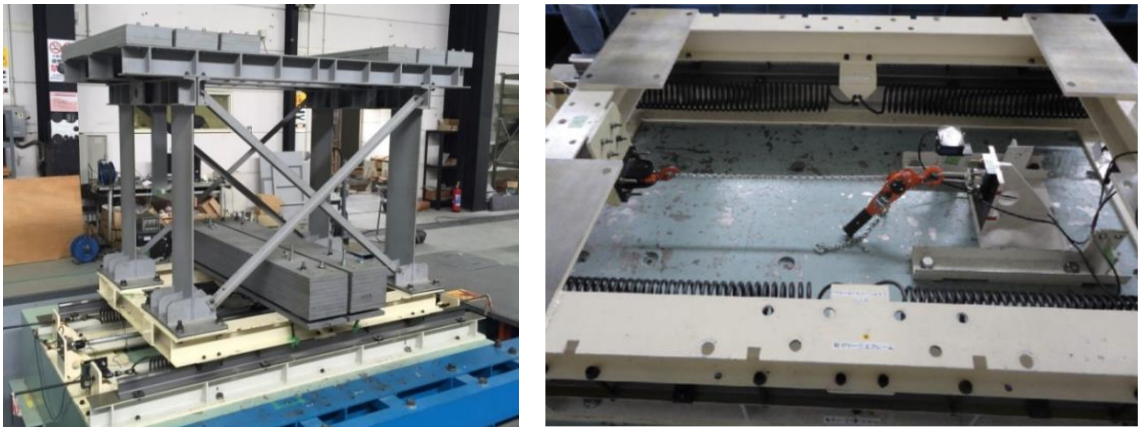

Figure 5.2 Single-story specimen (left) mounted on isolator (right)

5.2.3 Scaled structure and numerical substructure

The 10-DOF scaled structure is created by scaling the target structure down to be compatible with the experimental substructure and assuming SDOF behavior above the isolation layer. The total mass of the upper stories of the target structure is 14,920 metric tons, almost 3000 times larger than the specimen. The mass of floors 1 through 9 are taken as 1/3000 of the mass of floors 1 through 9 of the target structure. The mass of floor 10 is taken as 1/3000 of the total mass of the 6 upper floors of the target structure, equal to that of the test specimen.

The stiffness of the 10^{th} story of the scaled structure is scaled down such that the natural frequency of the upper stories matches that of the test specimen, 0.25 Hz. The stiffness of the remaining stories of the scaled structure are uniformly scaled down to achieve similar natural frequencies and mode shapes as the target structure. Mass and stiffness values are reported in Table 5.2. The natural frequencies of the total structure are 0.24 Hz, 0.83 Hz, 2.32 Hz, 3.88 Hz, 5.49 Hz, which compare well to the target structure

of 0.29 Hz, 1.04 Hz, 2.93 Hz, 4.89 Hz, and 6.89 Hz. Figure 5.3 shows the first three mode shapes of the target structure and the total structure normalized with respect to the mass matrix (i.e., modal participation vector), respectively calculated by the parameters in Table 5.1 and Table 5.2. It can be observed that the equivalent numerical substructure and experimental specimen can well represent the dynamics of the simplified model of IFB.

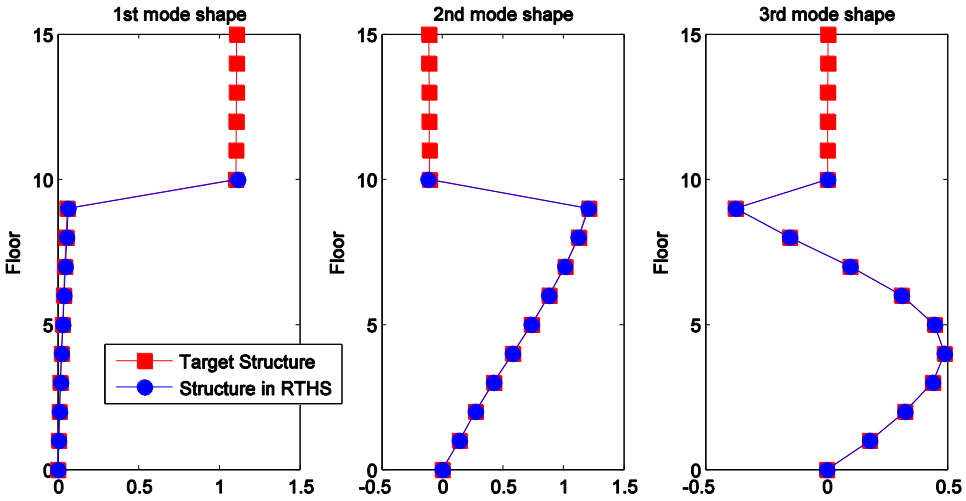

Figure 5.3 First three mode shapes of the target structure and scaled structure

Table 5.2 Parameters of the prototype structure

Floor/Story	Floor Mass (kg)	Story Stiffness (kN/m)	Story Damping (kN·s/m)
1	1,847	2,642	20.0
2	1,880	2,752	20.0
3	1,770	2,354	20.0
4	1,763	2,109	20.0
5	1,760	1,959	20.0
6	1,730	1,836	20.0
7	1,670	1,710	20.0
8	1,670	1,602	20.0
9	4,317	1,539	20.0
10	5,000	12.30	0.376

The damping coefficient of the prototype structure's 10th story is chosen as 0.376 kN·s/m to match the 2.4% damping of the test specimen without supplemental damping. For the lower stories, a damping coefficient is selected as 20.0 kN·s/m for each floor. This achieves 2.41% damping in the first mode of the lower stories. The damping ratios of the total structure are thus 2.23%, 2.80%, 7.74%, 12.9%, and 18.1% in the first five modes.

5.2.4 Supplemental damping

The target structure contains supplemental dampers in the isolation layer, which are not yet considered in the above models. To replicate the supplemental dampers, a physical MR damper is added to the isolation layer of the test specimen. Figure 5.4 shows the schematics of the long-stroke MR damper. The length of the damper in neutral position is 2,305 mm and the stroke is ± 400 mm.

Based on sine wave tests of the MR damper, the MR damper combined with the inherent friction damping produces approximately 7% and 28% damping for the passive-off state (0V) and passive-on state (30V), respectively.

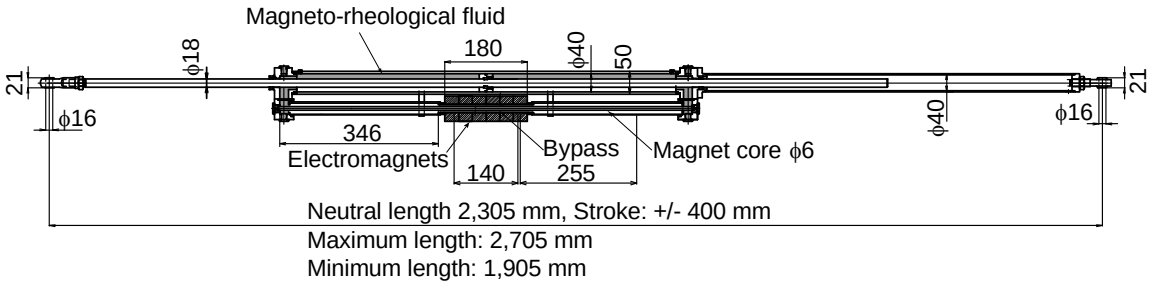

Figure 5.4 Schematic diagram of the MR damper

The MR damper is also incorporated into the isolation layer of the scaled specimen. A phenomenological model, based on a Bouc-Wen hysteretic model, is used to model the MR damper behavior (Spencer et al., 1997). The parameters of the model are fit to sine wave tests of varying amplitude and frequency, as well as for two different levels of current: passive-off (0V) and passive-on (30V). Figure 5.5 illustrates the underlying mechanics of the model. The model returns a restoring force F based on a given input displacement x and velocity $\dot{x}$. The restoring force can be described by equating the forces on either side of the right-hand-side rigid bar in Figure 5.5.

$$F = \alpha z + c_0\left(\dot{x} - \dot{y}\right) + k_{xy}\left(x - y\right) + k_x x \tag{5.1}$$

The model includes an evolutionary variable z modeled by a Bouc-Wen hysteretic element (Wen, 1976).

$$\dot{z} = -\gamma\left|\dot{x} - \dot{y}\right|z\left|z\right|^{n-1} - \beta\left(\dot{x} - \dot{y}\right)\left|z\right|^{n} + A\left(\dot{x} - \dot{y}\right) \tag{5.2}$$

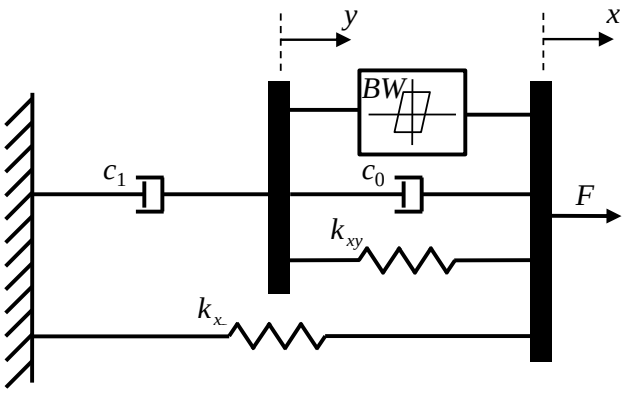

Figure 5.5 Phenomenological model of the MR damper

Three parameters, shown in Eq. 5.3 to Eq. 5.5, are given a linear relationship with input voltage v_c to model current-dependent behavior. The model parameters are provided in Table 5.3.

$$\alpha = \alpha_{\mathrm{a}} + \alpha_{\mathrm{b}} v_{\mathrm{c}} \tag{5.3}$$

$$c_0 = c_{0,\mathrm{a}} + c_{0,\mathrm{b}} v_{\mathrm{c}} \tag{5.4}$$

$$c_1 = c_{1,\mathrm{a}} + c_{1,\mathrm{b}} v_{\mathrm{c}} \tag{5.5}$$

Table 5.3 Parameters of the MR damper model

Parameter	Value	Parameter	Value
$c_{0,\mathrm{a}}$	4.000 N·s/cm	α_{a}	2.000 N/cm
$c_{0,\mathrm{b}}$	0.0017 N·s/cm/V	α_{b}	0.1134 N/cm
k_{xy}	1.469 N/cm	γ	0.0363 cm^{-2}
$c_{1,\mathrm{a}}$	12.00 N·s/cm	β	0. 0363 cm^{-2}
$c_{1,\mathrm{b}}$	2.6295 N·s/cm/V	A	301.0
k_x	0.05 N/cm	n	2.000
x_0	0 cm	η	190.0 s^{-1}

5.3 RTHS Using a Shake Table for Substructuring

To illustrate the framework for shake table RTHS applied to high-rise buildings with an inter-story isolation, the 15-DOF target structure is considered for substructuring as shown in Figure 5.6(a). Note that the framework is applied to the 10-DOF scaled structure in this research, however allowing for multiple DOF in the experimental substructure results in a more general presentation in this section. Parameters m_i, c_i, and k_i are the mass, damping, and stiffness of the *i*-th story, x_i is displacement relative to the ground of the *i*-th story, $\ddot{x}_g$ is the ground acceleration, and dots represent differentiation with respect to time. For substructure RTHS, the structure is separated into numerical and experimental substructures as shown Figure 5.6(b). The numerical substructure is selected as the lower 9 stories (below inter-story isolation), while the upper 6 stories including the isolation layer are tested experimentally. Structural

parameters as well as DOF associated with the experimental substructure are indicated by the superscript "E". Structural parameters as well as DOF associated with the numerical substructure are indicated by the superscript "N". The DOF at the interface between components are indicated by the superscript "I".

Numerical integration is performed solely on the numerical substructure. This approach is consistent with the dynamic substructuring approach of Shing (2008). The numerical substructure is described by the following equations of motion:

$$\mathbf{M}^{\mathrm{N}}\ddot{\mathbf{X}}^{\mathrm{N}} + \mathbf{C}^{\mathrm{N}}\dot{\mathbf{X}}^{\mathrm{N}} + \mathbf{K}^{\mathrm{N}}\mathbf{X}^{\mathrm{N}} = -\mathbf{M}^{\mathrm{N}}\boldsymbol{\Gamma}_{\mathbf{1}}\ddot{x}_g + \boldsymbol{\Gamma}_{\mathbf{2}} f_9^{\mathrm{I}} \tag{5.6}$$

Where $\mathbf{M}^{\mathrm{N}}$, $\mathbf{C}^{\mathrm{N}}$, and $\mathbf{K}^{\mathrm{N}}$ are the mass, damping, and stiffness matrix of the numerical substructure; $\boldsymbol{\Gamma}_1$ and $\boldsymbol{\Gamma}_2$ are the force distribution vectors; and f_9^{I} is the shear force measured from the experimental substructure and returned to the numerical substructure. With a lumped-mass assumption, the base shear is from the inertial forces of the experimental substructure.

$$f_9^{\mathrm{I}} = -\sum_{i=10}^{15} m_i^{\mathrm{E}} \ddot{\hat{x}}_{i,\mathrm{abs}}^{\mathrm{E}} \tag{5.7}$$

where $\hat{x}_i^{\mathrm{E}} = x_i^{\mathrm{E}} - x_9^{\mathrm{I}}$ is the displacement of *i*-th story of the experimental substructure relative to the interface DOF, meaning $\ddot{\hat{x}}_{i,\mathrm{abs}}^{\mathrm{E}} = \ddot{\hat{x}}_i^{\mathrm{E}} + \ddot{x}_{9,\mathrm{abs}}^{\mathrm{I}}$ and $\ddot{x}_{9,\mathrm{abs}}^{\mathrm{I}} = \ddot{x}_9^{\mathrm{I}} + \ddot{x}_g$.

For shake table testing, the experimental substructure follows the equations of motion below, excited by the absolute acceleration of the interface DOF:

$$\mathbf{M}^{\mathrm{E}}\ddot{\hat{\mathbf{X}}}^{\mathrm{E}} + \mathbf{C}^{\mathrm{E}}\dot{\hat{\mathbf{X}}}^{\mathrm{E}} + \mathbf{K}^{\mathrm{E}}\hat{\mathbf{X}}^{\mathrm{E}} = -\mathbf{M}^{\mathrm{E}}\boldsymbol{\Gamma}_3\ddot{x}_{9,\mathrm{abs}}^{\mathrm{I}} \tag{5.8}$$

where $\boldsymbol{\Gamma}_3$ is the force distribution (influence coefficient) vector for the experimental substructure.

The numerical and experimental substructures are illustrated in Figure 5.6(c). The block diagram of RTHS with shake table control can be found in Figure 3.2. In summary, the numerical substructure is excited by ground acceleration and the numerical and interface DOF values are determined through numerical integration. The absolute acceleration of the interface DOF is taken as the desired acceleration for the shake table. This acceleration is not known prior to testing, requiring a special class of shake table control strategies that can track accelerations determined online. The base shear of the experimental substructure is returned to the numerical substructure as the contribution from upper stories. This loop of action and reaction is carried out in real time until the entire time history response has been evaluated.

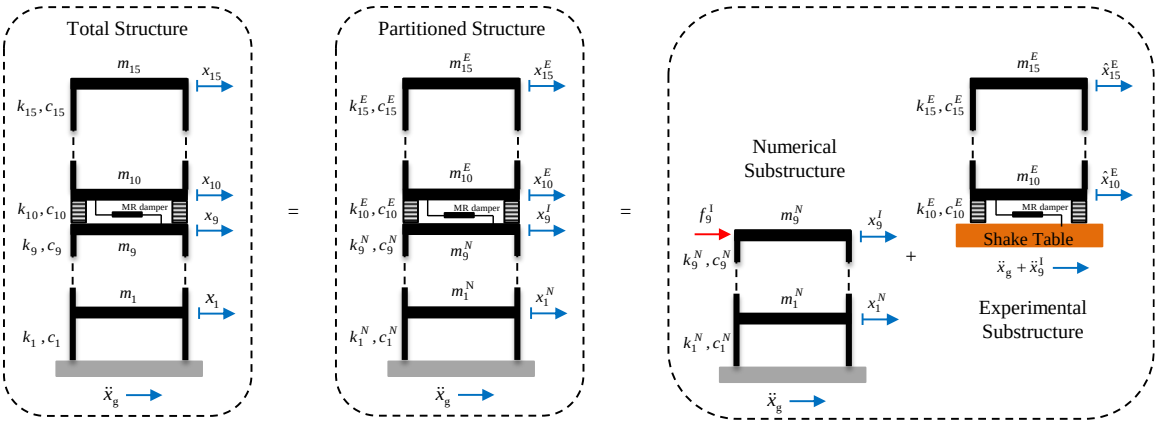

Figure 5.6 RTHS configuration using a shake table for IFB model with inter-story isolation

5.3.1 Earthquake ground motions

Four well-studied earthquake ground motion records with different magnitudes and frequency content are selected as the input to the structure (Ohtori et al., 2004): (1) El Centro: The N-S component recorded at the Imperial Valley Irrigation District substation

in El Centro, California, during the Imperial Valley, California earthquake of May 18, 1940, (2) Hachinohe: The N-S component recorded at Hachinohe Harbor during the Tokachi-oki earthquake of May 16, 1968, (3) Northridge: the N-S component of the Sylmar County Hospital parking lot in Sylmar, California during the Northridge earthquake of January 17, 1994, and (4) Kobe: the N-S component of the Japanese Meteorological Agency station during the Kobe earthquake of January 17, 1995. The reference earthquakes are passed through a 2-pole Butterworth high-pass filter with a cutoff frequency of 0.25 Hz. This pre-filtering removes the low-frequency behavior without altering the desired frequency content to avoid significant shake table drift. In RTHS, the desired acceleration (e.g., the absolute acceleration of the interface DOF) includes any drift from the ground motion record. The earthquake records are scaled down as shown in Figure 5.7 during RTHS due to the stroke limitation of the shake table.

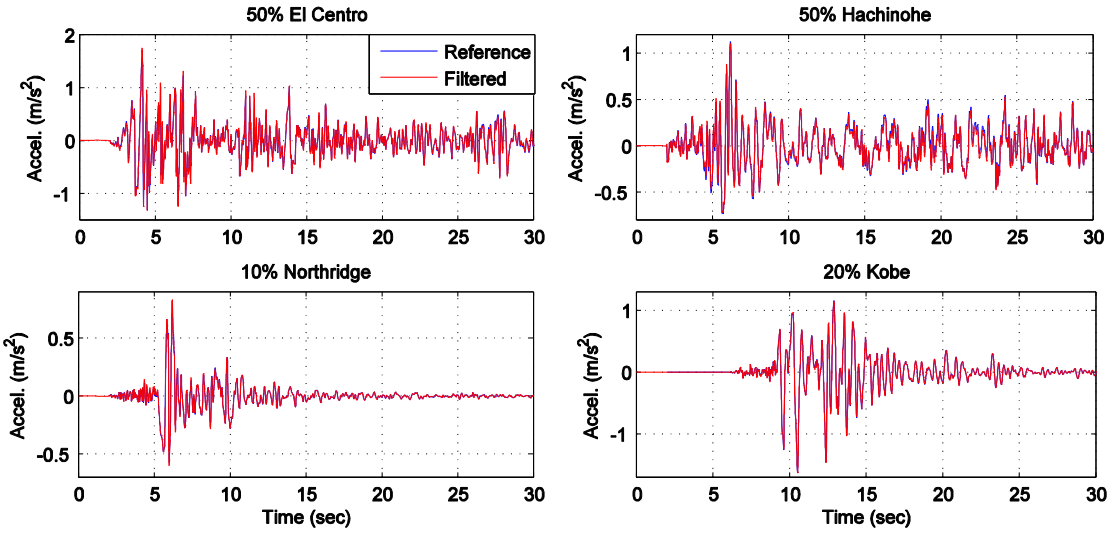

Figure 5.7 Historic ground motions

5.4 Favorable Stability of RTHS for Base-Isolated Specimens

One of the challenges for RTHS is that it requires a small, fixed sampling time in execution of each cycle. Moreover, unless properly compensated, time delays and time lags introduced by the experimental equipment are likely to lead to stability and accuracy problems. When negative damping exceeds the inherent structural damping of the system, the RTHS loop can become unstable.

Inter-story isolation, however, has a very low natural frequency (i.e., very low stiffness). Equivalent delays in the desired response at lower frequencies have a smaller impact of the stability of the RTHS. Furthermore, the base shear of base-isolated specimens is small compared to traditional structural systems. Thus, the relative influence of the experimental substructure to the numerical substructure on the total structural response is smaller, a favorable condition for RTHS stability. Also, there is in general a significant amount of structural damping in the isolation layer which can mask any issues with negative damping.

To illustrate this benefit using base-isolated specimen, a purely numerical simulation of substructure RTHS is investigated. Two total structures are considered, one with a base-isolated and one with a fixed-base upper substructure. The lower substructures are same and chosen as the first nine stories in Table 5.2 (i.e., the scaled structure). The base-isolated upper substructure is equal to that of the scaled structure without supplemental damping in the isolation layer. The fixed-based upper substructure has a stiffness adjusted to achieve 4.81 Hz, the same natural frequency of the upper stories of the target structure without inter-story isolation. The damping of both upper substructures is taken as 2.4% to avoid favorable bias toward a more highly damped

system. Both total structures are subject to the 50% El Centro record with varying levels of simulated delay in the RTHS loop.

Table 5.4 summarizes the time delay tolerance on maximum and RMS base shear of the experimental substructure with and without isolation. The base shears are much lower in magnitude for the experimental substructure with isolation, resulting in much larger time delay tolerance. Figure 5.8 shows the time histories of the base shear for the two cases with different level of time delay. From Figure 5.8, the structure without inter-story isolation only has 5 ms delay tolerance and becomes unstable when T_d reaches 10 ms. By using inter-story isolation, the structure has a larger tolerance on time delay up to 50 ms without compromising the accuracy significantly. The system remains stable even as the time delay approaches ten times larger than the tolerance of the structure without isolation, though accuracy is compromised. This simple numerical study clearly demonstrates favorable behavior of base-isolated specimens in RTHS.

Table 5.4 Base shear of the experimental substructure

Time delay (ms)	Structure with inter-story isolation		Structure without inter-story isolation	
	Max (kN)	RMS (kN)	Max (kN)	RMS (kN)
0	1.5184	0.4490	8.1215	2.3386
5	1.5245	0.4527	7.8268	2.1715
10	1.5304	0.4565	3.05×10^{27}	1.86×10^{26}
15	1.5363	0.4605	Unstable	
50	1.5778	0.4955		
100	1.6337	0.5742		
150	1.8446	0.7103		

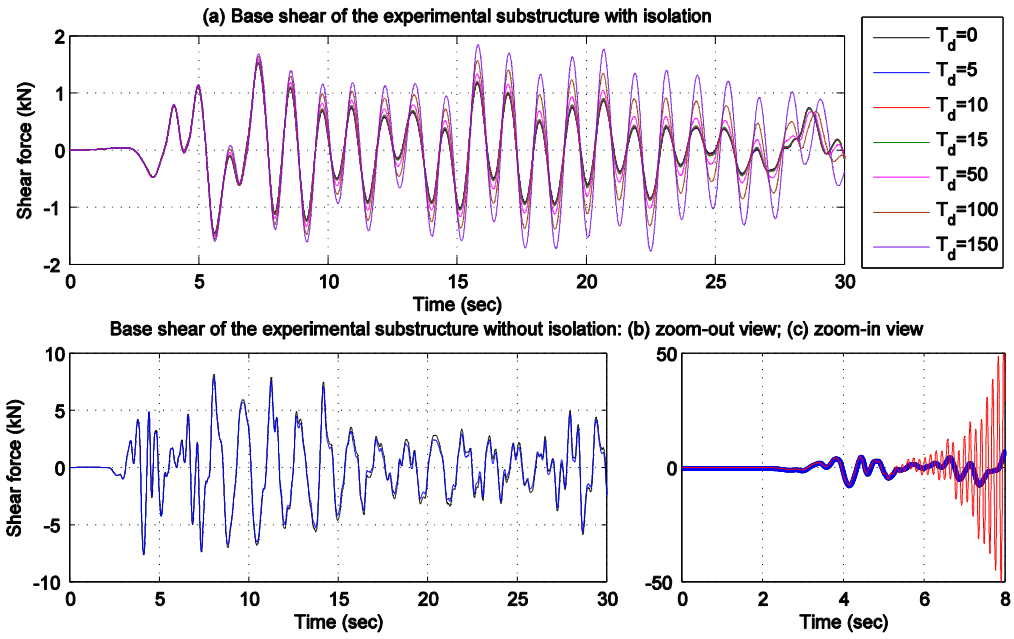

Figure 5.8 Influence of time delay on time histories of base shear of experimental substructure with or without seismic isolation

5.5 Experimental Setup

The proposed RTHS procedure is developed and verified using a large-scale bi-directional shake table. The setup consists of a large-scale shake table, a base-isolated single-story specimen as the experimental substructure, and a control and data acquisition system. The dynamic properties of both the experimental substructure and the total structure were presented in the second section. The specimen and equipment are located at Tohoku University.

5.5.1 Large-scale bi-directional shake table and sensors

The shake table used in this study is in large scale with a size of 3 m by 3 m, driven by two actuators in X-direction and one actuator in Y-direction. The stroke is ± 50 mm in X-direction and ± 150 mm in Y-direction. In addition to the two translational DOF, the

shake table has one extra rotational DOF in the horizontal plane with a maximum angle of $\pm 2^{\circ}$. The shake table has a maximum payload of 10 metric tons. The shake table is depicted in Figure 5.2. The control hardware for the RTHS consists of a dSPACE DS1103 Controller Board described in Chapter 3.

5.5.2 Shake table identification

The shake table model was determined using a 0-5 Hz band-limited white noise voltage command to the shake table and measured table acceleration. Figure 5.9 shows the experimentally measured transfer function of the shake table along with the identified model.

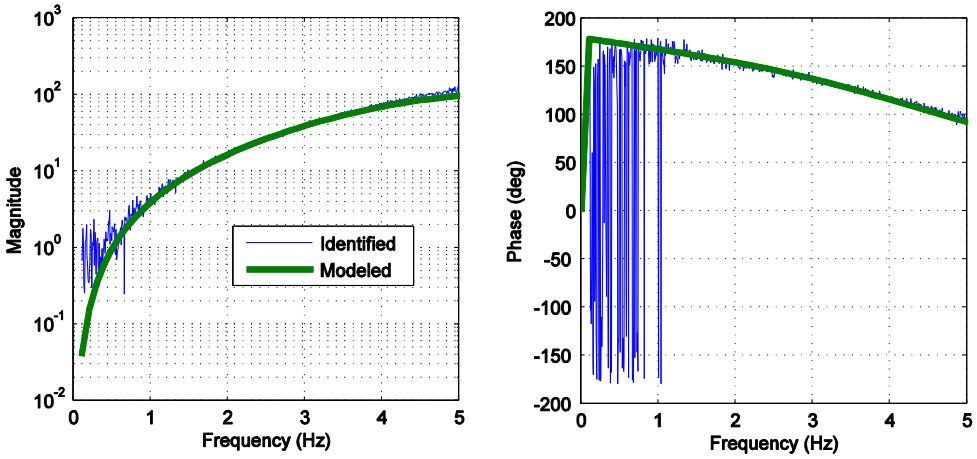

Figure 5.9 Transfer function of shake table with experimental specimen

The output acceleration approaches zero at zero frequency since the command to the shake table is approximately proportional to the displacement. During identification, the base-isolated single-story experimental specimen is mounted on the shake table to include the effects of control-structure interaction (CSI). The CSI in this study is observed to be very small as no specimen dynamics are immediately apparent in the measured transfer function. Although the specimen weighs 5 metric tons compared to the maximum payload of 10 metric tons, the base-isolation layer provides a very small

restoring force and thus small interaction between specimen and table. A good model is identified using 2 poles and 2 zeros, shown in Eq. 5.9.

$$G_{au}(s) = \frac{103.4515\,s^2}{s^2 + 33.12s + 1036} \tag{5.9}$$

5.5.3 Controller development

The feedforward controller (FF), designed to compensate for the linear dynamics of the shake table, is created as an inverse of the identified shake table model. In this study, the FF controller alone is found to be effective and sufficient to regulate the shake table performance because the shake table is accurately described by the identified linear model and also the base-isolated structure leads to very small CSI.

In RTHS, high frequency measurement noise will enter into the RTHS loop. A feedforward controller with a large magnitude at high frequencies may turn the measurement noise into high-frequency commands to the table. To avoid spurious excitation, a 2nd order Butterworth low-pass filter with a cutoff frequency of 50 Hz is added in series with the inverse model. The filter is designed to reduce the influence of signal noise on table commands without altering the desired performance over the expected frequency range of structural response. The filtered FF controller is shown in Eq. 5.10 with 2 extra poles.

$$G_{FF\_filt} = \frac{954.0322\,(s^2 + 33.12s + 1036)}{s^2\,(s^2 + 444.3s + 98700)} \tag{5.10}$$

Feedforward control alone provided adequate acceleration tracking performance of the shake table due to low CSI between the base-isolated specimen and shake table and low friction of the shake table itself. Therefore, feedback control was not needed for this

study. Feedback control details as applied to the tracking of a pre-defined acceleration signal (though applicable herein) can be found in (Phillips et al., 2014).

5.5.4 Filtering of measured accelerations

In addition to reducing the sensitivity of the FF controller to high-frequency noise, an approach to avoid the introduction of noise into the system is employed. A Kalman filter based on a SDOF model for the specimen is added in line with the measured accelerations as shown in Figure 3.2 to prevent measurement noise from entering the numerical substructures. The process noise is assumed to enter the specimen the same way as the ground motion and system output weighting is used for measured accelerometer. For the SDOF specimen, these assumptions result in two tunable parameters for the Kalman filter, which are the unbiased process noise q and the measurement noise r. Parameters are selected as $q = 1\times10^5$ and $r = 1$, tuned offline using recorded data. An online reduction in measurement noise is demonstrated in Figure 5.10, showing the acceleration before and after filtering. In this test, the 10-DOF scaled structure was subject to 50% El Centro through RTHS with MR damper in passive-on mode. The filtered signal was used for feedback from the specimen. From the zoomed-in view, it is clear that the Kalman filter reduces the noise contained in the measured accelerations without altering the dominant structural response. Most importantly, the Kalman filter does not introduce any phase lag which would lead to stability problems in the RTHS loop.

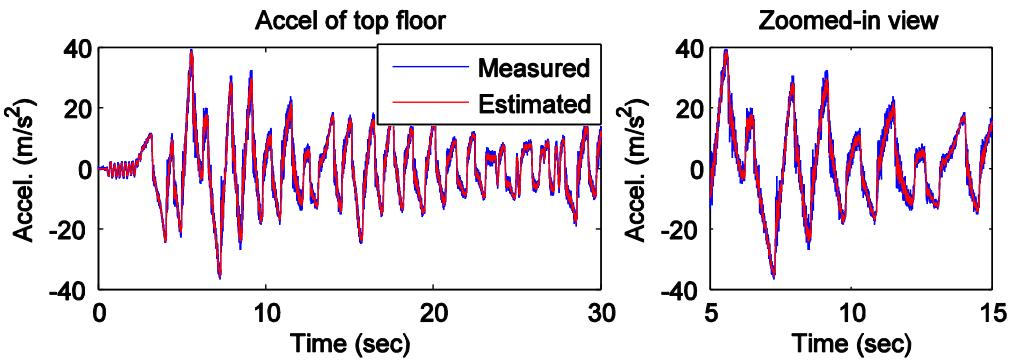

Figure 5.10 Effect of Kalman filter on acceleration measurements

5.6 Performance of RTHS and Inter-story Isolation

This section investigates the performance of the proposed RTHS technique focusing on the tracking of the desired acceleration signal at the interface DOF and achieving overall accurate RTHS performance when compared to numerical simulations. In addition, the benefits of inter-story isolation as a structural design alternative are demonstrated. First, acceleration tracking performance of feedforward control (FF) is presented for both predefined accelerations and accelerations determined online during RTHS. Second, RTHS results are compared to numerical simulations to verify the overall performance of the proposed RTHS techniques. Last, the overall responses of the structure with inter-story isolation are presented. The benefits of high-rise buildings with inter-story isolation are confirmed through RTHS. All time-domain measurements are passed through a low-pass filter with a cutoff frequency of 8 Hz in post processing. The results and conclusions are based on the inter-story isolated structure with passive-on MR damper unless otherwise explicitly stated. For traditional shake table tests, the structure is the physical base-isolated specimen. For the RTHS, the structure is the scaled structure substructured

into numerically simulated lower stories and experimentally evaluated upper stories represented by the base-isolated specimen.

5.6.1 Acceleration tracking performance

Acceleration tracking performance of the FF controller is presented for both predefined accelerations and accelerations determined online during RTHS. Figure 5.11 shows the acceleration tracking performance for the FF controller from traditional shake table testing with experimental specimen excited by 100% El Centro and Hachinohe records. Analysis in both time domain and frequency domain demonstrate excellent reproduction of the desired predefined ground motions. During RTHS, the shake table will instead track the absolute acceleration of the interface DOF (i.e., the 9^{th} floor). Figure 5.12 shows the online acceleration tracking performance on the interface DOF during RTHS when the total structure is subjected to 50% El Centro and Hachinohe earthquakes. Through the developed FF controller, excellent tracking performance is observed regardless of whether the desired acceleration is determined online or offline. In addition, from the power spectral density (PSD) of the interface DOF acceleration, higher energy is observed at the natural frequencies of the total structure (e.g., 0.24 Hz, 0.83 Hz, and 2.32 Hz for the first three modes), reflecting that the numerical and experimental substructures behave like the total structure. Better tracking above 5 Hz could be achieved by fitting an accurate model-based controller beyond 5 Hz (i.e., in Figure 5.8). Quantitative tracking results are summarized in Table 5.5 including the results of the total structure subjected to 10% Northridge and 20% Kobe during RTHS. Because the shake table is accurately described by a linear model and the CSI is very small, FF control alone provides adequate tracking and no additional controller improvements are necessary.

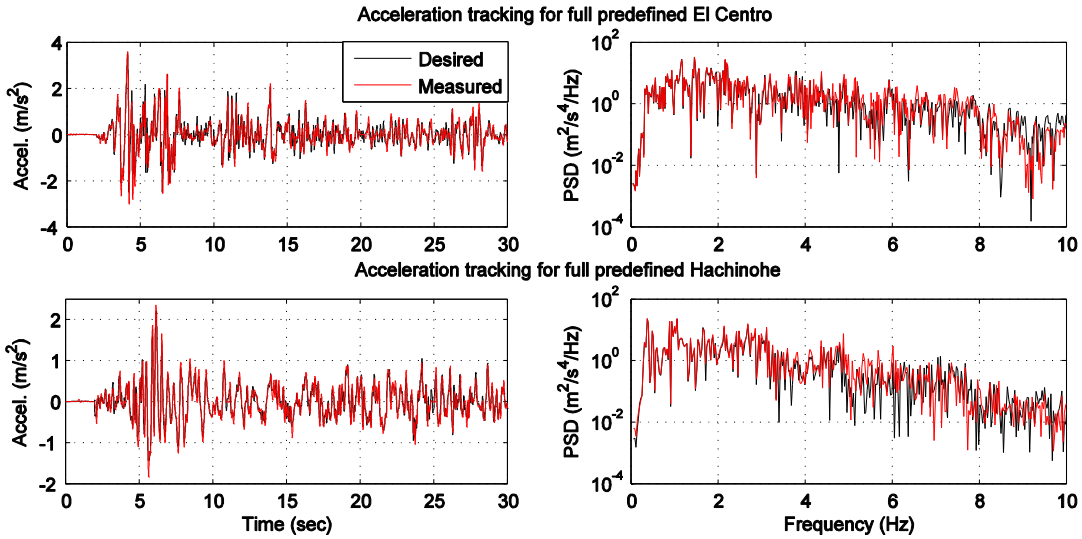

Figure 5.11 Acceleration tracking performance during traditional shake table testing

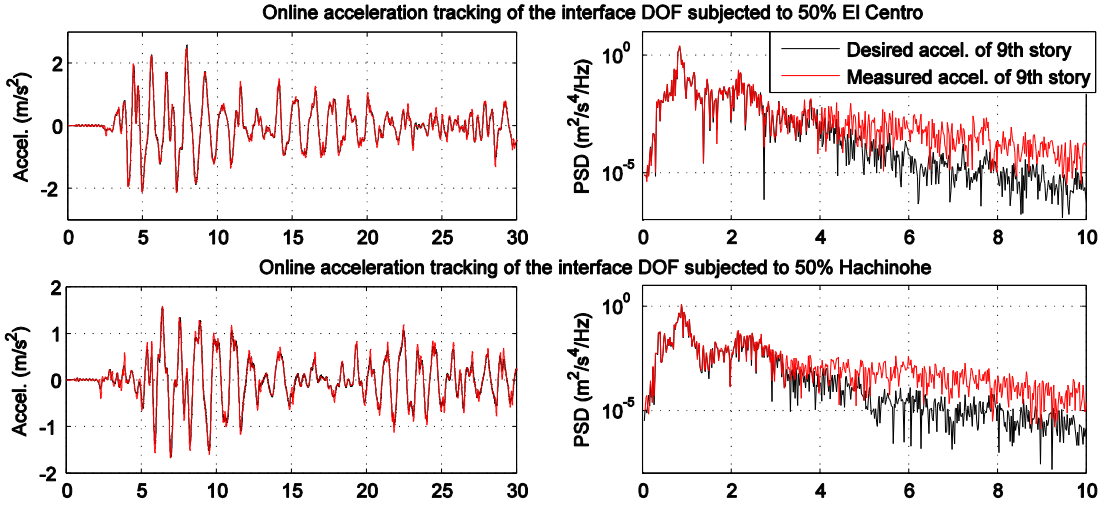

Figure 5.12 Online acceleration tracking performance during RTHS

Table 5.5 Predefined and online acceleration tracking performance

Acceleration tracking	Ground motion	(1) Time history analysis		(2) PSD analysis	
		Max tracking error (m/s^2)	RMS tracking error (m/s^2)	Max tracking error ($m^2/s^4/Hz$)	RMS tracking error ($m^2/s^4/Hz$)
Predefined acceleration	100% El Centro	0.0851	0.0151	1.9112	0.2275
	100% Hachinohe	0.1416	0.0229	0.4841	0.2344
Online acceleration in RTHS	50% El Centro	0.0885	0.0131	0.0976	0.0045
	50% Hachinohe	0.0151	0.0141	0.0505	0.0023
	10% Northridge	0.1774	0.0070	0.0012	0.0003
	20% Kobe	0.0190	0.0073	0.0196	0.0023

5.6.2 Performance of RTHS

In this section, the performance of the proposed RTHS techniques is presented for two inter-story isolated structures, one with the MR damper in passive-off mode and one in passive-on mode, achieving different levels of damping in the isolation layer. Both structures are subjected to 50% El Centro, 50% Hachinohe, 10% Northridge, and 20% Kobe records. In addition, numerical simulations of each RTHS are performed using the phenomenological MR damper model presented previously to represent MR damper nonliearities. The two cases for comparison are listed as below:

1. Numerical simulation of the 10-story structure with passive-off and passive-on MR damper (SIM); and
2. RTHS of the 10-story structure, substructured into a 9-DOF numerical substructure for the lower 9 stories and an experimental base-isolated single-story specimen with passive-off and passive-on MR damper (EXP-RTHS).

Table 5.6, 5.7, and 5.8 summarize the overall RTHS performance on absolute accelerations, interstory drifts, and the damping force of MR damper for the two inter-story isolated structures with passive-off and passive-on MR dampers subjected to four reference earthquake records. The maximum and RMS tracking errors of EXP-RTHS are calculated by comparing the respective results to the numerical simulation case SIM. From Table 5.6, 5.7, and 5.8, it is observed that both maximum and RMS tracking errors of EXP-RTHS are small which indicates excellent RTHS performance. Both passive-off and passive-on MR damper cases result in similar levels of RTHS accuracy. Because the system is very stable, added damping does not noticeably contribute to improved RTHS performance as compared to numerical simulation. The difference between the actual and modeled MR damper is the largest source of error, which helps to justify the need for RTHS. Another observation from Table 5.6, 5.7, and 5.8 is that the errors for the total structure subjected to 10% Northridge and 20% Kobe earthquake are larger compared to the structure subjected to 50% El Centro and 50% Hachinohe records. These records have regions of relatively low amplitude, leading to low amplitude commands to the shake table (see Figure 5.12). Friction in the shake table makes it difficult to accurately track these low-amplitude accelerations. Furthermore, when the isolation layer drift is small, both the MR damper and base-isolation slider can lock, causing larger accelerations than predicted from the numerical model and also spikes in acceleration when the specimen unlocks due to larger drift.

Figure 5.13 shows the time histories of the absolute accelerations for the inter-story isolated structure with passive-on MR damper subjected to 50% El Centro and 20% Kobe records. The RTHS techniques perform well not only on the peak responses but

also throughout the entire time history. The RTHS performance is also demonstrated by comparing interstory drifts, as shown in Figure 5.14, for the inter-story isolated structure with passive-on MR damper subjected to 50% El Centro and 20% Kobe records. Figure 5.15(a) shows the time histories of the passive-on MR damper forces for the total structure subjected to 50% El Centro and 20% Kobe earthquakes. It is clear that the numerical nonlinear MR damper model can generally represent the dynamic properties of the long-stroke MR damper used in RTHS tests. It can be further demonstrated by the hysteresis loop of the passive-on MR damper shown in Figure 5.15(b), for the total structure subjected to 50% El Centro and 20% Kobe earthquakes.

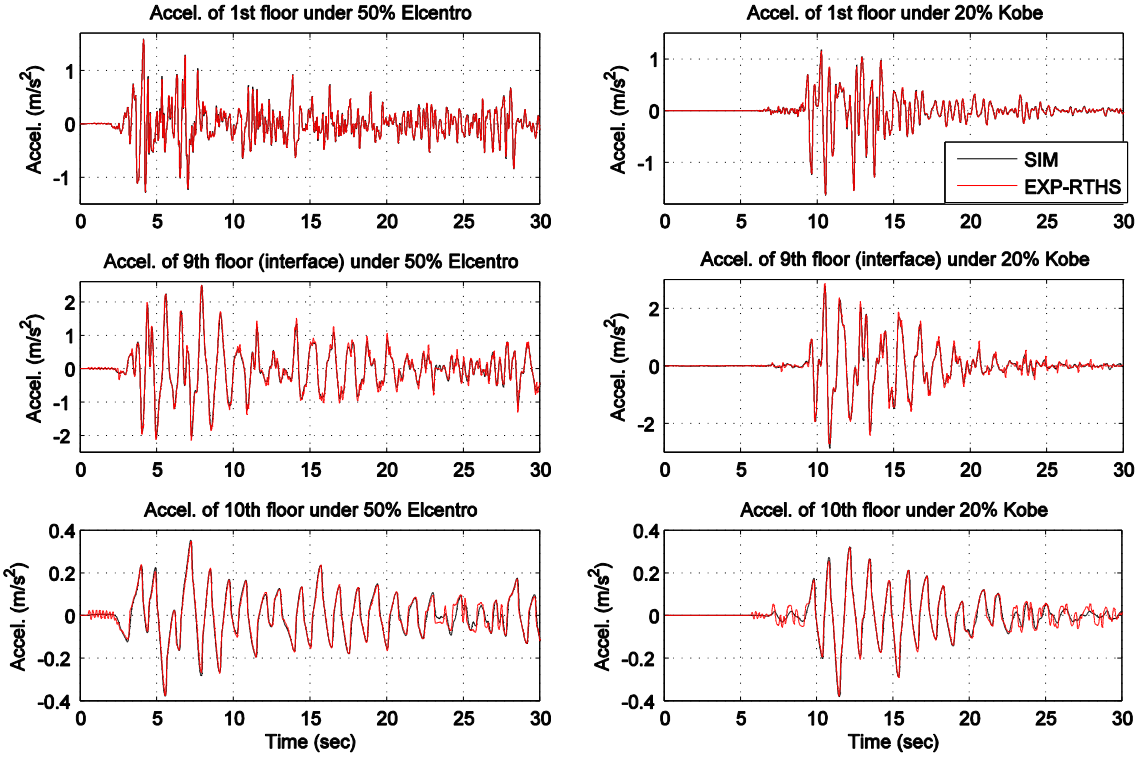

Figure 5.13 RTHS performance of absolute accelerations

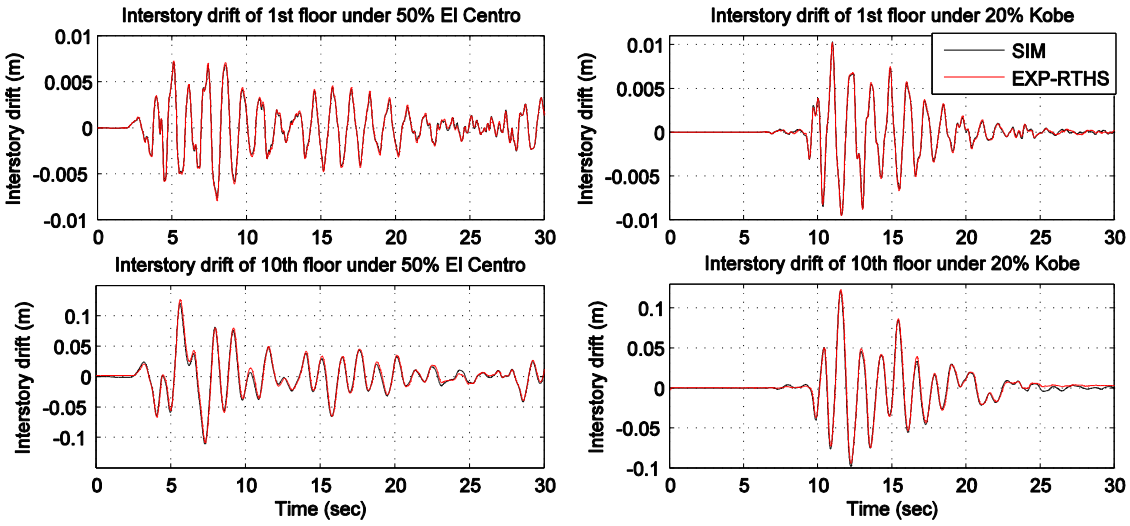

Figure 5.14 RTHS performance of interstory drifts

(a)

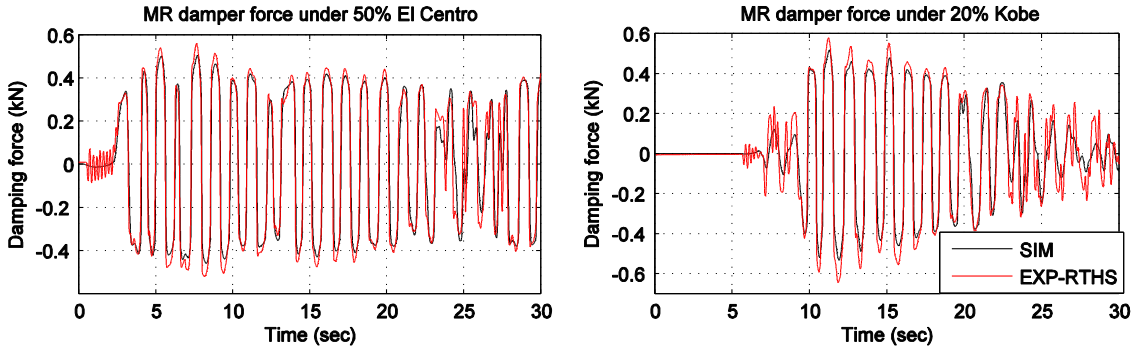

(b)

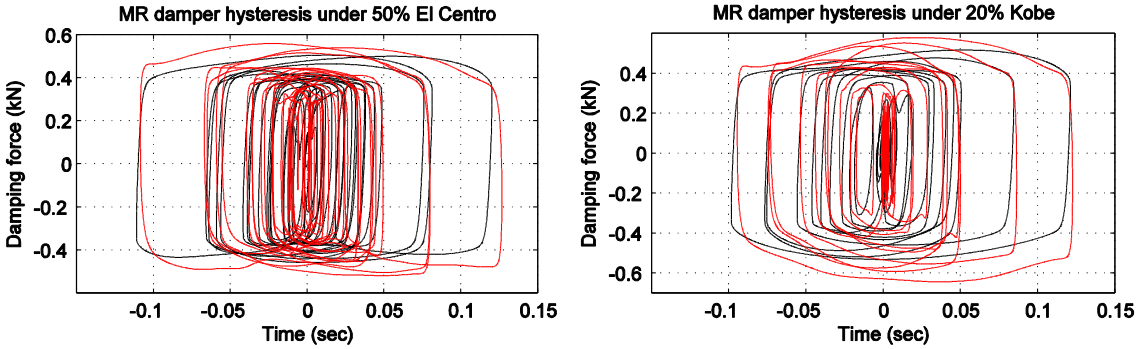

Figure 5.15 RTHS performance of (a) MR damper forces; (b) MR damper hysteresis

Table 5.6 RTHS performance of absolute accelerations

Earthquake excitation	Story	Structure with passive-on MR damper		Structure with passive-off MR damper	
		Max error (m/s^2)	RMS error (m/s^2)	Max error (m/s^2)	RMS error (m/s^2)
50% El Centro	1st	0.0135	0.0029	0.0127	0.0011
	9th	0.0131	0.0294	0.0286	0.0728
	10th	0.0018	0.0047	0.0083	0.0015
50% Hachinohe	1st	0.0168	0.0017	0.0125	0.0010
	9th	0.0108	0.0126	0.0817	0.0275
	10th	0.0058	0.0059	0.0051	0.0023
10% Northridge	1st	0.0149	0.0003	0.0136	0.0004
	9th	0.2087	0.0145	0.2157	0.0136
	10th	0.0020	0.0034	0.0313	0.0047
20% Kobe	1st	0.0151	0.0009	0.0150	0.0005
	9th	0.0275	0.0161	0.0356	0.0179
	10th	0.0027	0.0029	0.0001	0.0020

Table 5.7 RTHS performance of interstory drifts

Earthquake excitation	Story	Structure with passive-on MR damper		Structure with passive-off MR damper	
		Max error (mm)	RMS error (mm)	Max error (mm)	RMS error (mm)
50% El Centro	1st	0.30	0.08	0.52	0.27
	9th	0.16	0.05	0.35	0.14
	10th	6.50	0.64	9.50	3.30
50% Hachinohe	1st	0.06	0.01	0.32	0.06
	9th	0.08	0.004	0.02	0.04
	10th	2.00	0.58	6.50	2.10
10% Northridge	1st	0.01	0.03	0.05	0.02
	9th	0.07	0.03	0.12	0.02
	10th	0.66	0.34	7.10	0.99
20% Kobe	1st	0.07	0.03	0.10	0.04
	9th	0.03	0.02	0.12	0.02
	10th	1.50	0.04	2.60	0.21

Table 5.8 RTHS performance of MR damper forces

Earthquake excitation	Structure with passive-on MR damper		Structure with passive-off MR damper	
	Max error (kN)	RMS error (kN)	Max error (kN)	RMS error (kN)
50% El Centro	0.0532	0.0221	0.0112	0.0002
50% Hachinohe	0.0687	0.0139	0.0054	0.0073
10% Northridge	0.0843	0.0378	0.0692	0.0353
20% Kobe	0.1120	0.0342	0.0836	0.0350

5.6.3 Performance of inter-story isolation

This section investigates the structural responses of the total scaled structure with inter-story isolation through the proposed RTHS techniques. Figure 5.16 shows the absolute accelerations and interstory drifts of the total structure with passive-on MR damper subjected to 50% El Centro earthquake. The acceleration of the DOF above the isolation layer (i.e., the 10^{th} floor) is much lower in amplitude, while the interstory drift is much larger than lower stories, as expected. Table 5.9 summarizes the maximum accelerations and interstory drifts of the lower stories and the isolated top floor subjected to multiple earthquake excitations. Aside from providing isolation of the upper stories, the isolation layer allows the upper stories to behave similar to a mass damper, absorbing energy from the lower stories and thus reducing the response of the lower stories. This phenomenon can be more clearly seen when responses are compared to the structure without inter-story isolation, considered next as an unretrofitted versus retrofitted structure study.

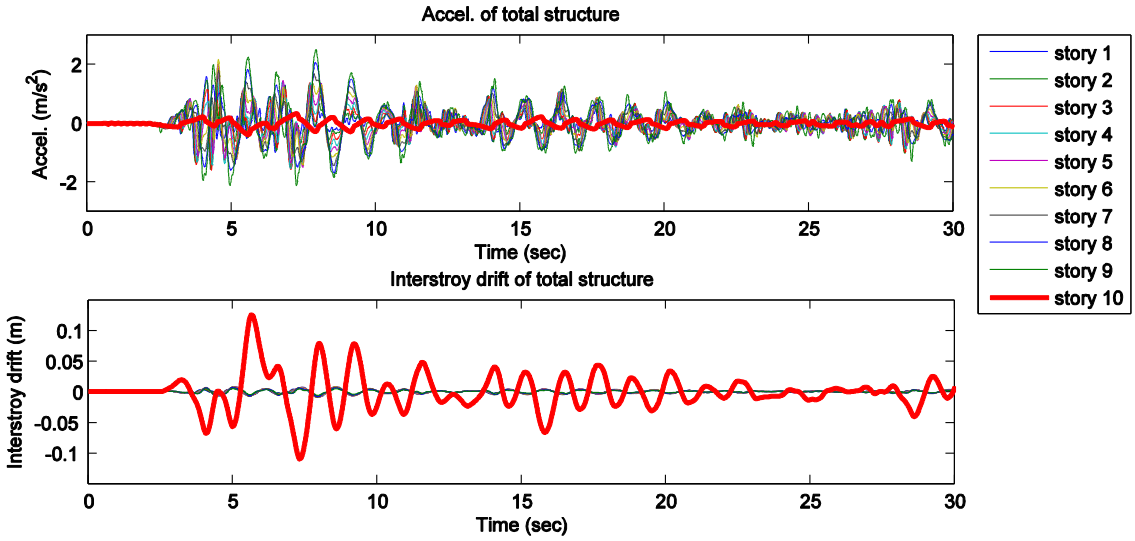

Figure 5.16 Absolute accelerations and interstory drifts of the total structure

Table 5.9 RTHS performance of structure with inter-story isolation

Earthquake excitation	Floor(s)	Structure with passive-on MR damper		Structure with passive-off MR damper	
		Max accel. (m/s^2)	Max interstory drift (m)	Max accel. (m/s^2)	Max interstory drift (m)
50% El Centro	1-9	2.4943	0.0063	2.7820	0.0109
	10	0.3759	0.1267	0.3251	0.1265
50% Hachinohe	1-9	1.6844	0.0067	1.9383	0.0083
	10	0.3469	0.1093	0.2955	0.1147
10% Northridge	1-9	1.7789	0.0059	1.7901	0.0061
	10	0.2507	0.0724	0.2260	0.0788
20% Kobe	1-9	2.8489	0.0103	3.0090	0.0110
	10	0.3777	0.1227	0.3593	0.1363

Another benefit of implementing inter-story isolation is for retrofit applications. By using inter-story isolation, the accelerations of the extra floors can be greatly reduced, allowing additional floors to be built on an existing structure without increasing the base shear demand. The benefits of high-rise buildings with inter-story isolation, assumed

herein as a retrofit technique, are further confirmed by comparing the base shear demands with a 9-story structure (i.e., unretrofitted) and a 10-story structure without inter-story isolation (i.e., retrofitted with a traditional structural system). The three structures are shown in Figure 5.17. Both the 9-story structure and the 10-story structure without inter-story isolation were analyzed in numerical simulation while the 10-story structure with inter-story isolation was analyzed in RTHS.

Figure 5.18 shows the base shear of the unretrofitted structure and both retrofitted structures (with and without inter-story isolation) subjected to 50% El Centro and 20% Kobe earthquakes. The base shear is reduced by the inter-story isolation not only on the peak responses but also throughout the entire time histories. Although similar performance observed for 10-story structure without inter-story isolation, the mechanism behind the base shear reduction is different. For the 10-story structure with inter-story isolation, a new and unique first mode is created at 0.24 Hz (see Figure 5.19). The upper stories act as a mass damper and absorb some seismic energy, protecting the lower stories. Note that the second mode (0.83 Hz) matches well with the first mode of the 9-story structure (0.81 Hz) in both shape and frequency. For the 10-story structure without inter-story isolation, the natural frequency is decreased from 0.81 Hz to 0.64 Hz by the addition of the 10^{th} floor. The entire structure, including the 10^{th} floor, behaves as one structure with a lower first natural frequency, protecting it from the frequency content of the input ground motions. Table 5.10 summarizes the maximum and RMS base shears of the unretrofitted structure and two retrofit structures subjected to multiple earthquake excitations. With passive-on MR damper, the base shears are in lower magnitude as expected due to improved energy dissipation in the isolation layer.

Figure 5.20 shows the interstory drift and absolute acceleration of the 9th floor of the three structures subjected to 50% El Centro and 20% Kobe earthquakes. The unretrofitted structure and retrofitted structures behave differently, indicating the importance of accurately capturing the interactions between lower and upper stories (e.g., through shake table RTHS). In the case of inter-story isolation, even with the low isolation layer shears, the interaction of the substructures cannot be ignored. This interaction leads to a difference in the response of the unretrofitted structure and structure retrofitted with inter-story isolation. The isolation layer enables the upper stories to behave similar to a mass damper, absorbing energy from the lower stories and thus noticeably reducing the response of the lower stories.

RTHS provides a cost-effective tool to investigate the structural responses of inter-story isolated structures with accurate experimental representation of the isolation layer. Through the proposed RTHS techniques, the responses of high-rise building with inter-story isolation are investigated, and the benefits of the inter-story isolation are evaluated.

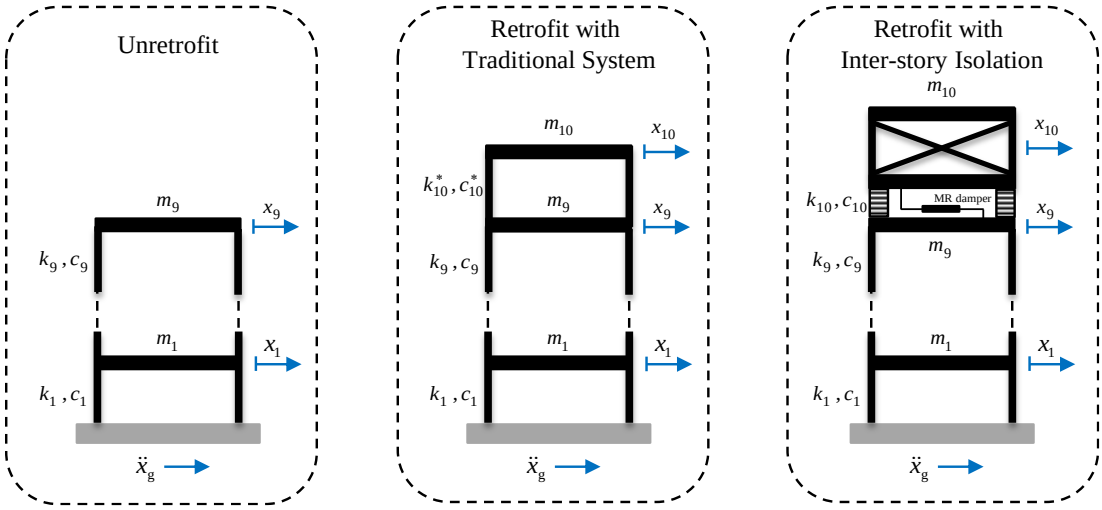

Figure 5.17 Structure systems for investigation

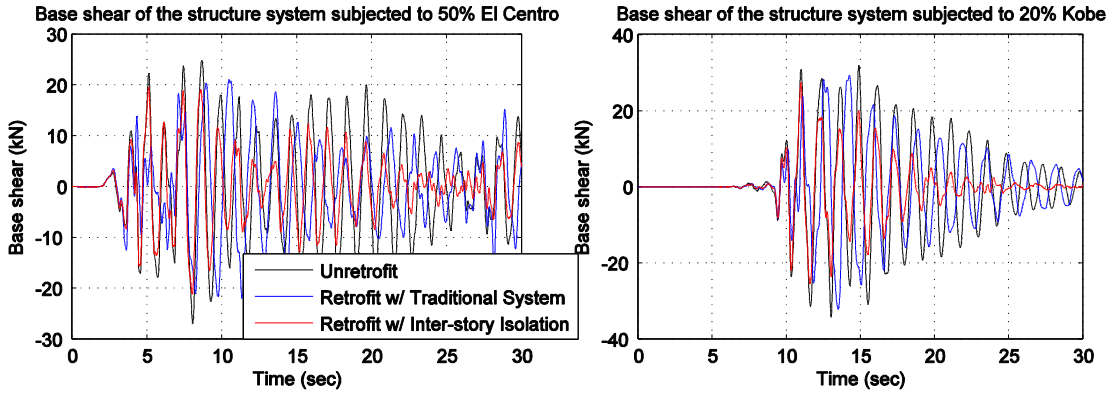

Figure 5.18 Base shear of the unretrofitted structure and two retrofitted structures with passive-on MR damper

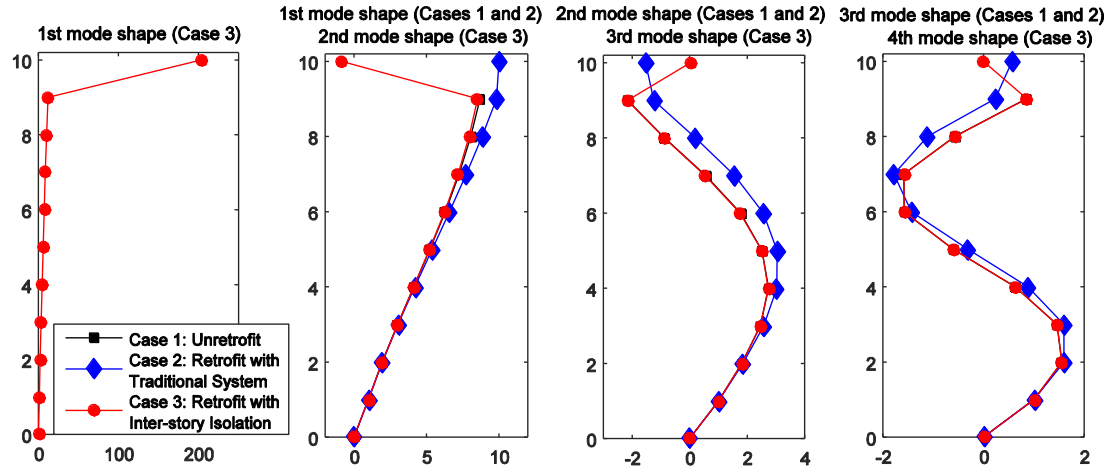

Figure 5.19 Mode shapes of the unretrofitted structure and two retrofitted structures

Table 5.10 Scaled structure base shear (kN) of the unretrofitted structure and retrofitted structure subjected to multiple excitations

Earthquake excitation	Criteria	9-story unretrofitted	10-story without isolation	10-story RTHS passive-on	10-story RTHS passive-off
50% El Centro	Max	27.0274	22.0693	21.1841	24.8365
	RMS	10.3233	8.3665	6.6590	9.1194
50% Hachinohe	Max	20.3083	13.0333	16.2348	20.0033
	RMS	6.7055	4.6423	4.9001	6.0298
10% Northridge	Max	17.7583	19.5401	15.7187	16.2414
	RMS	3.4062	8.5306	2.4519	2.7015

20% Kobe	Max	34.2842	32.2200	27.3426	29.0685
	RMS	11.3435	9.8475	6.5553	7.7909

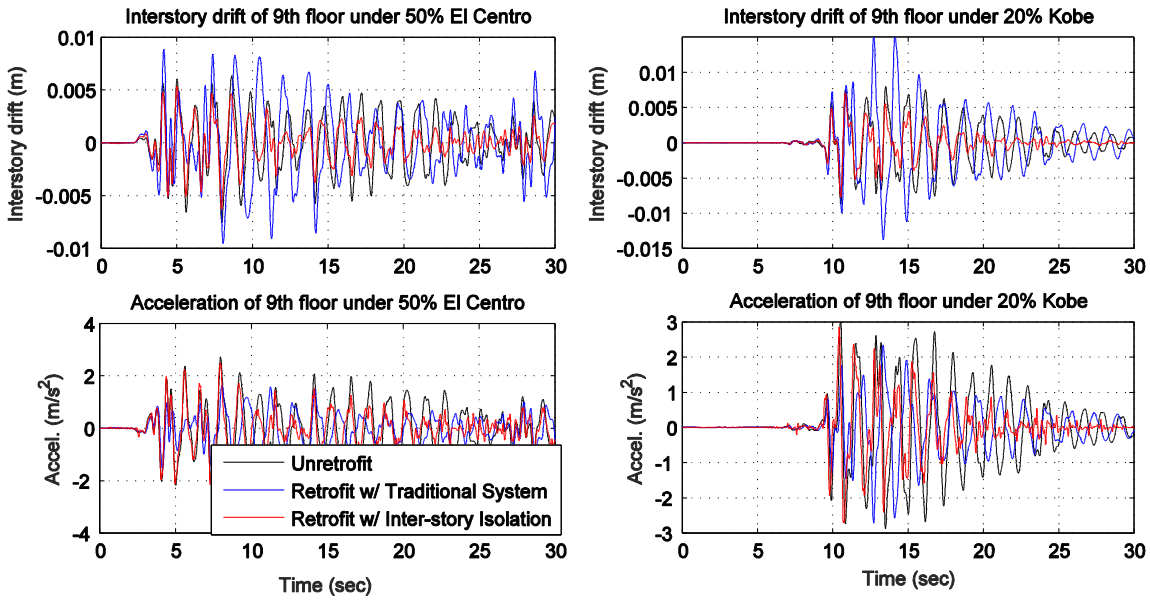

Figure 5.20 Interstory drift and acceleration of the unretrofitted structure and two retrofitted structures with passive-on MR damper

5.7 Summary

This chapter proposes a shake table RTHS framework for the performance evaluation of inter-story isolation and associated structural control strategies. The substructure below inter-story isolation is simulated numerically while the superstructure including inter-story isolation is tested experimentally. The shake table used in this study is 3 m by 3 m with a capacity of 10 metric tons and a specimen of 5 metric tons. Large-scale specimens are needed to accurately capture the nonlinear behavior of representative control devices, isolation systems, and hybrid isolation systems. The RTHS framework is demonstrated to be accurate for evaluating large-scale experimental specimens as a substructure of an

even larger structural system, a great benefit for structural control studies. Furthermore, the techniques are simple, applicable to specimens regardless of scale, and make use of readily available equipment in laboratories worldwide.

The experimental substructure investigated is a SDOF base-isolated specimen, demonstrated to be sufficient to model multiple upper stories above and including the inter-story isolation layer. The scaled structural model used in this study can represent the target model accurately with similar mode shapes and natural frequencies. The response of the structure with inter-story isolation was investigated through the proposed RTHS techniques. The stability of RTHS was found to be very tolerant to delay in the RTHS loop, owing to the low natural frequency and base shear of the specimen. Thus, RTHS based on the proposed strategies is demonstrated as an excellent method to study inter-story isolation.

The proposed strategy for shake table control in the context of RTHS was verified to offer a good online and offline acceleration tracking performance. The effectiveness of the overall RTHS in reproducing the total structural behavior was verified through comparisons with numerical simulations. This confidence will enable studies of more complex inter-story isolation systems that may not be easily modeled numerically, including large-scale nonlinear isolator specimens and supplemental control devices in semi-active or active control modes. Experimental studies through RTHS will open the door to future development of technologies for inter-story isolation.

In the application study, the benefits of implementing inter-story isolation such as on retrofit application were confirmed through RTHS. Base shear is maintained at low levels relative to the structure before retrofit. Furthermore, the stories above the isolation

layer exhibit very low levels of acceleration. Inter-story isolation is shown to be an attractive alternative to traditional structural systems, creating nominally decoupled systems with large architectural and structural design freedom. The capability of the existing foundations to vertically support the additional floors must be carefully checked before the retrofit and, if necessary, they should be reinforced.

More advanced studies into inter-story isolation are enabled by the methods proposed in this research. Future studies will focus on applying the technique proposed in this paper to taller buildings (requiring rotational DOF) to investigate and compare the performance of seismic isolation techniques to other energy dissipation techniques for seismic protection.

CHAPTER 6 DEVELOPMENT OF A CYBER-PHYSICAL OPTIMIZATION FRAMEWORK USING SUBSTRUCTURE RTHS

In this chapter, a novel technique for structural optimization using cyber-physical systems is proposed. In the cyber-physical system, the exploration of the solution space is numerically guided while candidate design solutions are experimentally evaluated. Additionally, the cyber-physical framework incorporates the RTHS approaches developed in Chapters 3 and 4 for the efficient and cost-effective evaluation of candidate design solutions. The performance of the proposed framework is demonstrated for the optimization of a shear building. The building is linear elastic, serving as a proof-of-concept for the approach which will be extended in Chapter 7. The goal of this study is incorporating state-of-the-art optimization techniques in a cyber-physical approach to structural optimization.

6.1 Background

Structural optimization is an important tool to iteratively improve structural designs to meet performance objectives in an efficient and cost-effective way. The performance of candidate designs are traditionally evaluated using numerical simulation. The major benefit of numerical simulation is that physical specimens do not have to be iteratively constructed and evaluated in the laboratory. However, when dealing with complex structures which are difficult to model numerically, large errors could exist between the numerical model and the physical structure. In that case, the optimization is less meaningful because the best results achieved are optimal for the numerical models instead of the physical structure. To bring more confidence to the optimal results,

experiments can be included in the optimization algorithm for those complex structures or components. However, the time and cost for conducting multiple experimental tests of complete structural systems may be prohibitive. RTHS provides a cost-effective experimental alternative to evaluate candidate designs as shown in Figure 6.1, suitable for use in a cyber-physical approach to optimization.

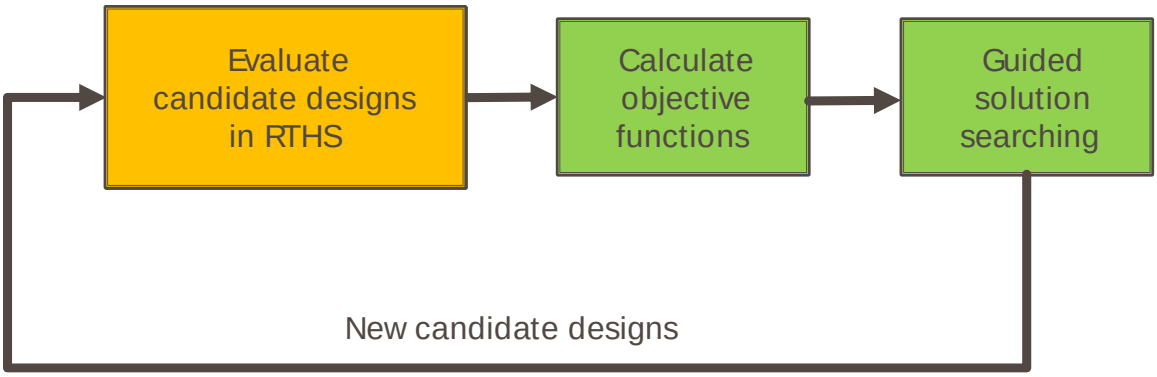

Figure 6.1 Block diagram of the optimization framework using RTHS

In this chapter, a novel technique for structural optimization through cyber-physical systems using substructure RTHS is proposed. A proof-of-concept study of a base-isolated structure is presented to validate the approach. Potential solutions overcoming the challenges and the process of this study are discussed. The particle swarm optimization (PSO) is used to guide the exploration of the solution space.

6.2 Cyber-Physical Substructure Optimization (CPSO) Framework

This section presents the development of the proposed CPSO framework. A 2-story base-isolated structure is used for illustration. The RTHS framework development can be found in Chapter 3. The particle swarm optimization (PSO) introduced in Chapter 2 is used as an example of the optimization algorithm in this study to illustrate the framework

development of CPSO. The PSO can be replaced by other optimization algorithms for different problem formulations and objectives.

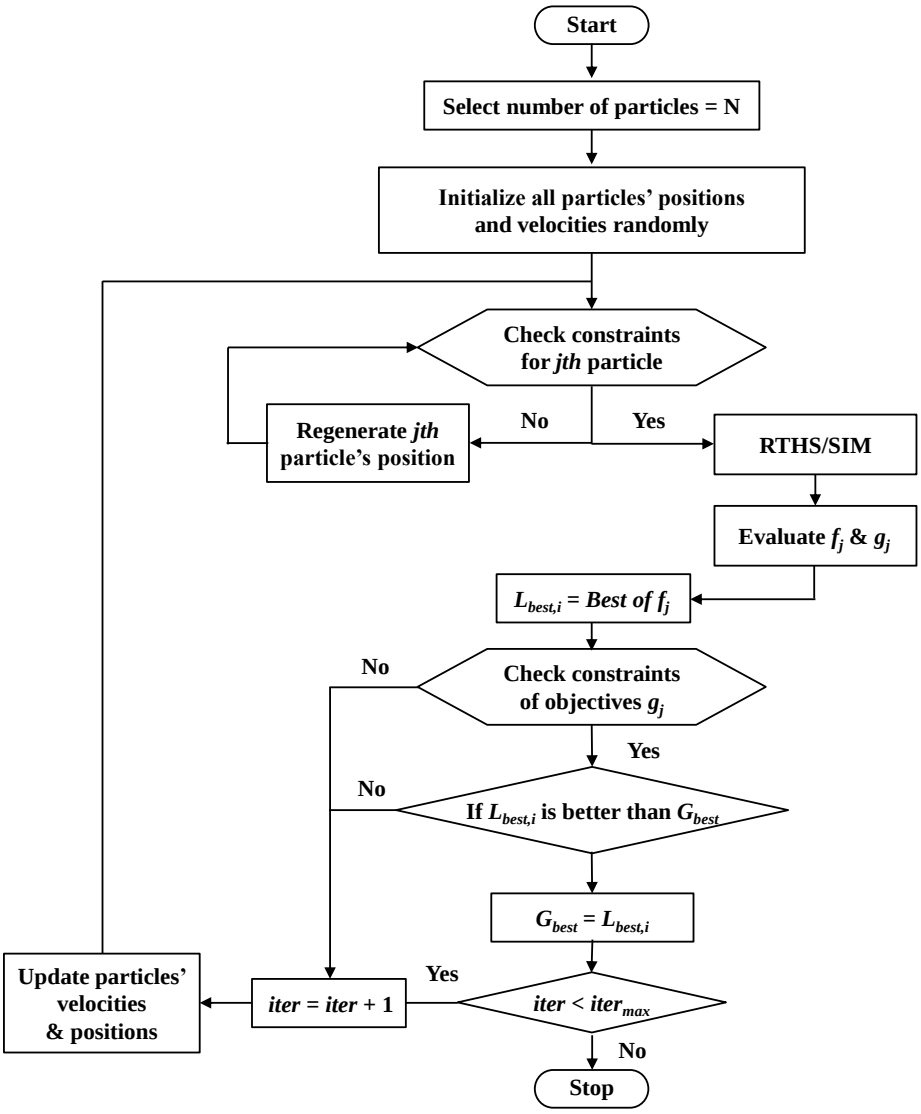

Figure 6.2 Flowchart of CPSO

The CPSO framework is developed by replacing the numerical simulation with RTHS as shown in Figure 6.2. The objectives calculated from the measured structural responses are used to guide the particles' movements in solution searching. RTHS, as illustrated in Figure 3.2, is conducted for each candidate design solution (particle) under each evaluation case (excitation). The process continues until an acceptable solution is

found. The fundamental challenges of RTHS resurface in the CPSO framework. Each RTHS experiment much be stable such that the experiment can be conducted. The design variables must be properly constrained to avoid RTHS instability.

Another major challenge in optimization through RTHS is that how to build an efficient platform controlling the RTHS testing with automatic updates in particle positions based on the objectives from RTHS testing. The realization of the proposed CPSO framework requires automatic control, data exchange, and update. A platform is developed in AutomationDesk embedded with ControlDesk, MATLAB, and Python to achieve data exchange and update in RTHS and optimization algorithm. AutomationDesk is a powerful test authoring and automation tool for hardware-in-the-loop (HIL) testing. Testing routines can be created graphically in AutomationDesk with libraries containing a large number of functions. The automation of testing with predefined variables can be realized in AutomationDesk. However, programming becomes more challenging in an optimization setting where the variables are determined online.

Figure 6.3 shows the testing sequence executed in AutomationDesk. Numerical substructure and excitations are defined in MATLAB with the initialization of variables and particle positions. Python scripts are used as the bridge for data exchange between MATLAB and AutomationDesk. In each iteration, the particle positions are updated as Eq. 2.2 and ready for RTHS testing after checking them within the boundaries to ensure the RTHS stability. The RTHS testing is conducted by dSPACE hardware with a software of ControlDesk controlling the parameters, testing process, and measurements. A sequence of conducting RTHS testing through ControlDesk is created in AutomationDesk as shown in Figure 6.3(b). After each test, the measurements are post-

processed in MATLAB to calculate the objective functions. Local best position is updated when a better solution is found for each particle. The global best position is then updated if the local best position in a swarm is a better solution. The RTHS testing continues in following iteration with updated particles' velocities and positions until reaching the maximum iteration or triggering the stopping criteria which is added to increase the efficiency of the framework. In addition, a stop and resume algorithm is added.

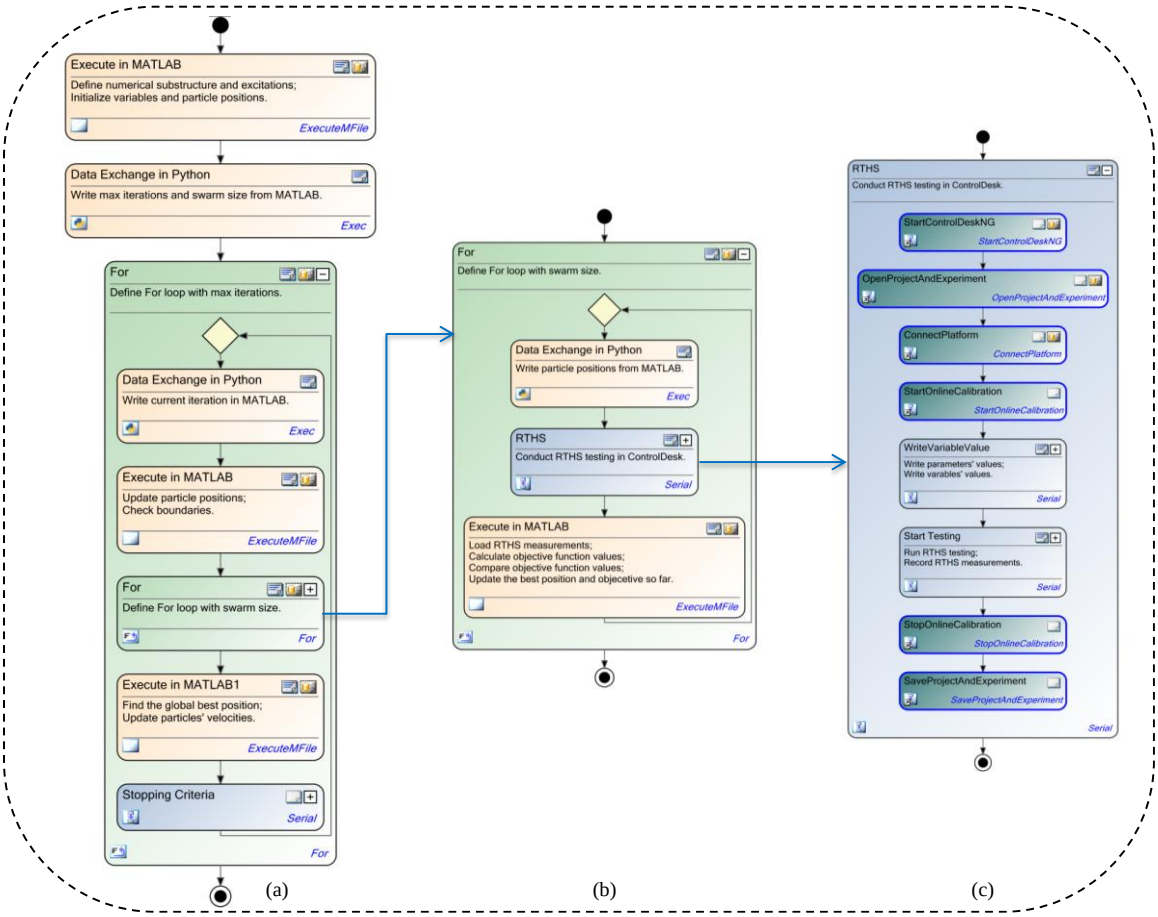

Figure 6.3 Testing sequence of CPSO in AutomationDesk

6.3 Experimental Setup

The proposed framework of structural optimization through substructure RTHS are verified using a small-scale experimental setup. The setup consists of a uni-axial shake table, a two-story steel shear building model as the experimental specimen, and a control and data acquisition system. Detailed information of shake table and data acquisition system can be found in Chapter 3 (Section 3.3.1). The dynamic properties of both the experimental substructure and the total structure are presented in this section. The specimen and equipment are located at the University of Maryland and is part of the Structural Engineering Laboratory.

6.3.1 Experimental substructure and total structure

The same two-story steel shear building mentioned in Chapter 4 (Section 4.4.2) is used as the experimental specimen in this study. The bare steel structure as shown in Figure 4.7 exhibited very low inherent damping, approximately 0.95% and 0.23% for the 1st and 2nd modes, which are insufficient for stability during RTHS. The damping ratios of the specimen are increased to 5% in both modes through the artificial specimen damping technique proposed in Chapter 4 (Zhang and Phillips, 2017).

The total base-isolated structure consists of a numerically simulated base isolation and experimentally represented upper stories as shown in Figure 6.4. The mass of the isolation is chosen as the average of the mass of the upper two stories. The stiffness of the isolation is determined as 0.61 kN/m, resulting in undamped natural frequencies of 0.85 Hz, 3.82 Hz, and 6.44 Hz. The damping ratio of base isolation is considered as the variable in optimization and given in the following section.

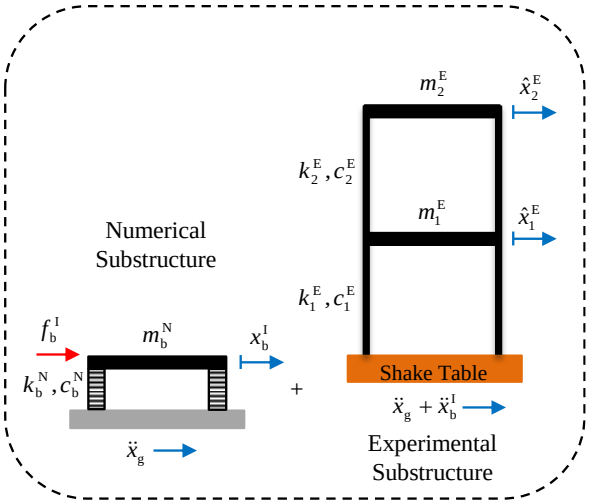

Figure 6.4 Illustration of 2-story base-isolated structure

6.3.2 Earthquake ground motions

The framework was analyzed and verified using a group of ground motions developed previously by Somerville (1997) for use in the FEMA project on steel moment-resisting frames. The group consists of 20 horizontal ground acceleration records adjusted so that their mean response spectrum matches the 1997 NEHRP design spectrum. In this study, the group of earthquakes corresponding to downtown Los Angeles was selected for seismic hazard levels corresponding to a 10% probability of exceedance in a 50-year period. These 20 earthquake records, designated as LA01-LA20, were derived from fault-parallel (FP) and fault-normal (FN) orientations of ten earthquake records. The reference earthquakes are passed through a 2-pole Butterworth high-pass filter with a cutoff frequency of 0.25 Hz to remove the low-frequency behavior without altering the desired frequency content. The earthquake records are scaled down to 5% for LA15 and LA16 and 10% for all other records (relative to the magnitudes shown in Table 6.1) in experiments due to the stroke limitation of the shake table.

Table 6.1 Earthquake index for structural optimization

Index	Description	Magnitude	Distance	Scale Factor	PGA (g)
LA01	FN Imperial Valley, 1940, El Centro	6.9	10.0	2.01	0.46
LA02	FP Imperial Valley, 1940, El Centro	6.9	10.0	2.01	0.68
LA03	FN Imperial Valley, 1979, Array #05	6.5	4.1	1.01	0.39
LA04	FP Imperial Valley, 1979, Array #05	6.5	4.1	1.01	0.49
LA05	FN Imperial Valley, 1979, Array #06	6.5	1.2	0.84	0.30
LA06	FP Imperial Valley, 1979, Array #06	6.5	1.2	0.84	0.23
LA07	FN Landers, 1992, Barstow	7.3	36.0	3.20	0.42
LA08	FP Landers, 1992, Barstow	7.3	36.0	3.20	0.43
LA09	FN Landers, 1992, Yermo	7.3	25.0	2.17	0.52
LA10	FP Landers, 1992, Yermo	7.3	25.0	2.17	0.36
LA11	FN Loma Prieta, 1989, Gilroy	7.0	12.0	1.79	0.67
LA12	FP Loma Prieta, 1989, Gilroy	7.0	12.0	1.79	0.97
LA13	FN Northridge, 1994, Newhall	6.7	6.7	1.03	0.68
LA14	FP Northridge, 1994, Newhall	6.7	6.7	1.03	0.66
LA15	FN Northridge, 1994, Rinaldi RS	6.7	7.5	0.79	0.53
LA16	FP Northridge, 1994, Rinaldi RS	6.7	7.5	0.79	0.58
LA17	FN Northridge, 1994, Sylmar	6.7	6.4	0.99	0.57
LA18	FP Northridge, 1994, Sylmar	6.7	6.4	0.99	0.82
LA19	FN North Palm Springs, 1986	6.0	6.7	2.97	1.02
LA20	FP North Palm Springs, 1986	6.0	6.7	2.97	0.99

6.4 Performance of the Proposed CPSO for 2-story Base-Isolated Structure

This section presents the performance of the proposed framework of structural optimization through substructure RTHS. Particle swarm optimization is used for optimal solution searching in this study with multiple objectives of minimizing maximum structural acceleration and keeping base drift under 2 cm as a drift limitation of the isolation. The damping coefficient c_b of base isolation is the only variable in this study and is optimized in PSO to improve the seismic performance of the 2-story base-isolated structure (see Figure 6.4). To ensure the RTHS stability, c_b is restrained with a lower limit of 4.55 Ns/m which gives a 2% damping ratio in 1st mode. An upper limit of 201.73 Ns/m is used to ensure that the damping ratio of fundamental mode does not exceed

100%. For PSO, a swarm with five particles and a maximum iteration of 50 are considered in this study. The inertia weight in Eq. 2.1 is 1.0 and acceleration coefficients are 2.0. The study starts with the optimization under a single earthquake excitation for demonstration. Then, it follows with a more complex scenario of optimization under several earthquakes. Last, to show the versatility and efficiency of the proposed CPSO framework, the optimization under all 20 designed earthquakes is conducted. For better illustration, results of optimization from RTHS testing are compared with those from pure numerical simulation. Two cases are listed below.

1. Optimization of the 2-story base-isolated structure in numerical simulation (OPT-SIM); and
2. Cyber-physical system optimization of the 2-story base-isolated structure, where the upper two stories are physically tested and the base isolation is numerically analyzed (CPSO-RTHS).

Overall agreements in optimization between RTHS and pure numerical simulation (SIM; OPT-SIM) are expected since a linear structure is considered in this study focusing on the performance demonstration of the proposed framework. Nonlinear systems can be investigated as more practical applications (e.g., optimization of external control devices such as MR damper illustrated in next section). All acceleration measurements in time-domain are passed through a low-pass filter with a cutoff frequency of 20 Hz in post processing.

6.4.1 Structural optimization in RTHS under single earthquake

The seismic performance of the base-isolated structure subjected to LA02 is investigated. The objective is to minimize the maximum structural acceleration under LA02 as Eq. 6.1 through optimization of c_b.

$$\text{minimize} \quad \max_{LA02} |\ddot{x}_{abs}| \tag{6.1}$$

The particle positions over iterations from optimization in RTHS and SIM are shown in Figure 6.5 (a) and Figure 6.5 (b), respectively. Figure 6.6 (a) and Figure 6.6 (b) show the iteration history of the objective function values for optimization in RTHS and SIM respectively. The convergence of particle position and objective function can be clearly observed from both figures. For CPSO-RTHS, the damping coefficient of base isolation is found as 47.98 Ns/m achieving the smallest maximum absolute acceleration of 0.47 m/s^2. The damping ratio is around 19.0% in the fundamental mode. The optimal solution obtained using CPSO framework (CPSO-RTHS) compares well with the optimal solution from OPT-SIM which is 61.41 Ns/m minimizing the maximum structural acceleration as 0.44 m/s^2. Good agreement is observed between CPSO-RTHS and OPT-SIM as expected, demonstrating the favorable performance of the proposed CPSO framework in achieving optimal solution in RTHS. Discrepancies can be attributed to error in modeling of the experimental specimen and noise in accelerometer measurements. Figure 6.7 shows the structural responses with the optimal damping of base isolation. Results match well between CPSO-RTHS and OPT-SIM. The base drift is within the restraint of 0.02 m.

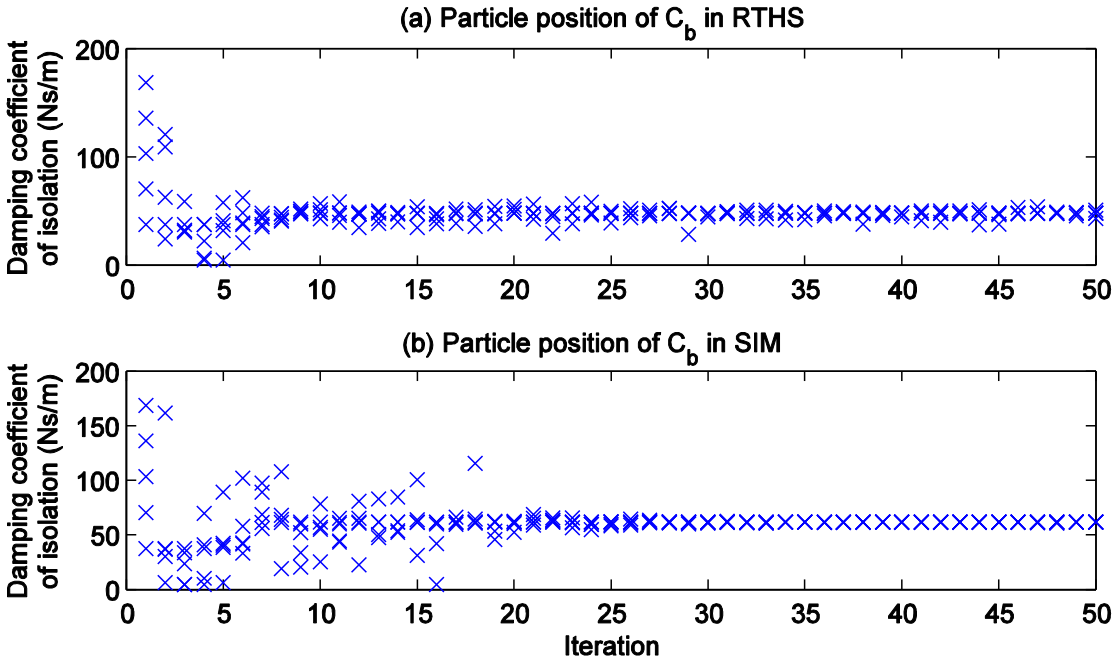

Figure 6.5 Particle positions in optimization in (a) RTHS; (b) SIM

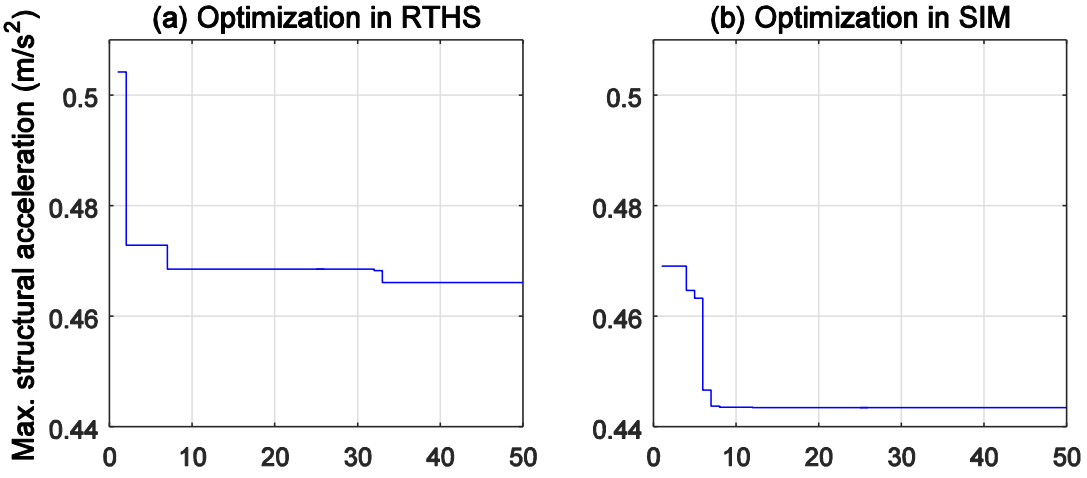

Figure 6.6 Iteration history of objective functions for optimization in (a) RTHS; (b) SIM

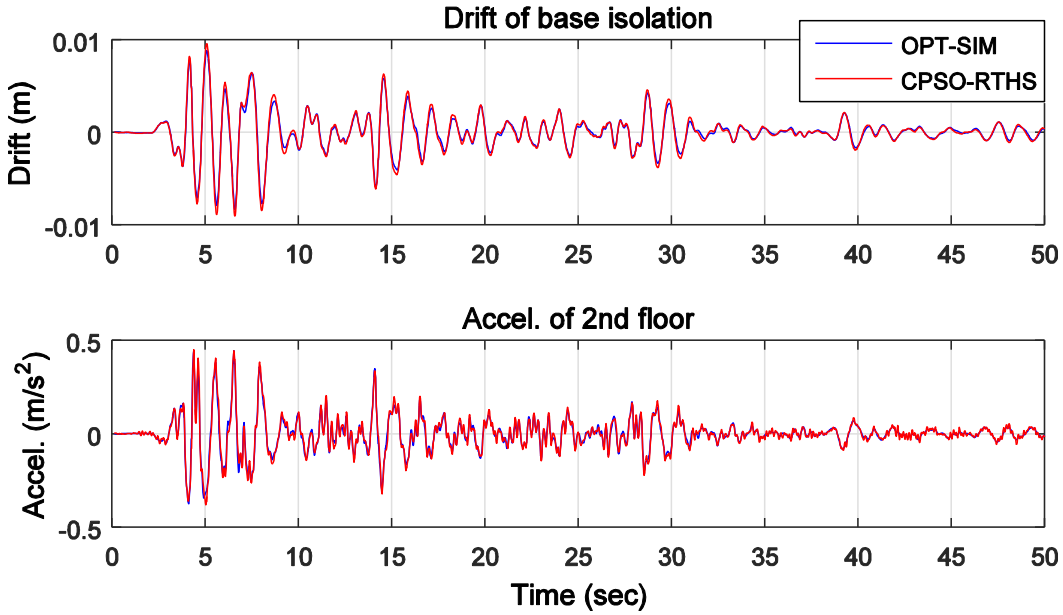

Figure 6.7 Time history analysis of the optimal structural responses in CPSO-RTHS and OPT-SIM

6.4.2 Structural optimization in RTHS under several select earthquakes

The structural optimization under three earthquakes was conducted and investigated. The earthquakes were selected as LA02, LA17, and LA19. The objective is to minimize the maximum structural acceleration considering all three earthquakes. The objective function can be expressed as:

$$\text{minimize} \quad \max_{[LA02,\ LA17,\ LA19]} \left|\ddot{x}_{abs}\right| \tag{6.2}$$

The particle positions over iterations from optimization in CPSO-RTHS and OPT-SIM are shown in Figure 6.8 (a) and Figure 6.8 (b), respectively. Figure 6.9 (a) and Figure 6.9 (b) show the iteration history of the objective function values for optimization in CPSO-RTHS and OPT-SIM respectively. The damping coefficient of base isolation converges at 43.83 Ns/m in CPSO-RTHS which compares well to the damping coefficient in OPT-SIM converging at 50.41 Ns/m. The optimal structural acceleration is

0.49 m/s^2 and 0.48 m/s^2 in CPSO-RTHS and OPT-SIM, respectively. The damping ratio is around 17.3% in the fundamental mode for CPSO-RTHS. Good agreement is observed between CPSO-RTHS and OPT-SIM as expected, again demonstrating the favorable performance of the proposed CPSO framework in achieving optimal solution in RTHS in a more complex scenario. Figure 6.10 shows the structural responses with the optimal damping of base isolation. Results match well between CPSO-RTHS and OPT-SIM. The base drift is within the constraint of 0.02 m. At the optimal solution, the dominant earthquake with the largest structural acceleration is LA17.

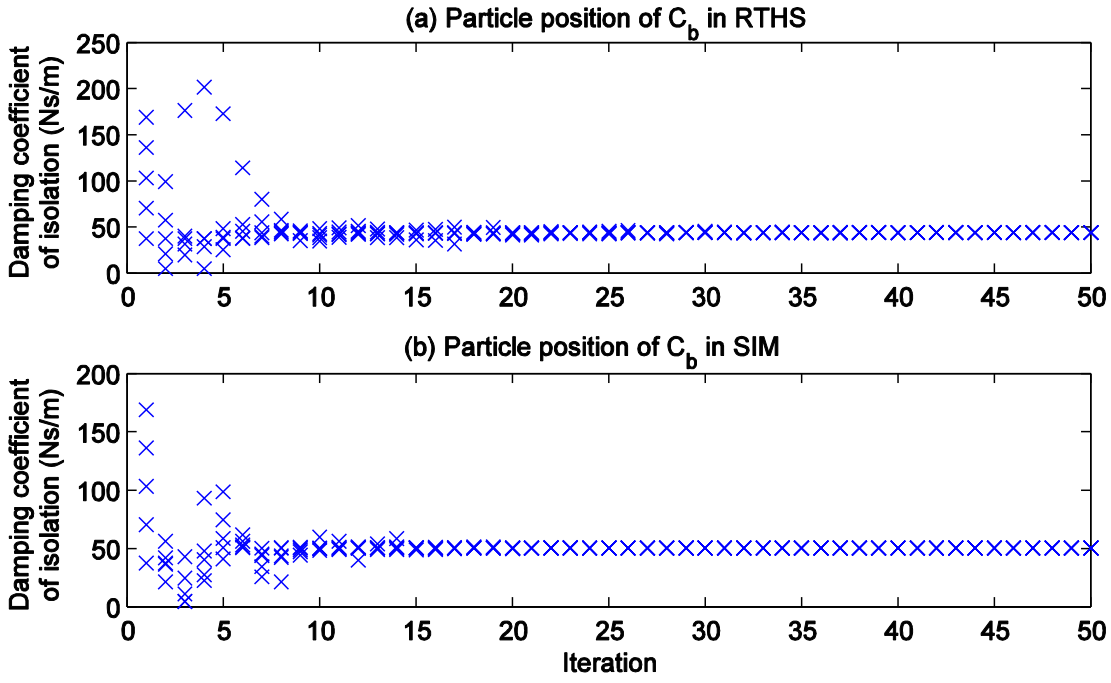

Figure 6.8 Particle positions in optimization in (a) RTHS; (b) SIM

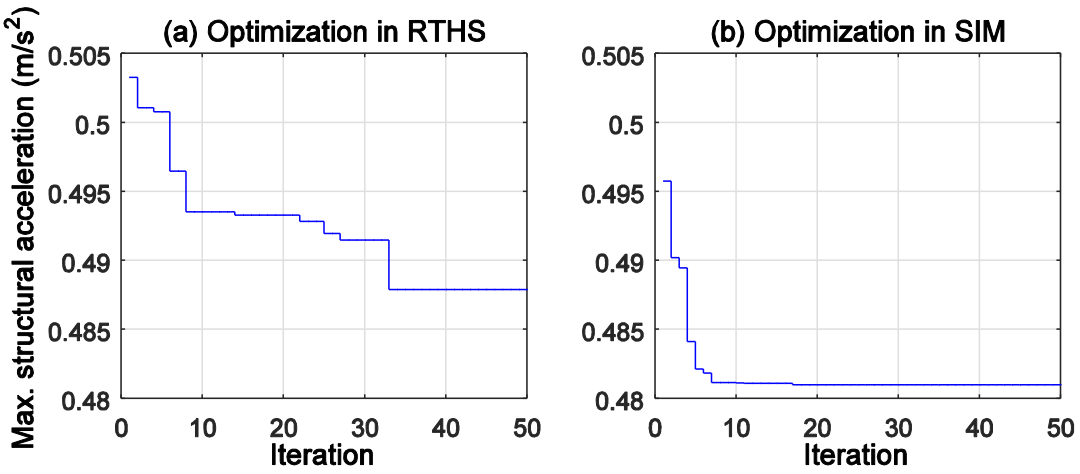

Figure 6.9 Iteration history of objective functions for optimization in (a) RTHS; (b) SIM

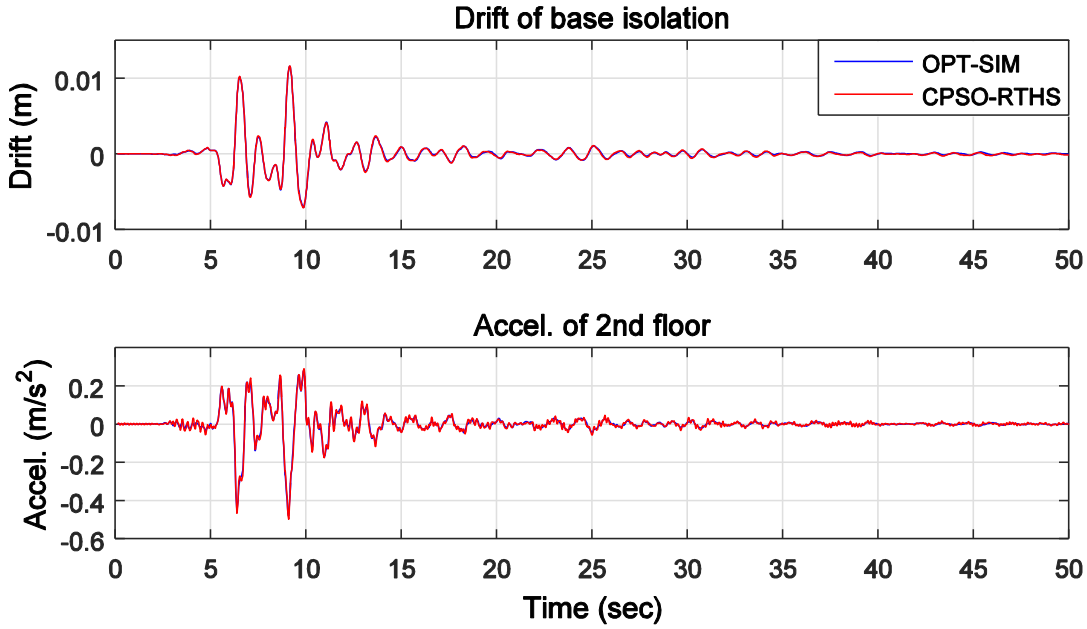

Figure 6.10 Time history analysis of the optimal structural responses in CPSO-RTHS and OPT-SIM

6.4.3 Structural optimization in RTHS under a suite of design earthquakes

Seismic design of building structures sometimes considers a group of earthquakes with the response spectrum matching the design spectrum near the site for performance demonstration (e.g., LA01-LA20). In this section, the damping of base isolation is

optimized to improve structural responses considering all design earthquakes. The objective, therefore, is to minimize the maximum structural acceleration under the worst earthquake excitation as Eq. 6.3.

$$\text{minimize} \quad \max_{LA01}^{LA20} \left| \ddot{x}_{abs} \right| \tag{6.3}$$

It is time-consuming and inefficient to run through all 20 earthquakes during optimization in RTHS. To realize the objective efficiently, a preliminary test matrix is evaluated to determine the general relationship of damping coefficient of isolation and maximum structural acceleration under all 20 earthquakes. Five discrete damping coefficients uniformly distributed in [4.55, 201.73] Ns/m are selected as 37.41, 70.28, 103.14, 136.00, and 168.87 Ns/m. The bar plot in Figure 6.11 shows the maximum structural accelerations at the five damping coefficients under all designed earthquakes. Note that is not an optimization run, rather a test matrix used to narrow down the earthquakes considered. For each damping coefficient, the worst earthquake resulting in the maximum acceleration can be found. To be more conservative, the worst two earthquakes for each damping coefficient are selected as the dominant earthquake candidates. From Figure 6.11, it can be clearly seen that the maximum acceleration happens under the worst two earthquakes {LA20, LA14}, {LA18, LA20}, {LA18, LA19}, {LA19, LA18}, and {LA19, LA18} for the five damping coefficients respectively. Consistent conclusion is obtained from both simulation and RTHS analyses of these select damping cases. Therefore, earthquakes LA14, LA18, LA19, and LA20 are determined as the dominant earthquake candidates for structural optimization. This approach works well when the number of design variable is small, e.g., in this case the only design variable is the supplemental viscous damping in the isolation layer. More

efficient algorithms to select governing excitations (e.g., run in parallel with the optimization) will be developed for many design variables in Chapter 7.

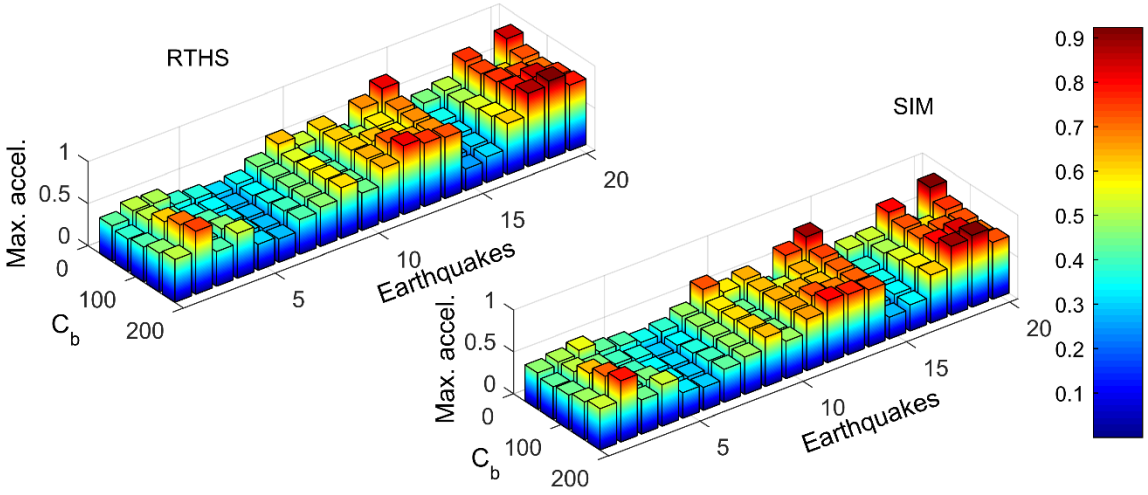

Figure 6.11 Relationship of damping ratio and earthquakes on structural acceleration

Based on the governing earthquakes selected, optimization was run for both CPSO-RTHS and OPT-SIM cases. Figure 6.12 shows the particle positions of damping coefficients during optimization in RTHS and SIM. The optimal damping coefficient is found as 77.20 Ns/m in RTHS with a damping ratio of 30.7% in 1st mode, compared well to the optimal damping coefficient in SIM as 101.89 Ns/m. The iteration history of objectives is shown in Figure 6.13 (a) and (b) for optimization in RTHS and SIM respectively. The achieved optimal objective is 0.71 m/s^2 in RTHS and 0.68 m/s^2 in SIM. Good agreement is observed between CPSO-RTHS and OPT-SIM in optimizing the structural performance subjected to all 20 designed earthquakes. Figure 6.14 shows the time history of the base drift and acceleration of top floor under the dominant earthquake LA20 determined in optimization. Responses match well between CPSO-RTHS and OPT-SIM, demonstrating favorable performance and robustness of the proposed CPSO framework. Note that the optimal solutions for both RTHS and SIM determined under the

selected earthquakes were finally evaluated under all 20 earthquakes. This final comprehensive evaluation of the optimal solution confirms that the selected earthquakes do indeed govern for the optimal solution.

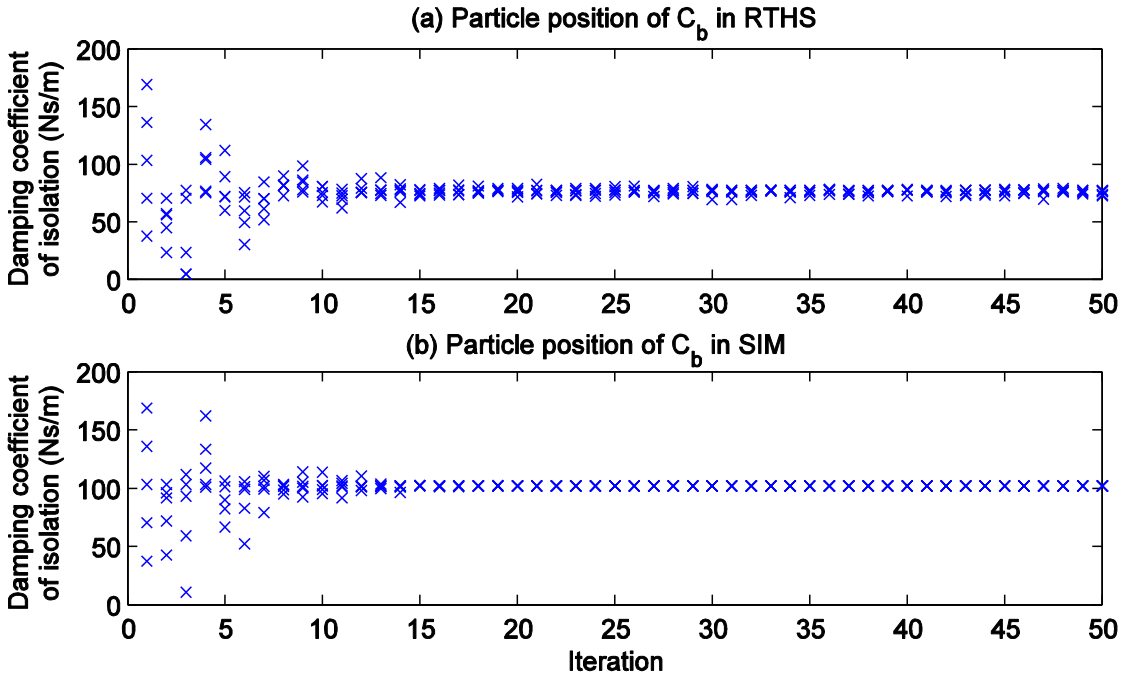

Figure 6.12 Particle positions in optimization in (a) RTHS; (b) SIM

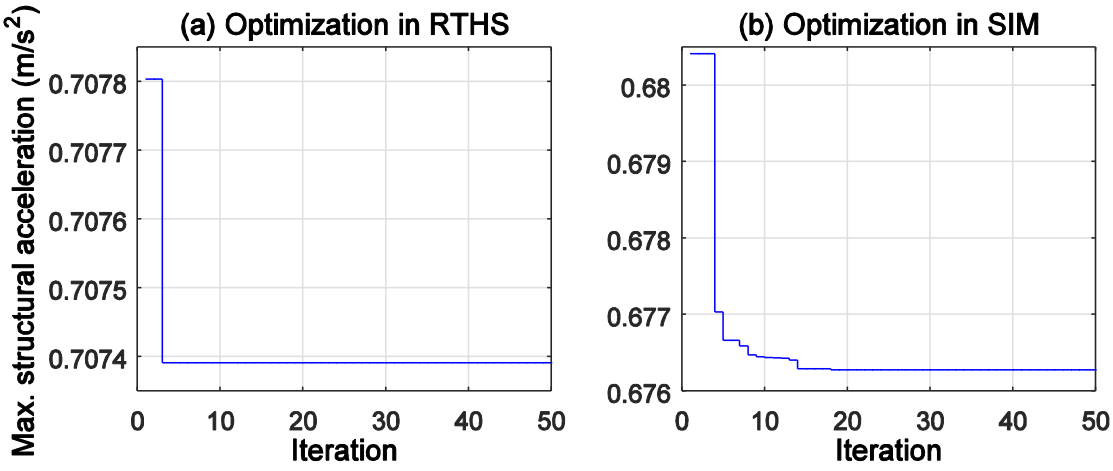

Figure 6.13 Iteration history of objective functions for optimization in (a) RTHS; (b) SIM

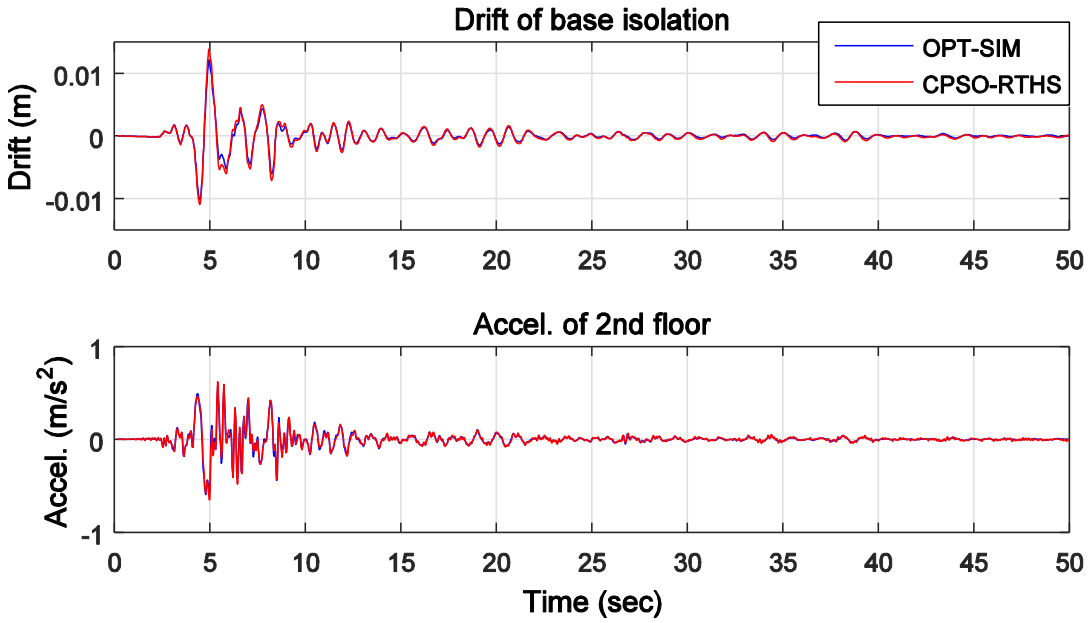

Figure 6.14 Time history analysis of the optimal structural responses in CPSO-RTHS and OPT-SIM

6.5 Summary

This study presents a novel framework for conducting structural optimization through substructure RTHS. The proposed technique is demonstrated to be robust and efficient in achieving optimal design of structure or supplemental devices with nonlinear and complex components which are difficult to model numerically. The development of the CPSO framework is discussed in detail with particle swarm optimization (PSO) selected to guide the solution searching. Through the CPSO technique, the base isolation design is optimized for the seismic protection of a two-story simple shear building. The optimal design against single and multiple earthquakes are considered. The results using CPSO technique are compared with pure numerical simulation. Overall good agreement is observed between OPT-SIM and CPSO-RTHS, demonstrating the performance of CPSO and confidence in applying CPSO framework for studying complex systems (e.g.,

nonlinear systems). Slight differences between experiment and simulation are caused by the inaccuracy of the numerical model for the specimen and sensor noise.

The proposed CPSO framework is a versatile and robust technique for structural design and control against multi-hazards. This technique combines the accuracy and efficiency of RTHS to cost-effectively evaluate structural behaviors and the benefits of optimization to efficiently explore different design alternatives and achieve optimal design. This new technique has many potential opportunities and applications in civil engineering.

It is worth noting that not every structural system is suited for iterative experimental evaluation. In particular, structures that are subject to permanent damage will not return to their initial condition after every iteration. However, there are many cases, such as supplemental damping devices, where the substructure of interest is both difficult to model and will not undergo permanent damage. For example, the parapmeters and control laws for structural control devices can be developed and tuned. These cases are well-suited for a cyber-physical approach to optimization through RTHS.

CHAPTER 7 OPTIMIZATION OF A NONLINEAR SYSTEM USING A CYBER-PHYSICAL SUBSTRUCTURE OPTIMIZATION FRAMEWORK

In this chapter, the cyber-physical substructure optimization (CPSO) framework proposed in Chapter 6 is applied to a nonlinear system. An MR damper is installed in the isolation layer of a 5-story base-isolated structure. The semi-active control algorithm for the MR damper is optimized through the CPSO technique. The MR damper is experimentally evaluated while the rest of system is modeled numerically using RTHS. The optimal design is conducted for the seismic protection of the structure against single and multiple design earthquakes. PSO is used to guide the solution search across multiple design variables. In addition, a new exploration approach is proposed to improve the efficiency of PSO under multiple earthquake inputs. This study further demonstrates the accurate performance of the proposed CPSO framework, as well as the value when studying nonlinear systems or devices that are difficult to model numerically.

7.1 Structural Model and RTHS Setup

Supplemental control is often added to the isolation layer of base isolated structures to reduce base drift and improve overall structural responses against earthquakes. In this chapter, an MR damper is considered as a supplemental control device in the isolation layer of a base-isolated structure. The semi-active controller design of the MR damper is optimized using the proposed CPSO framework. The goal is to minimize the maximum structural acceleration while maintaining the base drift within a safe range.

This section presents the structure used in this study, a 5-story base-isolated structure with supplemental control provided by an MR damper. The MR damper is

experimentally represented by a 200 kN MR damper specimen while the 5-story base-isolated structure is simulated numerically (see Figure 7.1). The total response of the structure is evaluated using RTHS. In RTHS, the earthquake ground motion is applied to the numerical substructure. The isolation layer displacement then is tracked by the servo-hydraulic actuator, exciting the MR damper specimen. The restoring force measured by the actuator's load cell is then returned to the numerical substructure, completing the RTHS loop. This loop of action and reaction is run at 2000 Hz.

A numerical model for the MR damper is also given. This model is used in numerical simulations to contrast with RTHS when investigating nonlinear systems.

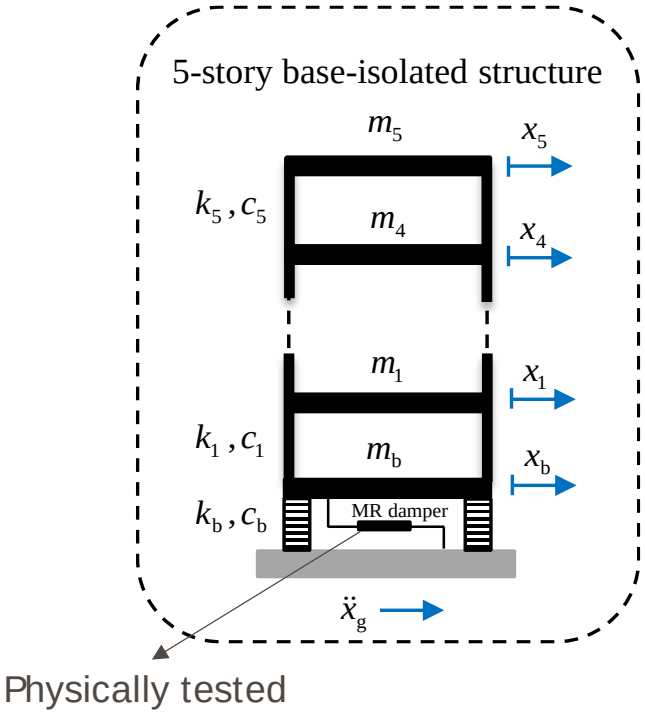

Figure 7.1 5-story base-isolated structure with an MR damper at isolation layer

7.1.1 5-story base-isolated structure

A 5-story base-isolated structure is adapted from Kelly et al. (1987) and Johnson et al. (1998). The superstructure parameters from these studies are reported for a one-third

scale model and have been scaled up to represent a full-scale superstructure herein. The model parameters are listed in Table 7.1. The base stiffness and damping are chosen to achieve the same fundamental natural period of 2.5 s and 4% damping ratio as in Johnson et al. (1998). The building is a lumped-parameter model with one degree-of-freedom on each story. This model is assumed to remain linear-elastic during all external dynamic excitations. This assumption facilitates a simple study focused on protective systems and is consistent with a scenario where major structural members remain functional while nonstructural components may be damaged.

Table 7.1 Parameters of the 5-story base-isolated structure

Floor	Floor Mass (kg)	Story Stiffness (kN/m)	Damping Coefficient (kg/s)
Base	m_b = 61,200	k_b = 2,129.8	c_b = 69,938
1	m_1 = 53,073	k_1 = 101,196	c_1 = 348,140
2	m_2 = 53,073	k_2 = 87,279	c_2 = 301,380
3	m_3 = 53,073	k_3 = 85,863	c_3 = 296,180
4	m_4 = 53,073	k_4 = 74,862	c_4 = 259,810
5	m_5 = 53,073	k_5 = 57,177	c_5 =197,450

7.1.2 MR damper and semi-active control

A damper is added to the isolation layer for supplemental control, represented by a physical substructure. The damper is a second-generation, large-scale 200 kN MR damper manufactured by the Lord Corporation. Figure 7.2 shows the configuration of the MR damper. The damper has a stroke of ±292 mm (±13 in) and can generate forces slightly higher than the nominal 200 kN. The damper has an accumulator charged to 5.17 MPa (750 psi) to compensate for the thermal expansion of the MR fluid (Christenson et al., 2008). The unique properties of MR dampers are derived from the internal MR fluid. In the presence of a magnetic field, the fluid changes from a linear viscous fluid to a

semi-solid with controllable yield strength (Carlson and Jolly, 2000). This yield strength is dependent upon the strength of the magnetic field, while the maximum yield strength is determined by the composition of the MR fluid. The source of the magnetic field is an electromagnet located in the piston head, excited by an external current which can vary as required by a structural control algorithm.

The current to the MR damper is controlled using a pulse-width modulator (PWM), which consists of an Advanced Motion Controls model PS2x300W unregulated power supply providing 80 VDC to an Advanced Motion Controls model 30A8 analog servo-drive, shown in Figure 7.3. The analog servo-drive can measure the current in the closed-loop circuit for current feedback control, which is suitable for MR damper applications. The benefit of using a PWM is power efficiency and quick response time. An AC line filter is added to prevent noise from the PWM from leaking into the AC supply and contaminating nearby equipment. A ferrite suppression core is added to attenuate noise from the switching of the PWM.

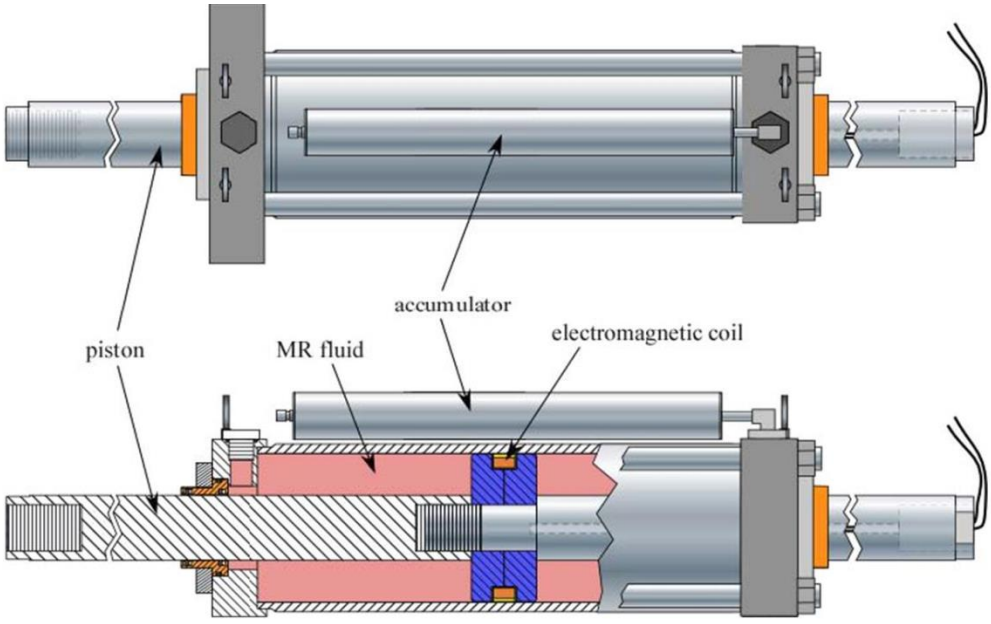

Figure 7.2 Configuration of the large-scale 200 kN MR damper

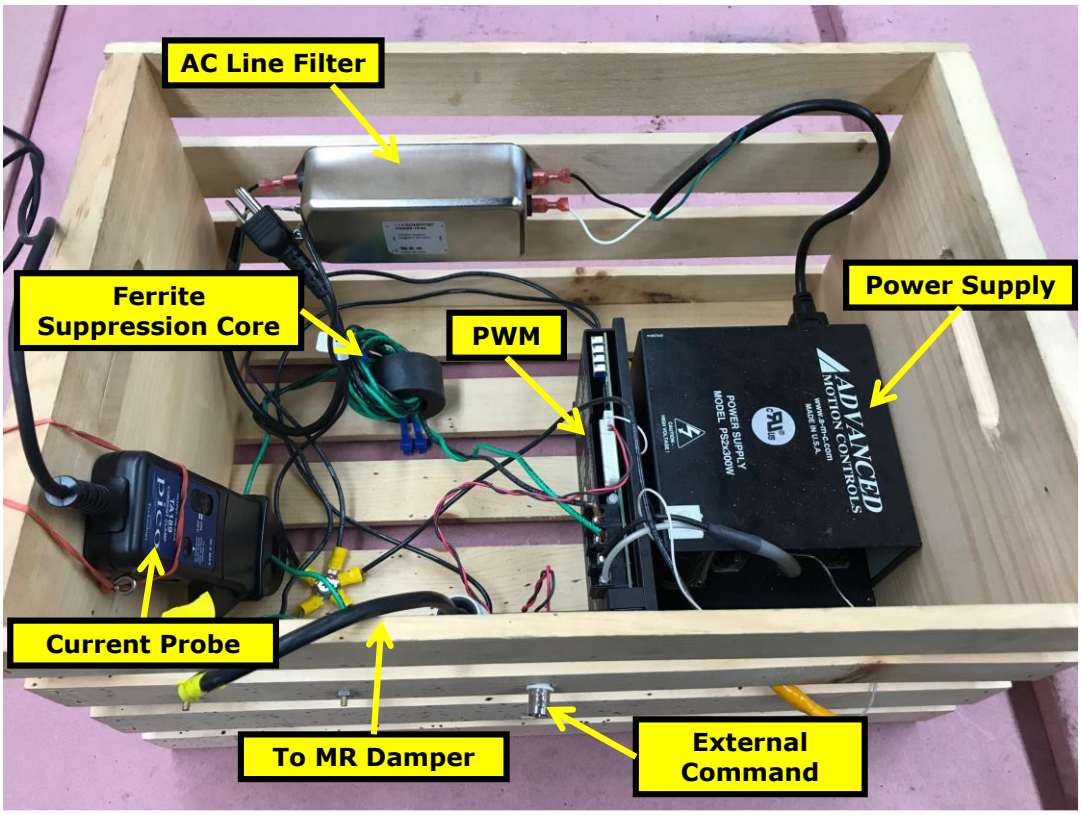

Figure 7.3 PWM for MR damper current excitation

The MR damper semi-active control is split into a primary and secondary controller. The primary controller determines the desired force in the damper. The secondary controller attempts to achieve this desired force through a command current to the damper.

For the secondary controller, an over-driven back-driven clipped-optimal controller (ODBDCO) is implemented, adapted from Phillips, et al. (2010). This controller is based on a clipped-optimal control (COC) algorithm (Dyke et al., 1996) with incorporation of over-driven back-driven concepts in order to achieve quicker response. When the current is switched on by the clipped-optimal control algorithm, instead of jumping to the maximum current (2.5 Amps), a PI feedback loop is used. Through the feedback loop, more current is applied when the force error is greater (over a range of 0

to 7.5 Amps). A rate limiter is also implemented to prevent the dramatic increase or decrease of the current. To prevent the MR damper coils from overheating, the maximum allowable current is decreased (to 2.5 Amps) after a few seconds. This improved clipped-optimal controller is verified to offer accurate tracking performance of the desired force.

For the primary controller, the desired force is determined through a casual method to realize rate-independent damping (Keivan et al., 2017). Rate-independent linear damping provides direct control over displacement, a desirable feature for low-frequency structures such as base-isolated structures. When low-frequency structures are subjected to high-frequency ground motions, rate-independent linear damping produces similar response displacements and velocities in comparison to other damping types; however, the damping forces and resulting floor accelerations are substantially smaller. In rate-independent linear damping, the restoring force is proportional to displacement but advanced in phase π/2 radians, a non-causality that has limited its practical applications. To realize the benefits of direct displacement control for low-frequency structures, a causal realization of rate-independent linear damping is proposed by Keivan et al. (2017) and implemented herein. This method uses a first-order all-pass filter to approximate the desired rate-independent linear damping force.

The true frequency domain representation of rate-independent linear damping is:

$$F_{\mathrm{D}}(\omega) = \eta k\, i\, sign(\omega) X(\omega) \tag{7.1}$$

where k is the stiffness between the two DOF connected by rate-independent linear damper and η is the loss factor. The force can be broken into two components, the constant $k\eta$ and the transfer function:

$$H_{\mathrm{TF}}(\omega) = i\, sign(\omega) \tag{7.2}$$

Passing the response displacement through the transfer function of Eq. 7.2 and then multiplying by $k\eta$ will produce the corresponding rate-independent linear damping force. Thus, Eq. 7.2 is taken as the target filter for causal realization. The target filter has unity magnitude and phase advance of $\pi/2$ radians over all positive frequencies. The target filter is not implementable; however, it can be approximated over a specified frequency range using a first-order all-pass filter:

$$H_{\mathrm{AP}}(\omega) = \frac{i\omega - \omega_f}{i\omega + \omega_f} \tag{7.3}$$

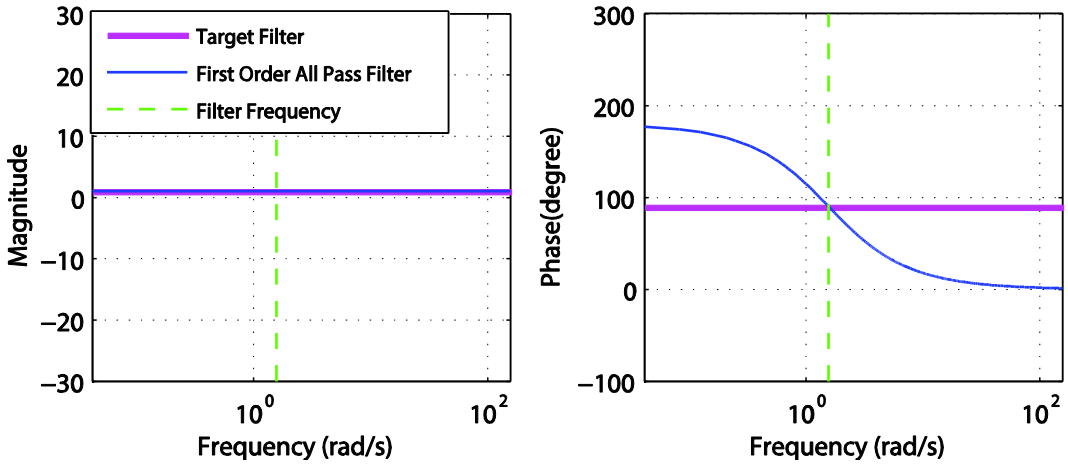

Figure 7.4 Magnitude and phase of the target and all-pass filters

Figure 7.4 compares the magnitude and phase of the target filter with the first-order all-pass filter. At all frequencies, the proposed filter design matches the magnitude of the target filter. At and around a specific design frequency (e.g., the natural frequency of a structure), the filter design matches the phase of the target filter. Including the terms k and η, the desired force representing causal rate-independent linear damping is given by:

$$F_{\mathrm{D,causal}}(\omega) = k\eta\left(\frac{i\omega - \omega_f}{i\omega + \omega_f}\right) \tag{7.4}$$

The controller shown in Eq. 7.4 is taken as the desired force for the MR damper. The two design variables include the loss factor η (ratio between the loss and storage modulus) and filter frequency ω_f. The loss factor η affects the magnitude of the force hysteresis while the filter frequency ω_f affects the skew of the hysteresis. Without knowledge of the structural response frequency, selecting ω_f as the fundamental natural frequency of the structure produces the best match between causal (Eq. 7.4) and ideal non-causal rate-independent linear damping (Eq. 7.1). This design creates a hysteresis with very little skew. If the response frequency exceeds the filter frequency ω_f, the hysteresis will exhibit a positive skew; if the response frequency is less than the filter frequency ω_f, the hysteresis will exhibit a negative skew.

Both η and ω_f influence the desired force and therefore the MR damper performance. It is difficult to select these parameters without considering the forced vibration frequency under earthquake excitation. Parameters η and ω_f are selected as design variables in this study and optimized through the proposed CPSO framework to achieve the optimal MR damper control and structural performance against a suite of design earthquakes.

A high-fidelity MR damper model is identified for comparison with the RTHS results. The Bouc-Wen hysteretic model introduced in Chapter 5 is used to model the MR damper behavior. The mechanics of the model are shown in Figure 5.5. The equations to calculate the restoring force can be found in Eq. 5.1 and Eq. 5.2. To model the current-

dependent behavior of this large-scale MR damper, Eq. 7.5 through Eq. 7.9 are incorporated into the model, where i_c is the input current. Parameters with the subscript "a" were fit to passive-off mode data (0.0 Amp) while parameters with subscript "b" were fit to passive-on mode data (2.5 Amp). An exponential relationship between the extremes was found best to match the behavior intermediate levels of current, with the rate of change described by the parameters with subscript "c". A comprehensive evaluation of MR damper models can be found in Jiang and Christenson (2011). Model parameters of this large-scale MR damper are presented in Table 7.2 (Phillips, 2012).

$$\alpha = \alpha_{\mathrm{b}} + (\alpha_{\mathrm{a}} - \alpha_{\mathrm{b}}) \times \exp(-\alpha_{\mathrm{c}} i_{\mathrm{c}}) \tag{7.5}$$

$$c_0 = c_{0,\mathrm{b}} + (c_{0,\mathrm{a}} - c_{0,\mathrm{b}}) \times \exp(-c_{0,\mathrm{c}} i_{\mathrm{c}}) \tag{7.6}$$

$$c_1 = c_{1,\mathrm{b}} + (c_{1,\mathrm{a}} - c_{1,\mathrm{b}}) \times \exp(-c_{1,\mathrm{c}} i_{\mathrm{c}}) \tag{7.7}$$

$$\beta = \beta_{\mathrm{b}} + (\beta_{\mathrm{a}} - \beta_{\mathrm{b}}) \times \exp(-\beta_{\mathrm{c}} i_{\mathrm{c}}) \tag{7.8}$$

$$\gamma = \gamma_{\mathrm{b}} + (\gamma_{\mathrm{a}} - \gamma_{\mathrm{b}}) \times \exp(-\gamma_{\mathrm{c}} i_{\mathrm{c}}) \tag{7.9}$$

Table 7.2 Phenomenological Model Parameters of 200 kN MR Damper

Parameter	Value	Parameter	Value	Parameter	Value
$c_{0,\mathrm{a}}$	0.08 kN·s/mm	α_{a}	0.20 kN/mm	k_{xy}	0.0 kN/mm
$c_{0,\mathrm{b}}$	0.32 kN·s/mm	α_{b}	0.30 kN/mm	k_x	0.0 kN/mm
$c_{0,\mathrm{c}}$	1.5 A^{-1}	α_{c}	1.0 A^{-1}	x_0	0.0 mm
$c_{1,\mathrm{a}}$	3.0 kN·s/mm	β_{a}, γ_{a}	0.050 mm^{-2}	A	300
$c_{1,\mathrm{b}}$	15.0 kN·s/mm	β_{b}, γ_{b}	0.002 mm^{-2}	n	2
$c_{1,\mathrm{c}}$	2.0 A^{-1}	β_{c}, γ_{c}	5.2 A^{-1}		

7.2 Multi-Interval PSO for Dynamic Excitations (MI-PSO)

A suite of at least three appropriate ground motions shall be considered for seismic design as per ASCE/SEI 7-10 (ASCE/SEI, 2010). The typical practice in structural design is to use not less than seven ground motion records for the prediction of mean response according to the acceptance criteria of ASCE/SEI 7-10 (ASCE/SEI, 2010). The efficiency of PSO algorithms are greatly reduced when considering the optimal design against a large number of ground motion records or other dynamic excitations.

The design variables and dynamic excitations can be viewed as two sets of variables with competing influence on the objective. For example, the optimization algorithm should seek design variables that minimize the objective function while at the same time seek the excitations that maximize the objective function (i.e., worst case loading). If the optimization procedure simultaneously selects the variables and excitations that minimize the objective function, then the worst-case excitations are not considered.

For optimization problems where the variables should minimize and the excitations should maximize the objective function, the most direct but inefficient way is to run through all dynamic excitations. Alternatively, in Chapter 6, a method to estimate the worst-case dynamic excitations from a larger set is proposed by investigating the relationship of optimization variables, input excitations, and objective functions. The efficiency of this method depends on the number of variables and the discrete evaluation points selected for each variable, creating a test matrix. Although pre-determining the governing excitations improves the optimization efficiency for simple systems under a small to medium numbers of excitations, this method is time-consuming when

considering a complex system with several design variables under a large number of earthquakes since the number of tests is proportional to the numbers of variables squared. In addition, this method is not intelligent since the worst excitation candidates are not determined during optimization. I.e., the worst-case excitations are predetermined and selected for use in the optimization. In this section, a multi-interval PSO (MI-PSO) algorithm is proposed to guide the solution searching during optimization with the capability to iteratively update the worst-case dynamic excitations.

The first step of MI-PSO is to divide the entire optimization run into intervals. Each interval contains a predefined number $i_{interval}$ of iterations of PSO. Only a small set of N excitations are selected as the active input excitations during each interval from a larger group of M design excitations. The initial active input excitations are determined by checking all M design excitations with a random set of design variables and selecting those N that result in the worst objective function values. The optimization continues within an interval only considering active input excitations. At the end of each interval, the best design from that interval is evaluated under all M design excitations to determine the N active input excitations for the following interval. The phase between intervals is called the excitation update phase.

During the excitation update, three cases are possible: (Case 1) the update of one or more (but not all) active input excitations, (Case 2) the updates of all active input excitations, and (Case 3) no update of active input excitations. For Cases 1 and 2, the initialization procedure for particles at the next interval is the same. One particle will assume the position (and velocity) from the update phase while also assuming the worst cost determined from all M excitations during the update phase. The global best position

and cost are then adopted from that particle. All other particle positions and velocities are reset to a random value, consistent with the PSO initialization procedure. Unique to Case 2, a total $N + 1$ excitations will be considered as the active input excitations for the following interval. The $N + 1$ records include the N worst excitations found during the update phase as well as the worst active input excitation from the previous interval. This is a temporary increase in the number of active excitations to ensure continuity between iterations of at least one excitation. For Case 3, the reset trigger for both particle positions and objectives is disabled. The active excitations remain the worst loading cases and will continue to be active in the following interval.

After sufficient intervals, the worst case excitation is found and the optimal solution against the worst scenario is determined. A flowchart of the MI-PSO method is shown in Figure 7.5 assuming $N = 2$ excitations. The details of block of PSO is depicted in Figure 6.2. Figure 7.6 shows the relationship of the objective and intervals or iterations. The excitations are updated at each interval while the system variables are optimized within each interval. Convergence will be non-monotonic as new worst-case excitations are discovered.

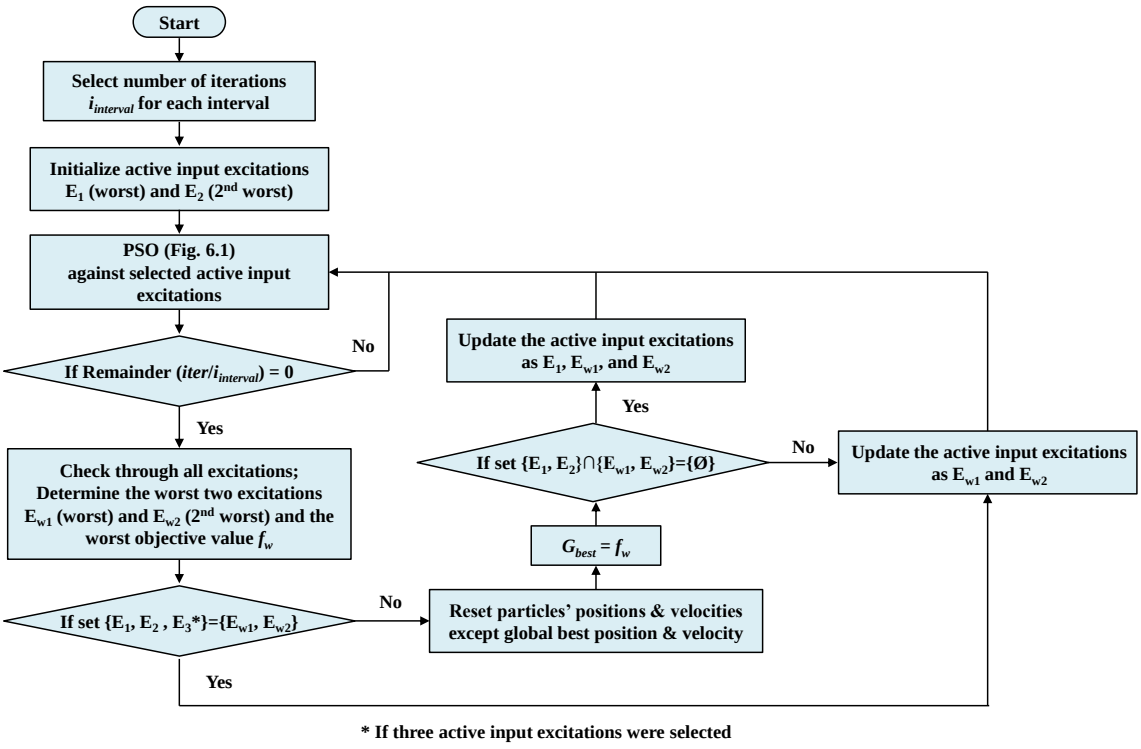

Figure 7.5 Flowchart of MI-PSO assuming N = 2 excitations

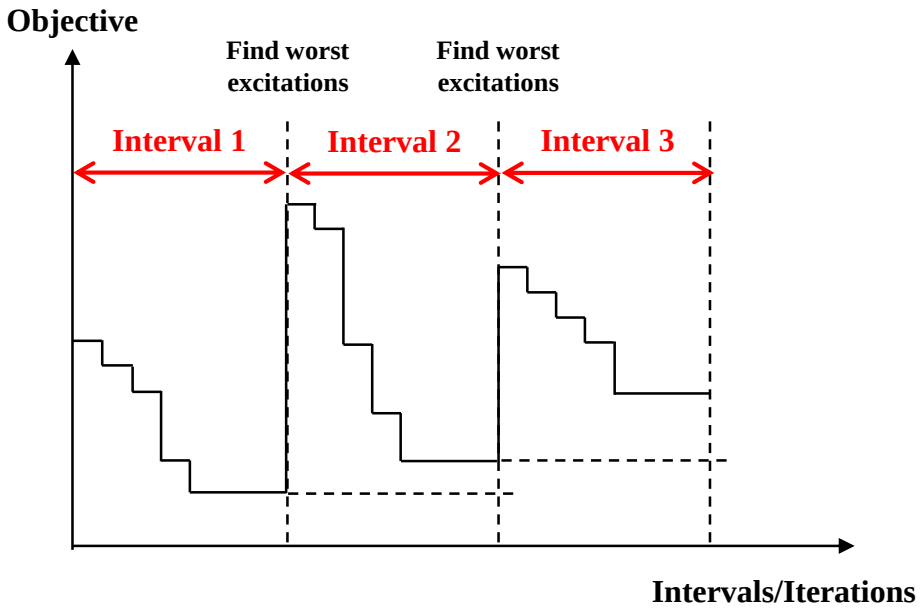

Figure 7.6 Relationship of objective and intervals

To illustrate the efficiency of the proposed MI-PSO for multiple dynamic excitations, the running time is estimated and compared to the other two methods listed below.

1. Method of exhaustion (ME). The optimization is conducted through running through all design excitations;
2. Discrete relationship (DR). A discrete relationship of optimization variables, input excitations, and objective is investigated first to narrow down the worst dynamic excitation candidates. The optimization is then conducted through running through the selected excitations; and
3. The proposed MI-PSO.

The equations to calculate the running time T are shown in Eq. 7.10, Eq. 7.11, and Eq. 7.12 for the ME, DR, and MI-PSO methods, respectively.

$$T(\text{ME}) = (n_{EQ} \cdot n_{swarm} \cdot iter + n_{EQ}) \cdot t \tag{7.10}$$

$$T(\text{DR}) = (n_{EQ} \cdot n_{dp}^{var} + n_{EQ,se} \cdot n_{swarm} \cdot iter + n_{EQ}) \cdot t \tag{7.11}$$

$$T(\text{MI - PSO}) = \left\{ n_{EQ} \cdot \left[\text{roundup}\left(\frac{iter}{i_{interval}} \right) + 1 \right] + 2 \cdot n_{swarm} \cdot iter \right\} \cdot t \tag{7.12}$$

where n_{EQ} is numbers of design excitations, n_{swarm} is the swarm size, *iter* is maximum iterations, n_{dp} is numbers of discrete points selected for each variable, *var* is numbers of control variables for optimization, $n_{EQ,se}$ is numbers of selected worst excitation candidates from the discrete relationship, $i_{interval}$ is the iterations contained in each interval, and t is the running time for a cycle of testing. Assuming that the optimal solution is achieved in the same number of iterations and that only the worst two

excitations determined in each interval are active in RTHS, a rough estimation for the optimization runtime can be calculated. Table 7.3 shows the comparison of running time with parameters given in the table. It can be clearly seen that the running time is greatly reduced through MI-PSO approach when a complex system (e.g., more control variables) is studied.

Table 7.3 Summary and comparison of running time

n_{EQ}	n_{dp}	*var*	n_{swarm}	*iter*	$n_{EQ,se}$	$i_{interval}$	*t* (hours)	T_ME (hours)	T_DR (hours)	T_MI-PSO (hours)
20	5	2	5	50	4	20	0.0083	41.83	12.67	4.83
40	5	2	5	50	4	20	0.0083	83.67	17.00	5.50
20	5	4	5	50	4	20	0.0083	41.83	112.67	4.83
20	10	2	5	50	4	20	0.0083	41.83	25.17	4.83
40	5	4	5	50	4	20	0.0083	83.67	217.00	5.50

7.3 Experimental Setup

The proposed CPSO technique is applied to the optimal control of a large-scale MR damper for seismic protection of a base-isolated structure through RTHS. The setup consists of a servo-hydraulic actuator, a large-scale MR damper as the experimental substructure, and a digital signal processor running the numerical model, numerical integration, and semi-active controller. The building model, MR damper properties, and semi-active controller are presented in Section 7.1. The specimen and equipment are located in the Structural Engineering Laboratory at the University of Maryland College Park.

7.3.1 Large-scale structural testing facility

A servo-hydraulic controlled test system is used for this large-scale testing, including a MTS actuator with displacement feedback, a 60 gpm hydraulic power supply, a 50 gpm hydraulic service manifold, a 4-channel servo-control system with FlexTest 60 controller,

and MTS test software. The actuator has a maximum capacity of 55 kips. The stroke is ±5 inches. The actuator and MR damper are mounted on steel angle plates placed on top of I-beam as shown in Figure 7.7. The I-beam is secured to the strong floor using tie-downs to prevent flexure. The actuator and MR damper are connected through a plate with a large threaded rod and four high strength bolts.

Figure 7.7 Testing setup of large-scale MR damper for RTHS testing

The displacement of the actuator is measured using an internal LVDT. A load cell is mounted in line with the actuator measuring the restoring force of the MR damper. The current in the MR damper circuit is measured using a Tectronix model A622 current probe.

The control hardware of RTHS consists of a dSPACE DS1103 Controller board and a windows-based host PC as mentioned in Section 3.3. The board is used perform numerical integration for the numerical substructure, apply the outer-loop actuator controller, and control the MR damper current based on semi-active control algorithms. The MTS controller is configured to accept analog external commands from the dSPACE controller via a BNC cable. The LVDT and load cell are conditioned by the MTS controller and analog signals are passed to the dSPACE controller via BNC cables. An

analog low-pass filter with a cutoff frequency of 500 Hz is used to filter the LVDT and load cell signals before they are sampled by the dSPACE controller.

7.3.2 Actuator identification and controller development

System identification of the servo-hydraulic actuator with the MR damper specimen is performed using a 0-30 Hz band-limited white noise voltage command to the actuator and the measured displacement of the actuator. Because the current to the MR damper can change during RTHS testing, the servo-hydraulic dynamics are investigated at multiple current levels, including a current of 0 Amps for passive-off mode and a current of 2.5 Amps for passive-on mode. The results are then averaged to create a third transfer function appropriate for the semi-active mode with changing currents. Figure 7.8 shows the averaged displacement transfer function of the servo-hydraulic system along with the corresponding identified model. A nonparametric system identification technique MFDID (Kim et al., 2005) was used to fit the experimental transfer function data to a single-input single-output model with poles and zeros. A model with 3 poles and no zeros shown in Eq. 7.12 is found sufficient to accurately represent the dynamics of the servo-hydraulic system over the desired frequency range.

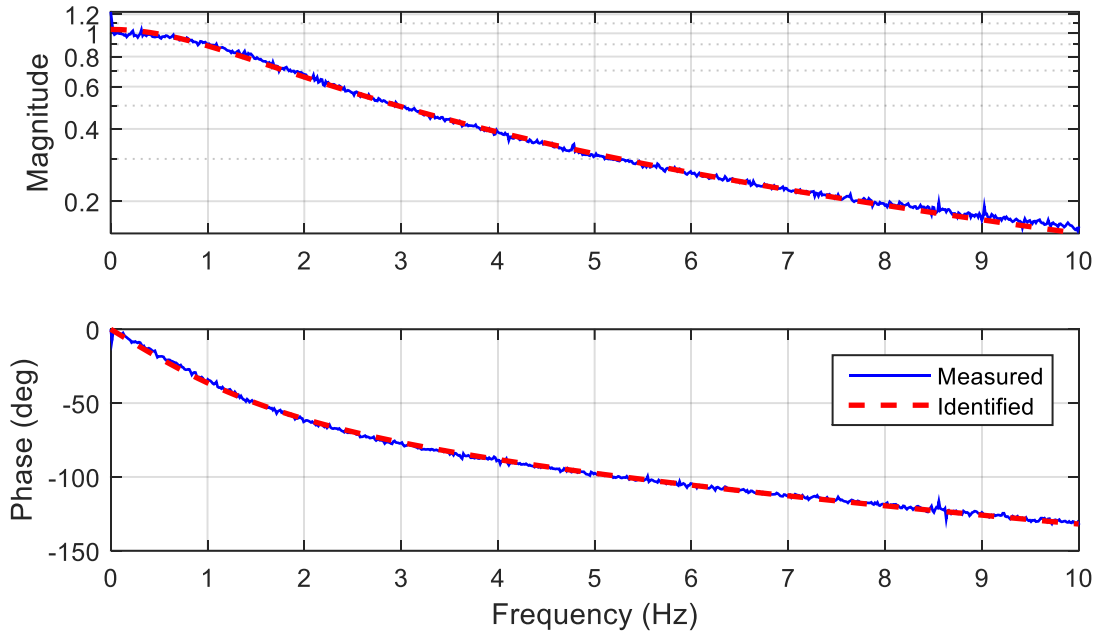

Figure 7.8 Measured and identified transfer function of the actuator

$$G_{xu} = \frac{1.526 \times 10^5}{(s + 10.38)(s^2 + 202.6s + 1.416 \times 10^4)} \tag{7.13}$$

A model-based strategy proposed by Phillips, et al. (2014) is used for the actuator controller design and demonstrated to provide favorable tracking performance. The model-based feedforward controller based on an inverse of the identified servo-hydraulic model shown in Eq. 7.12 to cancel the modeled dynamics. Since the model has three poles and no zeros, the inverse of the model is improper. Direct implementation of the feedforward controller, which has three zeros and no poles, requires the calculation of displacement, velocity, acceleration, and jerk (derivative of the acceleration). Methods for calculating these higher-order derivatives include the central difference method (CDM) with linear acceleration extrapolation and the backward-difference method (BDM). In this study, higher-order derivatives are estimated in real-time using the CDM

with linear acceleration extrapolation (Phillips and Spencer, 2012). The feedforward controller of the actuator model in Eq. 7.12 is determined as shown:

$$u_{FF,i} = 6.40\times10^{4}\,x_i^I - 1.86\times10^{5}\,x_{i-1}^I + 1.80\times10^{5}\,x_{i-2}^I - 5.81\times10^{4}\,x_{i-3}^I \qquad (7.13)$$

Between for each time step *i*, numerical integration is performed and the desired displacement x_i is determined. The corresponding actuator command $u_{FF,i}$ is determined from Eq. 7.13. At each time step *i*, the actuator command $u_{FF,i}$ is sent to the servo-controller to achieve x_i and restoring force is measured.

7.3.3 Earthquake ground motions

A set of 20 earthquakes, LA01-LA20 introduced in Chapter 6 (Section 6.3.2), are selected as the input ground motions to the structure. All earthquake records are scaled down to 20% of the original amplitude in the RTHS testing due to the stroke limitations of the actuator.

7.4 Optimal Performance of the Nonlinear System using CPSO

This section presents the optimization of the MR damper's primary semi-active controller for the seismic protection of the 5-story base-isolated structure. The two design variables considered are the loss factor η and radial frequency ω_f given in Eq. 7.4. PSO is used to guide the search of the solution space. Optimal design is first investigated under a single earthquake to validate the performance of the proposed CPSO for nonlinear system with multiple design variables. Then, the optimization of the nonlinear system against a set of 20 design earthquakes are investigated. The MI-PSO proposed in Section 7.2 is used to guide the solution searching under multiple excitations. In all cases, the objective function is minimizing the maximum structural absolute acceleration considering all DOF.

A constraint is placed on the base drift, restricting it to within 10 cm for valid solutions (i.e., solutions beyond this limit are rejected).

In addition, all optimal results are compared to optimal results determined through numerical simulation alone. The phenomenological MR damper model presented in Section 7.1 with parameters from Table 7.2 is used to represent the MR damper in numerical simulations. The two cases for comparison are listed as below:

1. Optimization of the 5-story base-isolated structure with semi-active MR damper model in numerical simulation (OPT-SIM); and
2. Cyber-physical optimization of the 5-story base-isolated structure with semi-active MR damper through substructure RTHS, where the MR damper is physically tested and the 5-story base-isolated structure is numerically simulated (CPSO-RTHS).

Different optimal solutions and performance are expected between OPT-SIM and CPSO-RTHS for some cases since the numerical MR damper model does not accurately capture the dynamics of the device for responses outside of the range for which it was calibrated.

7.4.1 Application of CPSO for seismic protection of nonlinear system under single earthquake

The seismic performance of the 5-story base-isolated structure subjected to LA02 is first investigated. The MR damper installed at base level is optimized using PSO through the proposed CPSO. A swarm of five particles and a maximum iteration of 50 are selected. Each particle corresponds to a set of two variables, η and ω_f. The objective is to minimize maximum structural acceleration and restrict isolation drift under 10 cm for safety concern. The intensity of earthquake LA02 is selected as 20% in this study.

Figure 7.9 shows the particle positions over iterations for the optimization in CPSO-RTHS. The optimal positions of both η and ω_f are found as 0.27 and 4.23 rad/s, respectively. The global best cost history is shown in Figure 7.10 with a minimum maximum structural acceleration of 0.46 m/s^2 achieved. The convergence of multiple variables and objective function can be clearly seen from both figures.

The results of the RTHS for the optimal solution will be investigated in detail. Figure 7.11 shows the actuator tracking performance using the feedforward controller in Eq. 7.10. Good agreement is observed between desired and measured responses. Also, drift of base isolation is shown to be within 10 cm. Figure 7.12 shows the MR damper control performance, i.e., the performance of the secondary semi-active controller to achieve the desired force. The hysteresis of MR damper is shown in Figure 7.13. Generally, good agreement is observed between desired and measured behavior. Additionally, MR damper exhibits an elliptical hysteresis, consistent with ideal rate-independent linear damping.

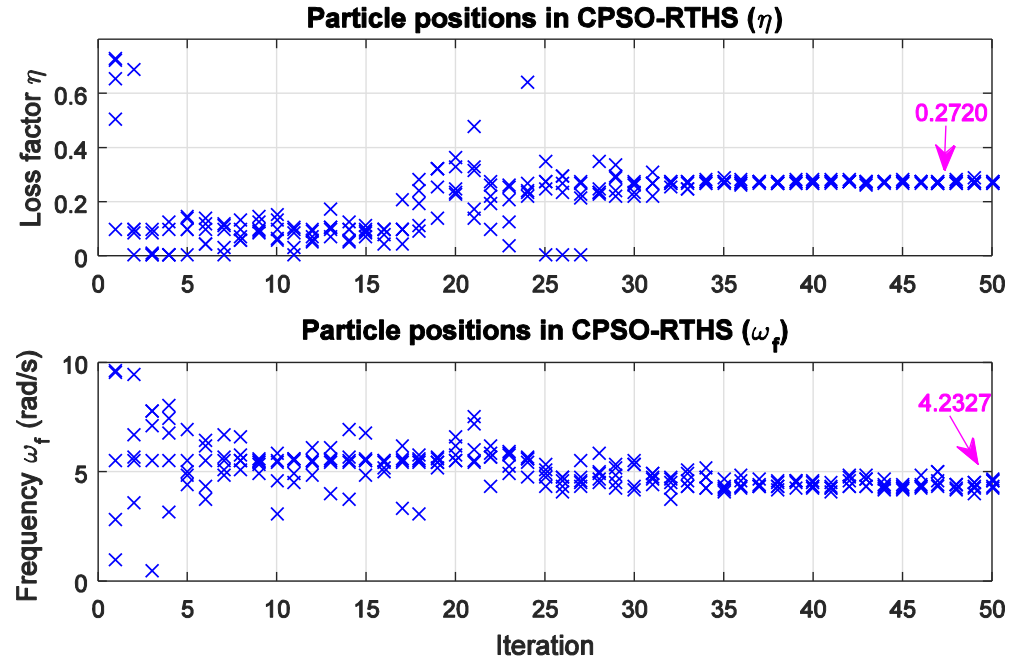

Figure 7.9 Particle positions in CPSO-RTHS

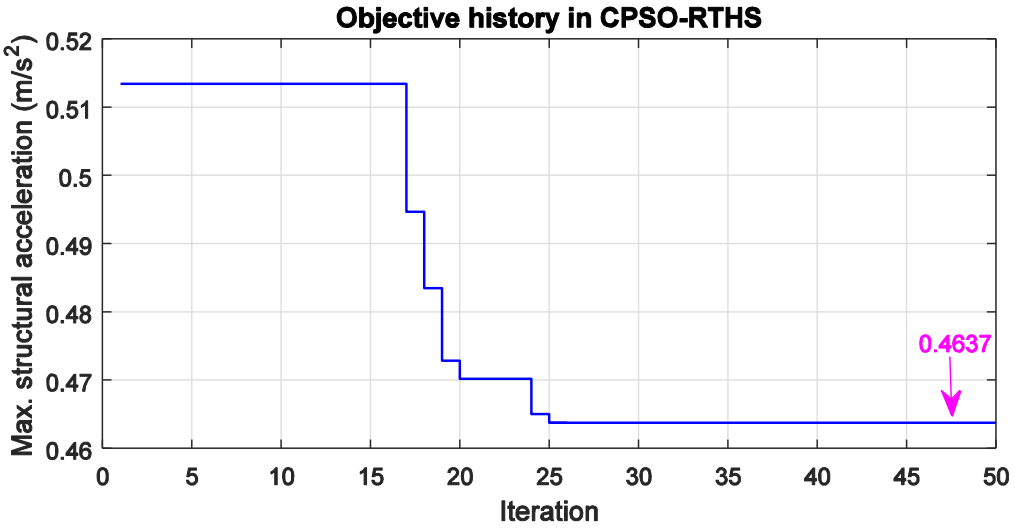

Figure 7.10 Global best cost history in CPSO-RTHS

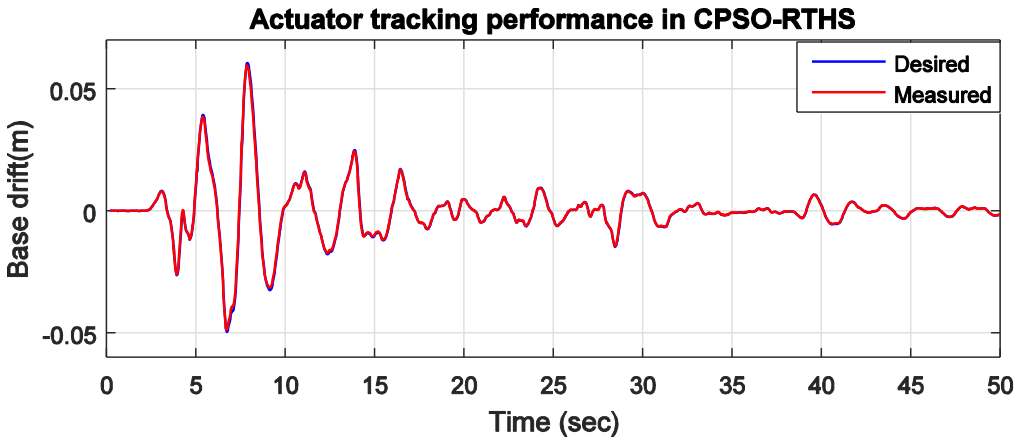

Figure 7.11 Performance of actuator control in CPSO-RTHS

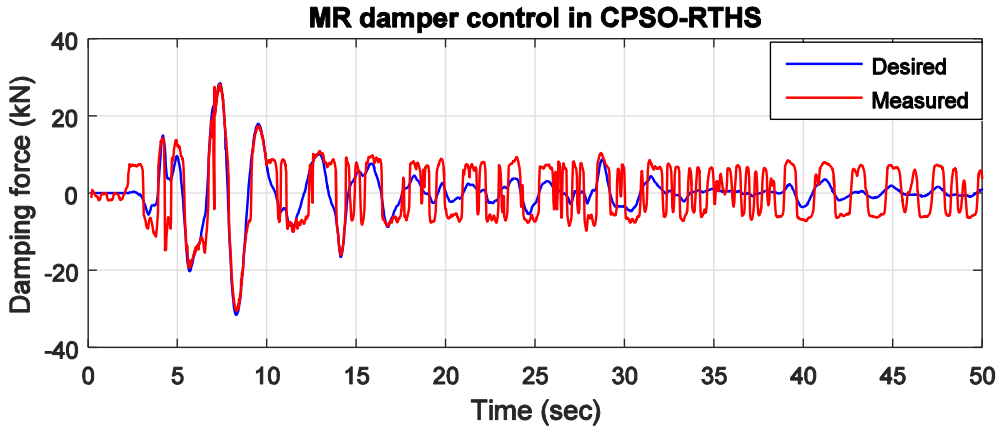

Figure 7.12 MR damper control performance in CPSO-RTHS

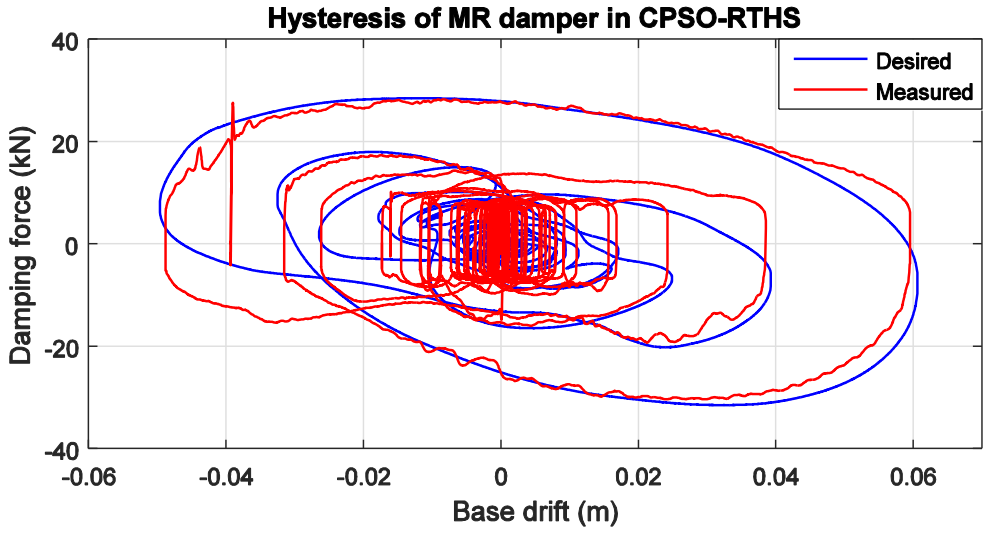

Figure 7.13 Hysteresis of MR damper in CPSO-RTHS

The results from CPSO-RTHS are compared with optimal results obtained in OPT-SIM. Figure 7.14 shows the particle positions over iterations for both variables in OPT-SIM and Figure 7.15 shows the iteration history of the objective in OPT-SIM. The maximum structural acceleration is minimized to 0.46 m/s^2 with an optimal control of η as 0.27 and ω_f as 5.54 rad/s. Different base drift is observed between OPT-SIM and CPSO-RTHS as shown in Figure 7.16. Figure 7.17 shows the comparison of the optimal MR damper performance from numerical simulation and experimental testing. The damping force in the numerical model is smaller than the physical MR damper at their respective optimal solutions. The difference between OPT-SIM and CPSO-RTHS can be further observed in the hysteresis comparison shown in Figure 7.18. The error is mainly due to the inaccuracy of MR damper model when the damping force is relatively small. This study demonstrates the benefits of the proposed CPSO framework in structural evaluation and optimization when the numerical model cannot accurately represent the physical behavior of structural components.

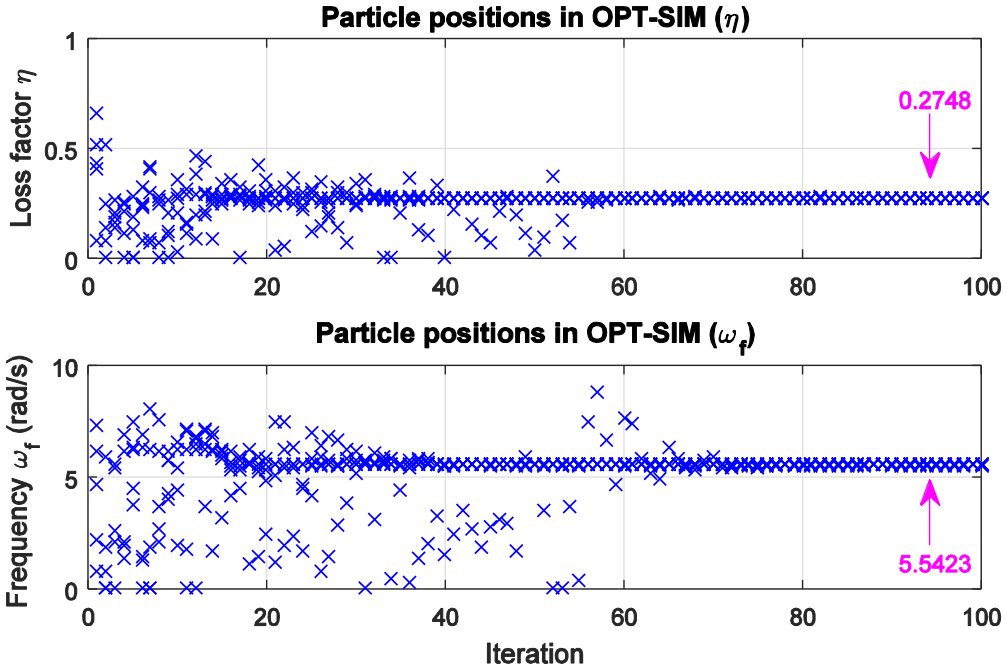

Figure 7.14 Particle positions in OPT-SIM

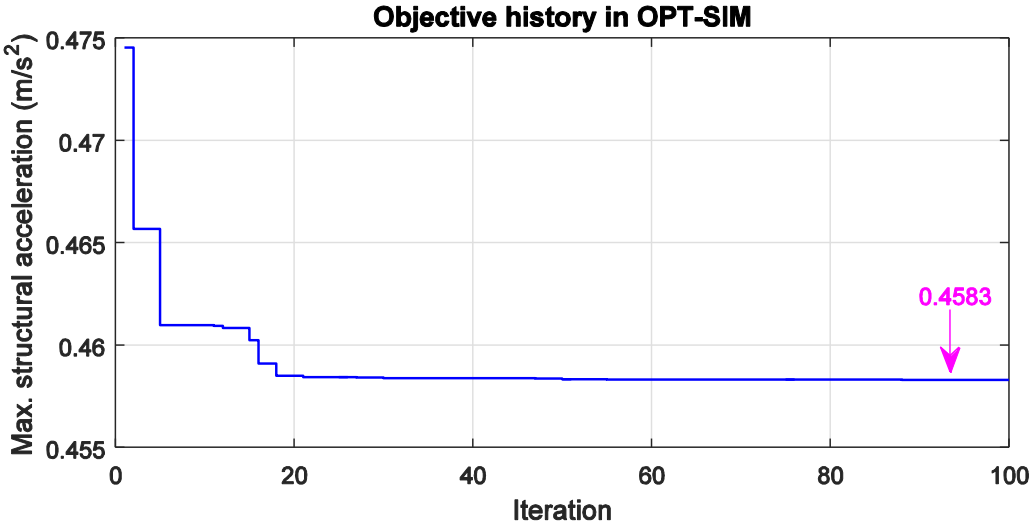

Figure 7.15 Iteration history of objective function in OPT-SIM

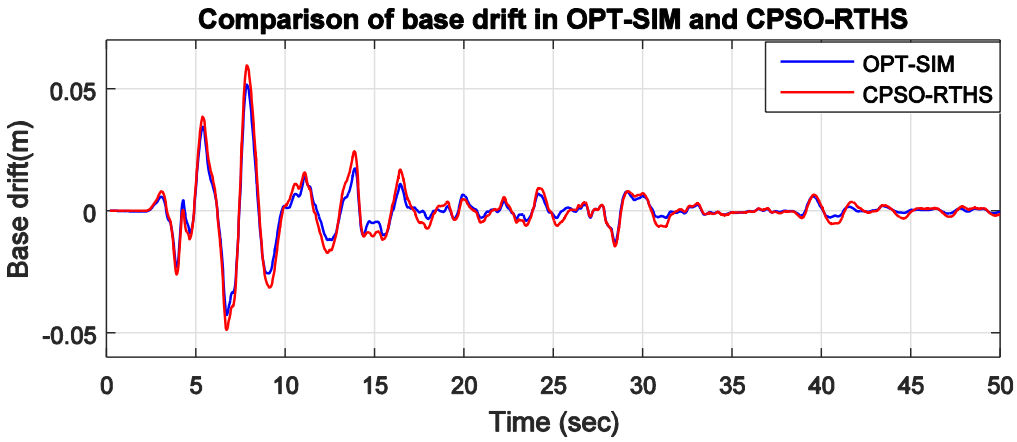

Figure 7.16 Base drift comparison between OPT-SIM and CPSO-RTHS

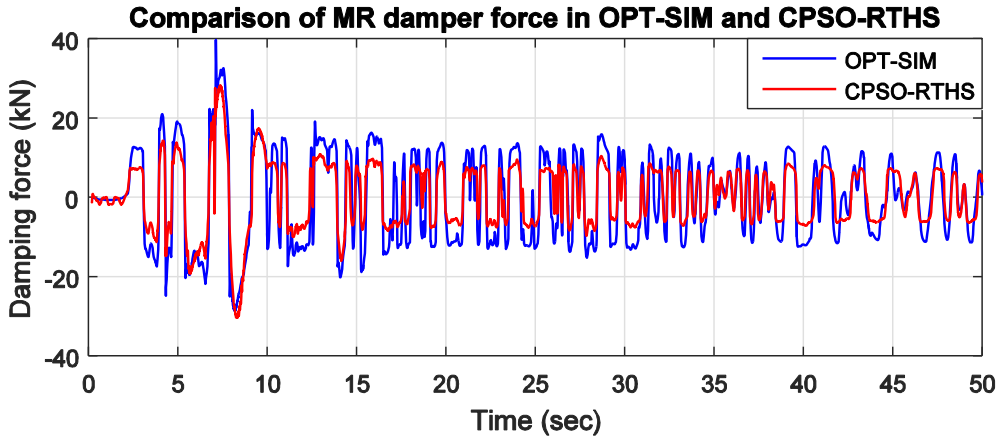

Figure 7.17 Comparison of MR damper force between OPT-SIM and CPSO-RTHS

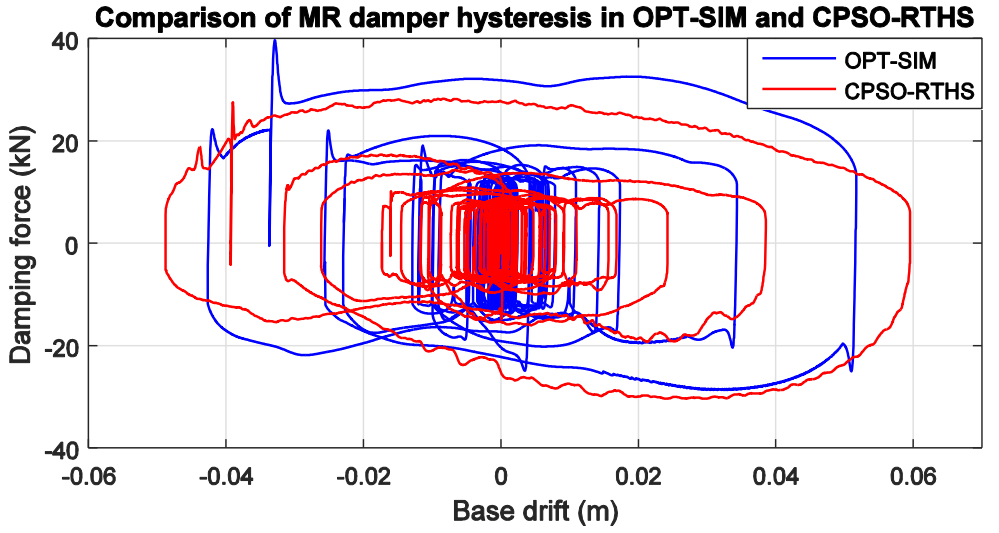

Figure 7.18 Comparison of MR damper hysteresis between OPT-SIM and CPSO-RTHS

7.4.2 Application of CPSO for seismic protection of nonlinear system under a set of 20 design earthquakes

The optimal seismic design of the 5-story base-isolated structure with a MR damper at base is conducted through the proposed CPSO framework considering a set of 20 design earthquakes with the response spectrum matching the design spectrum near the site. The MI-PSO proposed in Section 7.2 is used to guide the solution searching during optimization with the capability to efficiently update the worst-case earthquakes. The structural performance is evaluated under all design earthquakes between each interval to determine the worst-case earthquakes for use in the next interval. An interval of 20 iterations is selected, meaning the worst earthquake candidates are updated every 20 iterations. Optimization within each interval is always under the worst earthquake candidates.

Figure 7.19 shows the iteration history of the active input earthquakes during the optimization process for CPSO-RTHS. The red line represents the worst earthquake determined for an interval while the blue one represents the second worst earthquake. The initial two worst earthquakes are determined by checking all 20 LA earthquakes with a random position for the design variables. From Figure 7.19, it can be seen that the initial input active earthquakes are LA15 & LA14. For intervals 2 and 3, LA15 & LA16 and LA20 & LA15 are selected as the active input earthquakes respectively. For interval 4, the active input earthquakes are not updated although the order is changed. Thus, the swarm continues converging on the best position without resetting the particle positions until the end of iteration. The updates of active input earthquakes also can be distinguished from the iteration history of particle positions and objectives as shown in

Figure 7.20 and Figure 7.21, respectively. From Figure 7.20, we can see the particle positions are reset at the start of interval 2 (21st iteration) and interval 3 (41th iteration) where the active input earthquakes are updated. From Figure 7.21, it can be seen that the objective jumps to a higher value at the start of interval 2 and interval 3 reflecting a worse earthquake is found. The optimal η and ω_f are found as 0.78 and 3.22 rad/s with a minimum maximum structural acceleration of 0.51 m/s^2 under all twenty design earthquakes.

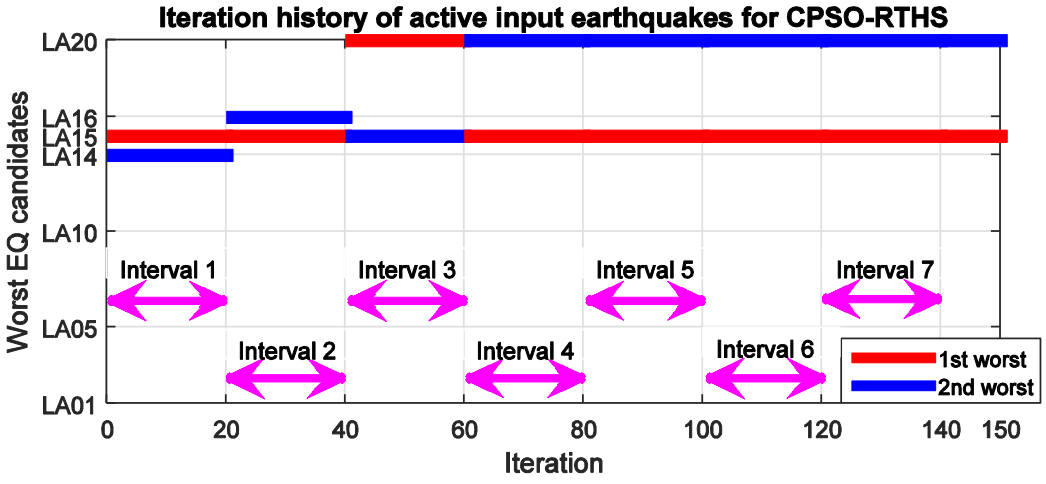

Figure 7.19 Active input earthquakes in each interval in CPSO-RTHS

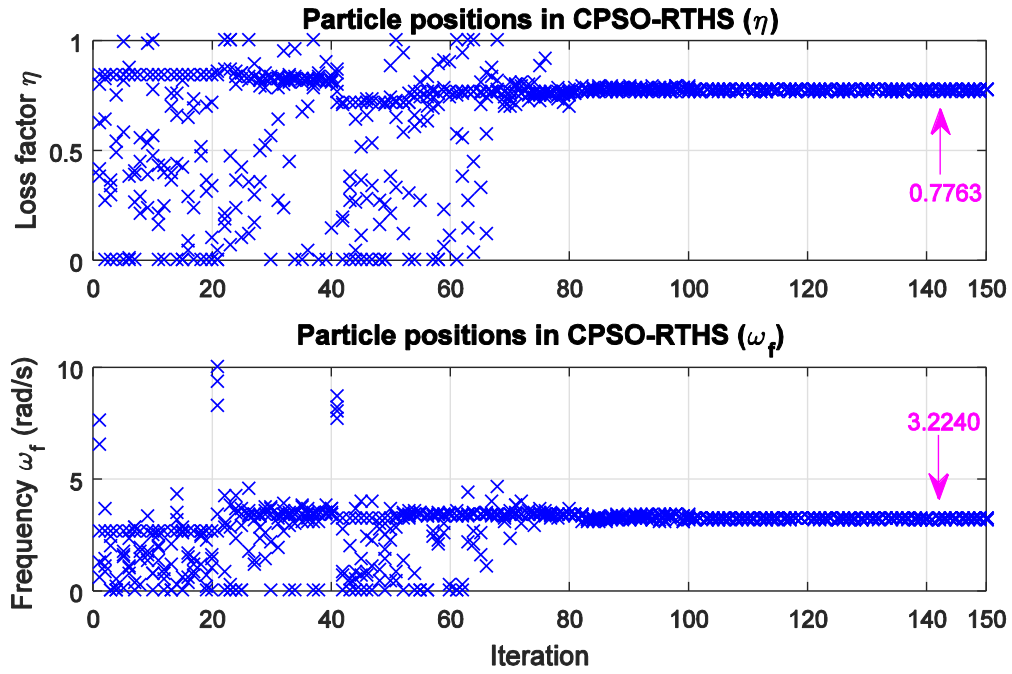

Figure 7.20 Particle positions in CPSO-RTHS

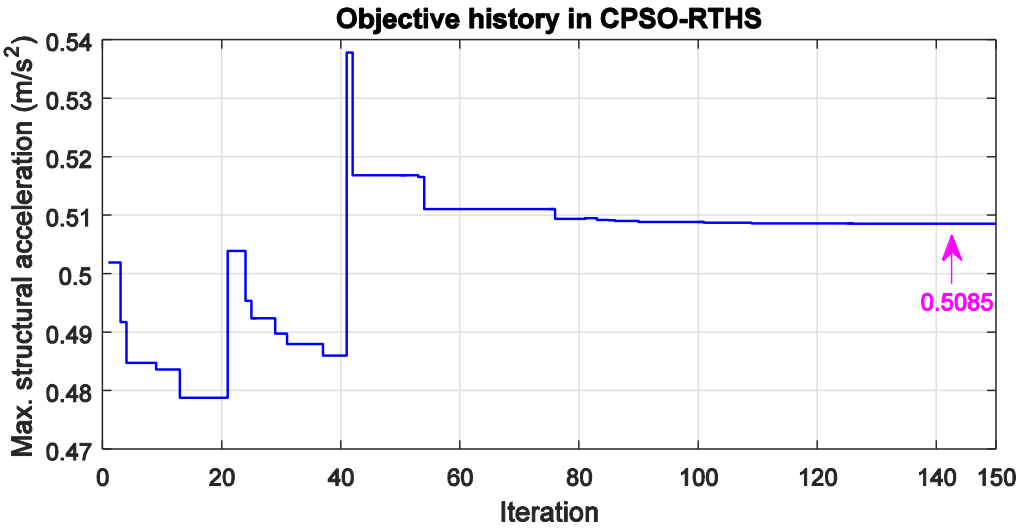

Figure 7.21 Iteration history of objective function in CPSO-RTHS

The optimal structural performance achieved through CPSO-RTHS is presented under the worst input active earthquake LA15. First, the control performance is shown in Figure 7.22 with very good agreement between desired and measured displacement, reflecting the accurate boundary condition provided by the servo-hydraulic actuator. The secondary

semi-active controller of MR damper also performs well generating and tracking the desired damping force as shown in Figure 7.23. Figure 7.24 shows the input command to MR damper from the semi-active controller. The hysteresis of MR damper is shown in Figure 7.25 with good agreement between the desired and measured signals.

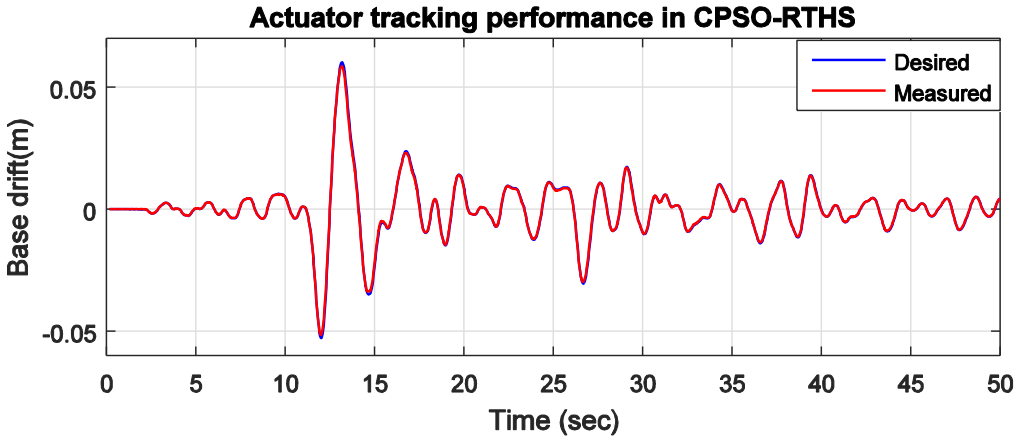

Figure 7.22 Performance of actuator control in CPSO-RTHS

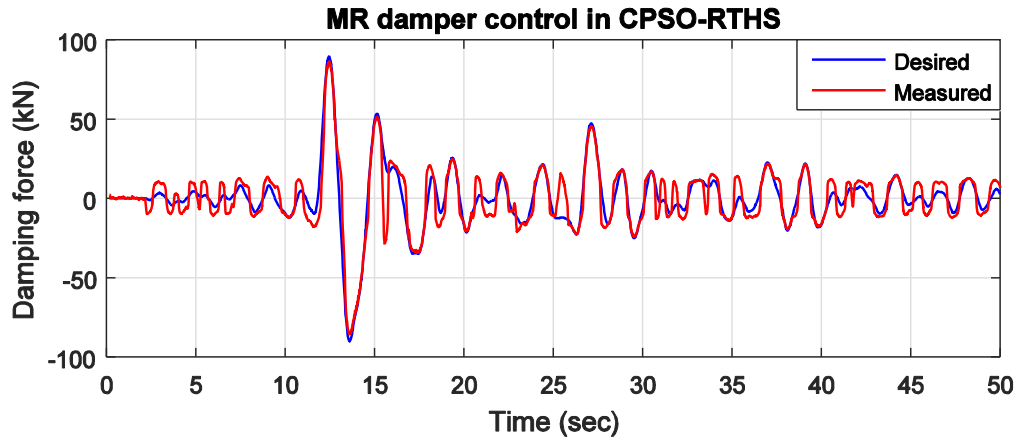

Figure 7.23 MR damper control performance in CPSO-RTHS

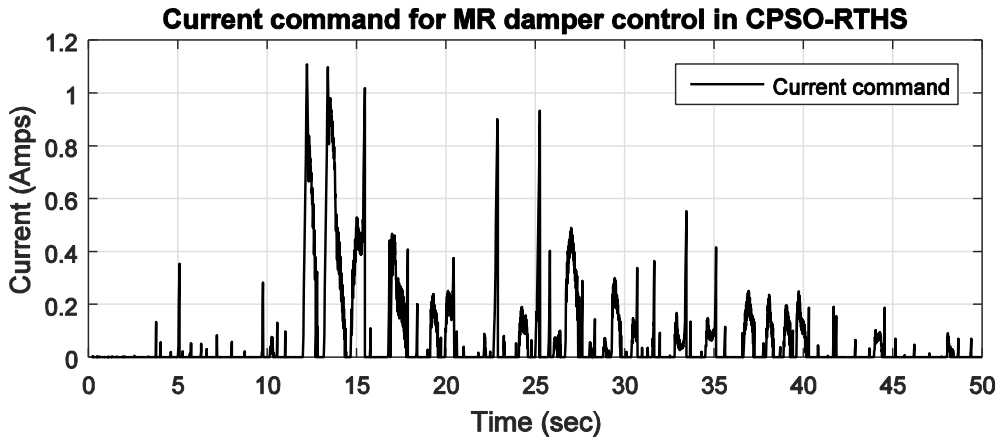

Figure 7.24 Current command to MR damper in CPSO-RTHS

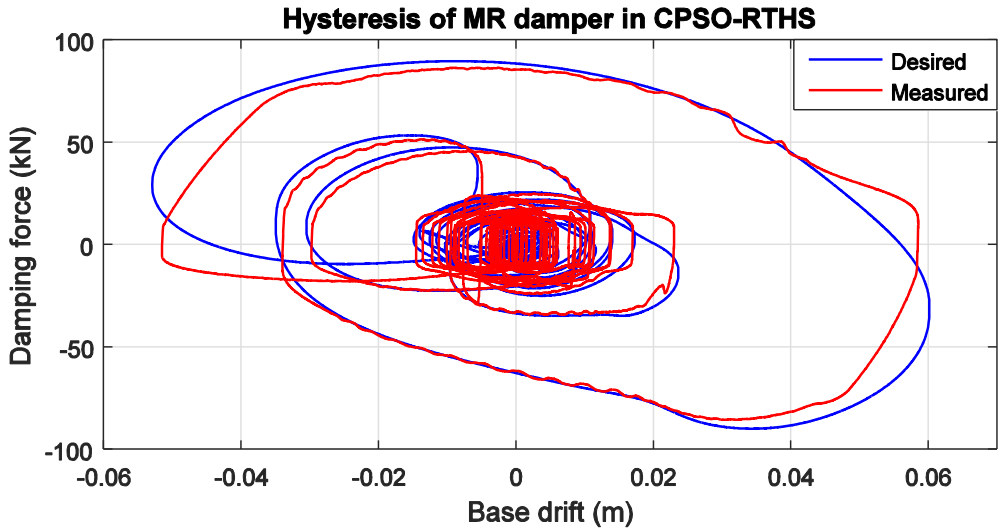

Figure 7.25 Hysteresis of MR damper in CPSO-RTHS

The numerical results in OPT-SIM are presented and compared to the results using CPSO-RTHS. Figure 7.26 shows the iteration history of the active input earthquakes for OPT-SIM. The active input earthquakes are updated during the first four intervals. Three active input earthquakes are determined during interval 2 and interval 4. From interval 5, optimization continues processing without finding new worse earthquakes. Figure 7.27 and Figure 7.28 show the iteration history of particle positions and objective respectively. It can be seen that the particles converge to the optimal

solution of η as 0.81 and ω_f as 3.30 rad/s with a minimum maximum structural acceleration of 0.56 m/s^2 under all 20 design earthquakes. Although the optimal η and ω_f are found to be similar in both OPT-SIM and CPSO-RTHS, the optimal structural acceleration is much different. Figure 7.29 and Figure 7.30 show the comparison of base drift and MR damper force respectively in OPT-SIM and CPSO-RTHS. As compared to the previous optimization under LA02 alone, the MR damper force is higher. At higher forces, the MR damper model is found to be more accurate. Figure 7.31 shows the comparison of MR damper hysteresis in OPT-SIM and CPSO-RTHS. A good match is observed in this case.

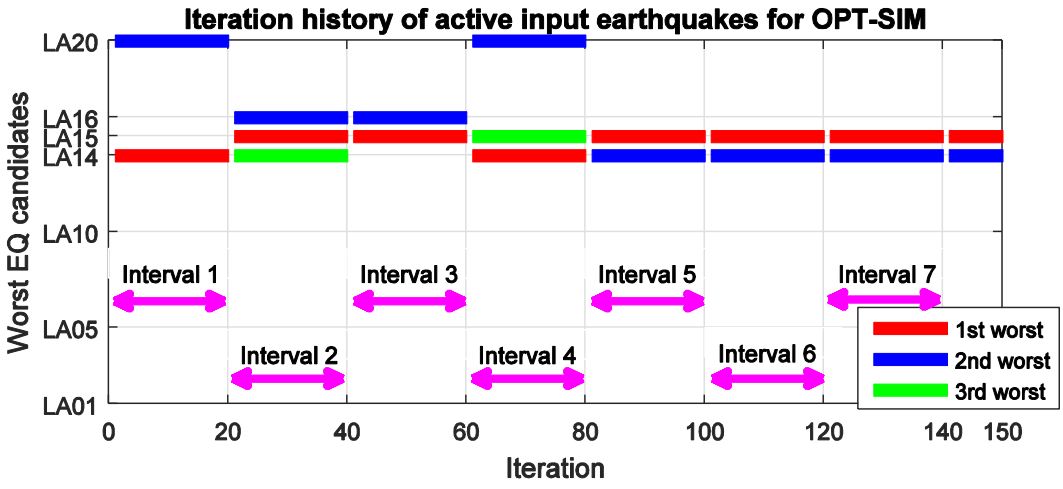

Figure 7.26 Active input earthquakes in each interval in OPT-SIM

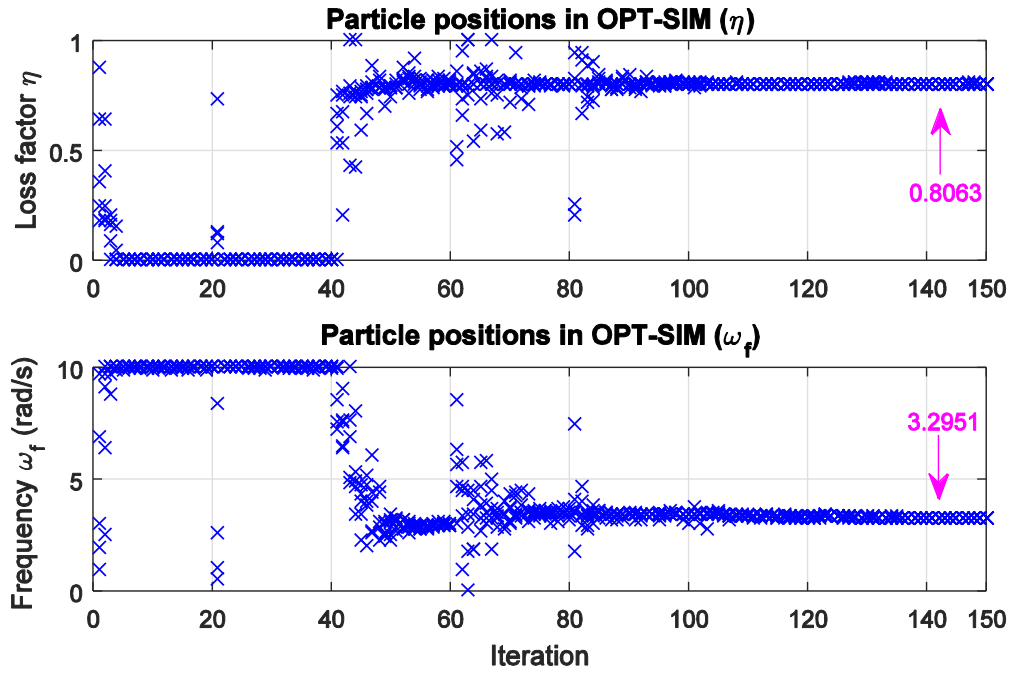

Figure 7.27 Particle positions in OPT-SIM

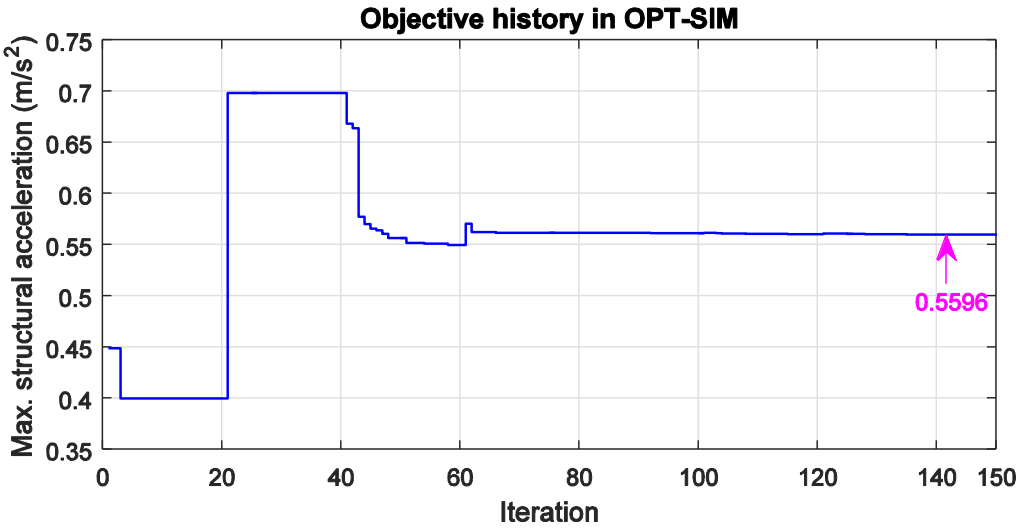

Figure 7.28 Iteration history of objective function in OPT-SIM

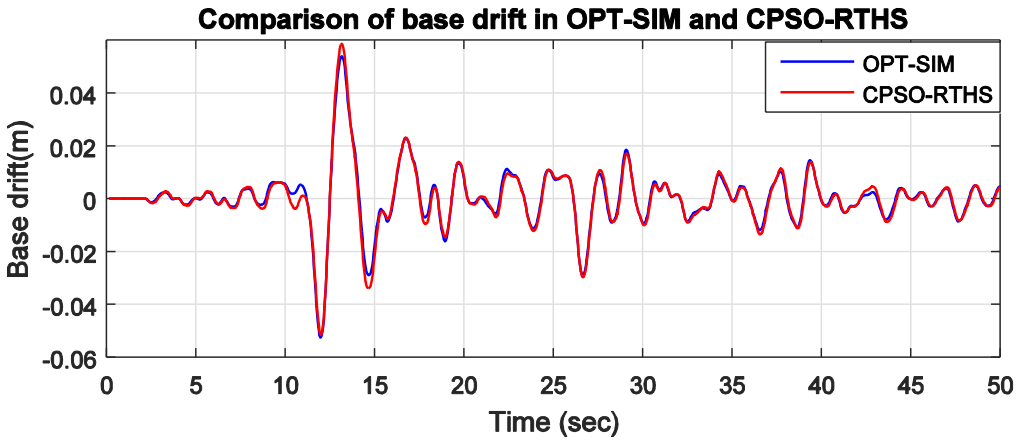

Figure 7.29 Base drift comparison between OPT-SIM and CPSO-RTHS

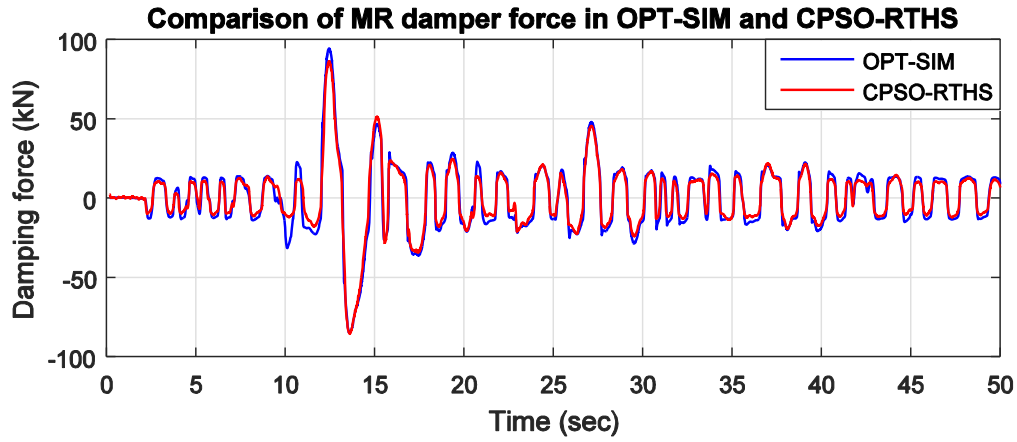

Figure 7.30 Comparison of MR damper force between OPT-SIM and CPSO-RTHS

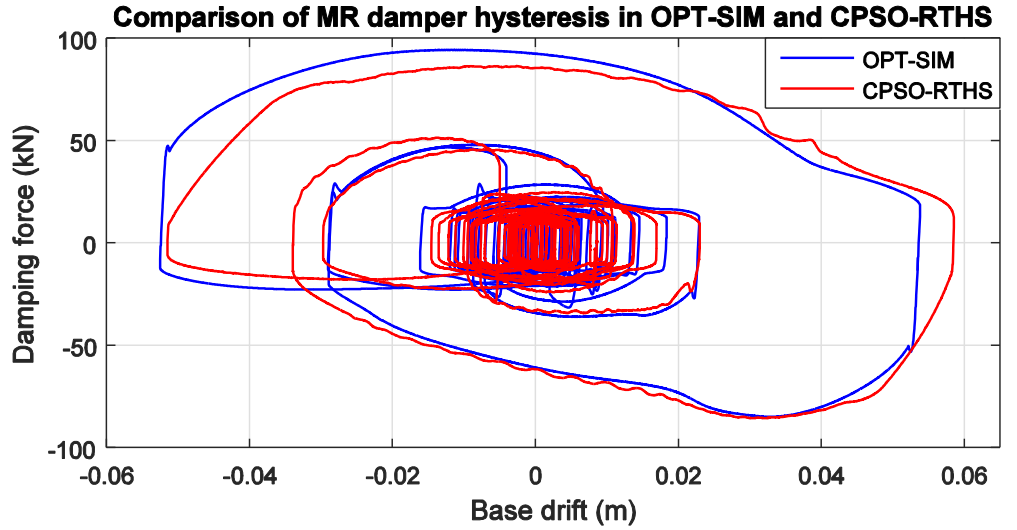

Figure 7.31 Comparison of MR damper hysteresis between OPT-SIM and CPSO-RTHS

7.5 Summary

This chapter presents the application of the CPSO framework proposed in previous chapter for the seismic protection of a nonlinear system using substructure RTHS. The MR damper is physically tested while the 5-story base-isolated structure is numerically simulated. The total structural response is evaluated using RTHS. Through the CPSO, the MR damper installed at base level is optimized to achieve the minimum peak structural absolute acceleration considering all DOF under design the earthquakes. A semi-active controller is used to control the MR damper behavior. Two variables involved are loss factor η and radial frequency ω_f, which are optimized through CPSO framework.

The proposed CPSO framework is validated for structural optimization under single earthquake with a nonlinear specimen. To improve the efficiency of the CPSO for structural protection against multiple ground motion records, a MI-PSO approach is proposed. In MI-PSO, the optimization run is divided into intervals. Only the worst-case excitations, determined before an interval begins, are used to evaluate candidate solutions during that interval. The design variables are optimized within each interval. The efficiency of optimization is greatly increased especially for complex systems with multiple design variables against a large number of design excitations. A comparison of running time is presented to show the efficiency of different methods.

The optimal design of MR damper against single earthquake and a set of 20 design earthquakes is conducted and presented respectively. The optimal results using CPSO framework are compared with pure numerical simulation. It is found that the numerical model of MR damper is not sufficiently accurate to represent the real behavior

of MR damper in some cases, demonstrating the benefits of the proposed technique. This technique is a significant contribution to optimal structural design against multiple earthquakes or other natural hazards. In particular, when studying a device or behavior for which a numerical model is unavailable.

In summary, the proposed CPSO framework is a versatile and robust technique for structural design and control against multi-hazards. This technique combines the accuracy and efficiency of RTHS to cost-effectively evaluate structural performance and the benefits of numerically-driven optimization to efficiently explore different design alternatives and achieve an optimal design.

CHAPTER 8 CONCLUSIONS AND FUTURE STUDIES

8.1 Conclusions

This dissertation provides systematic studies on the development and validation of substructure RTHS using shake tables, novel techniques to increase RTHS stability by introducing artificial damping to an under-actuated physical specimen, and a cyber-physical substructure optimization framework using RTHS. This dissertation enables many more structures to be evaluated in cost-effective experimental frameworks including inter-story isolated structures and lightly damped structures. Additionally, the proposed cyber-physical substructure optimization procedure will instill more confidence that the solution space is being exhaustively and accurately explored by eliminating modeling error for complex components.

8.1.1 Substructure RTHS framework development and validation

This research proposes a simple and versatile shake table RTHS framework for accessing structural dynamic responses. The proposed RTHS framework is demonstrated to be effective and reliable for structures with low damping, an important development for shake table RTHS of realistic structures. The proposed framework includes a model-based feedforward-feedback controller for acceleration tracking. Modeled dynamics of the shake table, including the substantial coupling with the specimen (CSI), are included in the development of the feedforward and feedback controllers. In this application, the strong CSI, low damping, and large experimental substructure relative to the total structure led to considerable actuator control challenges. An accurately designed feedforward controller across all significant frequencies was found to provide excellent

performance which can be supplemented by a feedback controller for robustness in the presence of specimen or shake table nonlinearities.

The Kalman filter added to the RTHS loop prevented high frequency sensor noise from being introduced to the numerical substructure and leading to high-frequency commands to the shake table. The Kalman filter also avoided introducing phase lag associated with many filters that could lead to RTHS instability. In addition, a low-pass filter was added to the feedforward controller such that the controller was less sensitive to high frequency noise. The filter was designed such that it did not impact the performance of the controller over the frequency range of interest. The proposed framework was validated using a uni-axial shake table and two-story shear building specimen with low damping. The strategy for shake table control in the context of RTHS was verified to offer a good offline and online acceleration tracking performance. The effectiveness of proposed techniques on overall RTHS accuracy were verified through comparisons with numerical simulations. The results from RTHS and numerical simulations exhibit a good agreement for the linear structure, offering confidence toward broader application studies of shake table RTHS.

The proposed RTHS framework uses readily available equipment, providing a new experimental tool to laboratories worldwide. The dynamics of shake table should be identified with the specimen attached to accurately capture CSI. Additionally, specimen system identification should be carried out to implement any model-based filter such as the Kalman filter. Note that the Kalman filter and the Butterworth filter are not necessary and can be introduced as needed. These filtering techniques helped push the limits on RTHS capabilities.

8.1.2 Artificial specimen damping – a simple technique to increase RTHS stability

In RTHS, stability and accuracy is related to the ability of the actuator system to track the desired interface trajectory. Time delays and time lags can introduce negative damping which can supersede the inherent structural damping and lead to instability. In addition, the RTHS stability is sensitive to higher modes especially for those high-rise building models. RTHS stability can be improved by introducing damping to higher modes without changing the structural responses which are dominated by lower modes. Driven by this need, this dissertation proposes a novel technique to introduce artificial damping to a dynamic experimental specimen for both traditional shake table testing and shake table RTHS. The target damping of the experimental specimen is achieved through modified shake table control, greatly reducing labor and cost when compared to other methods to realize specimen damping. The proposed method does not alter the specimen stiffness or introduce nonlinearities. Additionally, the proposed technique can target specific modes, something that discrete devices cannot realize.

The proposed AD-FF method is a modification to a model-based feedforward shake table control strategy. Instead of tracking the input acceleration, the AD-FF controller generates an acceleration that achieves the target structure behavior, i.e., with larger damping. The AD-FF controller is created using the target specimen dynamics and an inverse of original specimen dynamics. The performance of the proposed techniques is investigated in both traditional shake table testing and RTHS through a uniaxial shake table and a two-story shear building specimen with very low damping. In traditional shake table testing, extra damping was added to all vibrational modes of the specimen. In RTHS, two studies were conducted. In one study, damping was selectively added to the

higher specimen modes, and in the other study, damping was added to all modes. The target system behavior was consistently achieved in the experiments.

8.1.3 Application of the proposed RTHS approach on the protection of low-frequency structures

The proposed RTHS approach was further validated on a large-scale specimen in an NSF-sponsored research project at Tohoku University in Japan for the performance evaluation of inter-story isolation and associated structural control strategies. The substructure below inter-story isolation was simulated numerically while the superstructure including inter-story isolation is tested experimentally. The shake table used in this study was 3 by 3 m with a capacity of 10 metric tons and a specimen of 5 metric tons. Large-scale specimens are needed to accurately capture the nonlinear behavior of representative control devices, isolation systems, and hybrid isolation systems. The RTHS framework is demonstrated to be accurate for evaluating large-scale experimental specimens as a substructure of an even larger structural system, a great benefit for structural control studies. Furthermore, the techniques are simple, applicable to specimens regardless of scale, and make use of readily available equipment in laboratories worldwide.

The experimental substructure investigated is a SDOF base-isolated specimen, demonstrated to be sufficient to model multiple upper stories above and including the inter-story isolation layer. The scaled structural model used in this study can represent the target model accurately with similar mode shapes and natural frequencies. The response of the structure with inter-story isolation was investigated through the proposed RTHS techniques. The stability of RTHS was found to be very tolerant to delay in the RTHS

loop, owing to the low natural frequency and base shear of the specimen. Thus, RTHS based on the proposed strategies is demonstrated as an excellent method to study inter-story isolation.

The effectiveness of the overall RTHS in reproducing the total structural behavior was verified through comparisons with numerical simulations. This confidence will enable studies of more complex inter-story isolation systems that may not be easily modeled numerically, including large-scale nonlinear isolator specimens and supplemental control devices in semi-active or active control modes. Experimental studies through RTHS will open the door to future development of technologies for inter-story isolation.

The benefits of implementing inter-story isolation such as on retrofit application were confirmed through RTHS. Base shear is maintained at low levels relative to the structure before retrofit. Furthermore, the stories above the isolation layer exhibit very low levels of acceleration. Inter-story isolation is shown to be an attractive alternative to traditional structural systems, creating nominally decoupled systems with large architectural and structural design freedom. The capability of the existing foundations to vertically support the additional floors must be carefully checked before the retrofit and, if necessary, they should be reinforced.

8.1.4 Development and application of CPSO using substructure RTHS

This research presents a novel framework of cyber-physical substructure optimization (CPSO) for conducting structural optimization using substructure RTHS. The proposed technique is demonstrated to be robust and efficient in achieving optimal design of structure or supplemental devices with nonlinear and complex components which are

difficult to model numerically. The development of the CPSO framework is discussed in detail with particle swarm optimization (PSO) selected to guide the solution searching. Two studies are presented as a proof-of-concept of the proposed technique. Through the CPSO technique, the base isolation design is optimized for the seismic protection of a simple two-story shear building against single and multiple earthquakes. Furthermore, a nonlinear system consisting of a 5-story base-isolated structure with an MR damper in the isolation layer is investigated to show the benefit of the proposed CPSO-RTHS framework for difficult-to-model components. The results using CPSO technique are compared with numerical simulation. The numerical model of MR damper is not accurate enough to represent the true behavior of MR damper, highlighting the benefits of the proposed technique.

The proposed CPSO framework is validated to be efficient for structural optimization under single earthquake. To improve the efficiency of CPSO for structural protection against multiple ground motion records, a multi-interval PSO (MI-PSO) approach is proposed. The optimization run is divided into multiple intervals so that the worst dynamic excitations are determined and iteratively updated across intervals. The efficiency of optimization is greatly increased especially for complex systems with multiple control variables against a large number of design excitations. This technique is significant contribution of this study for optimal structural design against multiple earthquakes or other natural hazards.

In summary, the proposed CPSO framework is a versatile technique for multi-variate optimization under multiple excitations. This technique combines the accuracy and efficiency of RTHS to cost-effectively evaluate structural behaviors and the benefits

of numerically-driven optimization to efficiently explore different design alternatives and achieve optimal design. This new technique has many potential opportunities and applications in civil engineering.

8.2 Future Studies

This dissertation presents a proof-of-concept study on the use of cyber-physical systems to evaluate structural performance and achieve optimal designs through substructure RTHS under earthquake excitations. Several unique contributions were presented, including the artificial specimen damping technique and a framework for cyber-physical substructure optimization framework in civil engineering. A number of exciting future research avenues exist, detailed below.

- Substructure RTHS framework. There are a few limitations to the proposed method which warrant further study. These include the need for system identification in the creation of the model-based control and limitation to uni-axial shake table motion. These limitations can be overcome through improved shake table control algorithms including multi-axial control algorithms. In its current form, the proposed approach offers a versatile framework for shake table RTHS studies that can be adapted for individual testing needs. Future studies will focus on the extension of the proposed techniques to increasingly more realistic structural systems.
- Artificial specimen damping. One limitation of the method is that it would require updating if the natural frequency of the specimen were to drift, say under

significant damage. Also, with only one control point (the shake table), reduced success is anticipated if adding damping to many specimen vibrational modes.

- Inter-story isolation. More advanced studies into inter-story isolation are enabled by the methods proposed in this research. Future studies will focus on applying the technique proposed in this paper to taller buildings (requiring rotational DOF in modeling and shake table control) to investigate and compare the performance of seismic isolation techniques to other energy dissipation techniques for seismic protection.
- CPSO framework. PSO was selected for the optimization algorithm and was subsequently modified to be suitable for multiple design earthquakes while limiting the number of experiments required. Future work should consider other optimization alternatives, including gradient-based algorithms, which may be more efficient for simpler problems.
- CPSO framework. CPSO presents an opportunity to design multi-hazard resistant structures with accurate physical modeling of critical structural components (e.g., considering both earthquake and wind loads in the design).
- Cyber-physical systems. There is a strong need to enhance community resilience in the face of man-made and natural catastrophes. However, most research still remains at a conceptual level. The challenges remain in the development of standard metrics, risk assessment, risk communication, and efficient models to evaluate the disaster resilience of communities. Cyber-physical systems are exciting tools with potential opportunity to deliver sustainable, intelligent, and resilient infrastructure.

REFERENCES

ASCE/SEI (2010). Minimum Design Loads for Buildings and Other Structures, American Society of Civil Engineers, Structural Engineering Institute: Reston, VA.

Azadivar, F. (1992). "A tutorial on simulation optimization." *In Proceedings of the 24th conference on Winter simulation*, pp. 198-204. ACM.

Baskar, N., Asokan, P., Prabhaharan, G. and Saravanan, R. (2005). "Optimization of machining parameters for milling operations using non-conventional methods." *The International Journal of Advanced Manufacturing Technology*, 25(11): 1078-1088.

Blondet, M. and Esparza, C. (1988). "Analysis of shaking table-structure interaction effects during seismic simulation tests." *Earthquake Engineering and Structural Dynamics*, 16(4):473-90.

Carlson, J. D. and Jolly, M. R. (2000). "MR fluid, foam, and elastomer devices." *Mechatronics*, 10(4-5): 555-569.

Carrion, J. E. and Spencer Jr., B. F. (2007). "Model-based strategies for real-time hybrid testing." *Newmark Structural Engineering Laboratory Report Series*, University of Illinois at Urbana-Champaign, Urbana, IL, No. 6.

Carrion, J. E., Spencer Jr., B. F., and Phillips B. M. (2009). "Real-time hybrid simulation for structural control performance assessment." *Earthquake Engineering and Engineering Vibration*, 8(4), 481-492.

Charney, F. A. (2008). "Unintended consequences of modeling damping in structures." *Journal of structural engineering*, 134(4), 581-592.

Christensen, R. E., Lin, Y., Emmons, A., and Bass, B. J. (2008). "Large-scale experimental verification of semi-active control through real-time hybrid simulation." *Journal of Structural Engineering*, 134(4): 522-534.

Davis, L. (1987). Genetic algorithms and simulated annealing. Pitman, London, England.

Dutta, A., Sumnicht, J. F., Mayes, R. L., Hamburger, R. O., and Citipitioglu, A. (2008). "An innovative application of base isolation technology." *Proceedings of 18th Analysis and Computation Specialty Conference*, ASCE Structures Congress, Vancouver, BC, Canada (pp. 18-20).

Dyke, S. J., Spencer Jr., B. F., Quast, P., and Sain, M. K. (1995). "Role of control-structure interaction in protective system design." *Journal of Engineering Mechanics*, 121(2): 322-338.

Dyke, S. J., Spencer, Jr., B. F., Sain, M. K., and Carlson, J. D. (1996). “Modeling and control of magnetorheological dampers for seismic response reduction.” *Smart Materials and Structures*, 5(5): 565-575.

Fletcher, J. N. (1990). “Global simulation: new technique for multi-axis test control.” *Sound and Vibration*, 24(11), 26-33.

Glynn, P. W. (1987). “Likelilood ratio gradient estimation: an overview.” *In Proceedings of the 19th conference on Winter simulation*, pp. 366-375. ACM.

Goldberg, D. E. (1989). “Genetic algorithms in search optimization and machine learning.” Addison-Wesley, Reading, Mass.

Hakuno M., Shidawara M., and Hara T. (1969). “Dynamic destructive test of a cantilever beam controlled by an analog computer.” *Transactions of the Japan Society of Civil Engineers*, 171:1-9.

Hall, J. F., Heaton, T. H., Halling, M. W., and Wald, D. J. (1995). “Near-source ground motion and its effects on flexible buildings.” *Earthquake Spectra*, 11(4), 569-605.

He, S., Wu, Q. H., Wen, J. Y., Saunders, J. R., and Paton, R. C. (2004). “A particle swarm optimizer with passive congregation.” *Biosystems*, 78(1), 135-147.

Hilber, H. M., Hughes, T. J., and Taylor, R. L. (1977). "Improved numerical dissipation for time integration algorithms in structural dynamics." *Earthquake Engineering and Structural Dynamics*, 5(3), 283-292.

Holland, J. H. (1975). “Adaptation in natural and artificial systems.” University of Michigan Press, Ann Arbor, Mich.

Horiuchi, T., Nakagawa, M., Sugano, M., and Konno, T. (1996). “Development of a real-time hybrid experimental system with actuator delay compensation.” *Proceedings of the 11th World Conf. Earthquake Engineering*, Paper No. 660.

Jiang, Z. and Christenson, R. E. (2011). “A Comparison of 200 kN magneto-rheological damper models for use in real-time hybrid simulation pretesting.” *Smart Materials and Structures*, 20(6).

Jeary, A. (1997). “Damping in structures.” *Journal of Wind Engineering and Industrial Aerodynamics*, 72, 345-355.

Johnson, E. A., Ramallo, J., Spencer, Jr., B. F., and Sain, M. K. (1998). ‘‘Intelligent base isolation systems.’’ *Proc., 2nd World Conf. on Structural Control*, Wiley, New York.

Juan, H., Yu, S.F. and Lee, B.Y. (2003). “The optimal cutting-parameter selection of production cost in HSM for SKD61 tool steels.” *International Journal of Machine Tools and Manufacture*, 43(7): 679-686.

Keivan, A., Phillips, B. M., Ikenaga, M., and Ikago, K. (2017). “Causal Realization of Rate-Independent Linear Damping for the Protection of Low-Frequency Structures.” *Journal of Engineering Mechanics*, 04017058.

Kelly, J. M., Leitmann, G., Soldatos, A. G. (1987). "Robust control of base-isolated structures under earthquake excitation." *Journal of Optimization Theory and Applications*, 53, 159-180.

Kennedy, J., Kennedy, J. F., Eberhart, R. C., and Shi, Y. (2001). “Swarm intelligence.” Morgan Kaufmann.

Kim, S. B., Spencer Jr., B. F., Yun, C. B. (2005). “Frequency domain identification of multi-input, multi-output systems considering physical relationships between measured variables.” *Journal of Engineering Mechanics*, 131(5): 461-473.

Kuehn J., Epp, D., Patten, W. N. (1999). “High-fidelity control of a seismic shake table.” *Earthquake Engineering and Structural Dynamics*. 28(11):1235-1254.

Kurdi, M. H., Schmitz, T. L., Haftka, R. T., and Mann, B. P. (2004). “Simultaneous optimization of removal rate and part accuracy in high-speed milling.” *In ASME 2004 International Mechanical Engineering Congress and Exposition*, pp. 1001-1009. American Society of Mechanical Engineers.

Kurdi, M. H. (2005). “Robust multicriteria optimization of surface location error and material removal rate in high-speed milling under uncertainty.” Doctoral dissertation, University of Florida.

Li, H., and Li, X. (2000). “Modelling and simulation of chatter in milling using a predictive force model.” *International Journal of Machine Tools and Manufacture*, 40(14), 2047-2071.

Lin, F., Maghareh, A., Dyke, S. J., and Lu, X. (2015). “Experimental implementation of predictive indicators for configuring a real-time hybrid simulation.” *Engineering Structures*, 101, 427-438.

Mahin, S. A. and Shing, P. B. (1985). “Pseudodynamic method for seismic testing.” *Journal of Structural Engineering*, 111(7): 1482-1503.

Mahin, S. A., Shing, P. B., Thewalt, C. R., and Hanson, R. D. (1989). “Pseudodynamic test method. Current status and future directions.” *Journal of Structural Engineering*, 115(8): 2113-2128.

Murakami K, Kitamura H, Ozaki H, Yamanashi T. (1999). "Design of a building with seismic isolation system at the mid-story." *Journal of Technology and Design*, Architectural Institute of Japan 1999; 7, 51-56.

Nakashima, M., Kato, H., and Takaoka, E. (1992). "Development of real-time pseudo dynamic testing." *Earthquake Engineering and Structural Dynamics*, 21(1): 79-92.

Nakata, N. (2010). "Acceleration trajectory tracking control for earthquake simulators." *Engineering Structures*, 32(8): 2229-2236.

Nakata, N., and Stehman, M. (2014). "Compensation techniques for experimental errors in real-time hybrid simulation using shake tables." *Smart Structures and Systems*, 14(6), 1055.

Ohtori, Y., Christenson, R. E., and Spencer Jr., B. F. (1994). "Benchmark control problems for seismically excited nonlinear buildings." *Journal of Engineering Mechanics*, 130(4): 366-385.

Phillips, B.M., Chae, Y., Jiang, Z., Spencer Jr., B.F., Ricles, J.M., Christenson, R.E., Dyke, S.J., and Agrawal. A. (2010). "Real-Time Hybrid Simulation Benchmark Structure with a Large-Scale MR Damper." *Proc., 5th World Conference on Structural Control and Monitoring*, Shinjuku, Tokyo, July.

Phillips, B. M. and Spencer Jr., B. F. (2011). "Model-based feedforward-feedback tracking control for real-time hybrid simulation." *Newmark Structural Engineering Laboratory Report Series*, University of Illinois at Urbana-Champaign, Urbana, IL, No. 28.

Phillips, B. M., and Spencer Jr, B. F. (2012). "Model-based feedforward-feedback actuator control for real-time hybrid simulation." *Journal of Structural Engineering*, 139(7), 1205-1214.

Phillips, B. (2012). "Model-based feedforward-feedback control for real-time hybrid simulation of large-scale structures." *Doctoral dissertation*, University of Illinois at Urbana-Champaign.

Phillips, B. M., Takada, S., Spencer, B. F., and Fujino, Y. (2014). "Feedforward actuator controller development using the backward-difference method for real-time hybrid simulation." *Smart Structures and Systems*, 14(6), 1081-1103.

Rayleigh, J. W. S. B. (1896). "The theory of sound (Vol. 2)." Macmillan.

Rea, D., Abedi-Hayati, S., and Takahashi, Y. (1977). "Dynamic analysis of electrohydraulic shaking tables." Earthquake Engineering Center, University of California.

Rinawi, A. M., and Clough, R. W. (1991). “Shaking table-structure interaction.” Earthquake Engineering Research Center, University of California at Berkeley.

Rozvany, G. I. (2009). “A critical review of established methods of structural topology optimization.” *Structural and multidisciplinary optimization*, *37*(3), 217-237.

Ryan, K., and Hall, J. F. (1998). “Aspects of building response to near-source ground motions.” *Structural Engineering World Wide 1998*.

Seki, K., Iwasaki, M., Kawafuku, M., Hirai, H., and Yasuda, K. (2009). “Adaptive compensation for reaction force with frequency variation in shaking table systems.” *Industrial Electronics*, IEEE Transactions on, 56(10), 3864-3871.

Shao, X., Reinhorn, A. M., and Sivaselvan, M. V. (2010). “Real-time hybrid simulation using shake tables and dynamic actuators.” *Journal of Structural Engineering*, 137(7), 748-760.

Shi, Y., and Eberhart, R. (1998). “A modified particle swarm optimizer.” *In Evolutionary Computation Proceedings*, 1998. IEEE World Congress on Computational Intelligence. The 1998 IEEE International Conference on, pp. 69-73. IEEE.

Shing, P. B. and Mahin, S. A. (1983). “Experimental error propagation in pseudodynamic testing.” UCB/EERC-83/12, Earthquake Engineering Research Institute. University of California, Berkeley, CA.

Shing, P. S. B., and Mahin, S. A. (1987). “Cumulative experimental errors in pseudodynamic tests.” *Earthquake engineering and structural dynamics*, 15(4), 409-424.

Shing, P. B., Nakashima, M., and Bursi, O. S. (1996). “Application of pseudodynamic test method to structural research.” *Earthquake Spectra*, 12(1): 29-54.

Shing, P. B. (2008). “Real-time hybrid testing techniques.” *Modern Testing Techniques for Structural Systems*, Eds. O. S. Bursi and D. J. Wagg, Springer, Vienna, pp. 259-292.

Simova, M. and Mamucevski, D. (1980). “On-line control of single component shaking table.” *Proceedings of 7th World Conf. on Earthquake Engineering*, Istanbul, Turkey, pp. 63-69.

Somerville, P. (1997). “Development of ground motion time histories for Phase 2 of the FEAM/SAC steel project.” *SAC Background document SAC/BD-91/04*, SAC joint venture, Sacramento, California.

Song, W., & Dyke, S. (2013). “Development of a cyber-physical experimental platform for real-time dynamic model updating.” *Mechanical Systems and Signal Processing*, 37(1), 388-402.

Spencer Jr., B. F., Dyke, S. J., Sain, M. K., and Carlson, J. D. (1997). "Phenomenological model for magnetorheological dampers." *Journal of Engineering Mechanics*, 123(3), 230-238.

Spencer Jr., B. F., Yang, G. (1998). "Earthquake simulator control by transfer function iteration."
Proceedings of the 12th ASCE engineering mechanics conference.

Sueoka, T., Torii, S., and Tsuneki, Y. (2004). "The application of response control design using middle-story isolation system to high-rise building." *In 13th World Conference on Earthquake Engineering*.

Tagawa, Y., and Kajiwara, K. (2007). "Controller development for the E-Defense shaking table." *Proceedings of the institution of mechanical engineers*, Part I: *Journal of Systems and Control Engineering*, 221(2), 171-181.

Tandon, V., El-Mounayri, H., and Kishawy, H. (2002). "NC end milling optimization using evolutionary computation." *International Journal of Machine Tools and Manufacture*, 42(5), 595-605.

Tasaka, M., Mori, N., Yamamoto, H., Murakami, K., and Sueoka, T. (2008). "Applying Seismic Isolation to Buildings in Japan - Retrofitting and Middle-Story Isolation." *In Proc. 18th Analysis and Computation Specialty Conference*, ASCE Structures Congress, Vancouver, BC, Canada, pp. 18-20.

Wang, Z. G., Rahman, M., Wong, Y. S., and Sun, J. (2005). "Optimization of multi-pass milling using parallel genetic algorithm and parallel genetic simulated annealing." *International Journal of Machine Tools and Manufacture*, 45(15), 1726-1734.

Wen, Y. K. (1976). "Method for random vibration of hysteretic systems." *Journal of the Engineering Mechanics Division*, 102(2), 249-263.

Yamane, K., Tsubaki, H., Tanaka, T., and Sumi, A. (2003). "Isolation story structure of Umeda Tower, Osaka, Japan: Structures subjected to extreme natural and man-made hazards." *Structural Engineering International*, 13(4), 225-227.

Zapateiro, M., Karimi, H. R., Luo, N., and Spencer, B. F. (2010). "Real-time hybrid testing of semiactive control strategies for vibration reduction in a structure with MR damper." *Structural Control and Health Monitoring*, 17(4), 427-451.

Zhang, R., Lauenstein, P. V., and Phillips, B. M. (2016). "Real-time hybrid simulation of a shear building with a uni-axial shake table." *Engineering Structures*, 119, 217-229.

Zhang, R., and Phillips, B. M. (2017). "Artificial Specimen Damping for Substructure Real-Time Hybrid Simulation." *Journal of Engineering Mechanics*, 143(8), 04017052.